Calibrating the cosmic-ray energy scale of the Pierre Auger Observatory using radio detection of extensive air showers in AERA

Zur Erlangung des akademischen Grades eines

Doktors der Naturwissenschaften

von der KIT-Fakultät für Physik des
Karlsruher Instituts für Technologie (KIT)
und der
Universidad Nacional de San Martín (UNSAM)
genehmigte

Dissertation

von

Max Büsken
aus Raesfeld

Tag der mündlichen Prüfung: 7. Februar 2025
Erster Gutachter: Prof. Dr. Ralph Engel
Zweiter Gutachter: Prof. Dr. Brian Wundheiler
Betreuer: Prof. Dr. Tim Huege

Abstract

The Pierre Auger Observatory is the largest facility for the detection of ultra-high energetic cosmic rays. With multi-hybrid observations of extensive air showers it measures key properties of the cosmic particles. One detection technique whose relevance to the community has grown significantly in the past years, is the measurement of coherent radio signals release in air showers. At the Auger Observatory, radio detection has been taken on in a small part of the observatory with the Auger Engineering Radio Array (AERA) for over ten years. The experiences and successes made with AERA resulted in the recently installed new Radio Detector (RD) that is on to expand on studies made with AERA and enhance the sensitivity and physics results of the Pierre Auger Observatory in general. One particular task that can be done with radio detectors is determining the absolute energy scale of cosmic rays. Providing an accurate energy scale is crucial to the interpretation of almost all results about the properties of cosmic rays that can be obtained with the Auger Observatory. We bring together several ingredients for calibrated energy measurements of air showers with AERA to perform a cross-calibration of its energy scale with the established energy scale of the Pierre Auger Observatory from the fluorescence detector (FD). As the first ingredient, we make use of unprecedented statistics of hybrid measurements with the dense surface detector array (SD-750) and AERA. The AERA data are cleaned for periods affected by strong atmospheric fields in thunderstorms using existing electric field mills. To be able to conduct a follow-up analysis of the radio energy scale with the RD in the future, we deployed five new remote stations with electric field mills spread across the Pierre Auger Observatory. The stations are designed to automatically provide an absolute calibration of their electric-field measurements with an accuracy of 6.5%. Further ingredients for the energy-scale analysis with AERA include a well-developed radio reconstruction and an accurate calibration of AERA using the diffuse Galactic emission. The Galactic calibration plays a key role in the radio energy scale. To understand its accuracy, we perform a dedicated study on models of the Galactic radio sky finding a global systematic uncertainty estimate of 7.2% on the cosmic-ray energy scale that reduces to 5.9% in the case of the radio detectors at the Auger Observatory. With all ingredients collected, we select around 600 hybrid air-shower events (SD-750 – AERA) of high quality that we simulate in CORSIKA and CoREAS with their energy estimated on the FD energy scale. These events have energies from 3×10^{17} eV to 4×10^{18} eV and zenith angles up to 55°. By data-to-simulation comparison of the radio energy estimators, we find that the radio energy scale is set 12% higher than the FD energy scale. We discuss the systematic uncertainties extensively, which currently are of the order of the difference between the energy scales. This result constitutes an important independent cross-check of the energy scale of the Pierre Auger Observatory. Perspectively, the FD and radio energy scales could be combined. A validation and extension of the presented analysis to inclined events and to the highest energies will be done with the RD.

Zusammenfassung

Das Pierre Auger Observatorium ist die größte Einrichtung für die Detektion ultrahochenergetischer kosmischer Strahlung. Mit Multi-Hybrid-Beobachtungen ausgedehnter Luftschauer misst es Schlüsseleigenschaften der kosmischen Teilchen. Eine Detektionsmethode, deren Bedeutung für die wissenschaftliche Gemeinschaft in den letzten Jahren stark zugenommen hat, ist die Messung kohärenter Radiosignale, die in Luftschauern freigesetzt werden. Am Auger Observatorium wird die Radiodetektion seit über zehn Jahren in einem kleinen Teil des Observatoriums mit dem Auger Engineering Radio Array (AERA) durchgeführt. Die mit AERA gesammelten Erfahrungen und Erfolge führten zum kürzlich installierten neuen Radiodetektor (RD), der die mit AERA gemachten Studien erweitern und die Empfindlichkeit und die physikalischen Ergebnisse des Pierre Auger Observatoriums im Allgemeinen bereichern wird. Eine besondere Aufgabe, die mit Radiodetektoren erfüllt werden kann, ist die Bestimmung der absoluten Energieskala der kosmischen Strahlung. Die Bereitstellung einer genauen Energieskala ist entscheidend für die Interpretation fast aller Ergebnisse über die Eigenschaften der kosmischen Strahlung, die mit dem Auger Observatorium gewonnen werden können. Wir bringen mehrere Komponenten für kalibrierte Energiemessungen von Luftschauern mit AERA zusammen, um eine Kreuzkalibrierung von dessen Energieskala mit der etablierten Energieskala des Pierre Auger Observatoriums von dem Fluoreszenzdetektor (FD) durchzuführen. Als ersten Baustein nutzen wir eine beispiellose statistische Aussagekraft von Hybridmessungen mit dem dicht gereihten Oberflächendetektor (SD-750) und AERA. Die AERA-Daten werden mit Hilfe bestehender elektrischer Feldmühlen um untaugliche Zeiträume bereinigt, die durch starke atmosphärische Felder in Gewittern beeinflusst sind. Um in Zukunft eine Folgeanalyse der Radioenergieskala mit dem RD durchführen zu können, haben wir fünf neue fernliegende Stationen mit elektrischen Feldmühlen über das Pierre Auger Observatorium verteilt aufgestellt. Die Stationen sind so konzipiert, dass sie automatisch eine absolute Kalibrierung ihrer Messungen des elektrischen Feldes mit einer Genauigkeit von 6,5% liefern. Weitere Bausteine für die Energieskalenanalyse mit AERA sind eine gut entwickelte Radio-Rekonstruktion und eine genaue Kalibrierung von AERA mithilfe der diffusen galaktischen Emission. Die galaktische Kalibrierung spielt eine Schlüsselrolle in der Radioenergieskala. Um ihre Genauigkeit zu erfassen, führen wir eine dedizierte Studie über Modelle des galaktischen Radiohimmels durch und finden eine globale Abschätzung der systematischen Unsicherheit von 7,2% auf der Energieskala der kosmischen Strahlung, die sich im Fall der Radiodetektoren des Auger Observatoriums auf 5,9% reduziert. Mit allen gesammelten Bausteinen selektieren wir etwa 600 hybride Luftschauerereignisse (SD-750 – AERA) von hoher Qualität aus, die wir mit CORSIKA und CoREAS simulieren wobei deren Energie auf der FD-Energieskala angesetzt ist. Diese Luftschauerereignisse haben Energien im Bereich zwischen 3×10^{17} eV und 4×10^{18} eV und Zenitwinkeln bis zu 55°. Durch den Vergleich von Daten und Simulationen der Radioenergie-Schätzer stellen wir fest, dass die Radioenergieskala 12% höher liegt als die FD-Energieskala. Wir diskutieren ausführlich die systematischen Unsicherheiten, die derzeit in der Größenordnung der Differenz zwischen den Energieskalen liegen. Dieses Ergebnis stellt eine wichtige unabhängige Gegenprüfung der Energieskala des Pierre Auger Observatoriums dar. Perspektivisch könnten die FD- und die Radioenergieskala kombiniert werden. Eine

Validierung und Ausweitung der vorgestellten Analyse auf geneigte Luftschauer und auf die höchsten Energien wird mit dem RD durchgeführt werden.

Resumen

El Observatorio Pierre Auger es la mayor instalación de detección de rayos cósmicos de ultra alta energía. Mediante observaciones multihíbridas de cascadas atmosféricas extensas, mide propiedades clave de las partículas cósmicas. Una técnica de detección cuya importancia para la comunidad ha crecido significativamente en los últimos años, es la medición de las señales de radio coherentes liberadas en las cascadas atmosféricas. En el Observatorio Auger durante más de diez años la detección de radio se ha llevado a cabo en una pequeña parte del observatorio con el Auger Engineering Radio Array (AERA). La experiencia y los éxitos realizados con AERA dieron lugar a la instalación reciente del nuevo Radio Detector (RD), que está en marcha para ampliar los estudios realizados con AERA y mejorar la sensibilidad y los resultados de la física del Observatorio Pierre Auger en general. Una tarea particular que puede realizarse con los detectores de radio es determinar la escala de energía absoluta de los rayos cósmicos. Proporcionar una escala de energía precisa es crucial para la interpretación de casi todos los resultados sobre las propiedades de los rayos cósmicos que pueden obtenerse con el Observatorio Auger. Reunimos varios ingredientes de las mediciones obtenidas con la calibración de energía de AERA para realizar una calibración cruzada con la calibración obtenida mediante el detector de fluorescencia (FD) del observatorio Pierre Auger. Como primer ingrediente, hacemos uso de estadísticas sin precedentes de mediciones híbridas con el arreglo de detectores de superficie densa (SD-750) y AERA. Los datos de AERA se limpian para los periodos afectados por fuertes campos atmosféricos en tormentas eléctricas utilizando los molinos de campo eléctrico existentes. Para poder realizar en el futuro un análisis de seguimiento de la escala de radioenergía con el RD, desplegamos cinco nuevas estaciones remotas con molinos de campo eléctrico repartidas por todo el Observatorio Pierre Auger. Las estaciones están diseñadas para proporcionar automáticamente una calibración absoluta de sus medidas de campo eléctrico con una precisión del 6,5%. Otros ingredientes para el análisis a escala energética con AERA incluyen una reconstrucción de radio apropiada y una calibración precisa de AERA utilizando la emisión difusa galáctica. La calibración galáctica desempeña un papel clave en la escala de energía de radio. Para comprender su precisión, realizamos un estudio dedicado sobre modelos del cielo galáctico en radio encontrando una estimación de la incertidumbre sistemática global del 7,2% en la escala de energía de rayos cósmicos, la cual que se reduce al 5,9% en el caso de los detectores de radio del Observatorio Auger. Con todos los ingredientes recogidos, seleccionamos alrededor de 600 eventos híbridos de lluvia de aire (SD-750 – AERA) de alta calidad que simulamos en CORSIKA y CoREAS con su energía estimada en la escala de energía FD. Estos eventos tienen energías entre 3×10^{17} eV y 4×10^{18} eV y ángulo cenital de hasta 55°. Mediante la comparación de los datos con la simulación de los estimadores de energía de radio, descubrimos que la escala de energía de radio es un 12% más alta que la escala de energía FD. Discutimos ampliamente las incertidumbres sistemáticas, las cuales son del orden de la diferencia entre las escalas de energía. Este resultado constituye una importante verificación independiente de la escala de energía del Observatorio Pierre Auger. En perspectiva, las escalas de energía FD y radio podrían combinarse. Una validación y extensión del análisis presentado a eventos inclinados y a las energías más altas se realizará con el RD.

Contents

1

Introduction

The research of cosmic rays, in particular ultra-high energy cosmic rays (UHECRs), has grown to become a topic of great interest. At the highest energies, cosmic rays get so rare that very large detectors are needed to observe them. Then, only the indirect detection of these rare particles through the observation of extensive air showers offers a foundation for drawing scientific conclusions. In recent years, the construction of large observatories has facilitated precise measurements of key properties of cosmic rays. However, open questions remain: *What are the sources of UHECRs? How do they accelerate the particles to such extreme energies? What exact types of particles arrive at Earth and how are they distributed? How can we improve our understanding of the physics of air showers?*

Optimized upgrades of existing instruments and the addition of new detector systems are required to work out the answers to those questions. A particularly interesting technique for the detection of UHECRs that has arisen in the past 20 years and has reached a mature stage is the measurement of pulsed radio emission from particle showers in the MHz regime. While several radio detector arrays are in development worldwide, two important representatives of this technique are the Auger Engineering Radio Array (AERA) and the follow-up Radio Detector (RD) at the Pierre Auger Observatory. AERA was built as a pathfinder leading to the RD on the full scale of the Auger Observatory and in doing so it collected many air-shower events over the years that contain interesting physics results.

One special quality of the radio detection technique is that it is able to probe the absolute cosmic-ray energy scale. With this feature, it stands next to the fluorescence technique that is the established technique to provide the energy scale for the published UHECR-physics results. As a central ingredient in most analyses a good accuracy of the energy scale is essential. At the Pierre Auger Observatory, the presence of detectors of both detection techniques gives the unique opportunity to cross-check the respective energy scales directly.

Based on hybrid air-shower events from AERA and the dense sub-array of the surface detector (SD-750) of the Pierre Auger Observatory, an analysis has been developed over the past decade to establish the access of the radio detection technique to the absolute cosmic-ray energy scale via AERA and to compare it to the established energy scale set by the fluorescence detector (FD). In this thesis, we aim to follow up and conclude this analysis with a recipe that can be adopted in a subsequent work also for the RD.

It takes several ingredients to obtain useful data from radio detectors and properly reconstruct candidate events for a high-level analysis as we aim for here. One aspect of data quality control is monitoring the atmosphere that the showers develop in for the presence of strong electric fields associated with thunderstorms. Under such conditions, the radio signals can be heavily disturbed, which introduces biases in higher-level

analyses. In the case of AERA, thunderstorm-affected periods can be spotted rather easily by locally monitoring the atmospheric electric field with an electric field mill (EFM). The instruments and procedures for a thunderstorm veto for AERA have already been put in place. However, the local electric-field measurement at AERA is not sufficient to provide a reliable thunderstorm monitoring for the much more extended RD. Within this work, we set up a network of new electric field mills at the Pierre Auger Observatory with the main objective to provide large-scale monitoring of atmospheric electricity that will help to identify thunderstorm periods for the operation of the RD. This network constitutes one step towards high-quality data selection for analyses with the RD. As a byproduct, the electric field measurements can become useful to cosmo-geophysics related research.

With regard to the energy-scale analysis with AERA, several more ingredients need to be collected. In the past years, the necessary high-quality statistics have been recorded and many efforts have been made to provide an absolute calibration of AERA. To this end, we present an involved study, in which we compare sky models for the prediction of the diffuse Galactic radio emission that is used to calibrate AERA. We keep the study at a generalized level to estimate systematic uncertainties in the Galactic calibration for current and upcoming radio detection arrays in astroparticle physics.

With the gathered statistics, calibrated detectors, high-precision simulations of the radio emission in air-showers and a validated event reconstruction, we perform the analysis on the cosmic-ray energy scale. We conduct a cross-calibration of the FD energy scale with the radio energy scale via AERA. We perform an event-by-event comparison of the radio emission released by measured and matched simulated air showers that on average provides a metric for the agreement between the two energy scales. The analysis probes the phase space of energies from 3×10^{17} eV to 4×10^{18} eV and shower inclinations up to 55°. We conduct several studies in search for systematic effects and collect a list of systematic uncertainties.

The thesis is structured as follows: In Chap. 2, the foundations of the physics of UHECRs and extensive air showers, in particular their radio emission, are provided. Next, the Pierre Auger Observatory and its detectors are introduced in Chap. 3. Chap. 4 presents the deployed network of electric field mills, and a brief investigation of the first two years of its data as well as an outlook on their application in the contexts of the RD and of cosmo-geophysics. In Chap. 5, we present the uncertainty study for the Galactic calibration of radio detection arrays. Then, we introduce the calibration of AERA and its event reconstruction in Chap. 6. After an introduction to energy measurements of air showers at the Pierre Auger Observatory and the previous work on the radio energy scale in Chap. 7, we present our new approach and the results of the calibration of the energy scale of the Pierre Auger Observatory with the radio detection technique in AERA in Chap. 8. Lastly, a summary of this thesis is given in Chap. 9.

2

Cosmic rays & air showers

This thesis presents work on auxiliary instrumentation, experimental techniques and analyses on the foundations for measurements of extensive air showers for the study of ultra-high energy cosmic rays (UHECRs). We put the work into context by first reviewing the physics of UHECRs and air showers – with focus on their radio emission – in Secs. 2.1 and 2.2, respectively.

2.1 Ultra-high energy cosmic rays

Cosmic rays are atomic nuclei that get accelerated in astrophysical processes and travel through space. Cosmic rays originate from various sources, including the Sun, the Milky Way and galaxies or other astrophysical objects far beyond. Typically, particles from single protons to iron nuclei are considered. They span a wide range of energies [1]. We speak of *ultra-high energy* cosmic rays if their energy surpasses 10^{18} eV. Such energies are exceeding the possibilities of human-made accelerators by several orders of magnitude. It is of fundamental interest to the research field of UHECRs to understand the extreme conditions and processes that allow atomic particles to reach those energies.

2.1.1 Discovery

Cosmic rays were discovered by Viktor Franz Hess in 1912 when he found during several balloon flights that the rate of ionizing radiation increases with altitude after having reached a certain flight height [2]. He deduced that the radiation must come from above the atmosphere. A pure solar origin could be excluded from flights at night and during a solar eclipse that did not yield lower radiation rates.

In the following decades, cosmic rays became a nature-given laboratory for particle physics. Since accelerators were not yet advanced enough, high-energy interactions of elementary particles were studied with the observation of cosmic rays [3]. The research on these particles became an important discipline in astroparticle physics, combining the still fundamental aspect of particle physics at the highest energies and the prospect of cosmic rays serving as astronomical messengers.

2.1.2 Key properties

The observation of cosmic rays segregates into the identification and reconstruction of fundamental properties. Higher-level studies, in which theoretical ideas are examined with experimental results, rely on these pillars. A few key properties are discussed here.

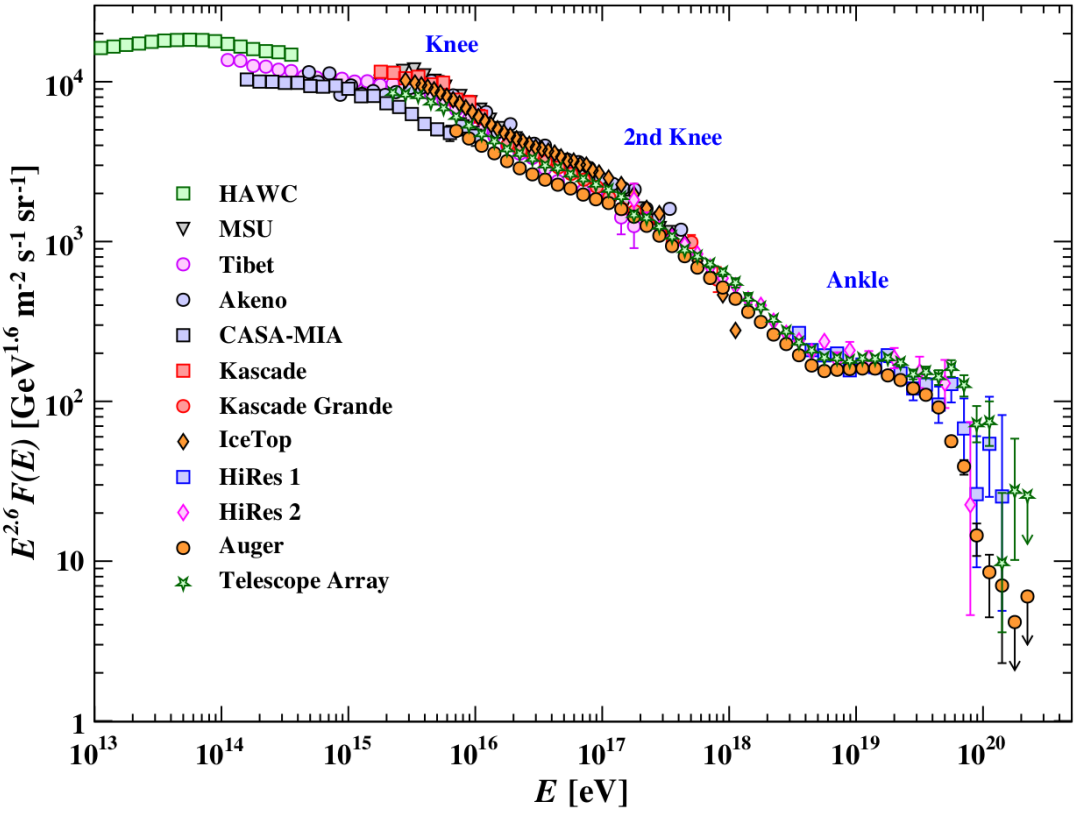

Figure 2.1: Energy spectrum measurements from various observatories above 10^{13} eV. Taken from [4].

Energy spectrum

Measured energy spectra of cosmic rays from several observatories over a wide energy range from 10^{13} eV up to the highest measured energy around 2×10^{20} eV are shown in Fig. 2.1. The shape of the particle flux $F(E)$ can be described quite well by a power law of the form

$$F(E) \propto E^{-\gamma} \tag{2.1}$$

with a spectral index γ that varies as a function of energy. The particle flux measurements in Fig. 2.1 are multiplied with a factor $E^{2.6}$ to provide a better perception of changes in the spectrum. Increased precision and accumulated statistics have led to the discovery of several features over the years.

Up to 10^{15} eV, the measurements yield a scaling of the flux with $E^{-2.7}$ [5]. The spectrum exhibits a steepening, described as its *(first) knee*, between 10^{15} eV and 10^{16} eV beyond which it falls with approximately $E^{-3.1}$ [5]. A *second knee* is found above 10^{17} eV when the spectral behavior hardens to approximately $E^{-3.3}$ [6, 7]. Interestingly, a flattening is seen between 10^{18} eV and 10^{19} eV, known as the *ankle*, followed again by a light steepening, called *instep* just above 10^{19} eV [6]. Beyond 4×10^{19} eV, the spectrum falls off rapidly.

Interpretation of the overall energy spectrum and its features is still very much ongoing work by the theoretical side of cosmic-ray physics as experimental uncertainties

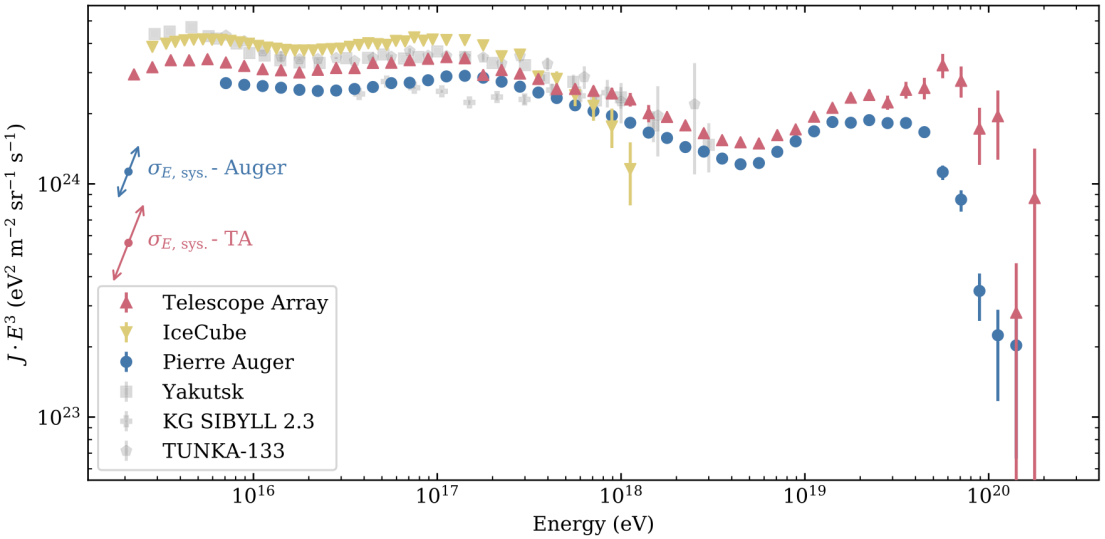

Figure 2.2: Energy spectrum measurements from cosmic rays at the highest energies. Systematic energy scale uncertainties of the Pierre Auger Observatory and Telescope Array are indicated with the arrows. Taken from [8].

fade from the spotlight. The mentioned features of the first and second knee are hypothesized to stem from different primary nuclei populations of Galactic origin dying out at distinct energies. Around the ankle, the Galactic contribution is theorized to overall fall below an extragalactic flux of UHECRs. [8]

An excerpt of the energy spectra is shown in Fig. 2.2 for the highest energies, measured by the two largest observatories – the Pierre Auger Observatory in the southern hemisphere and Telescope Array (TA) in the northern hemisphere. In that diagram, the cosmic-ray flux, which is denoted as J, is multiplied with E^3. The ankle and instep are clearly visible as well es the cutoff around 10^{20} eV. Also for the hypothesized extragalactic contribution, individual populations of primary nuclei types with different masses may drop off at separate energies being reflected in features like the instep. The *suppression* of the spectrum above 10^{20} eV demands a solid interpretation as well. One explanation is driven by the *GZK effect* [9, 10]. Under the assumption of a proton-dominated primary composition at the highest energies, there is a maximum possible energy that the cosmic rays can maintain for a long propagation distance. Ultimately, protons will be sufficiently energetic to interact with the photons of the cosmic microwave background (CMB) via the delta resonance. The processes

$$\begin{aligned} p + \gamma_{\mathrm{CMB}} \rightarrow\ & \Delta^+ \rightarrow p + \pi^0 \\ & \Delta^+ \rightarrow n + \pi^+, \end{aligned} \tag{2.2}$$

require a minimum energy of the primary cosmic ray of approximately 5×10^{19} eV. Particles at higher energies rapidly suffer energy losses that could lead to the suppression of the measured energy spectrum in the form of a *GZK cutoff*. An second hypothesis sees the cause of the suppression in a limit within the sources with regard to their capabilities to accelerate the particles. This scenario is spurred on by hints for the mass composition getting heavier towards the highest energies. [11]

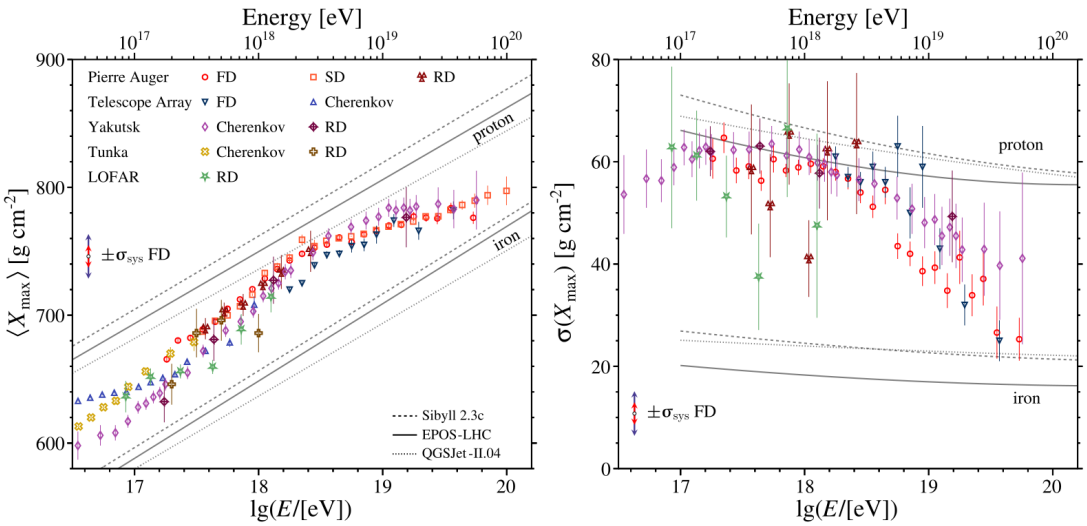

Figure 2.3: Measurements of the depth of shower maximum as a function of cosmic-ray energy. *Left:* average value per energy bin, *right:* size of the scatter per energy bin. Predictions from simulations are depicted by the gray lines. Taken from [8].

The energy spectra from the Auger Observatory and TA consistently show the mentioned features with an interesting exception for the shape of the tail of the spectrum. In general, they exhibit a systematic disagreement over the entire shared energy range. The flux measured by TA is about 9% larger. This offset lies well within the systematic uncertainties of the energy scales of each observatory, which are also shown in Fig. 2.2. The uncertainties are currently estimated at 14% for the Auger Observatory and at 21% for TA. Improving on them is an important challenge that will give a more profound understanding of the energy spectrum. In particular, if the collaborations were able to pin down whether the mismatch can be attributed to systematic differences in their energy scales or if a natural difference in the cosmic-ray flux from the two different hemispheres plays a role.

Mass composition

Intertwined with the energy spectrum is the measurement and reconstruction of the particle types in the flux of cosmic rays. The type of a particle can be inferred from information on its mass. At higher energies, cosmic rays are not detected directly but indirectly through the observation of particle cascades that get initiated when cosmic rays interact with the atmosphere. We discuss these cascades in Sec. 2.2.

An important observable that is sensitive to the mass of the primary cosmic ray is the amount of matter traversed by a particle cascade before it reaches the maximum number of particles. This observable is called *depth of shower maximum*, denoted as X_{max}. Shower-to-shower fluctuations give some inherent uncertainty to this observables for accessing the mass and in turn the particle type. Still, for a given energy, both the average value and the variance of X_{max} are expected to be lower for heavier primary cosmic rays than for lighter particles. In Fig. 2.3, these expectations are represented by the gray lines in the plots of the mean X_{max} and the scatter of X_{max} against cosmic-ray energy in the left and right panels, respectively. The lines are drawn from simulations with different

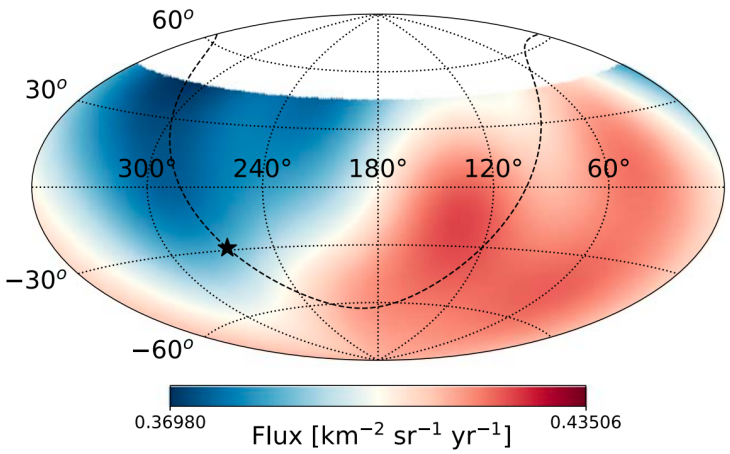

Figure 2.4: Cosmic-ray flux measurement above 8 EeV by the Pierre Auger Observatory in Galactic coordinates. The star denotes the position of the Galactic center. Taken from [12].

hadronic interaction models and show the expected range of the observables for the considered primary particle types. Measurements from several observatories are shown in different colors. Overall, the data consistently suggest a rather light mass composition up to about 2×10^{18} eV, as of which both $\langle X_{\mathrm{max}}\rangle$ and $\sigma_{X_{\mathrm{max}}}$ show a turn towards a heavier composition [8].

Arrival directions

Reconstructing the arrival directions of cosmic rays can directly give insights into what their sources are. With sufficient statistical power, studies about deviations of the distribution of arrival directions from isotropy are possible. These deviations can be separated into large-scale structures in the particle flux and excesses in small sky regions. A fundamental observation is the evidence for a dipolar anisotropy in the flux for energies beyond that of the ankle feature in the spectrum. This discovery has been made by the Pierre Auger Observatory finding a relative amplitude of the flux dipole of 7.4% with a statistical significance of 6.8σ [12]. A diagram of the observed flux is shown in Fig. 2.4. The direction of the dipole is far off from the Galactic center, which suggests that the highest energy cosmic rays are of extragalactic origin. A similar study by Telescope Array currently lacks statistical power in comparison and is only able to give an upper limit to the dipole amplitude of 7.3% (99% confidence level) with a slightly higher threshold energy than in case of the result by the Auger collaboration [13]

The TA collaboration has reported an anisotropy on a smaller scale for energies above the threshold, when the suppression in the energy spectrum sets in [14]. As the position of the reconstructed hotspot is outside of the common declination band between TA and the Auger Observatory, there is no leverage by the latter to provide a second measurement.

Possible sources

The discussed observational pillars of UHECR research are part of what is used in various approaches in search for the origin and the sources of these particles. With the information of the energy spectrum and the mass composition, hypothesized scenarios

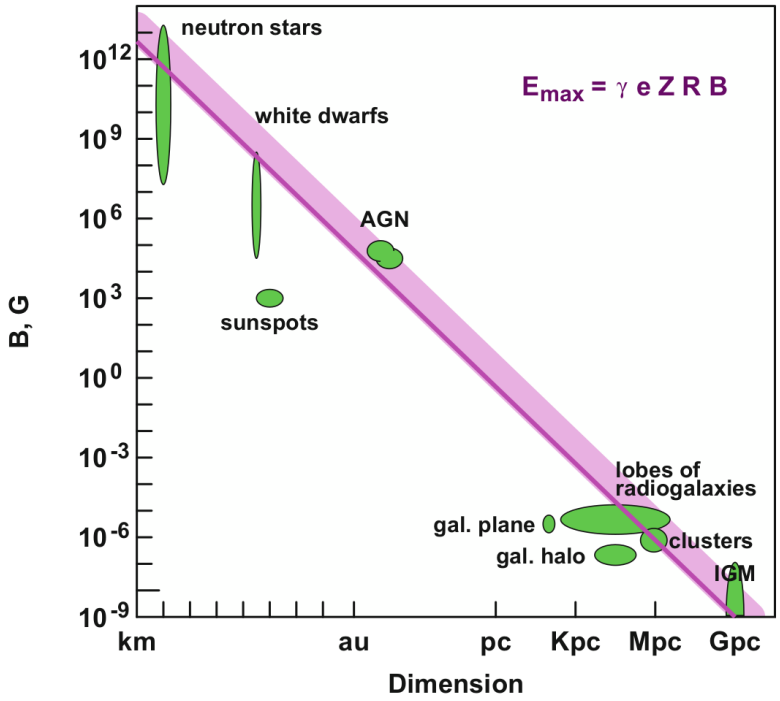

Figure 2.5: "Hillas plot" of the magnetic field strength against the dimension of astrophysical sources. The magenta band denotes the possible phase space for sources to be able to accelerate cosmic rays of mass between protons and iron nuclei to an energy of 10^{20} eV. Taken from [11].

for the necessary acceleration mechanisms are tested [15]. Arrival direction information is an important ingredient in trying to track back the particles to their sources. Also, combined fit analyses are done that take candidate sources with assumed particle emission spectra and simulate the propagation of the cosmic rays to see whether the expectations match the observed results [16]. However, a critical component between the sources and the detection at Earth are the Galactic and extragalactic magnetic fields. As charged particles, cosmic rays are deflected in the magnetic fields making propagation simulations rely on models of those fields [17].

General considerations can be used to narrow down the search for sources to a few candidate types of astrophysical objects. A source for UHECRs must be able to consistently accelerate these particles to the extreme energies above 10^{20} eV. While the acceleration process can be subject to various thinkable mechanics – one popular concept is diffuse shock acceleration of the particles based on ideas introduced by Enrico Fermi [11] – a source has to keep the particle contained during that process. Such containment requires either a strong magnetic field, a large range of influence or a compromise in between. This consideration is visualized in the *Hillas plot* [18]. In Fig. 2.5, the magnetic field B is plotted against the dimension R of a source. The magenta band shows the B, R phase space for potential UHECR sources that would be able to contain particles (range between proton and iron) for acceleration up to a maximum energy of 10^{20} eV. In the plot, also a few types of astrophysical objects are entered, some of which lie on the magenta band. However, several other aspects are important in the search for the origin of UHECRs and the potential sources remain openly discussed.

2.2 Extensive air showers

As is evident from the cosmic-ray energy spectrum shown in Figs. 2.1 and 2.2, the flux of cosmic rays steeply falls with energy. Over a wide energy range, it decreases by approximately three orders of magnitude for every order of magnitude increase in energy. While around 10^{12} eV, about one cosmic ray passes through a unit area of $1\,\mathrm{m}^2$ every second, above about 3×10^{19} eV this rate reduces to only one cosmic ray per unit area of $1\,\mathrm{km}^2$ per year. At low energies, cosmic-rays are directly detected in balloon or space-borne detectors. Covering enough area with detectors to compensate for the small flux in the direct detection of UHECRs would not be feasible, neither in space nor at ground. However, the atmosphere comes to the rescue by providing an interaction medium serving as a calorimeter. UHECRs hitting the Earth eventually interact with an air molecule initiating huge particle cascades, known as *extensive air showers*. In the previous section, we already mentioned that parameters of these air showers are used to infer properties of the primary cosmic ray. Indeed, the observation of air showers is providing the handle to indirectly detect UHECRs.

2.2.1 Discovery

Extensive air showers were discovered by Pierre Auger in 1938 [19]. In measurement campaigns in the Alps, he set up particle counters connected in a coincidence wiring. The coincidental signal rates dropped when increasing the distance between the counters but leaving a finite rate even at distances of 300 m. He concluded that cosmic rays must initiate showers of particles that become quite extended in air.

2.2.2 Development of air showers

A cosmic ray of ultra-high energy that enters the atmosphere of the Earth will collide with an air molecule at some point. In this collision, new particles are created that share the energy of the primary cosmic ray among themselves. The newly created particles propagate mostly in the same direction as the primary cosmic ray and in turn undergo interactions with the air molecules themselves. The process repeats and quickly a multitude of secondary particles is created that propagate towards Earth with some lateral extent around the *shower axis* [20]. At some point in the development of the shower – depending on the energy of the primary particle and on the geometry of the shower – the energies of the secondary particles reach a critical energy, below which ionization of the atmosphere becomes the dominating process. Most particles will be effectively stopped and the shower has died out. The point in the development of the shower, when the number of particles has reached its maximum is an important parameter that relates to properties of the primary cosmic ray. The majority of the shower particles consists of photons, followed by electrons and positrons. For comparability of showers arriving under different angles or atmospheric conditions, the evolution of air showers is measured in the traversed amount of matter, called *atmospheric depth*, until arriving at a point ℓ along the shower track, which is defined as

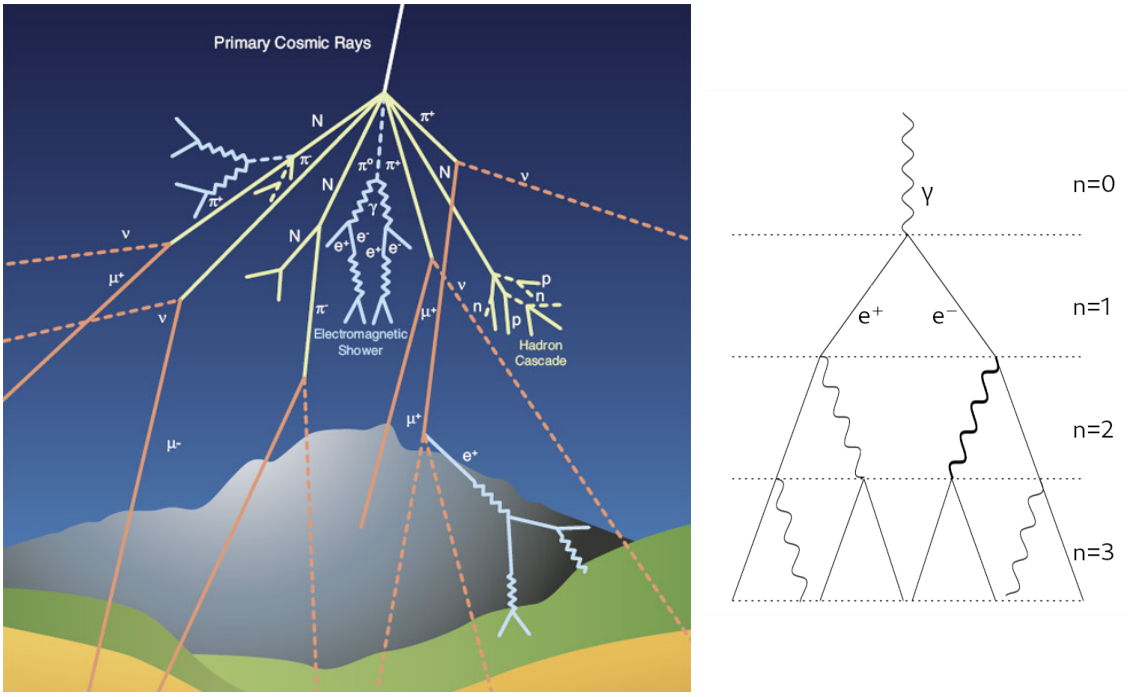

(a) Illustration of particles in an extensive air shower. The hadronic component is shown in yellow. The muonic component is depicted in orange and the electromagnetic component is marked in light blue. Taken from [22].

(b) Illustration of the first few generations of an electromagnetic shower in the Heitler model. Taken and modified from [23].

Figure 2.6: Illustrations of air shower developments.

$$X(\ell) = \int_{\ell}^{\infty} \rho_{\text{air}}(\ell')\,\mathrm{d}\ell' \tag{2.3}$$

with the density of air ρ_{air} along the shower track ℓ'. The *depth of shower maximum*, when the number of shower particles peaks, is denoted as X_{max} [21].

We discuss the shower development in more detail upon explaining its fundamental components. An illustration of an atmospheric particle cascade is shown in Fig. 2.6a.

Hadronic component

The cosmic rays undergo hadronic interactions when hitting air molecules generating secondary mesons, like charged and neutral pions, kaons and ρ-mesons. Also other hadrons can be created. All these particles carry away an amount of energy, which on average decreases with each new generation of secondary particles and which defines if and and how they further interact with the air [21]. In the beginning of the shower, they contribute with subshowers to the overall extension of the cascade. From the numerous pions of the shower, the charged pions will play a big role in this part as long as their energies are still large enough so that their interaction length in air is smaller than their decay length. Later in the shower, when charged pions are at lower energies, they decay into muons and neutrinos, feeding the *muonic component* of the shower. On the other hand, neutral pions quickly decay into photons, thereby initiating cascades of electromagnetic particles that make up the *electromagnetic component*.

Muonic component

The muonic component fed by the hadronic cascades is a reliable tracer for the observation of air showers at ground. With their comparably large decay length, the muons are mostly energetic enough to reach the ground before this component can die out. The number of muons in an air shower is a property that is sensitive to the mass of the primary particle and is therefore of great interest. However, related studies are dealing with the phenomenon that various measurements show larger muon numbers than compatible with any expectation from simulations, dubbed the *muon puzzle* [24].

Electromagnetic component

While the first interaction of the primary cosmic ray with the atmosphere is of hadronic nature, high-energetic photons are soon created in the decay process $\pi^0 \to \gamma\gamma$. Together with other interactions in the shower, this leads to the constitution of the electromagnetic component made up of photons, electrons and positrons.

The development of the electromagnetic shower can be described in a toy model, known as the *Heitler model* [25]. The photons in the cascade lead to the creation of electrons and positrons through pair production in the atmosphere. On the other hand, electrons and positrons emit bremsstrahlung in interactions with nuclei of the air generating new photons. Both processes have similar interaction lengths, commonly expressed as λ_{em}. Under the assumption that the energy is split equally among the new particles at each branching point, the Heitler model describes the shower evolution in a simple scheme, an illustration of which is shown in Fig. 2.6b. Starting with one particle, each generation – numbered by n, starting with $n = 0$ for the initial particle – contains 2^n particles that each have an energy $E_n = E_0/2^n$ if E_0 is the energy of the initial particle. There is a critical energy E_c, below which the particles quickly lose energy through ionization which becomes the dominant process over Bremsstrahlung, and the shower dies out. The generation n_{max}, in which the particles reach this critical energy, is given by the relation $E_0/2^{n_{max}} = E_c$. At this point, the shower traversed an amount of matter that is given by $X_{max} = n_{max}\lambda_{em} = \lambda_{em} \log_2(E_0/E_c)$.

The Heitler model yields a logarithmic dependency of the electromagnetic shower maximum on the energy of the initial particle and has shown to be a good description of the shower development albeit being quite simple. It can also be adapted for the hadronic shower component in the *Heitler-Matthews model* [23].

2.2.3 Simulation of air showers

Simulations of particle cascades are a fundamental ingredient in the development of analyses and methods for the research of cosmic rays and extensive air showers. Many efforts have gone into developing software frameworks for such simulations and into the numerical implementation of the various particle interactions. To this end, popular frameworks like CORSIKA (COsmic Ray SImulations for KAscade) [26] and AIRES (AIRshower Extended Simulations) [27] have been developed. A set of various models for the hadronic interactions at high and low energies are available and still under development. The upcoming CORSIKA 8 framework [28] employs a modern modular architecture that will allow for an easier implementation of different models for the interactions or propagation of particles. Moreover, it will allow for more direct

comparisons of individual ingredients, which helps to better understand systematic effects in air-shower simulations.

2.2.4 Fluorescence emission from air showers

Many of the particles in an air shower (mostly the electromagnetic particles) collide with the molecules of the atmosphere – in particular, with nitrogen molecules – and bring them into an excited state. The molecules subsequently deexcite in a fast fluorescence mechanism under the emission of ultra-violet light, mostly between 290 nm and 430 nm [29]. The emission of this fluorescence light is isotropic and provides a way to observe traces of the air shower from the side rather than just via the detection of the shower particles directly. Although very faint, fluorescence light can be detected and is very important in the research of UHECRs through air showers [30]. The fluorescence technique provides a near-calorimetric measurement of the air shower. However, the observation of fluorescence emission requires profound understanding and monitoring of the atmosphere and the various attenuation processes of the fluorescence light while propagating through it, like scattering and absorption [31]. We discuss aspects of the fluorescence detection technique in more depth in Secs. 3.1 and 7.2.

2.2.5 Radio emission from air showers

Extensive air showers release radio emission during their development. The first signature of this fact was reported in 1965 [32]. Early studies from the years after are reviewed in [33]. After decades of little advancement, the field steadily gained traction since the early 2000s [34]. Technical advancements towards affordable digital equipment allowed to build extended radio detection arrays that sparked new developments of this detection technique which nowadays yields important results on air showers and cosmic rays (see [35] and [36] for reviews).

Radio emission from particle cascades is produced over a wide frequency range. However, in practice mostly frequencies between about 30 MHz up to a few hundred MHz are of interest for the observation of this emission. The overwhelming majority of radio emission stems from the electrons and positrons in the shower. Fundamentally, the emission of radio waves rests on classical electrodynamics as each electron and positron in the shower is a fast moving electrical charge that emits radiation upon acceleration. With the directional development of the particle cascade, basically at the speed of light, the radio emission is coherent – since the shower front is thinner than the frequencies of the radio waves – and forward-beamed. A consequence of the coherent characteristic of the emission is that the strength of the emitted electric field scales linearly with the number of emitting particles, which in turn scales approximately linearly with the energy of the primary cosmic ray. This characteristic gives great value to the radio detection technique, as we discuss in Sec. 7.1. Practically, a key advantage of the observation of radio-frequency signals is the transparency of the atmosphere to these waves. With almost no absorption or scattering of the radio waves in air, no corresponding corrections need to be made to observations. Another important aspect of air-shower radio emission lies in the fact that the radio waves emitted in air propagate at a slightly lower speed

than the shower electrons that emit them due to the refractive index of the atmosphere that is larger than one. At some distance from the shower core, the pulses from all parts of the shower add up at the same observer time and give the strongest signal at ground. This distance is known as the *Cherenkov radius* as it stems from a Cherenkov-like time compression effect.

2.2.5.1 Macroscopic radio emission mechanisms

Over the years, it has proven useful in most applications to describe the radio signal from air showers in terms of macroscopic emission mechanisms. The two most important mechanisms from a geomagnetic and a charge-excess effect are briefly discussed here. A profound exploration on the connection between the macroscopic emission mechanisms and the microscopic radiation processes of the individual particles is given in [37]. Previously unidentified aspects of the macroscopic description of radio emission for inclined air showers developing in strong magnetic fields were found recently in [38].

Geomagnetic emission

The predominant mechanism for the production of radio waves for most air showers is caused by the deflection of the electrons and positrons in the geomagnetic field – contributions by other particles are negligible because of their much lower charge-to-mass ratio. The particles are accelerated onto curved tracks by the Lorentz force

$$\vec{F}_{\text{Lorentz}} = \pm e\, \vec{v} \times \vec{B} \tag{2.4}$$

with the elementary charge e, the velocity vector of a particle $\vec{v}$ and the geomagnetic field vector $\vec{B}$ (in opposite directions for electrons and positrons). This effect is illustrated in Fig. 2.7 to the left. However, the particles still interact with the air molecules and do not propagate uninterrupted. The acceleration in the geomagnetic field and the deceleration from atmospheric interactions balance out. Thereby, the populations of electrons and positrons macroscopically form net currents in opposite directions perpendicular to the shower axis and the geomagnetic field. These transverse currents are time dependent due to the evolution of the air shower and its particle numbers [39]. Propagating with the speed of light in the macroscopic picture they induce a pulsed radio signal. The geomagnetic emission is linearly polarized in the $\vec{v} \times \vec{B}$ direction.

Charge-excess / Askaryan emission

A second macroscopic emission mechanism is based on an excess of negative charges in the shower front and a time variation of it [41]. The excess results from the fact that the air shower ionizes the atmosphere. While the electrons freed in this process mostly move along with the shower, the ionized atoms stay behind, as is shown in the illustration in the right part of Fig. 2.7. This separation of charges with a time-varying excess of electrons in the front, again traveling at the speed of light, also induces a pulsed radio signal. The polarization of the charge-excess emission is in the radial direction in the plane perpendicular to the shower axis.

Usually, the geomagnetic emission dominates the total radio signal of air showers by approximately a factor of ten with respect to the electric field amplitudes. However, if the shower is aligned close to the direction of the geomagnetic field, the geomagnetic emission becomes weak and can become smaller than the charge-excess emission.

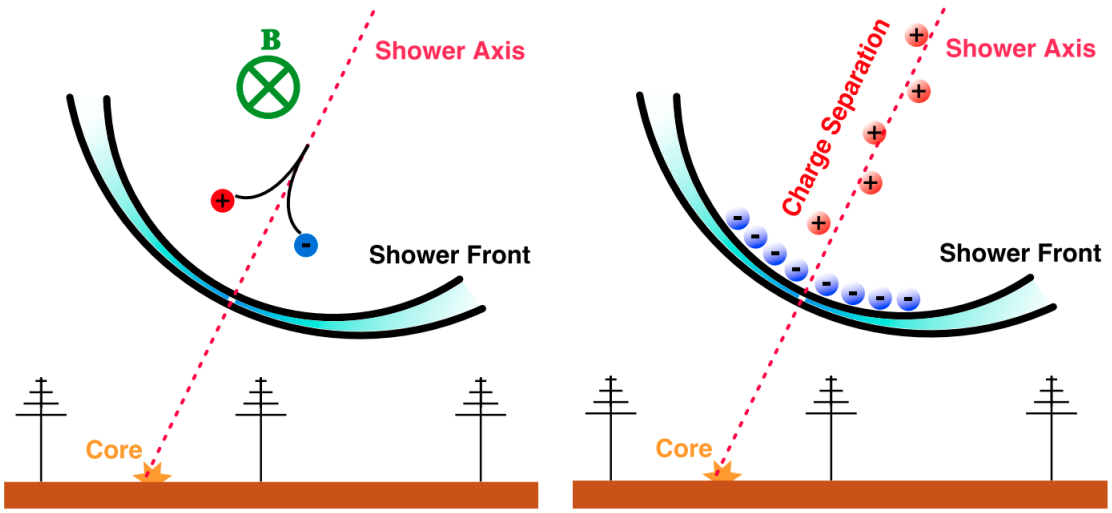

Figure 2.7: Illustrations of the geomagnetic (left) and charge-excess emission (right) of radio waves from air showers. Taken from [40].

2.2.5.2 Simulation of air-shower radio emission

Simulations of the radio emission from air showers are just as important as simulations of the particle cascades. Therefore, efforts have been made to implement the computation of radio signals. The already mentioned frameworks for particle-cascade simulations, CORSIKA and AIRES, were extended with the software packages CoREAS [42] and ZHAireS [43], respectively. Both packages simulate the radio emission of air showers by calculating the microscopic signals released by the acceleration of the individual particles. They employ different formalisms for the calculation but are fundamentally code translations of the same underlying electrodynamics. CoREAS uses the so-called *endpoints* formalism [44], while ZHAireS uses the *ZHS* formalism [45, 46]. In CORSIKA 8, both formalisms are implemented, which allows for a direct comparison of their radio emission predictions using the exact same particle showers. We discuss this topic in more detail in Sec. 8.1.8.2. At heart, the microscopic simulations just rely on first-principles classical electrodynamics. No freely configurable parameters are used that would steer the predicted radio emission from the charged particles. This circumstance is of fundamental importance for the ability to set the cosmic-ray energy scale with the radio detection technique.

Microscopic simulation codes require large amounts of computing resources if tuned for high precision results and if calculating the signals for many observers. To mitigate this problem, a few ideas are being tested. As an example, the template synthesis approach uses a very limited set of certain full Monte-Carlo simulations and semi-analytic relations to generate radio signals from showers with greatly varying parameters [47]. Macroscopic approaches to the simulation of radio emission exist as well, e.g. MGMR3D [48].

3

The Pierre Auger Observatory

The Pierre Auger Observatory [49] is the largest facility for the indirect detection of UHECRs via extensive air showers. It is situated near the city of *Malargüe* in the province of *Mendoza* in Argentina, close to the mountain range of the Andes. There, an elevated plain, the *Pampa Amarilla* offers a large flat surface area at an altitude of about 1400 m. Further criteria were met by this location for it to be chosen as the designated site of the Pierre Auger Observatory. The area covered by the detectors of the observatory amounts to ~3000 km^2. The proposal and design work for the observatory was done in the 1990s and the construction began in 2002.

A special feature of the Pierre Auger Observatory is that it is a multi-hybrid detector facility. Already in its first stage, whose construction was completed in 2008, the observatory employed hybrid air-shower detection with fluorescence telescopes and water-Cherenkov detectors. Other detection techniques, like the observation of radio pulses, were added in the years after. An overview of the scale of the observatory and the positions of the detectors is given in the map in Fig. 3.1.

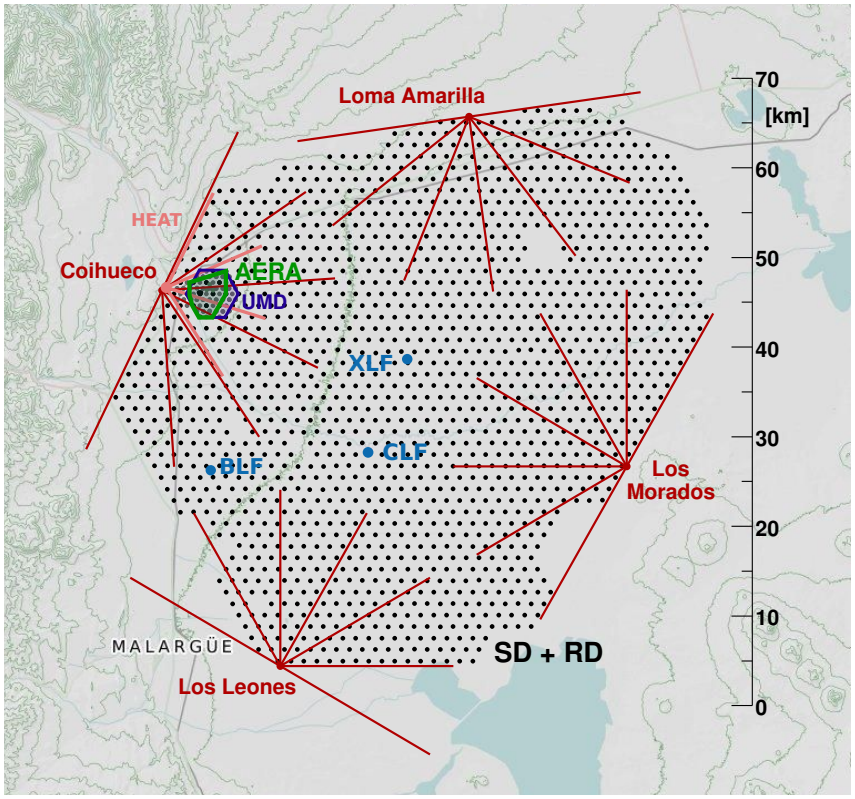

Figure 3.1: Map of the Pierre Auger Observatory.

The array is filled with 1660 surface detector (SD) stations and encompassed by four sites with telescopes of the fluorescence detector (FD) that overlook the atmosphere above the observatory. A region in the western part of the array in front of the Coihueco FD site, called *Infill region*, is used for denser detector arrangements that allow to extend physics studies to lower energies. This region is also, where other detection techniques were tested and engineered, like the Auger Engineering Radio Array (AERA). The individual detectors are presented in more details in the following sections.

The operation of such an extensive project requires adequate infrastructure, for both the data streams to and from the detectors and for maintaining and running the hardware. In the city of Malargüe, a campus was built that hosts the Central Data Acquisition System (CDAS), an assembly hall, offices, a storage yard and a visitor center. In order to be able to collect all data centrally, CDAS is connected to each of the FD sites via a microwave link that is operated with communication towers erected at each site. The detectors in the field are each connected to one of the FD sites, also via microwave links. Due to the number of detectors and the amount of signals processed by them every second, data streams via the microwave link have to be limited to stay within the available bandwidth. Therefore, the trigger system of the observatory is carefully designed [49]. Various trigger levels are differentiated, starting at station-level to only request data from multiple stations if deemed sensible.

The first period of operation of the Pierre Auger Observatory is called *Phase I*. At the time of writing this thesis, the observatory is entering a new period, called *Phase II*, that was initiated by a comprehensive hardware upgrade of the detector systems, called *AugerPrime* [50]. A major part of this upgrade is the installation of the Radio Detector (RD), a radio array built from extending all SD station by a radio antenna. Funding for the operation of the Pierre Auger Observatory for at least ten years after 2025 was recently secured, emphasizing its importance in the field of astroparticle physics at the highest energies.

3.1 The Fluorescence Detector (FD)

Inspired from the insights won with the Fly's Eye [51] ad HiRes [52] fluorescence detectors, the *fluorescence detector* [53] became a fundamental component of the Pierre Auger Observatory. Four sites with six telescopes each were constructed. The telescopes cover an azimuthal range of 30°, which gives a combined field of view (FOV) of 180° to each site since the FOVs of the individual telescopes are strung together. The FOVs are indicated in Fig. 3.1 by the red angles. Three additional telescopes were installed in the *High Elevation Auger Telescopes* (HEAT) project that are situated next to the regular FD telescopes at the Coihueco site. These three telescopes can be operated in a downward mode, in which their FOVs overlap with those of the Coihueco telescopes, and in an upward mode, in which their FOVs adjoin the upper borders of the Coihueco FOVs. This way, HEAT is able to observe lower-energetic air showers that do not penetrate the atmosphere deep enough to be seen by the regular FD telescopes.

A side-view schematic of an FD telescope is shown in Fig. 3.3. The fluorescence light emitted by the air showers passes through an aperture in front of the telescope with an included ultraviolet (UV) filter. In the back, the light is reflected by a segmented spherical mirror and collimated into the 440 pixels of the camera of the telescope. Each

Figure 3.2: Fluorescence detector site Los Morados. The windows with closed shutters to four of the six telescopes are seen. Behind the FD building, a communication tower of the microwave link to the central campus is erected. In the back, a facility with a round roof can be seen that containes a LIDAR instrument. This particular LIDAR is not in operation anymore but LIDARs at Coihueco and Loma Amarilla still are.

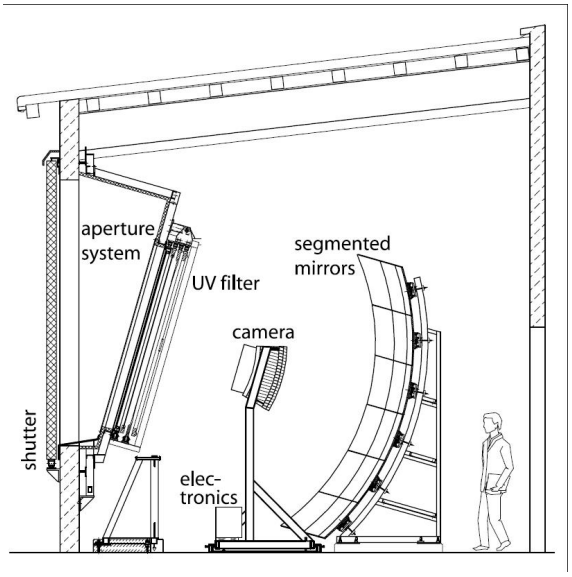

Figure 3.3: Schematic side-view on an FD telescope. A few fundamental components are labeled. Taken from [49].

pixel is a photomultiplier tube (PMT) with a photocathode sensitive in a UV range around 350 nm. The front-end electronics are capable of achieving 100 ns timing [53]. In front of the aperture, a shutter door is mounted that is only opened during operation.

Fluorescence photons induce electric pulses in the PMTs. The digitized signal counts in each pixel are proportional to the number of incident photons, which in turn are proportional to the energy deposited by the air shower in the observed part of the atmosphere. The hexagonal-shaped pixels, arranged to form a gapless coverage, allow

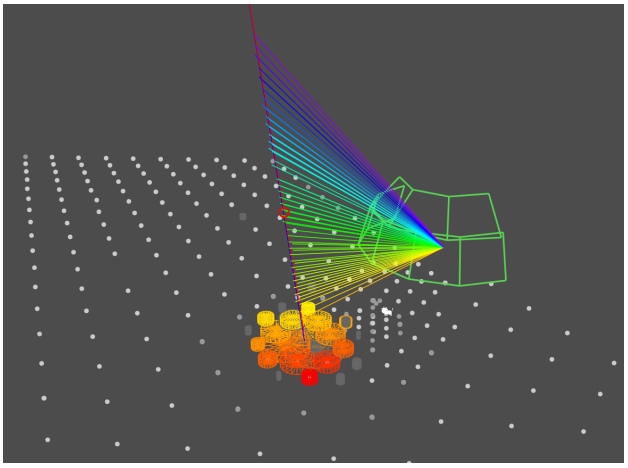

(a) 3D view of the reconstructed event. The FD telescope apertures from Coihueco and HEAT are shown as green polygons. White and gray dots denote positions of SD stations. The lines indicate lines of sight between FD pixels and the fluorescence emission by the shower, colored by the signals times. SD stations with signal are highlighted. Their color indicates signal arrive time and their size represents signal strength.

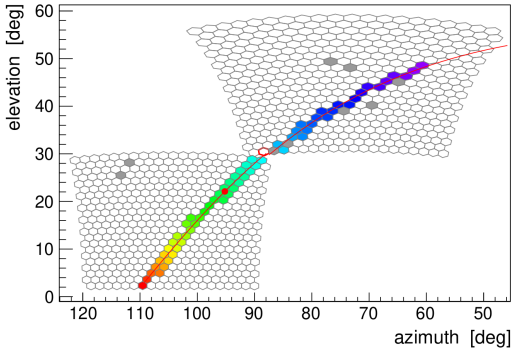

(b) Event view in the pixels of one telescope each of Coihueco and HEAT. Color denotes signal arrival times.

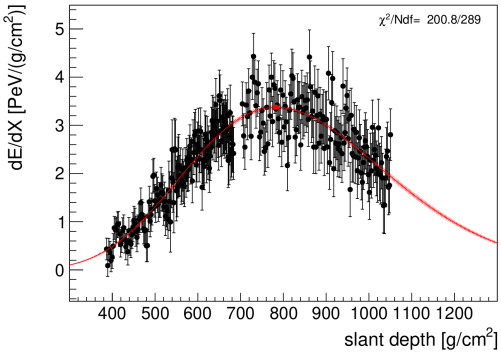

(c) Reconstructed energy deposit per atmospheric depth of the shower as a function of atmospheric depth.

Figure 3.4: Visualizations of the event reconstructed with the ID `152267599200`, measured on 2015/08/15 by the FD and the SD-750. Created with the `EventBrowser` within the Offline software framework (see Sec. 6.2).

to observe the longitudinal development of air showers. In Fig. 3.4a, an example event is shown that was measured in hybrid mode by the FDs Coihueco and HEAT and by the SD. The pixel-view from the triggered Coihueco and HEAT telescopes is shown in Fig. 3.4b with the signal times coded in color. From the timing information, the geometry of the shower is reconstructed. The estimated energy deposit per traversed depth of atmosphere is plotted in Fig. 3.4c with a Gaisser-Hillas function fitted to the longitudinal profile that provides an estimate of the depth of shower maximum of the event.

The PMTs of the telescope cameras are highly sensitive since the fluorescence light signals are very low. Therefore, operation of the FD telescopes is limited to moonless nights. Any bright light sources in the FOV would damage the electronics of the FD. Furthermore, operations have to be stopped in rainy or excessively windy conditions. In consequence, the duty cycle of the FD is only about 14%.

For a correct reconstruction of FD-measured air showers, atmospheric effects have to be taken into account appropriately, for example attenuation of the light from atmospheric molecules and aerosols. Moreover, clouds can block parts of the fluorescence emission of a shower towards the telescopes. In order to adequately take these effects into account, a set of instruments for monitoring the atmospheric conditions is put in place. In the map in Fig. 3.1, the positions of the *Central Laser Facility* (CLF) and the *eXtreme Laser Facility* (XLF) are indicated. These two facilities host lasers that are regularly shot into the atmosphere, from which scattered light is seen by the FDs. With the knowledge on the distance of the light source and on the strength of the laser, the properties of the atmosphere can be probed. Also indicated in the map is the location of the *Ballon Launch Facility* (BLF). In the past, radio sondes on weather balloons were launched from this site to measure the profiles of several atmospheric observables. At the FD sites, weather stations are installed as well as cloud cameras. Furthermore, facilities with *LIght Detection And Ranging* (LIDAR) instruments are used to scan the atmosphere with lasers and observe backscattered light from clouds and aerosols.

The FD currently sets the energy scale of the Pierre Auger Observatory. Its longitudinal view on the energy deposit of air showers allows to reconstruct the total calorimetric shower energy. With a correction for the remaining energy, the energy of the primary cosmic ray can be estimated, which poses a great purpose of the FD. An important ingredient in the scaling between the energy deposit of the shower in air and the observed fluorescence light, which is described by the *fluorescence yield*. In Sec. 7.2, we discuss energy measurements of air showers in more depth. The systematic uncertainty of the FD energy scale is estimated at 14% [54]. The absolute determination of the fluorescence yield and reducing its uncertainty has historically demanded a great deal of dedicated works [55]. Currently, the absolute calibration of the FD itself makes the dominant contribution to the uncertainty of the energy scale. Furthermore, the fluorescence-light attenuation effects of the atmosphere play an important role as well as the time drift of FD measurements due to aging of the detector components (PMTs) and due to dust accumulation on the telescope mirrors that affects its reflectivity.

3.2 The Surface Detector (SD)

Every black dot in Fig. 3.1 is one station of the *surface detector* array [56] of the Pierre Auger Observatory. In total, 1660 stations are placed in a triangular grid. Most of the stations are spaced at a distance of 1500 m. The resulting array is therefore named SD-1500 and is suitable for detecting both vertical and inclined air showers. In the Infill region, smaller station spacings of 750 m and 433 m are employed on smaller areas that span the SD-750 and SD-433 subarrays, respectively. These subarrays are able to extend studies with vertical showers to lower energies and they also work in synergy with other detector types installed in the same region.

In Fig. 3.5, an SD station is shown that is already fully equipped with the hardware from the AugerPrime detector upgrade. For Phase I of the Pierre Auger Observatory, the SD stations consisted only of *water-Cherenkov detectors*. With the upgrade, a *scintillator surface detector* [57] and a *short aperiodic loaded loop antenna* (SALLA) for the *radio detector* [58] were added. The water-Cherenkov detector was equipped with an additional PMT. Furthermore, the electronics of each station were upgraded to be able to handle the

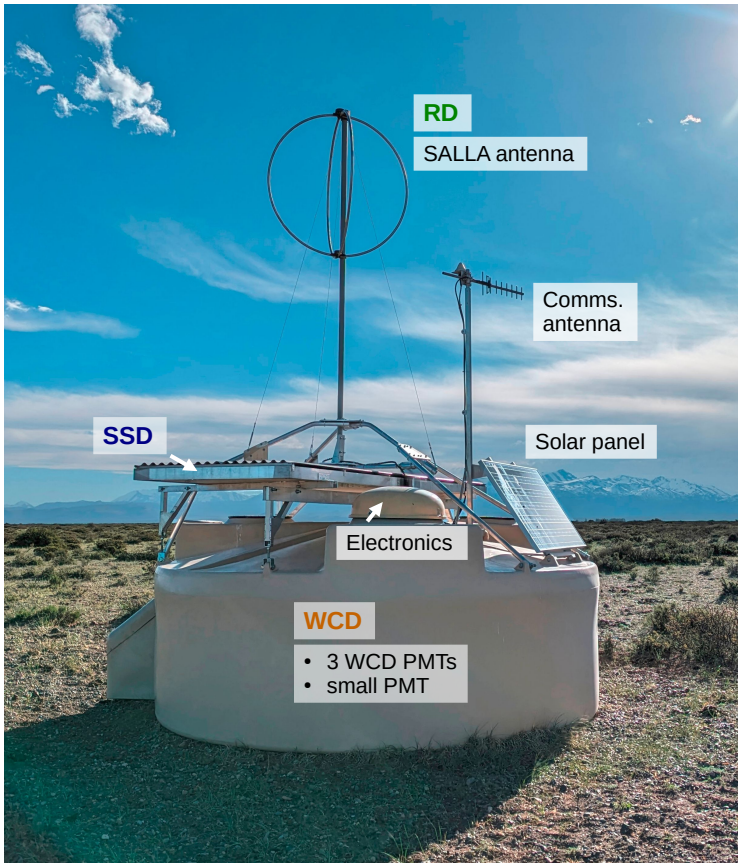

Figure 3.5: Picture of the upgraded SD station Nr. 1738 ("Granada").

additional data streams. The previously used *unified board* was upgraded to the *upgraded unified board* (UUB) [59]. Unlike the FD, these detectors can operate with a duty cycle of 100% from a technical point of view. Later, we will discuss a limitation of the real duty cycle for the radio detectors. In the following, the individual detector systems of the upgraded SD stations are presented.

3.2.1 The Water-Cherenkov Detector (WCD)

The base of each SD station is a cylindrical polyethylene tank that holds 12 m^3 of ultra-pure water. Inside, four PMTs are installed, three of which are of the same type and were part of the detector from the beginning. These PMTs detect the Cherenkov light produced by shower particles when they pass through the water. The unit of measure for the signal strength induced by the Cherenkov photons is called *vertical equivalent muon* (VEM). Like the name suggest, 1 VEM corresponds to the signal strength from a muon that passes through the WCD in a vertical track. With a threshold signal strength and a coincidence logic for the PMTs, a station-level trigger is constructed that is tested on the next highest rank in a comparison with neighboring stations. The new PMT added as part of the AugerPrime upgrade is smaller than the other three and is aimed at increasing the dynamic range of the WCD.

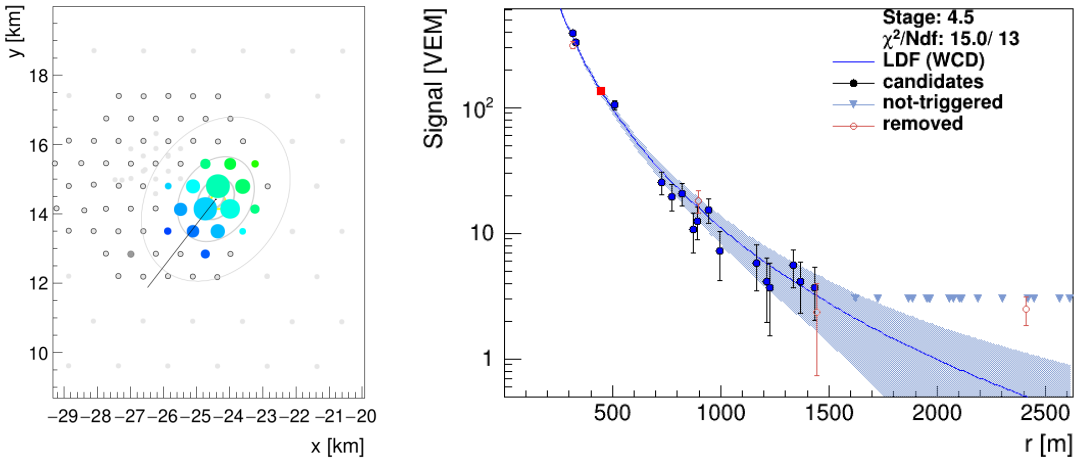

(a) 2D view on the SD signal stations. Signal arrival times are color-coded. The arrival direction of the shower is shown by the gray line.

(b) Lateral distribution of the reconstructed signal strengths from the WCD recordings. The signals are plotted against the distance to the shower axis. Data points are shown as dots and the blue line indicates a function fitted to the lateral distribution.

Figure 3.6: Visualizations of the SD reconstruction of the same event as shown in Fig. 3.4.

In Fig. 3.6a the same event as in Fig. 3.4 is shown but just the top-down view on the WCD signals from the SD-750 stations. The signal strength and signal time in each station are coded by size and color of the circles, respectively. Fig. 3.6b shows the recorded signal strengths as a function of the distance of the station to the shower axis.

3.2.2 The Surface Scintillator Detector (SSD)

On top of the WCDs of all SD stations, except for those on the border of the array, an SSD unit was installed. Such a unit contains two scintillator panels that in total cover an area of about 4 m^2. Like the WCD, the scintillators detect the muonic and electromagnetic component of an air shower. However, the responses are quite different between the two systems with the SSD having an increased sensitivity to the electromagnetic over the muonic component in comparison to the WCD. The SSD will mostly aid to improve studies of vertical showers (with zenith angles below 60°) together with the WCD and in hybrid mode with the FD. For inclined showers, the projected detection area of the scintillators is rather small.

3.3 The Underground Muon Detector (UMD)

A detector system unattached to the original design of the Pierre Auger Observatory is the *underground muon detector* [60]. It employs the idea of placing scintillator modules buried underground to be shielded from the electromagnetic component and only measure the muons that can still reach the depth of ~2.3 m. In total, the UMD will consist of 73 stations located close to SD stations of the SD-750 and SD-433 arrays. Each UMD station includes three scintillator modules of an area of 10 m^2 each. Most of the UMD array is already constructed and the remaining stations are on track to be deployed soon.

In combination with the other detector systems, the UMD will help to study the muons in air showers to greater detail.

3.4 Auger Engineering Radio Array (AERA)

Air shower detection with radio antennas was tackled at the Pierre Auger Observatory with a proper array after all SD and FD detectors had already started regular operation. In the second half of 2010, the first phase of the *Auger Engineering Radio Array* was deployed. Two additional phases followed and the last installation in 2015 completed the deployment. AERA was intended as a radio detector for testing and engineering several aspects in the radio detection technique. For example, different antenna types, station electronics and triggering mechanisms were tested. Besides serving as an engineering project for the Radio Detector of the AugerPrime upgrade, several physics results were achieved with measurements from AERA.

Deployment in phases

The location of AERA within the observatory is indicated in Fig. 3.1. A zoomed in map of the infill region in front of Coihueco containing AERA is shown in Fig. 3.7. In total, 154 antenna stations were installed comprising an area of about 17 km^2 with an irregular station spacing. For Phase I, 24 stations with *log-periodic dipole antennas* (LPDA) were set up at the densest spacing of 144 m. In 2013, 100 stations with active bowtie antennas, usually called *Butterfly*, were installed with a mixed spacing of 250 m and 375 m. Lastly, AERA Phase III added another 25 Butterfly stations, most of which were placed with the least dense spacing of 750 m in the southern half of the array, next to stations of the SD-750. The station numbers quoted here have varied throughout the lifetime of AERA due to changes made in several engineering projects. Details on the antenna types and the selection process for the employment in AERA are given in [61]. Pictures of an LPDA station and a Butterfly station are shown in Fig. 3.8.

Technical station details

Each station is equipped with electronics that process the raw analog signals. These include a *low-noise-amplifier* (LNA) that amplifies the signal with a 20 dB gain and a *filter amplifier* (FA), which restricts the frequency band that is used from the signal to the band from 30 MHz to 80 MHz. Afterwards, a digitizer converts the recorded voltage traces into ADC (*analog-to-digital converter*) counts that are computationally processable. Two different types of digitizers were developed and are utilized in AERA in different trigger concepts that we explain in the next paragraph. One digitizer type was developed jointly by the *Bergische Universität Wuppertal (BUW)* and *Karlsruhe Institute of Technology (KIT)*, while the other type was developed by the *National Institute for Subatomic Physics (Nikhef)* in the Netherlands and *Radboud University Nijmegen (RU)*. The BUW/KIT digitizers have a sampling rate of 180 MHz while the sampling rate of the Nikhef/RU digitizers is 200 MHz. With different numbers of samples per trace in the stations of the different AERA phases, the trace lengths range between 5 µs and 57 µs. The BUW/KIT and Nikhef/RU digitizers use a bit depth for the digitized signals of 12- and 14-bit, respectively. Both antennas have two polarization arms, one aligned with the geomagnetic field (called north-south) and one aligned in the perpendicular direction (called east-west). The stations are solar powered and include a metal box that holds the

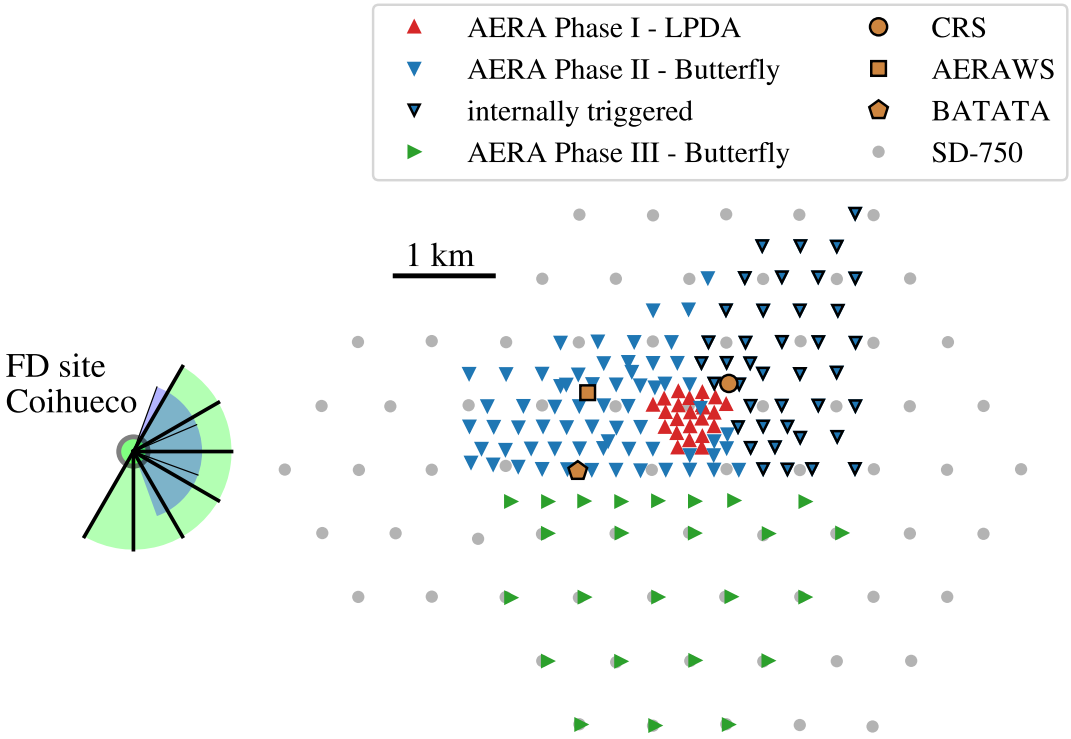

Figure 3.7: Map excerpt of the infill region. The SD-750 array as well as the Coihueco FD site are shown. The AERA station positions are shown for the individual phases.

battery and all electronics except for the LNA, which is mounted directly at the antenna. Fences protect the stations from larger animals[1].

Data acquisition

A field hub was erected close to the Phase I stations, called *Central Radio Station* (CRS), holding computing infrastructure and equipment for hardware work in the field. The Phase I stations are connected to the CRS via fiber cable [62]. In the beginning, the data acquisition of AERA was handled in the CRS but was later moved to machines inside the FD building at the Coihueco site. Communication between the DAQ machines and the stations for triggering and data readout is done via commercial WiFi links.

Most of the stations are in practice only operated with external triggers with the BUW/KIT-developed electronics. Those triggers are formed in CDAS with the signals from the other detectors – mostly signals from the SD. Upon receiving a trigger, the ring buffers of the AERA stations are read out and the data are sent for event building. In Sec. 6.2.1, the central data acquisition and subsequent processing is explained. External triggers from other sources are used in separate data streams as well. For example, periodic triggers are used to regularly monitor the noise picked up from each station, and triggers from airplanes allow to record their signals for accurate timing calibration [63].

[1] Mostly cows and horses; goats have been seen inside the fenced area.

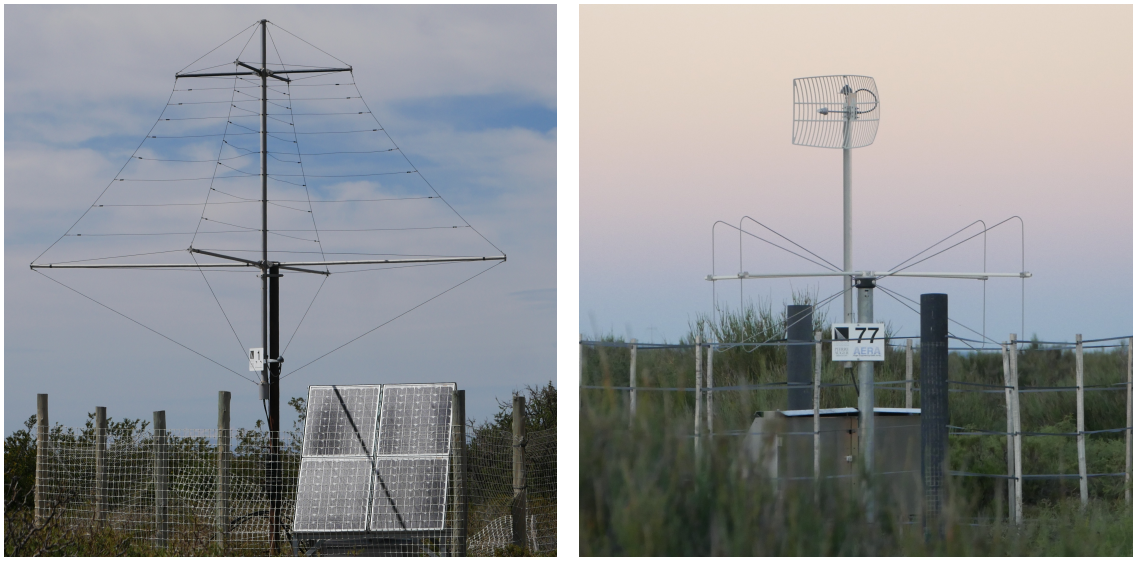

(a) Station 1 – LPDA **(b)** Station 77 – Butterfly

Figure 3.8: Two AERA stations with both of the employed antenna types in the field.

The 40 stations of AERA Phase II that are on the 375 m grid in the north-east part were equipped with Nikhef/RU-developed electronics with the intent of operating them in a purely internally triggered mode. Those stations can form triggers themselves built from parameters of the received radio pulses. Realizing this self-radio triggering is a challenging task as was also experienced at AERA but gained new traction recently, especially in the context of the future *Giant Radio Array for Neutrino Detection* (GRAND) [64, 65]. Some of the internally triggered stations also contain small scintillator detectors inside the electronics box for triggering the station upon a measured particle signal. The purely internally triggered stations were put out of operation at the beginning of 2023 to reduce the required personpower for maintenance – also in light of the deployment of the new Radio Detector – and to use components of these stations as spares for upkeeping the externally triggered stations. Ten of those stations are currently reused in the project GRAND@Auger [66].

Calibration

Many efforts were made to calibrate the components of AERA. The parameters of all electronics were measured in the laboratory before deployment in the field. The directional gain patterns of the antennas were simulated and measured in drone-borne calibration campaigns. The absolute signal strength was calibrated with the diffuse Galactic background signal. Some of these aspects are still being studied and refined. We review the calibration of AERA in depth in Sec. 6.1.

Auxiliary facilities at AERA

Two weather stations were installed within the AERA array. One station is mounted on top of the metal container of the CRS, while the other station, called AERAWS, is deployed in the field as marked in Fig. 3.7. Besides a set of typical meteorological sensors, the weather stations each include an electric-field mill (EFM) that monitors the atmospheric electric field at ground in order to detect thunderstorms that can affect the

radio signals from air showers. More information on these devices as well as a new network of EFMs that was installed within the work of this thesis are given in Chap. 4. One of the new EFMs is deployed at the BATATA detector testing site (marked in Fig. 3.7) and is therefore also within the AERA array.

At the Coihueco FD site, a reference beacon transmitter emits continuous narrowband signals at selected frequencies. These signals are clearly present in the recordings of the AERA stations and are used to perform per-event accurate timing calibrations that are necessary for interferometric studies [63].

3.5 The Radio Detector (RD)

As the last deployed part, the *radio detector* concludes the AugerPrime upgrade. With it, the SD stations also take their final Phase II appearance as shown in Fig. 3.5. Atop each SD stations, a SALLA antenna [67] is mounted with the highest point reaching about 5 m above ground. The mast that holds the antenna is stabilized against strong winds using guy wires attached to the mounting system.

Like the antennas at AERA, the SALLA covers two perpendicular polarizations with its loops that are oriented such that one points in the geomagnetic north-south direction while the other points in the east-west direction. Also alike AERA, the RD uses the frequency band from 30 MHz to 80 MHz. However, in comparison to the LPDA and Butterfly antennas, the directional gain pattern of the SALLA is better suited for measuring inclined air showers, which is in line with the envisaged main task of the RD to cover these higher inclinations.

Each unit of the RD has an LNA at the top crossing of the two loops, which is connected to the front-end board in the electronics housing of the station. There, the signal is passed through the FA tuned to the 30 MHz to 80 MHz band and processed further in the digitizer, which samples at a frequency of 250 MHz with a 12-bit resolution. The front-end board itself is connected to the UUB for communication with the other detector components and with CDAS.

The RD is expected to enhance the overall exposure of mass-sensitive measurements with the Pierre Auger Observatory and the sensitivity in the multitude of physics analyses through hybrid shower detection with the WCD. Especially for very inclined showers, the RD will be able to provide a measurement of the energy in the electromagnetic cascade of air showers, even though the electromagnetic shower component has died out in the atmosphere and the WCD is left to only observe the muonic component.

Readout of the radio traces is triggered by the WCD. However, a radio self-trigger is under development and could open up a new window of sensitivity, especially for neutral particles [68]. For example, ultra-high energy photons are expected to produce air showers with a comparably low muon component but a still high electromagnetic component. Such air showers are less likely to trigger the particle detectors compared to cosmic-ray induced showers. A working radio trigger could help to see these showers. However, designing such a trigger is a challenging task [69].

The expected performance of the RD in terms of cosmic-ray detection has been studied extensively in end-to-end simulations [70]. With several thousand expected events above an energy of 10^{19} eV to be measured in the next ten years, the RD holds out the prospect of rich physics and a deeper understand of UHECRs.

4

A new network of electric field mills

Parts of this chapter have been published in:

A new network of electric field mills at the Pierre Auger Observatory
M. Büsken for the Pierre Auger Collaboration
Journal of Physics: Conference Series, 2398(1):012004, 2022

A network of electric field mills at the Pierre Auger Observatory
M. Büsken & T. Huege
Collaboration-internal note, GAP-2024-014

Updates of the atmospheric monitoring at the Pierre Auger Observatory
M. Büsken & B. Keilhauer for the Pierre Auger Collaboration
AtmoHEAD 2024 contribution

Radio detection has proven to be successful, partly because of many advantages over other detection types, that come along with it. One example advantage over the FD is the lack of need for the monitoring of the air-shower calorimeter, the atmosphere. There is one substantial exception, which are thunderstorms or – to be more precise – atmospheric electric fields. Large electric fields in the atmosphere, as typically present during thunderstorms, can have a significant influence on the amplitude and polarization of air-shower radio signals [71, 72, 73, 74]. Therefore, time periods with large electric fields need to be tracked for the selection of thunderstorm-affected air-shower events.

At AERA, as at other radio detectors, this electric-field monitoring is done with electric field mills (EFMs). These sensors are simple devices that measure the atmospheric electric field near ground by the charge that is induced on a sensor electrode. During a periodic shielding phase of the electrode, the charge flows off and the induced voltage in an electric circuit is converted to an electric-field value. The name *mill* arose because the periodic shielding was traditionally realized with a rotating vane.

For AERA, one EFM is positioned at the CRS and operational since mid-2010 [75], the second one is located in the field at the AERAWS and operational since August 2014 [76] after it has been redeployed from the BLF. Pictures of both EFMs are shown in Fig. 4.1. Their locations within AERA are indicated in Fig. 3.7 and the distance between the two devices amounts to 1.4 km

(a) EFM mounted on top of the western edge of the CRS container together with multiple other weather sensors.

(b) EFM mounted in the field at the AERAWS station, also accompanied by other weather sensors.

Figure 4.1: Pictures of the two EFMs that have been in operation for years in the AERA region for thunderstorm detection.

With these two EFMs, characterizing the atmospheric electricity is possible locally for AERA. The rejection of thunderstorm-affected periods in AERA data is in place as we discuss later in more detail. This ingredient is an important prerequisite for the energy-scale analysis with AERA that we conduct in this thesis. However, the analysis shall be performed with the new RD in the future as well. And while AERA has a size of about 17 km^2, the RD covers the full area of the Pierre Auger Observatory of about 3000 km^2. Therefore, large-scale monitoring of the electric field is required, which is tackled with a new network of EFMs conceived, designed and deployed in the course of this work. Such a network will also be useful in other fields of research. There are several studies related to atmospheric electricity, especially on global scales, that could benefit from the data of the network.

Within this work, five new EFMs have been installed at the Pierre Auger Observatory with the additional goal to achieve an absolute calibration of the electric-field measurements. Sec. 4.1 describes the EFM station setup for a practical realization of the network while also meeting calibration requirements. A test setup at Karlsruhe Institute of Technology (KIT) is presented as well. In Sec. 4.2, the deployed stations at the Pierre Auger Observatory are shown and their individual details are given. The accuracy of the absolute calibration is estimated. Thereafter, the implementation of the data acquisition and instructions for data access are described in Sec. 4.3. First data recorded by the new network from more than one year are shown and analyzed on a basic level in Sec. 4.4. Finally, an outlook is given in Sec. 4.5 over how the data will be used in the future within the Pierre Auger Observatory but possibly also outside of it. At the end, the work is summarized in Sec. 4.6. In appendix A.2, tips are given for troubleshooting typical problems.

4.1 Technical setup

The general design of the new network of EFMs is based on the idea to have five sensor stations with the same technical setup to ensure comparability between stations and shareability of spare hardware. Deviations from the base setup are only made where necessary due to special conditions of a station's location. The station design is set to follow a number of requirements:

- Firstly, the stations need to be robust and persistent against the harsh conditions of the Pampa Amarilla, since a runtime of 10+ years is anticipated. Environmental conditions include a wide temperature range, strong solar irradiation, strong winds, dust dispersion and wildlife.
- The stations should run stably and autonomously, i.e. no regular maintenance is required.
- Data taken at all stations will be read out in a central place within the network of the Pierre Auger Observatory, from where they are uploaded to a globally accessible database. Therefore, each station needs to provide a communication channel to the central readout place.
- The anticipated runtime of the stations is at least 10 years, meaning that components should endure for such a long time, if possible.
- With reasonable additional efforts, an absolute calibration of the electric-field measurement is desired. By consultation with the manufacturer of the employed EFMs, a station design is chosen which has been calibrated by the manufacturer such that copying that design automatically results in having a calibrated setup [77, 78]. Requirements of this setup are:
  - The EFM is mounted such that the sensor plate is at 2 m height, flush with the earth and facing downward. The mounting height has a critical influence on the effective gain factor between the atmospheric electric field and the voltage that is measured by the sensor inside the EFM. This gain factor is split into a sensor-unique factor $M_{parallel\_plate}$, that was determined by the manufacturer in a lab and is provided in a calibration certificate, and a second factor, C_{site}, that reflects the setup of the EFM installation and its site conditions. With a mounting height of 2 m, C_{site} is 0.105 as determined by the manufacturer in a calibration campaign[1].
  - There may not be any object between the EFM and ground.
  - An area around the EFM with a radius of 7 m is kept clean of anything not necessary for the operation of the station. In particular, vegetation in this area should be avoided as much as possible.
  - No tall structures or objects are in the vicinity of the station, which could be the basis for corona currents that disturb the electric-field measurement. More precisely, no nearby object reaches higher than 18° elevation above the horizon from the point of view of the EFM station.

[1] A site factor of 1.0 would be valid in case of an installation of the EFM in which it is mounted flush with the earth and facing upward. However, for the application at Auger, this setup is impractical.

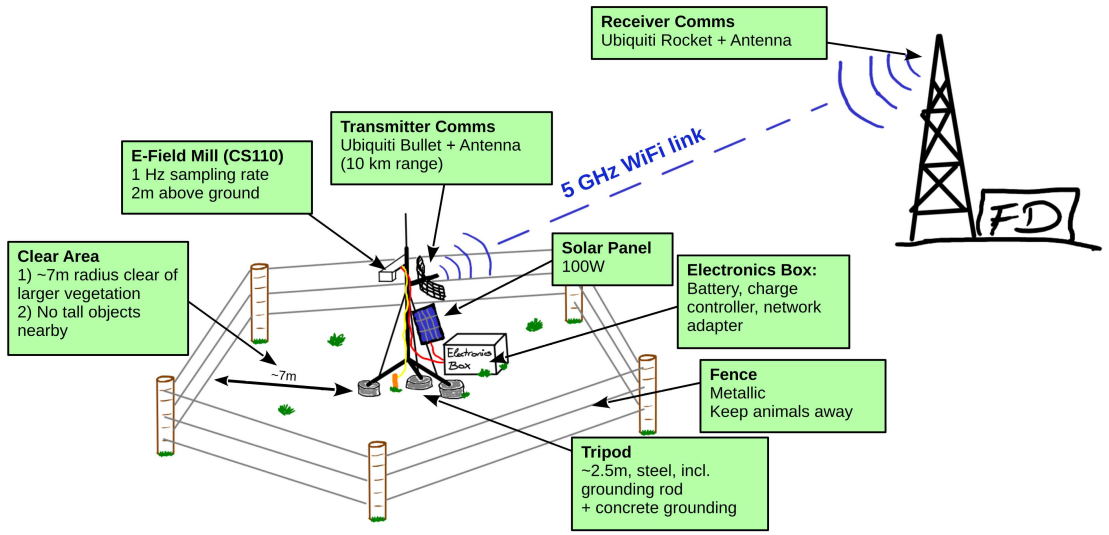

Figure 4.2: Sketch of the station design for the new EFM network. Key features and components are labeled. The basis of the design is a remote station with a WiFi link to a nearby FD site, which is only representative of four of the realized stations, while the design for the CLF station slightly differs. Still, most of the illustrated elements are the same, especially those regarding the calibration requirements.

– For avoiding distortions of the electric field, no object is mounted above the EFM.

On the basis of the listed requirements, a setup for the EFM station was designed. An illustration of the complete station design is shown in Fig. 4.2 including the main components and key parameters. All components are presented in the following list.

- **EFM:** The CS110 Electric Field Meter [79] by Campbell Scientific is an electric field sensing device with a measurement range from $-25\,000\,\mathrm{V/m}$ to $25\,000\,\mathrm{V/m}$. A picture of the CS110 is displayed in Fig. 4.3. This particular device was chosen to be employed in the new EFM network because it has been used already for similar purposes at the Pierre Auger Observatory for over a decade. In particular, the two EFMs in use at Auger Engineering Radio Array (AERA) are of the model CS110. Both EFMs have proven to be robust against environmental conditions and suitable for long-term operations. A comprehensive analysis of the electric-field data from these two EFMs was performed in [80].

  A sensor plate inside the CS110 accumulates electric charges when exposed to the atmospheric electric field resulting in a measurable voltage. During electric-field measurements, the EFM periodically closes its shutter to shield its sensor plate from the surrounding electric field. In the closed state, the voltage that had built up on the sensor goes back to an offset voltage when the accumulated charges flow off. The offset voltage is typically non-zero due to leakage currents or imperfect conditions of the electronic components and this is not a problem because during the closed state, the EFM takes reference measurements before and after sampling the electric field. The average value from these reference measurements

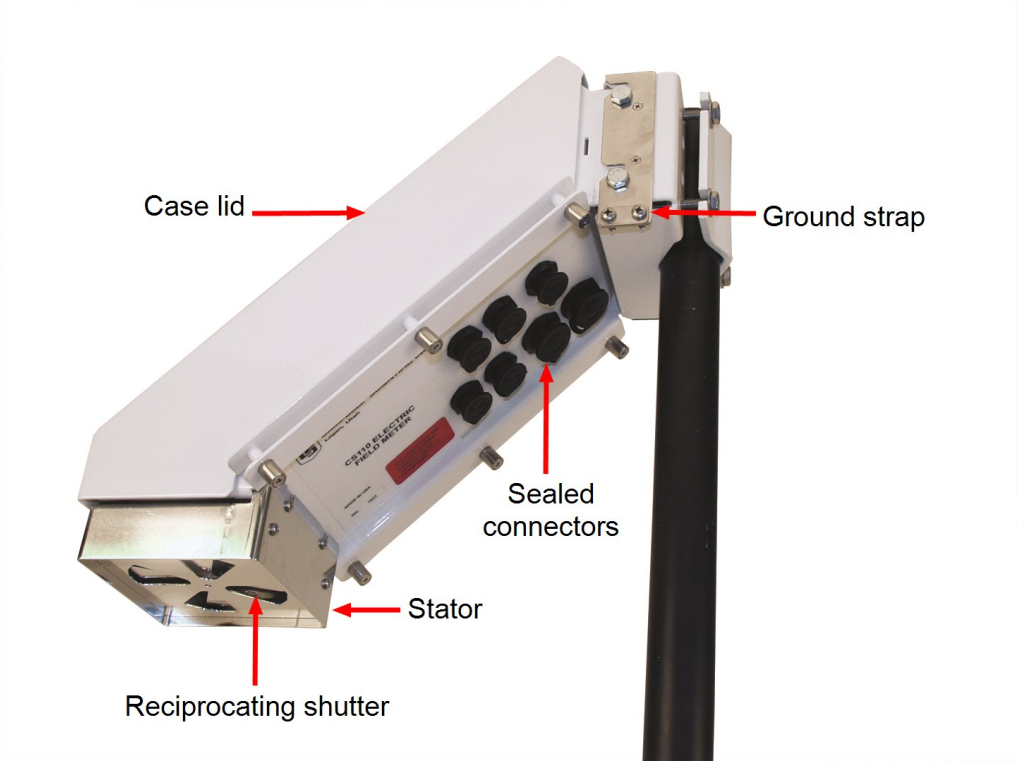

Figure 4.3: Side view of the Campbell Scientific CS110 electric field meter mounted on a pole.

is subtracted from the sampled electric-field value in order to correct for the offset. This cycle is repeated at the set sampling rate of the EFM.

The CS110 contains an embedded CR1000M data logger that processes and stores not only the electric-field data but also data of the panel board's temperature, the internal relative humidity (hygrometry), the delivered voltage from the power supply, the measured leakage current of the system and a status code that monitors problematic behavior of the system. The sampling rate of the CS110 is set to 1 Hz. Other sampling rates between 0.1 Hz and 5 Hz are possible. The data logger stores two tables: One table contains the data at the configured sampling rate, while the other table is filled with 60 sec averaged values. A connector for the power supply and an RS-232 serial port are placed on the bottom side of the device. Additional connectors for external devices and other meteorological sensors are also available but are not used in the presented setup.

- **Tripod:** The CM106BE tripod by Campbell Scientific is used to hold the EFM and WiFi antenna. A similar tripod was used in the calibration campaign by Campbell Scientific, from which the determined calibration constant will be adopted for the presented setup. The CM106BE is made of galvanized steel and is therefore expected to endure the environmental conditions of the Pampa at least for the foreseen runtime of the stations [81]. It is shipped with ground cables, a ground rod and a lightning rod. However, the lightning rod is not installed in order to avoid disturbances of the electric-field measurement. The ground rod is driven at least 50 cm into the ground and the ground cables connect the mounting frame of the CS110 to the ground rod. Guy wires are not installed as the tripod is used

without the optional mast extension and this setup can be used in environments with sustained wind speeds of up to 130 km/h and wind gusts up to 166 km/h. The expected conditions in the Pampa are well within those limits. At ground, the tripod feet are bolted down to concrete foundations.

- **Serial-to-Ethernet-Server:** The readout of the EFM station is realized via an Ethernet connection from the DAQ machine to the data logger of the EFM. Therefore, the RS-232 serial port of the CS110 is connected via cable to a Moxa NPort 5110 serial device server. The Moxa NPort 5110 has an RJ45 connector and supports Real COM/TTY drivers, that allow the server to be used as a serial port of the DAQ machine over network through its IP address.

- **Radio link:** As discussed in Sec. 4.2, bridging the distance between the EFM stations and the entry points to the network of the DAQ machine is not feasible with Ethernet cables. Therefore, a WiFi link using two connected radios is employed. Specifically, a system consisting of Ubiquiti airMAX Bullet AC and Rocket5AC lite is used. A very similar system is already in use at AERA and has proven to work well for distances up to almost 11 km [82]. On the EFM station side of the radio link, the Bullet is deployed and connected via Ethernet cable to the Moxa NPort. Since the Bullet is powered passively via Power over Ethernet (PoE), a PoE adapter is added between the Moxa NPort and the Bullet. The N-type antenna connector of the Bullet is connected via cable to a WiMo grid dish antenna, that can be used for frequencies between 5.15 GHz and 5.85 GHz and has a gain of 29 dBi. The antenna is mounted on the tripod mast below the EFM and facing the opposite direction.

  The Rocket is directly plugged into a Ubiquiti airMAX AM-5G90-20 sector antenna, that can be operated in the same frequency range as the grid dish antenna. The sector antenna has a beamwidth in azimuth of 90° at a gain of approximately 20 dBi. Like the Bullet, also the Rocket is powered via PoE and an Ethernet surge protector is installed to protect the Rocket against damages from lightning strikes.

- **Fiber Bridge (CLF only):** As discussed in Sec. 4.2, the EFM station at the CLF does not require a long-distance WiFi bridge with the aforementioned Bullet-Rocket-system. Instead, a distance of approximately 20 m from the station to the CLF has to be covered in the data communication line, which is done using fiber cables. Therefore, prior to connecting to the Moxa NPort, the RS-232 serial cable from the EFM goes into a Moxa TCF-90-M-ST serial to fiber converter. A customized duplex fiber cable with 3 mm armor against rodents is plugged into the converter at the EFM station. The other cable end connects to another Moxa TCF-90-M-ST inside the CLF container which is directly plugged into a Moxa NPort.

- **Power:** The self-sufficient power supply for all electrical components of the EFM station is realized with the typical setup of a solar panel, a charge controller and a battery. Summing up the power consumption of all components results in a conservative estimate of the total drain of 10.22 W for all stations except the one at the CLF which only requires 0.96 W as can be seen in Tab. 4.1. A typical rule-of-thumb suggests to use a solar panel with a peak power yield 10 times larger than the total drain, i.e. approximately 100 W, to ensure a continuous power supply.

Table 4.1: Power plan of the EFM station design. Values represent the average power consumption. For the Bullet, the maximum power consumption is listed, while the actual consumption depends on the distance to be covered by the radio link and may be lower than 8 W.

Component	Power consumption	Stations
CS110	0.72 W	all stations
Moxa NPort 5110	1.50 W	all stations except CLF
Moxa TCF-90-M-ST	0.24 W	only at CLF
Ubiquiti airMAX Bullet AC	8 W	all stations except CLF
Total	10.22 W / 0.96 W	non-CLF / CLF

A 36 V monocrystalline solar panel with 100 W peak power on an aluminum solar panel mount is used. To handle the relatively high voltage of the solar panel, a Maximum Power Point Tracking (MPPT) charge controller is required. In this setup, the Victron SmartSolar MPPT 75/10 is employed. The charge controller has built-in Bluetooth functionality for configuring and monitoring the controller. Also, an optional standard USB adapter is added that would provide a direct interface to the controller if needed in the future. A 12 V battery with a capacity of 170 Ah is used to buffer enough energy even in the case of multiple days without sunshine.

- **Storage box:** All electrical components of the station are stored inside a ZARGES K470 universal box that is IP65 certified. The dimensions of the box are 800 mm × 600 mm × 410 mm. Locks are installed on all boxes and share the same key. On the back wall of the box, a Conta-Clip KDS frame is installed that holds cable glands for cable dimensions fitting to individual needs. The frame and the cable glands are IP66 certified. Therefore, the components inside th box are shielded against water and dust entry. Both legs of the solar panel mount are spaced apart just enough that the box sits on the aluminum frames of the mount. Additional wire ropes tighten the solar panel mount to the handles of the box to ensure stability against strong winds. The solar panel is mounted approximately 10 cm above ground to prevent dust accumulation on the panel that might reduce the solar power yield.

- **Fence:** A chain-wire fence secures an area of 15 m × 15 m around the station to shield it from wildlife and livestock. The fence is held by metallic poles installed on concrete foundations.

A temporary setup of an EFM station was assembled at Campus North of Karlsruhe Institute of Technology to test the complete data line and the power system. All components of the final design except for the storage box were included in the test setup. A picture of the setup is shown in Fig. 4.4. The grid dish antenna of the 5 GHz WiFi link was pointed to a room, in which the Sector antenna and the Rocket were set up (about 20 m distance), the latter being connected to the institute's local network, allowing a connection to the EFMs data logger from anywhere in the network. With the sole purpose of validating all components' functionality, the setup was not meeting the requirements for an absolute calibration as described earlier.

The full chain of data transmission proved to be functional without any issues over the whole test period of roughly one week. Realistic large distances to be bridged by the

Figure 4.4: Test setup of a station for the new EFM network next to building 425 of IAP at KIT Campus North. On the right is a tripod with the EFM mounted on it and a lightning rod on top. The grid dish antenna points to a nearby office where the receiving system of sector antenna and rocket are placed and connected to the IAP network. In front of the tripod on the ground is a tool box wrapped in plastic foil holding all electronic components. On the left is a solar panel pointing south.

radio link could not be tested, however. The readout of the test setup was done manually but was based on the same software as is used in the final setup and described in detail in Sec. 4.3. The full data of the electric field recorded at the test setup are shown in Fig. 4.5 as a function of the record time. There were not thunderstorm conditions during the entire test period. This is reflected in the measured data, as the absolute value of the electric field never exceeded 300 V/m, while thunderstorm conditions would cause electric fields at ground of the order of kV/m or larger. The apparent base level of the measured electric field scatters around −10 V/m. This offset from zero is expected, as there is always a finite electrification present in the atmosphere. Throughout the test period, short peaks in the electric field, both in positive and negative direction, were recorded and can be seen in Fig. 4.5. Those peaks were likely caused by human activity

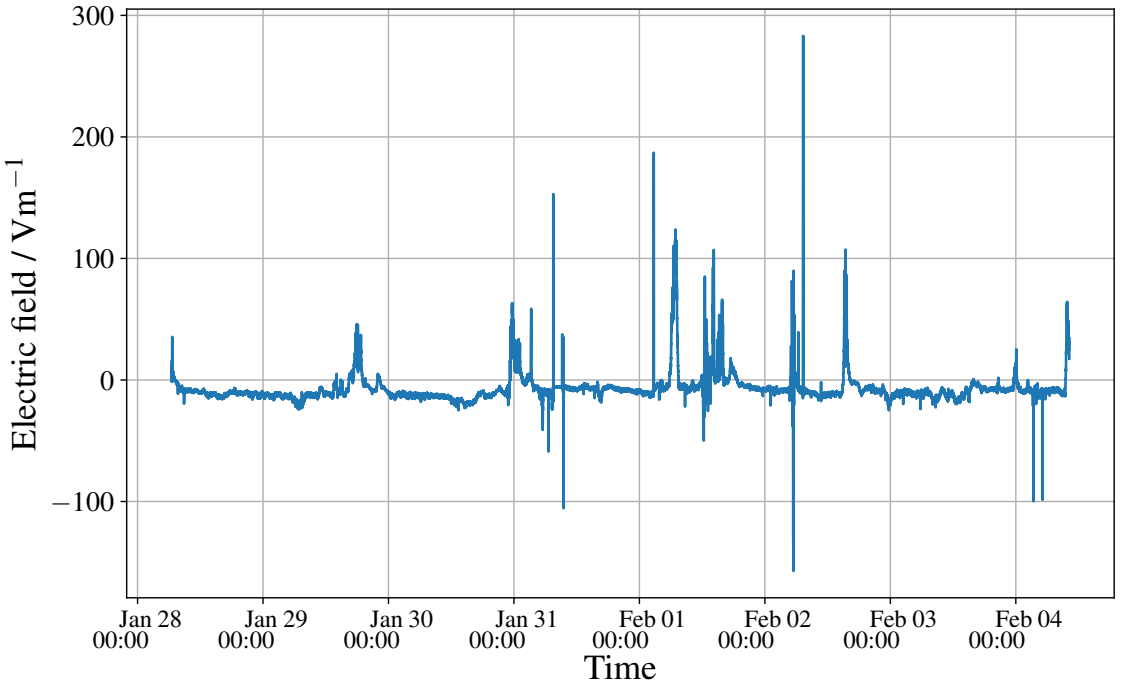

Figure 4.5: Complete time series of the electric field taken with the test setup.

close to the station, as the setup was located on the side of a parking lot. Some individual spikes can assuredly be attributed to people standing next to the EFM.

Unfortunately, the weather was bad during the test week with almost no sunshine at all. Therefore, the test battery, which only had a capacity of 51 Ah, was drained at the end of the week. Such bad weather is much less common in the region around Malargüe. Moreover, the solar panel was unfavorably positioned next to a tree that blocked part of the dimmed daylight. Later, the solar power system was tested separately once more on days with bright sunshine and at a different position that was not blocked by any tall objects. This test showed the expected performance of the system with peak power yields close to 100 W.

4.2 Stations at the Pierre Auger Observatory

The new network of EFMs at the Pierre Auger Observatory contains five EFM stations of the design presented in Sec. 4.1 (with small site dependent differences). By being so similar in their setup and by meeting the requirements for an absolute calibration of the electric field measurement, the stations' recordings are directly comparable and enable a large-scale analysis of the atmospheric electric field in the Pampa Amarilla. The current EFM stations, CRS and AERAWS, will remain in operation for now with the prospect of cross-calibrating them using the new network. In the future, their components may serve as spare parts for the network or they may be redeployed into another station of the network if considered useful. Possible spots may be the sites at the BLF and at the XLF due to the existing infrastructure or a place in the north-eastern corner of the array for a better areal coverage.

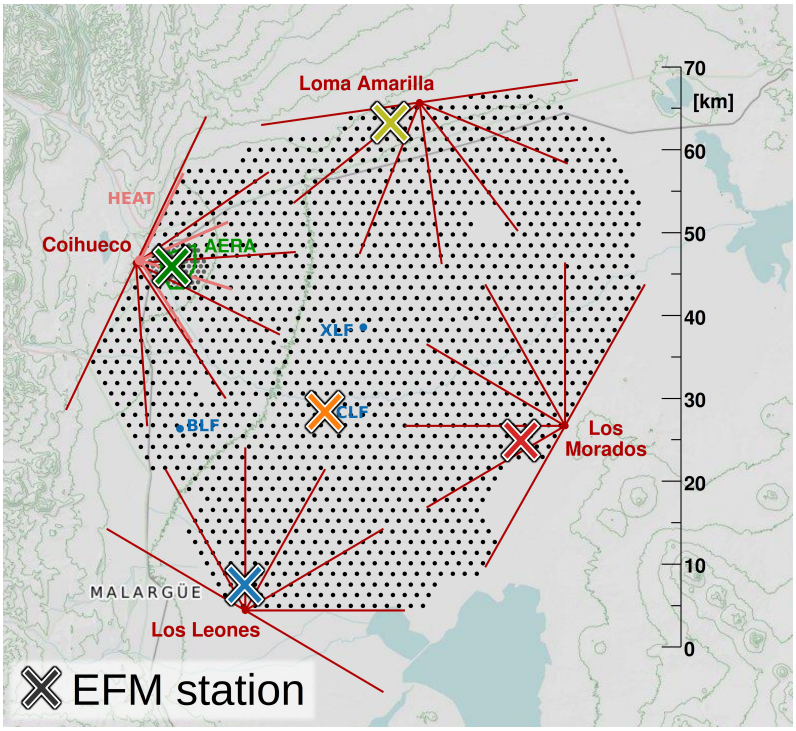

Figure 4.6: Map of the Pierre Auger Observatory with various infrastructure marked. The locations of the new EFM stations are denoted as crosses. In red, the positions and viewing angles of the four FDs are illustrated. Black dots are individual SD stations.

4.2.1 Layout and deployment of the new EFM network

The new stations of the EFM network should cover the detector array of the Pierre Auger Observatory as best as possible, while being logistically and technically feasible. The latter requirements pre-eminently include finding station positions within the range of the radio link to one of the FD sites with the permission by the respective landowner to install a station at that position.

The proposed communication link with the Bullet-Rocket-System and a range of approximately 11 km naturally predetermines the layout of the EFM network to have one station close to each FD site. The FD sites each have a tower for antennas to establish a communication network for the detector array of the Pierre Auger Observatory. These towers hold the Rockets and sector antennas of the EFM network with a cabled connection into the local network of the observatory. Another EFM station position is close to the CLF where a long-range radio link to the Coihueco FD site is already installed. The EFM network layout is displayed in Fig. 4.6.

Within the technical limit given by the radio link, suitable station positions were found near all FD sites, the longest distance between EFM station and FD site being approximately 7 km at Los Morados. The permission for the installation and operation of EFM stations at these positions is guaranteed through long-term contracts with the respective landowners. Exact deployment positions were searched for in visits to the field and from consultation with the local staff of the Pierre Auger Observatory. Special attention was paid to locations with flat ground, as low vegetation as possible and low risk of flooding during rain season. The new stations, as well as the two old stations

and their coordinates are listed in Tab. 4.2. There, also the serial numbers (SNs) of the installed EFMs are given.

All components of the stations were shipped to Argentina and arrived at the Pierre Auger Observatory in June 2022. The first station was deployed in August, the other four stations followed in November. Prior to the deployment, the metallic fences were installed by an external contractor and the fenced area was flattened and cleared of large vegetation. Specific details on the individual stations are given in the following. A few additional photos are shown in appendix A.3.

- **guanaCO / Coihueco (CO) / BATATA:**

  The first station of the new EFM network – guanaCO – was deployed at the BATATA site, which is within the AERA and SD Infill area and close to the FD Coihueco. It is marked in Fig. 3.7. The BATATA site is used to test prototypes for new air-shower detectors. It was chosen to host guanaCO because it is fenced and there is enough free space without large vegetation, which meets the requirements for the absolute calibration of the EFM. A picture of the station is shown in Fig. 4.7. Concrete foundations for the tripod could not be installed in time for the deployment. Instead, the tripod feet are fixed to the ground using earth nails and small cairns. This preliminary solution has worked well for over two years and has already proven to be sturdy against very strong winds. Therefore, there is currently no need to improve the setup.

  Since AERA already uses a Bullet-Rocket-system for communication between its stations and the Coihueco FD site, installing a new Rocket on the Coihueco communication tower would be redundant. However, the newly acquired Bullet radios are not compatible with the Rocket installed for AERA. Therefore, the Bullet in the setup design described in Sec. 4.1 is replaced with a spare Bullet from AERA, which is a slightly older model.

  The first data collected by guanaCO did not reveal any problems, giving green light for the deployment of the remaining stations as planned. The data are shown and discussed in Sec. 4.4.

- **armadiLLo / Los Leones (LL):**

  The first station of the deployment campaign in November 2022 was armadiLLo near the Los Leones FD site. Prior to the campaign, the Rocket radios and sector antennas were mounted on the communication towers at the FD sites Los Leones, Los Morados and Loma Amarilla by an external contractor. After resolving configuration issues, the remote connection to armadiLLo was established. The DAQ system was not set up at that time, but first data could be read out manually by directly connecting the Moxa NPort to a laptop. Those data looked as expected.

- **CaLaFate / CLF:**

  The station CaLaFate was deployed next to the CLF in the center of the array, i.e. not in the vicinity of any FD station, but with communication infrastructure provided by the CLF. Therefore, there are some differences in the station setup of CaLaFate with respect to the other stations. The WiFi link as described in Sec. 4.1 cannot be used to connect to any of the FD buildings due to the large distance.

Figure 4.7: First deployed station guanaCO at the BATATA site with the existing fence in the background.

Figure 4.8: EFM station armadiLLo close to the Los Leones FD site.

Figure 4.9: EFM station CaLaFate in front of the CLF container and the SD station Celeste.

Instead, the existing long-range link from the CLF to the Coihueco FD site is taken advantage of. This link was upgraded around the same time with devices that provide a larger bandwidth. CaLaFate is positioned at a distance of approximately 20 m to the CLF container as can be seen in Fig. 4.9. This distance is covered using fiber cable and a signal converter as described in Sec. 4.1. The fiber cable is buried approximately 10 cm deep in the ground in a straight line from the station to the CLF container, which it enters through a previously unused cable passage. Inside the CLF container, the connected Moxa NPort 5110 is tethered to a network port of the existing CLF infrastructure.

- **La Mara / Los Morados (LM):**

  Near the Los Morados FD site, the EFM station La Mara was deployed on a slightly elevated plateau, which is shown in Fig. 4.10. At La Mara the distance covered by the Bullet-Rocket link is the largest among the EFM stations, at approximately 7 km. The established connection could immediately be confirmed during deployment with a good signal strength considering the distance.

- **Las vAcas / Loma Amarilla (LA):**

  The last of the EFM stations to be deployed was Las vAcas in the northern part of the observatory, close to the LA FD site. At this station, there was no immediately established signal between the Bullet and the Rocket. In the pathway of the link, there is the crest of a small hill that was thought to be disturbing the connection by compromising the first Fresnel zone of the link. Tests were made, including bringing the Bullet closer to the LA communication tower and raising the grid dish antenna to about 6 m height. None of these tests succeeded in a functional connection. Later, the problem was found to be a misalignment of the sector antenna on the communication tower. After realigning the antenna towards Las vAcas, the remote link was established.

Tab. 4.2 also lists the mounting height of the EFM sensor for all stations. The sensors of the new stations were confirmed to be at 2 m height, whereas those at the CRS and AERAWS are at greater and smaller height above ground, respectively. It should be noted that the EFM at the CRS, although it is elevated, does not have a clear line of sight

Figure 4.10: EFM station La Mara near the Los Morados FD site.

Figure 4.11: EFM station Las vAcas near the Loma Amarilla FD site.

Table 4.2: All current EFM stations at the Pierre Auger Observatory and their geographical positions, the mounting height of their EFM sensors and the serial numbers of their EFMs.

Station	CS110 SN	Remote connection to	Coordinates	Sensor height / m
guanaCO	1625	CO	-35.11638, -69.55023	2.00
armadiLLo	1626	LL	-35.46810, -69.45119	2.00
CaLaFate	1663	CLF/CO	-35.28088, -69.33700	2.00
La Mara	1661	LM	-35.30785, -69.08364	2.00
Las vAcas	1662	LA	-34.95902, -69.24595	2.00
CRS	1181	CRS/CO	-35.10836, -69.53342	3.62
AERAWS	1061	CO	-35.10924, -69.54908	1.75

to the ground. It is positioned at the edge of the CRS container where there are solar panels immediately below it as can be seen in Fig. 4.1a.

The electronics boxes hold all electrical components of the stations except for the EFM and the solar panel. They are locked at both hinges with key locks, which are the same across all stations. Keys are stored at the Auger campus in Malargüe. A picture of the inside of the box at BATATA is shown in Fig. 4.12. Spare batteries from AERA were installed for the deployment. The battery at the BATATA station lost its capacity after a few months and could not provide the station with power anymore during the nights as shown in Sec. 4.4.4. Therefore, all batteries were replaced by fresh batteries of the same type in November 2023.

Revisiting all stations one year after their deployment for the exchange of the batteries allowed to examine the status of the vegetation at the stations. During the installment of the fences, the fenced area was evened out and vegetation was removed. However, since no vegetation-blocking flooring was laid, bushes could start growing again. This regrowth was observed, as an example two pictures taken from the same position at the LM station one year apart are shown in Fig. 4.13. In November 2022, there was no vegetation inside the fence. In November 2023, several bushes had grown up to 20 cm height. Vegetation in the vicinity of the EFM should be avoided to ensure the viability of the calibration. However, the cleaned state cannot be kept with reasonable effort for these remote stations. Over time, the vegetation may cause a drift of the C_{site} values of the stations. Such a drift could be determined directly from the electric field data and could be corrected for if relevant since the requirement of no vegetation was met in the beginning of the operation of the network.

After the stations had been deployed, the C_{site} values in the run scripts of the EFMs were noticed to be 0.1 instead of 0.105 (the correct value from the CS110 manual). Since the C_{site} factor is applied in these scripts during runtime, the electric-field data from all new stations were thus 5% off from the correct values. During the station visits in November 2023, the C_{site} values in the run scripts were replaced by 0.105. As a consequence of modifying the run scripts, the record numbers stored with each measurement were reset to start again from 1. All data taken with the wrong C_{site} value were scaled to the correct values before they were stored on the monitoring database (see Sec. 4.3).

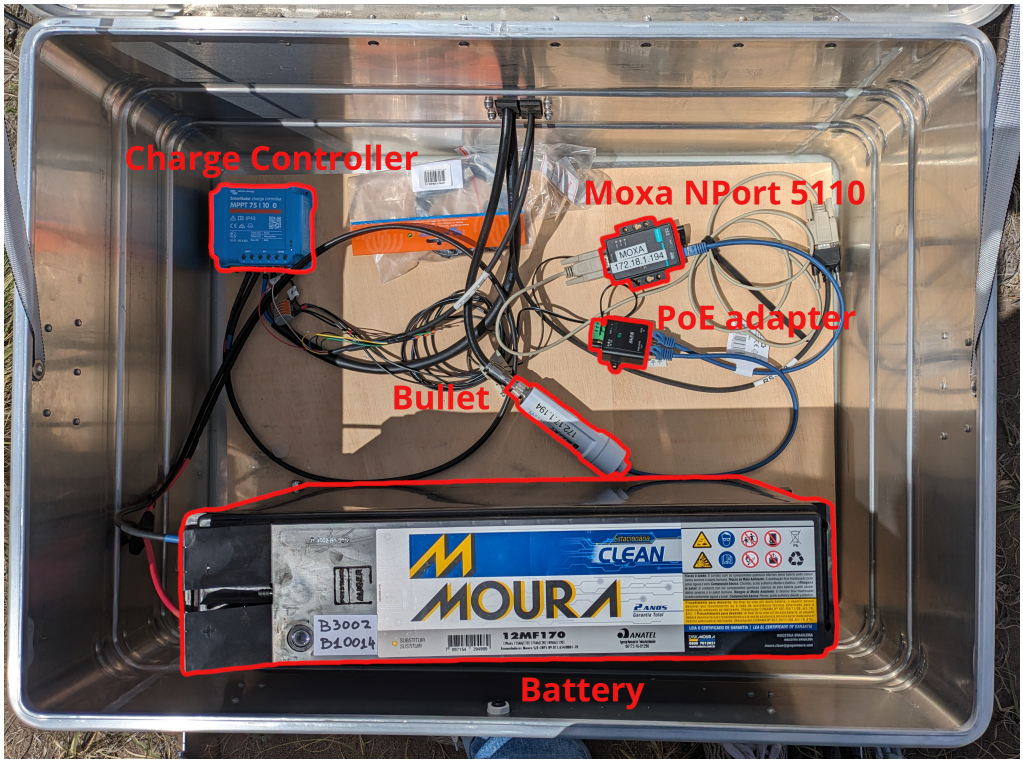

Figure 4.12: Electronics box of guanaCO. Some components are marked in red. At the top of the picture, the cable glands can be seen, through which the power cable for the solar panel, the power- and data cables for the EFM and the antenna cable between the Bullet and the antenna exit the box.

4.2.2 Accuracy of the new EFM stations

With the calibration requirements, which were discussed in Sec. 4.1, met – except for vegetation that might regrow but was completely removed at the time of commissioning – the recorded electric-field data from the new EFM stations have an absolute calibration. The accuracy of the calibration is determined from a summary of all sources of systematic uncertainties. These sources and their uncertainty contributions are listed in Tab. 4.3. The two factors that convert the measured voltage signal to electric field, $M_{\text{parallel\_plate}}$ and C_{site}, were determined in calibration campaigns by the manufacturer and have uncertainties of 1% and 4%, respectively. There is another systematic contribution estimated at 5% regarding a drift in the sensor from accumulating surface charges. This drift might evolve uniformly over time in a single direction which could be monitored with future zero-field measurements. If the drift turns out to be quantitatively determinable, it could be corrected for. The same logic applies to growing vegetation, a possible effect on the calibration whose potential extent is unknown.

The systematic effects with known or estimated sizes amount in total to an uncertainty of the electric field measurements of 6.5%. This level of accuracy is not primarily relevant for the application of the recorded data in thunderstorm flagging for cosmic-ray radio detection, but it is potentially useful for applications in cosmo-geophysics related studies.

(a) November 2022

(b) November 2023

Figure 4.13: Vegetation growth after one year at the LA station. Both pictures capture the same angle of the station.

4.3 Data acquisition (DAQ)

The readout of the EFM network is arranged in a way that is as centralized as possible but also reasonable with respect to the available infrastructure. All new Rockets are connected to the local network of the Pierre Auger Observatory at the respective FD site where they are mounted on the communication tower. They are incorporated into the so-called *Remote Monitoring Network* (RMN). However, guanaCO directly connects to the already existing Rocket at CO, which is used separately for AERA in a different network. Since the EFMs of the stations CRS and AERAWS are already incorporated into and read out via this network, the DAQ of guanaCO is naturally implemented in the same way as that of the CRS and AERAWS.

Table 4.3: Overview of systematic uncertainties of the electric-field measurements of the new stations.

Source of uncertainty	σ_E	Reference
CS110 $M_{parallel\_plate}$ calibration	1%	[78]
C_{site} calibration	4%	[78]
Expected range of drift over time	5%	[77]
Drift due to growing vegetation	?	
Total estimated uncertainty	6.5%	

The basic structure of the DAQ of the stations CRS and AERAWS is described in [76]. It relies on the Python package `PyCampbellCR1000` [83] and the npreal2 driver for the Moxa NPort5110 that allows to use the serial port of the NPort5110 as if it was a local TTY port. Finally, a set of scripts is used for reading out, sorting and archiving the EFM data in daily files starting and ending at midnight UTC. In the case of the stations CRS, AERAWS and guanaCO, these scripts are run on the AERA-DAQ13 machine that is a physical machine inside the CO building. In the case of armadiLLo, CaLaFate, La Mara and Las vAcas, the scripts are run on the efm-pc, which is a virtual machine in the Central Data Acquisition System (CDAS) of the Pierre Auger Observatory inside the RMN[1]. On the efm-pc, the readout scripts from AERA-DAQ13 were installed and slightly extended[2]. They are located at `/home/max/efm_readout/`. Some scripts are automatically executed as cron-jobs[3] and a few other scripts are intended for manual execution in case of problems. The cron-jobs for the different stations are spread around the hour to avoid overloading the npreal2 driver for the Moxa NPort5110 TTY ports, as this spreading appears to reduce driver failures.

Scripts executed automatically as cron-jobs:

- **`readout_station.py`**: This script takes as argument the initials of a station: LL/LM/LA/CLF. It is executed every hour.

  The buffer of the EFM is read out twice with the command `update` of `PyCampbellCR1000`. Readout is done twice, first for the table taken at the configured sampling rate of 1 Hz and subsequently for the table of 60 s-averaged values. The command synchronizes a local table file with the respective table. The table file is located in the subfolder `output_<station>` and named `<station>_Tab<sampling rate>sec.dat`, where `<station>` is replaced with the initials of the station and `<sampling rate>` is either 1 or 60.

  Sometimes, data transfer can be interrupted and the last line stored in the table file may be truncated causing an error in subsequent readout attempts. Therefore, the script first tries to catch these errors and deletes the truncated line if necessary.

[1] The efm-pc is reachable from inside the local network of the Pierre Auger Observatory via its IP address `192.168.218.8` or from the outside from a whitelisted IP address. The machine crc500 (IP `141.52.67.250`) in the KIT-IAP cluster is whitelisted. The username of the efm-pc is "max" and the password is one of Auger's legacy-passwords, hint: It is related to a fish restaurant near Malargüe.

[2] Scripts available at `gitlab.iap.kit.edu/auger-observatory/sandboxes/maxbuesken/efm-daq.git`

[3] The cron schedule is listed in appendix A.1

- **renamefile_station.sh**: This script takes as argument the initials of a station: LL/LM/LA/CLF. It is executed once a day between 4:38 UTC and 5:23 UTC (depending on the station).

  The local table files are copied to `output_<station>/<year>/<month>/` and renamed to `<station>_Tab<sampling rate>_<year>_<month>_<day>.dat` for the date of the last day with the station initials `<station>` and the two values 1 and 60 for `<sampling rate>`.

  The script is executed a few hours after midnight to await a number of readout cycles, that may catch up with the data synchronization in case the connection to a station was lost during the last day but restored after midnight. Overflow data from the next day are removed from the copied files. Accordingly, data from the last day are removed from the original table files.

  Next, the copied data with 1 Hz sampling are uploaded to the monitoring database into `AERA/Field<station>` using the script `WeatherReader` which is located at `/home/max/WeatherReader/`. It connects to the Malargüe server of the monitoring database and stores the data, which are then automatically synchronized to the mirror server in Wuppertal.

  In the last step, the locally copied files are compressed with `bzip2` to reduce the used disk space.

- **settime_station.py** This script takes as argument the initials of a station: LL/LM/LA/CLF. It is executed every 4 hours.

  The clock of the EFM data logger is synchronized with the clock of the efm-pc which is set in UTC. The synchronization is done via the `settime` command of `PyCampbellCR1000`.

- **recover_station.py** This script takes as argument the initials of a station: LL/LM/LA/CLF. It is executed every 6 hours.

  The script looks for potential problem in accessing the EFM station. First, the IP address of the Moxa NPort5110 is pinged to find out if there is a network issue. If the Moxa is reachable, the serial port is tested. In the case that the serial port is not working, the npreal2 driver is reinstalled and the ports are reconfigured by executing the script `reinstall_driver.py`. This way, some errors are fixed automatically without the need for manual intervention.

Scripts to be executed manually:

- **check_station_status.py** This script prints the last 20 lines of the log file of each station that contains all chronological standard output and standard error messages from the executed cron-jobs. It allows for a quick check of the current state of the readout and potential connection problems.

- **reinstall_driver.py** From time to time, the npreal2 driver can get stuck, at times in relation to a memory leak of the Linux kernel of the efm-pc. A possible solution for this problem is the re-installation of the driver. This script uninstalls the driver and does a fresh install from the source directory including the configuration of the TTY ports for the EFM stations.

This set of scripts is an update to the scripts on the AERA-DAQ13 machine that read out the EFM stations CRS, AERAWS and BATATA. However, the scripts on AERA-DAQ13 are kept unchanged as they are in a fully functional state for that machine and the readout has shown to be in general less prone to errors than the readout on the efm-pc.

The designated and the easiest way to access the EFM data is via MySQL queries to the Wuppertal mirror of the Auger monitoring database[1]. The EFM data are stored in the `AERA` database in the tables `Field<station>` with the abbreviation of a station inserted as `<station>` (for CRS, no abbreviation is used, i.e. its data are stored in the table `Field`)[2]. An overview of the formats of the tables on the monitoring database is given in Tab. 4.4. Documentation about the technical information about the EFM data is also collected on the Auger Wiki.

Table 4.4: Structure of the EFM tables in the monitoring database.
*Calculation and filling of this flag was done in the past but has been discontinued. For reference, see [84].

Stations	Table entries of `Field<station>`								
BATATA, LL, LM, LA, CLF	Time stamp	Record number	Electric field	IsTS flag	Status	Hygrometry	Panel temperature	Leakage current	Battery voltage
Format	`YYY-mm-dd HH:MM:SS`	`Int`	`Float`	`Tinyint`	`Tinyint`	`Float`	`Float`	`Float`	`Float`
Unit			$\mathrm{V m^{-1}}$			%	°C	nA	V
CRS, AERAWS	Time stamp	Record number	Electric field	IsTS flag*					
Format	`YYY-mm-dd HH:MM:SS`	`Int`	`Float`	`Tinyint`					
Unit			$\mathrm{V m^{-1}}$						

[1] A short user manual for the monitoring database can be found at https://wiki.auger.org.ar/doku.php?id=monitoring:mondb_usage

[2] Scripts and tools for automatic queries of the EFM tables and analysis of the data are collected at https://gitlab.iap.kit.edu/auger-observatory/sandboxes/maxbuesken/EFM_tools

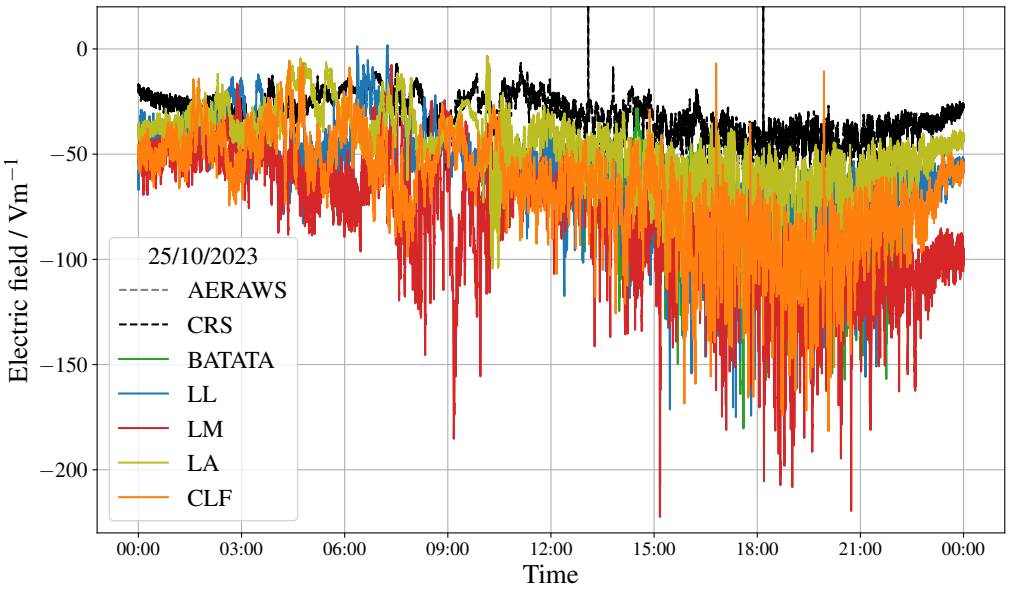

Figure 4.14: Electric-field traces of all live stations from 25/10/2023. No large electric fields were recorded.

4.4 Data

No in-depth analysis of the new EFM data is envisaged to be done in this work. A sophisticated study towards the main purpose of the EFM network, a thunderstorm flag for the RD, and an adequate software implementation of the latter, shall not be provided here. Nevertheless, a look at the first data is given to ensure the functionality of the new stations and basic ideas for the development of an array-wide thunderstorm flag are presented.

4.4.1 Basic data analysis

Large electric fields, that influence the cosmic-ray radio measurements, are rarely present. At AERA, the fraction of the duty cycle that was affected by large electric fields, was estimated around 4% [85]. Most of the time, the local weather conditions are fine. However, this does not mean that the atmospheric electric field is zero. Instead, there is always an electric field present in the atmosphere, whose absolute strength typically reaches up to 100 Vm^{-1} [86]. Moreover, this fair-weather electric field exhibits a daily variation with the minimum appearing around 19:00 UTC and the maximum appearing around 3:00 UTC. This phenomenon is called Carnegie curve [87].

The Carnegie curve was already seen in data from the CRS and AERAWS and different aspects about it were studied in [80]. On fair-weather days the phenomenon is also evident in the data from the new EFM stations. As an example, in Fig. 4.14 the electric field recordings from all stations are shown for the day 25/10/2023. Apart from some spikes, the electric fields in all stations vary between 0 Vm^{-1} and −150 Vm^{-1}, while the maxima lie between 4:00 UTC and 8:00 UTC and the minima lie around 18:00 UTC. Seasonal variations can cause shifts of the positions of the minimum and maximum

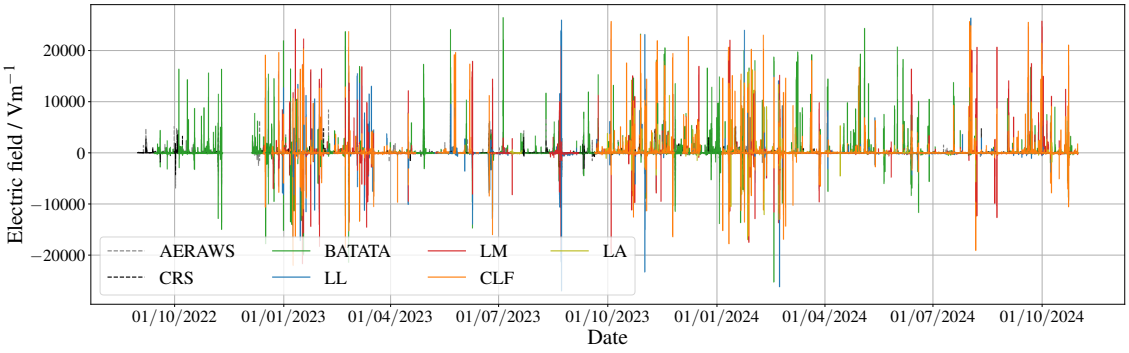

Figure 4.15: Electric-field traces of all stations from 09/2022 until 10/2024.

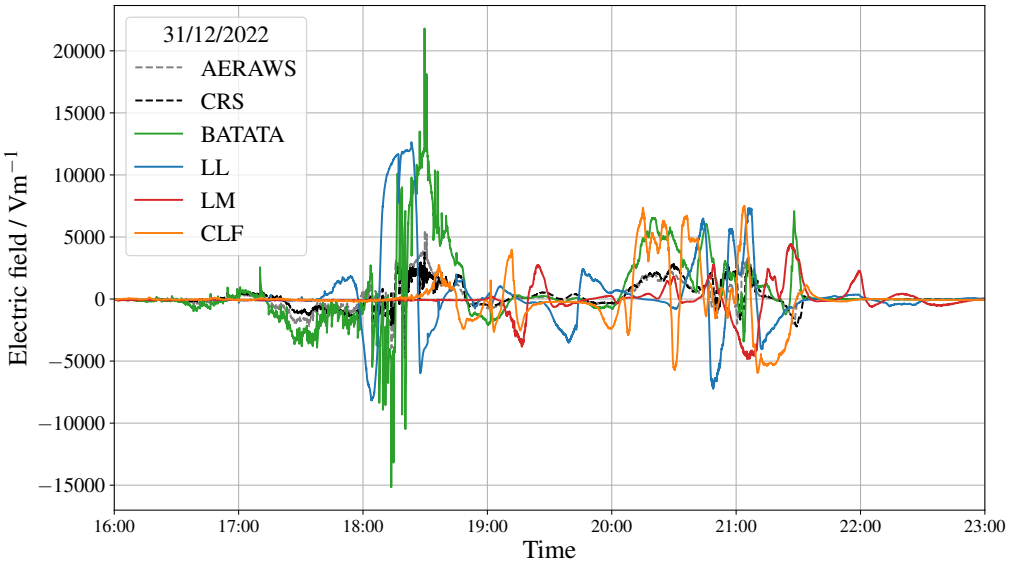

Figure 4.16: Electric-field traces of all live stations from 31/12/2022. Between 17:00 UTC and 22:00 UTC, thunderstorm conditions were recorded in all stations.

of the Carnegie curve by several hours [87, 80]. Data from days like shown in Fig. 4.14 confirm, that all new stations see the Carnegie curve under fair-weather conditions, which is an indicator for their functionality.

It should be noted that the term "fair weather" is used here to describe conditions in which no large electric fields were recorded at any location in the array throughout one day. In the context of atmospheric electricity however, there exist distinct criteria by which fair-weather conditions are defined [88]. These are necessary to be able to properly select data for the use in studies related to the Global Electric Circuit (GEC). Recently defined criteria from [88] require local monitoring of the wind speeds, clouds and aerosols. Wind speeds sensors are operated within a few kilometers of each EFM station which might be sufficient to check this criterion. Cloud and aerosol information are provided at least during moonless nights from the atmospheric instruments of the FDs. Therefore, providing fair-weather electric field data from the Pierre Auger Observatory might be possible and could help geophysics studies that require such data.

In Fig. 4.15, all electric-field traces of all EFMs are shown for the time range from September 2022 (start of DAQ of the BATATA station) until mid of October 2024. It is

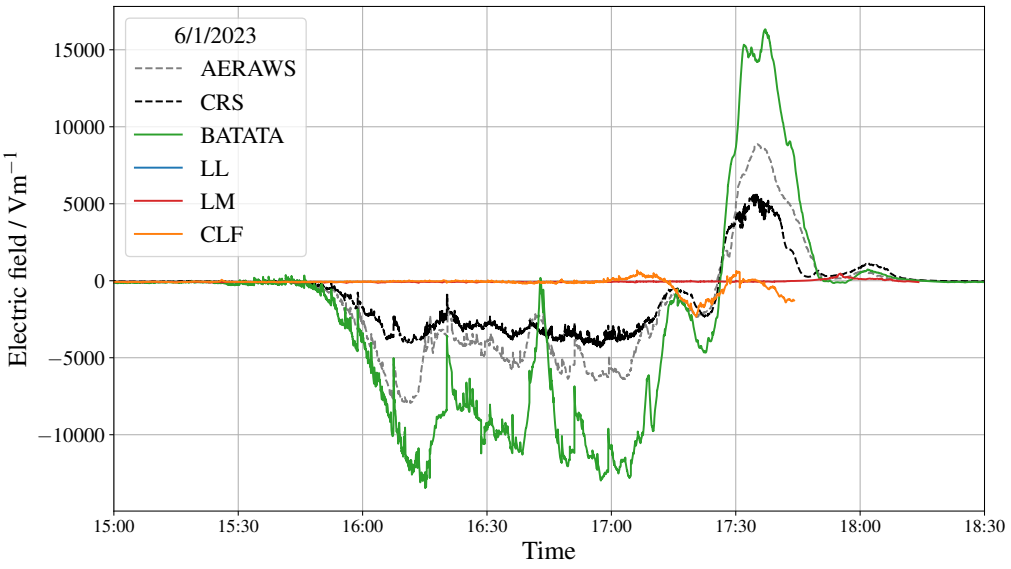

Figure 4.17: Electric-field traces of all live stations from 06/01/2023. A thunderstorm was recorded in the AERA region by CRS, AERAWS and BATATA.

clearly visible that the number of periods with large electric fields is higher in austral summer compared to winter. Various different thunderstorm signatures are found in the data. Fig. 4.16 shows the evening hours of 31/12/2022 when large electric fields were recorded by all seven EFMs. This event might have been a large thunderstorm spanning across the whole array or separate thunderstorm cells appearing across the array at the same time. The largest electric field amplitude was recorded by BATATA, reaching up to 20 000 Vm^{-1}, and in all stations the polarity of the electric field switched multiple times.

Fig. 4.17 shows the electric-field traces of a thunderstorm that was only observed by the three stations near AERA. Being relatively close, the stations recorded similar looking traces but with different gains. These gains reflect different C_{site} factors, that hold for each of the stations. In case of BATATA, $C_{site} = 0.105$ is given by design. The EFMs at CRS and AERAWS were not calibrated, but their C_{site} factors are per default internally set to 0.1. By using thunderstorm events like the one seen in Fig. 4.17, there is the possibility to cross-calibrate CRS and AERAWS with BATATA and determine their true C_{site} factors.

In a similar way, Fig. 4.18a shows another thunderstorm, where the electric-field traces from BATATA, CRS and AERAWS mostly differ by a gain factor. Additionally, the EFM at LL recorded an electric-field trace, which is very similar in shape to the one from BATATA but shifted in time by about one hour. This indicates that the thundercloud at both sites might have been the same one and has moved from AERA towards LL, assuming that it did not change much its shape and electrical structure in the time frame of one hour. A sketch of the possible movement of the thundercloud is illustrated in Fig. 4.18b. Reconstructing the movement of thunderclouds across the array would allow to generate thunderstorm flags for air-shower events, whose shower cores developed in the path of the thundercloud. At the same time, other parts of the array could be declared thunderstorm-free at the given time, if there were no large electric fields recorded by close-by EFM stations. This idea is illustrated by the red and green areas in Fig. 4.18a,

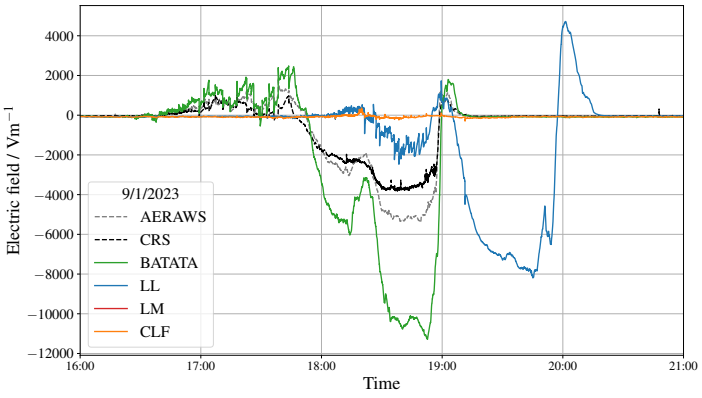

(a) Electric-field traces from all live stations. Large electric fields were recorded by CRS, AERAWS and BATATA between 17:00 UTC and 19:00 UTC and by LL between 18:00 UTC and 20:15 UTC.

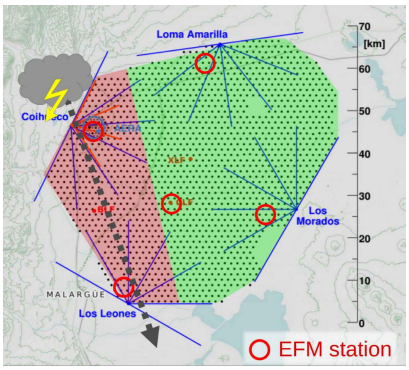

(b) Sketch of a possible movement across the array of the thundercloud that could explain the electric-field traces in BATATA and LL from Fig. 4.18a, which are similar in shape but shifted in time. The red and green colored areas mark a possible division of the array into thunderstorm-affected and fair-weather parts, respectively.

Figure 4.18: A thunderstorm recorded on 09/01/2023.

respectively. However, it should be noted that the shown illustration is only meant to explain the principle idea of creating array-wide thunderstorm flags. This specific sketch should not be used in analyses since, for example, no electric-field data were recorded at LA and LM and thus not considered in the sketch. The topic of developing a thunderstorm flag is further discussed in Sec. 4.4.2.

One aspect of characterizing the new EFM stations is their dynamic range. Fig. 4.19 shows normalized histograms of the complete electric-field data that was collected so far by the EFM network. The histograms for the CRS and AERAWS stations for the same time range are shown as well. In the figure, the two plots show the same data but the x-scale is linear in the top plot while it is symmetrical logarithmic in the bottom one. Most of the electric-field samples are at low values, in magnitude below a few 100 Vm^{-1} when fair-weather conditions are present. The most probable value varies per EFM station and ranges between $-20\,\mathrm{Vm}^{-1}$ and $-70\,\mathrm{Vm}^{-1}$. The shape of the electric-field distribution at low values also differs between the stations. For the new EFM stations, on average the tip of the distribution is flatter than for the CRS. This observation can be explained by a significantly different effective gain factor of the CRS compared to the new calibrated EFMs.

Furthermore, all histograms exhibit an asymmetry around $0\,\mathrm{Vm}^{-1}$ when looking at large electric fields, i.e. data taken during thunderstorm conditions. Positive electric fields occur more often than negative ones. This observation may allow for some conclusions on the types and characteristics of thunderclouds appearing in the Argentinian Pampa near Malargüe.

The histograms drop off at different electric-field strengths for the different stations. This is, to a big part, a consequence of the circumstance that the new stations are calibrated, while CRS and AERAWS are not. The latter stations reach lower maximum

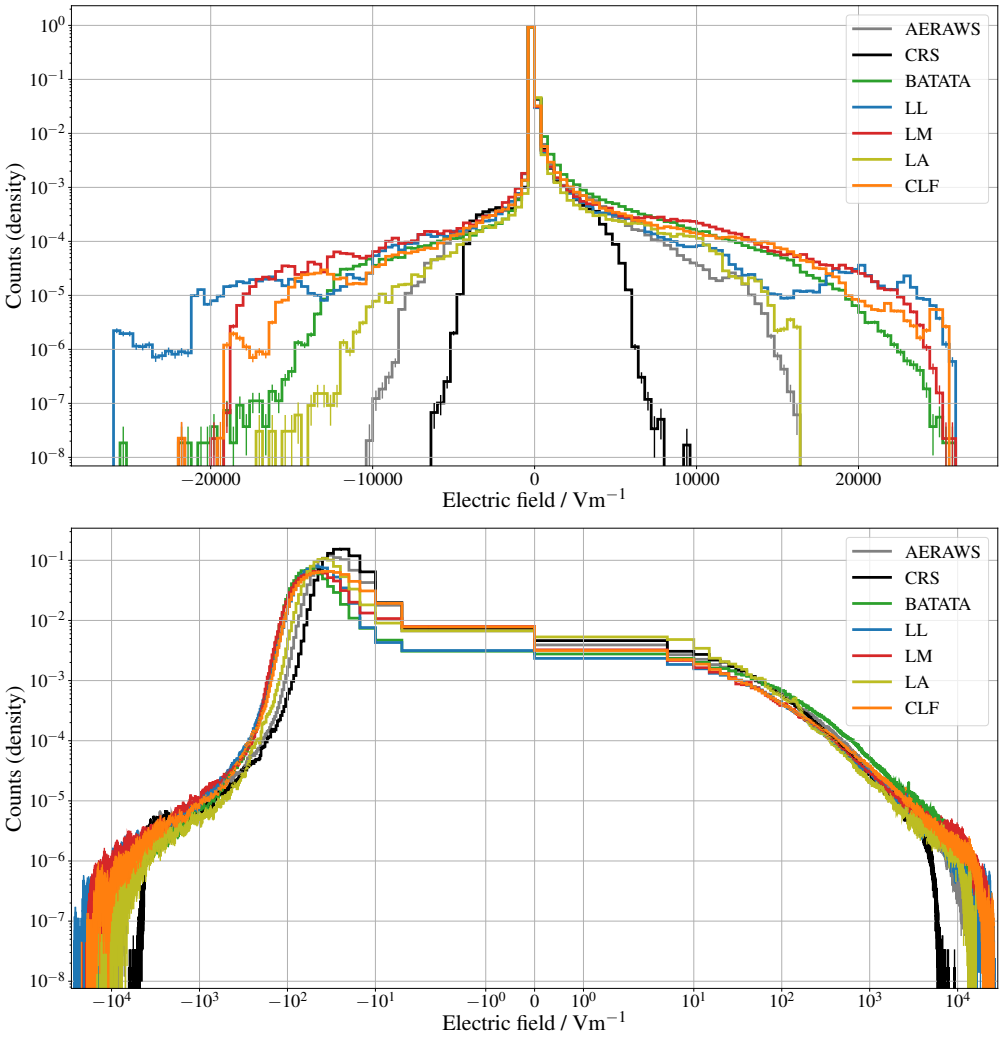

Figure 4.19: *Top:* Normalized histograms of all electric-field data collected by all stations between 09/2022 and 10/2024. No manual limits are imposed on the histograms, visible edges at the upper and lower ends are due to intrinsic limits in the data. Error bars are calculated per bin assuming Poisson errors. *Bottom:* Same plot but with a symmetrical logarithmic x-scale.

electric field strengths than the new stations. Only for positive electric fields, the LA histogram drops off around the same value as the AERAWS histogram. However, data from the LA station has been collected in only less than half of the considered time period and there just may not have been any recorded thunderstorms that would reach the range limit of LA. Still, also the other new stations show differences in the shapes of their histograms at the largest electric-field values. While this may be a consequence of statistical limitations, i.e. more heavy thunderstorms need to be recorded, there may be systematic differences between the sites. In the future, the new EFM stations should be characterized in an explorative analysis with more data. Such a study was performed in [80] for the CRS and AERAWS stations with about ten and eight years of data, respectively.

In rare occasions, electric fields are so large that the measuring range of an EFM is reached. Then, the EFM is saturated and stores a `NaN` instead of a number. At LL, saturation already happened during strong thunderstorms and as a consequence its histogram in Fig. 4.19 has a sharp drop-off at the negative end. However, the cases of saturation are very rare and make for an irrelevant fraction of the total data.

4.4.2 Towards a thunderstorm flag for the RD

The main purpose of the new EFM stations is to provide the data to build thunderstorm flags for the RD. There needs to be a reasoned decision made for each air shower measured by the RD, whether the radio signals of that shower were significantly affected by atmospheric electric fields. The full development of a usable thunderstorm flag for RD including the implementation into the pipeline of RD data analysis is out of the scope of this work. However, a few fundamental aspects of that topic shall be discussed.

First, the existing and established method for thunderstorm identification and flagging for high-level analyses with AERA is reviewed. Afterwards, a few considerations and ideas for the way towards a thunderstorm veto on the scales necessary for the RD are discussed.

4.4.2.1 Established thunderstorm flag for AERA

At AERA, several efforts were made to develop and implement a practical thunderstorm veto. Throughout these efforts, the performance of the method was improved in terms of reliably rejecting thunderstorm-affected events and not rejecting too many unaffected events at the same time [89]. Ultimately, for high-level analyses on the basis of ADST files, a `Python` script was put in place that queries the raw electric-field data from the CRS and AERAWS from the monitoring database and that updates the rejection status of individual events [90]. This script is available at `Tools/RadioTsFlag` in Offline and is what is used in the energy-scale analysis with AERA (see Sec. 8.1.3).

In the script, the algorithm developed in [85] is implemented, which was designed with the intent to work for inclined air-shower events but is also fully applicable to vertical events. From a given reconstructed event, its detection time t_{event} and reconstructed zenith angle are read. From that information, the geometrical distance at ground is calculated between the shower core and the location at which the shower axis crossed a typical cloud altitude of 5 km. Then, the time τ_{shift} is determined that it takes for a potential thunderstorm cloud – which might have affected the developing air shower – to move across that distance, assuming a cloud velocity of $50\,\mathrm{km\,h^{-1}}$. Considering that such a potential cloud would pass over the EFMs, if at all, either before or after interfering with the air shower, the electric field traces around both time stamps $t_{event} \pm \tau_{shift}$ are evaluated. Concretely, in an interval of ± 30 s around both time stamps, for the electric-field data from the CRS and AERAWS, checks are made whether the absolute electric-field strength exceeded $100\,\mathrm{V\,m^{-1}}$ at any time and whether the standard deviation of the electric field in that interval is larger than $20\,\mathrm{V\,m^{-1}}$. If either of the two checks is positive, the respective EFM is considered to have detected thunderstorm conditions. This method was tested to perform the best across all thunderstorm-flagging algorithms that have been developed for AERA [90].

In the Python implementation, the individual thunderstorm decisions from the CRS and AERAWS, or if a station did not record data at the time, are written into the ADST file containing the inspected event.

4.4.2.2 Challenges in designing a thunderstorm flag for the RD

The RD is designed to measure inclined air showers, thus facing the same issue of thunderstorms affecting shower signals at locations different from the signal detection. This issue is solved as much as possible with the method employed for AERA. In Sec. 4.4.1, the possibility of tracking thunderstorms moving over the array with the new stations spread out across the array was already discussed using the example of the thunderstorm shown in Fig. 4.18. Being able to estimate the path of movement of a thundercloud would provide useful information to refine the thunderstorm-flagging method for AERA and adapt it to the RD.

However, on top of the issue of a spatial and temporal distance between air-shower interference through a thundercloud and detection of that thundercloud, the size of the RD is much larger than the size of AERA and the size of most thunderclouds. Thus, the task of compiling thunderstorm flags for RD becomes a spatially extended problem. One fundamental ingredient for a spatially extended thunderstorm flag across the whole Pierre Auger Observatory is a definition of how to divide the array between the EFM stations. In other words, for each position inside (or potentially also outside) the array, there needs to be a defined way, by which the EFM data are used to determine the electrical state of the atmosphere above that position. One possible solution is to always allocate the spatially closest station to a given position. When translating this into a 2-dimensional geometrical problem, this solution is realized in a Voronoi diagram [91]. Dividing the array and its surrounding area by the EFM stations into a Voronoi diagram is shown in Fig. 4.20. Only the five new stations are used in creating the diagram. The diagram basically divides the array into a northern, western, eastern, southern and central part with LA, BATATA, LM, LL and CLF being the anchor points, respectively. The diagram extends indefinitely beyond the borders of the array. Partitions are colored in red, while the alpha value encodes the strength of the electric field measured at the associated station. This depiction allows to visualize the approximate situation of the atmospheric electricity over the array. Four plots show the Voronoi illustration at 4 different time stamps from the thunderstorm on 31/12/2022 that is also shown in Fig. 4.16. The electric-field time traces are shown in the top part of each plot with a red marker indicating the current time stamp. In this example, the thunderstorm was first present in the south-western part of the array with the largest recorded electric-field strengths. Later, large electric fields were recorded in the central and south-eastern part, while the electric field was weaker in the western part. Data from the station at LA was not obtained at that time.

In this example, air showers that developed over the eastern part of the array could have been declared unaffected by thunderstorms while later they could not. Developing further on the idea of Voronoi diagrams, data from different EFM stations could be used in combination with weights depending on the distance to the location of interest.

The spatial sensitivity of the EFMs to thunderclouds is mostly limited to the vertical direction and low in the horizontal direction. Therefore, it is clear that a thunderstorm-flag method for the RD only based on the EFM data is insufficient. The latter needs

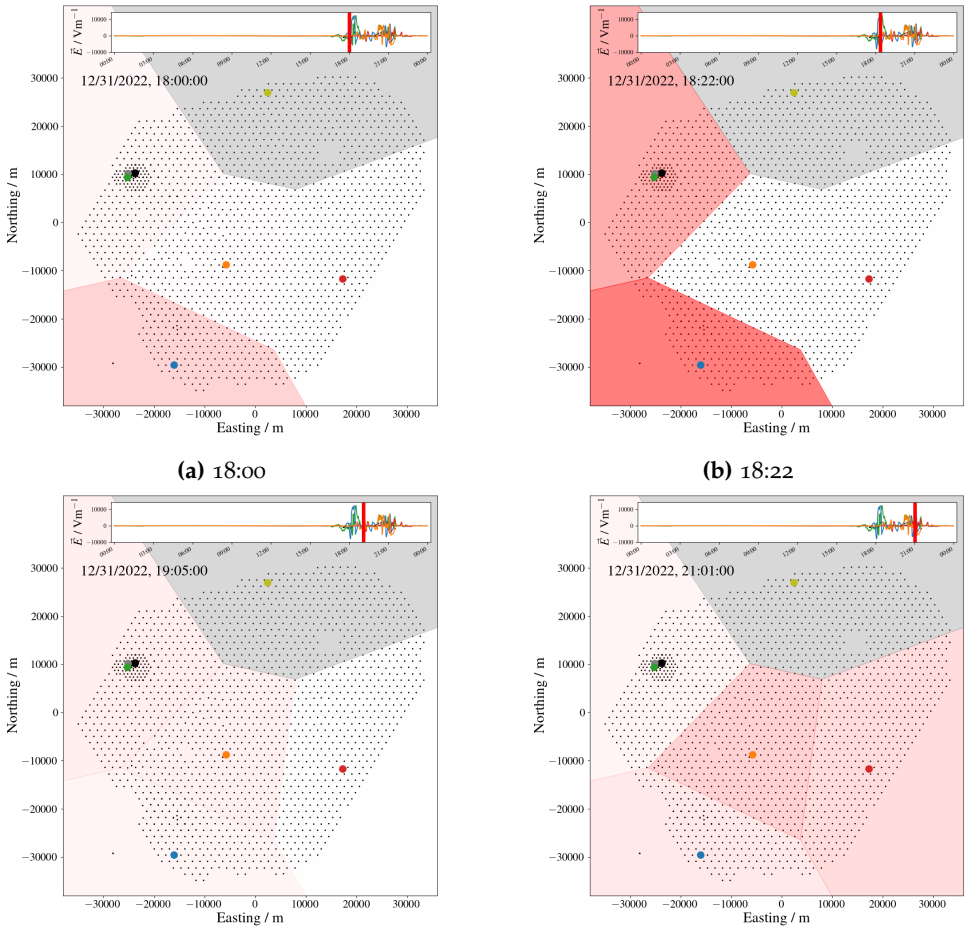

(a) 18:00 **(b)** 18:22

(c) 19:05 **(d)** 21:01

Figure 4.20: Division of the Auger array as a Voronoi diagram with the EFM stations as anchor points. CRS and AERAWS are marked in the plots but not used for the diagram as they are very close to BATATA. The legend for the alpha value of the colored partitions, which encodes the strength of the measured electric field, is not shown as this figure is just intended to provide a qualitative depiction. At the top of each plot, the complete electric-field time series from that day is shown with a red line marking the current timestamp.

to be combined with additional information on the atmospheric electrical condition above the array and around it. Recently, work has been started to explore the usage of publicly available resources [92]. Combining the EFM data, monitoring data from the RD and several weather observables allows to see thunderstorms in a wider phase space, indicating that building a thunderstorm veto for the RD is a complex but solvable task.

4.4.3 Zero-field measurements

In the environmental conditions where the EFMs are deployed, the electronics of the sensor part are not only exposed to the electric field but also to dirt, dust and water. These contaminants can result in surface charges near the sensor electrode which cause electric-field offsets in the measurement that may not be corrected for by zero-field

Figure 4.21: Picture of the zero-field cover mounted on the EFM at BATATA.

references taken when the shutter is closed. Those surface charges can build up over time resulting in a drift of the field offset. Such a drift can be monitored by conducting zero-field campaigns in which the sensor part of the EFM is mechanically closed off with a zero-field cover as is shown in Fig. 4.21. A zero-field cover by Campbell Scientific was acquired together with the new EFMs. It tightly fits on the CS110 and constrains the measured electric field to the contribution by residual surface charges. Zero-field measurements with the zero-field cover were so far conducted twice, in November 2022 and in November 2023 (at AERAWS only in November 2023). At each station, the zero-field cover was put on the EFM for at least one minute.

The mean electric fields from these campaigns are shown in Fig. 4.22. The gray band reflects a range of tolerance around $0\,\mathrm{Vm}^{-1}$ that is given by the manufacturer. This range is $\pm 60\,\mathrm{Vm}^{-1} C_{\mathrm{site}}$ which is $6.3\,\mathrm{Vm}^{-1}$ for $C_{\mathrm{site}} = 0.105$. Some zero-field measurements from both campaigns lie outside of this range. However, except for AERAWS, they only barely exceed the tolerance. Also, the indicated tolerance range only applies to the new EFMs as the C_{site} values for CRS and AERAWS are unknown. All new EFMs show a slightly larger zero-field values in November 2023 compared to one year before. Subsequent measurement could clarify if this trend is an ongoing drift or not. In contrast to the new EFMs, the zero-field value of the CRS drifted in the opposite direction.

Ideally, the electrodes of those EFMs outside the tolerance band should be cleaned. Instructions on how to clean the electrodes correctly are given in [78]. However, getting the EFMs from the field and bringing them into a clean environment for cleaning could be a large effort. As long as zero-field offsets are not drifting away too much from the tolerance band, this kind of maintenance is not worth the effort. But whenever it is possible and convenient for collaborators (i.e. there are field activities planned close to an EFM station) taking a new zero-field measurement by putting on the zero-field cover for a few minutes would be very helpful.

4.4.4 Supplementary data

Apart from the most important observable of the EFMs, the atmospheric electric field, there are additional sensors that provide supplementary data about the environmental

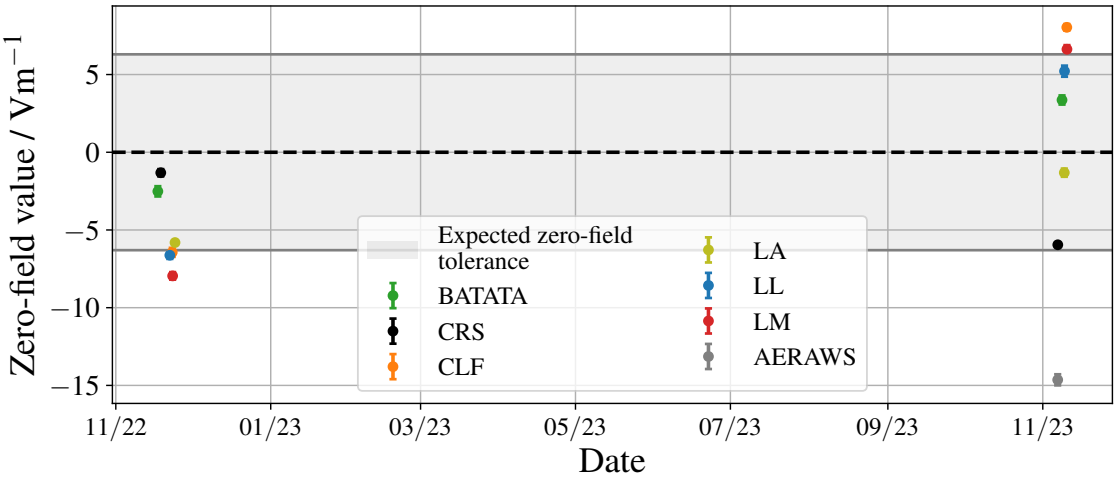

Figure 4.22: Plot of the mean values from all zero-field measurements versus time. Error bars show the standard deviation of the measured samples. The gray band marks a tolerance range suggested by the manufacturer of the EFM.

conditions and about the status of the EFM. As explained in Sec. 4.1, the CS110 also records the relative humidity of the air, the temperature on the electronics panel, the delivered voltage from the power supply, the measured leakage current of the system and a status code. Those are also recorded and stored on the Auger monitoring database as listed in Tab. 4.4. The supplementary data is useful to check if the EFM is operating properly.

First of all, one interesting meta information is the uptime of each EFM station. The uptime is calculated per day from the number of electric field samples divided by the total amount of seconds within one day. This data is plotted in Fig. 4.23 for each station as a function of time from 09/2022 until 10/2024. CRS shows the best uptime ratios which are 100% most of the time since it was already in a stable state at the start of the considered time period. AERAWS also has uptime ratios at 100% for the majority of the time until mid April 2024. After that, its uptime gradually declined. In November 2024, the charge controller of its solar power system was found to be broken and was replaced. Since then, the station is operating again during daytime. The battery is likely degraded and needs to be replaced to enable again full-cycle operation of the AERAWS.

The uptime of BATATA is very similar to the uptime of CRS with the exception of the period from May to November 2023 when it was around 50%. This reduced uptime was caused by a discharged battery. AERAWS, CRS and BATATA all show a larger gap in November 2022 when the DAQ13 machine was out of order. A few more gaps can be seen in all stations simultaneously which are probably due to technical issues with DAQ13 at that time. A loose cable caused the fluctuating uptime at AERAWS from September to November 2023.

In December 2022, the data acquisition of the other four stations was put in place on the efm-pc. In general, these stations show more and longer gaps in the uptime since the readout on the efm-pc was facing several software failures that sometimes went unnoticed for several days. The misalignment of the Rocket antenna at the LA tower prevented data taking of the LA station for several months. Some of the gaps were

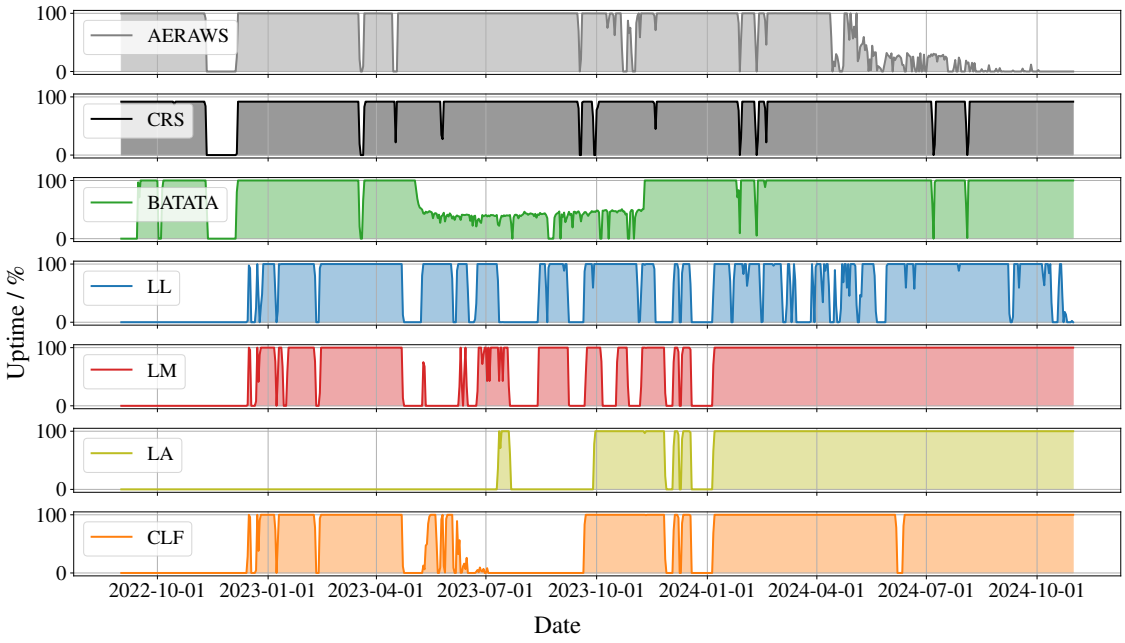

Figure 4.23: Uptime fractions per day of all EFM stations plotted over the complete time range since the commissioning of the new EFM network.

caused by lightning strikes destroying parts of the communication infrastructure that had to be replaced. So far, there are no indications that the EFMs themselves ever failed regular operation.

Since mid of January 2024, the driver failures on the efm-pc did not appear again and the uptime of the connected stations is much better. Only for the station at LL, there are still regular dropouts, which were found to be caused by connection issues between the central campus in Malargüe and the Rocket on the communications tower at the LL FD site. Those connection issues are being investigated and to be fixed. There are no hints that the connection between the Rocket and the EFM station has any problems. The script for recovering the driver on the efm-pc has also been improved to automatically correct failures like they had appeared before.

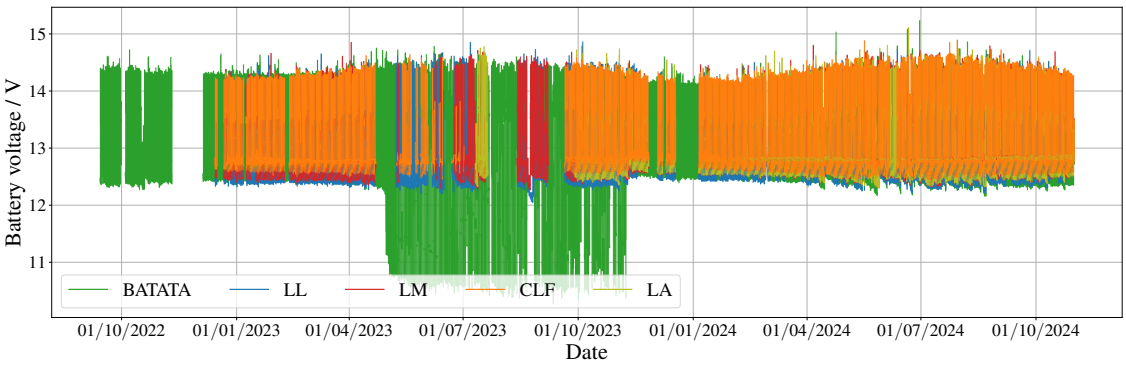

Figure 4.24: Plot of the supply voltages from the batteries measured by all EFMs from 09/2022 until 10/2024.

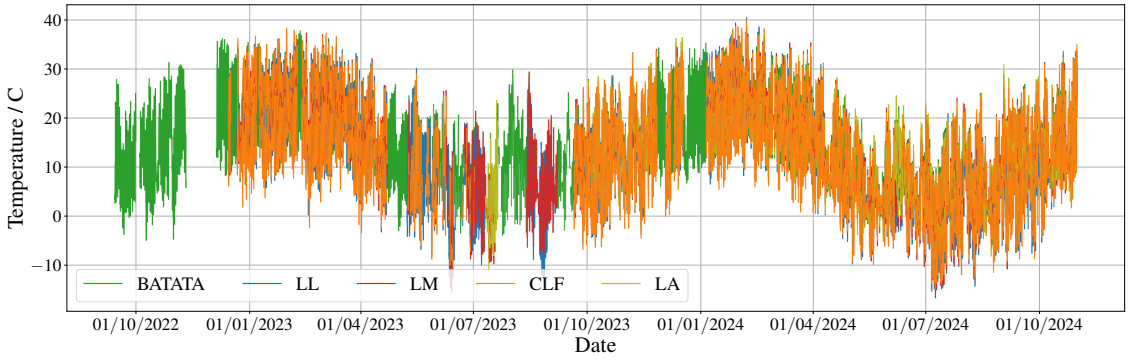

Figure 4.25: Plot of the electronics-panel temperatures of all EFMs from 09/2022 until 10/2024.

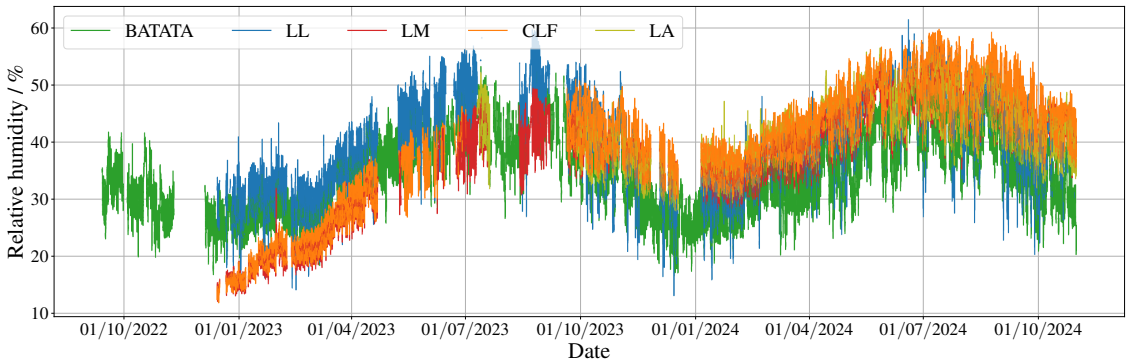

Figure 4.26: Plot of the internal relative humidity in all EFMs from 09/2022 until 10/2024.

The voltage supplied from the power system as a function of time is plotted for each of the new stations in Fig. 4.24. Clearly visible are the daily fluctuations between 12.5 V and 14.5 V from using the battery at night and charging it during the day. For BATATA, the battery voltage started to drop to lower values starting April 2023. From May to November 2023 the voltage even went below 11 V on some days and was not sufficient to power the station during the night. This explains the uptime fraction of that EFM to be around 0.5 during theses months. It indicated that the battery at BATATA was exhausted and needed to be exchanged. Since the batteries of all stations were replaced in November 2023, the voltages stayed well above 12 V in all cases. The data show no indication that the solar power system of the new EFM stations is of insufficient size.

Fig. 4.25 shows the temperature measurements from the electronics panel of the EFMs. The trend over time clearly exhibits the daily variations with a seasonal modulation. These temperature measurements are not equivalent to air temperature measurements from a weather sensor as they can be affected by heating of the EFM housing through solar irradiance.

Another sensor inside the EFM housing records the relative humidity which is plotted for all new stations in Fig. 4.26. The stations all show a clear seasonal modulation with a peak in the late winter months and a day-night variation on top. These trends indicate that the humidity inside the EFM housing strongly correlates with the environmental humidity. Differences between the stations could be the consequence of variations in the environmental conditions at the different locations in the Pampa.

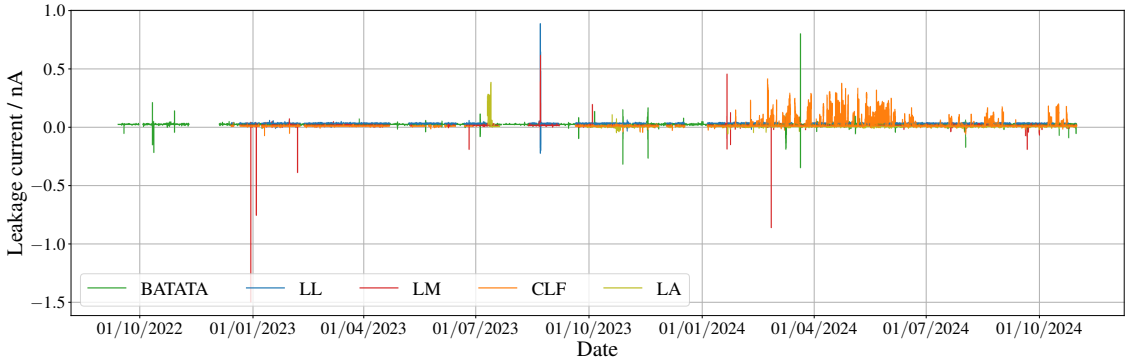

Figure 4.27: Plot of the leakage currents recorded by all EFMs from 09/2022 until 10/2024.

According to the manufacturer of the EFM, internal relative humidity values larger than 20% should be responded to with changing the desiccant inside the EFM [78]. The desiccant is placed inside the EFM housing to keep the sensitive electronics dry in order to prevent long-term drifts in the electric-field measurements. The threshold of 20% was exceeded so far by all stations at all times except for a period of two months at LM and CLF. At peak, the humidity even reaches almost 60% for LL. Therefore, changing the desiccants is advised for all stations. However, such a task would require significant effort that may not be justified, similar to a cleaning of the sensor electrode. Also, the recorded humidity levels are not expected to endanger the general operation of the EFMs. Humidity levels above 70% were measured by the EFM at AERAWS before, while it is still fully functional in its task of thunderstorm flagging for AERA aside from the current outage due to its degrading power system.

Furthermore, the EFMs also measure leakage currents from the sensor electronics. The CS110 is able to compensate for such currents up to ±4.2 nA in the electric-field measurement circuit. However, large and continuous leakage currents may still alter the measurements and make them unreliable. In Fig. 4.27, the leakage-current recordings of all new stations are shown. The currents stayed within ±0.05 nA for the majority of the considered time period, which is 1.2% of the maximum that can be compensated for. From February until June 2024 and during shorter periods afterwards, the leakage current of the EFM at the CLF regularly reached up to 0.4 nA. Those current values are still way below the maximum that can be compensated for. Some momentary leakage current peaks can be found for each of the stations, however never reaching beyond 1.5 nA in size.

Lastly, each recording sample of the EFMs also contains a status code that reflects the state of the system. A list of all status codes and their meaning are given in [78]. In case of unusual behavior of the EFM, the status code might help to find out if there is a problem with the system. The status codes of all new stations from beginning of operation until end of October 2024 are shown in Fig. 4.28. For the majority of the time, the status codes are either 1 or 4, denoting that the EFMs are in good health and are using a dynamic range suitable for low electric fields. The second most populated status codes are 2 and 5, also implying good instrument health but the dynamic range is adjusted for accurate measurements of larger electric fields. Compared to codes 1 and 2, the codes 4 and 5 indicate that the shutter of the EFM needed to be properly positioned, which is automatically done by the device. Aside from these four status codes, there

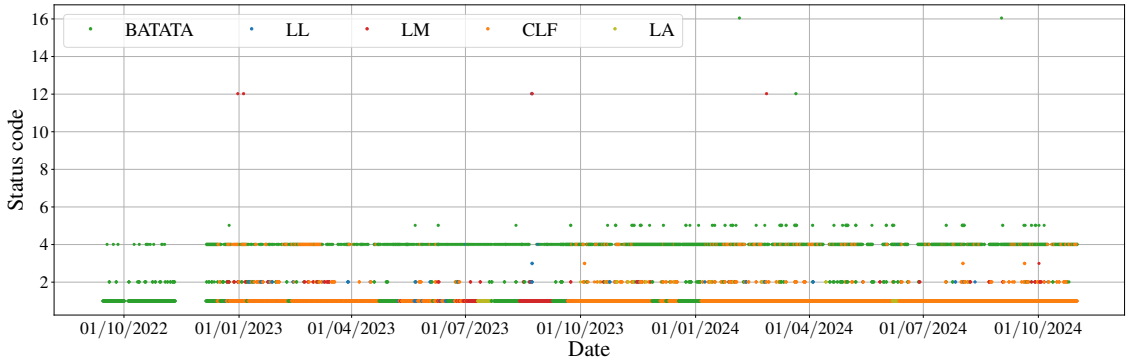

Figure 4.28: Plot of the status codes recorded by all EFMs from 09/2022 until 10/2024.

are only a few occurrences when different status codes were recorded. Status code 3 reports saturated electric-field measurements. Status code 12 denotes a failed self check of the charge-amplifier of the EFM and status code 16 is given if the positioning of the shutter was not possible. In these cases, a `NaN` is stored in the position of the E-field measurement. From Fig. 4.28, it is evident that the cases of improper operation are very rare and that the EFMs are in a fine state.

4.5 Prospects & Outlook

The main purpose of the development and deployment of the new EFM network is the monitoring of thunderstorm conditions on a large scale over the new RD array and beyond that. This main objective accompanied the analysis of the first data as already discussed in Sec. 4.4.2 with basic ideas for how to construct a thunderstorm-flagging algorithm from those new data. However, a full-fledged algorithm and an efficient software implementation of it embedded into standard analyses of air-shower events with the RD requires a dedicated study. In this context, a correlation analysis of the new EFM network data and plots like shown in Fig. 4.20 with other (external) meteorological data (i.e. lightning or weather satellite data) is desirable. Work on such an effort has been started and looks promising.

As for high-level analyses with AERA – like the energy-scale analysis, a thunderstorm veto is likewise required for future studies with the RD. Considering how strong of an influence strong atmospheric electric fields can have on the air-shower radio emission, any high-quality event set needs to be filtered for thunderstorm events.

Strong atmospheric electric fields in thunderstorm can also enhance the air-shower signals recorded by particle detectors [93]. Thus, studies at the Pierre Auger Observatory about cosmic-ray events during thunderstorms measured by the SD may profit from the electric-field monitoring of the EFMs. In addition, the new readout electronics of the AugerPrime detector upgrade has shown to be more sensitive to thunderstorm and lightning conditions [94]. Here, the EFMs could help to identify thunderstorm periods more clearly.

In the current situation, data are collected simultaneously by the new EFM stations and as well by the CRS and AERAWS. From the direct comparison of large electric fields recorded by the two old stations and BATATA, the former two could be cross-calibrated with the latter. Then, previous data from the CRS (since 2011) and from AERAWS (since

2014) could be calibrated retroactively, which would increase the value of those data. Cross-calibration may also be possible by comparing average values and integrated distributions of the electric-field data, following up on attempts made in this regard in [80].

Besides detecting thunderstorms and providing flags for radio-measured air-shower events, the electric-field data is also useful in other applications. There are several ongoing studies in the field of cosmo-geophysics at the Pierre Auger Observatory. For example, studies of Terrestrial Gamay-ray Flashes (TGFs) investigate signals in the SD that might have been induced by TGFs [95, 96]. TGFs are accompanied by thunderclouds and lightning. If there are recordings of the atmospheric electric field by EFMs at times when TGF-candidate events are detected, the evolution of the accompanying thunderstorm may be reconstructed. It would allow to determine the temporal position of the candidate event within the evolution of the thunderstorm.

Further studies deal with Transient Luminous Events, some of which can also be observed with the Pierre Auger Observatory. In dedicated works, the meteorological conditions around those events are characterized [97]. The electric-field data recorded by the EFMs could help determine those conditions more profoundly.

The transregional character of atmospheric electricity is an active research topic. Many studies are connected to the concept of the GEC, which is strongly tied to the phenomenon of the Carnegie curve. Open questions revolve around: meteorological factors that impact the GEC, the contribution of thunderstorms and electrified shower clouds, differences between storms over land and storms over the ocean. The GEC also provides a monitor for climate [98]. Of the ongoing and recent studies around the GEC, some are concerning the situation in Argentina [99], and more are concerning global aspects (see [100] for a recent overview). EFMs are a fundamental instruments in many of these works and the EFM data taken at the Pierre Auger Observatory could well contribute to this field of research. Possibly, other meteorological data taken at the observatory would be helpful in conjunction with the electric-field data.

In particular, a study of the Carnegie curve signature in the EFM data with a preceding classification of fair-weather periods would be valuable. Although meteorological sensors are installed at the Pierre Auger Observatory, it is unclear to which extent their data could be used for fair-weather characterizations as discussed in [88]. However, fair-weather conditions may also be defined without additional meteorological data but from the EFM data themselves as was done in [101]. Such a methodology may be a useful approach in the context of the EFMs at Auger.

Recently, an agreement was concluded between the Pierre Auger Collaboration and José Tacza about sharing the accumulated data from the EFMs and meteorological sensors at the Auger Observatory for research on electric fields at ground level and their relation to solar and atmospheric phenomena. The cooperation was initiated by an interest in the electric-field data from the EFM network at the Auger Observatory during a geomagnetic storm between May 9 – 12, 2024. Various space weather and atmospheric phenomena are possibly related to changes in the fair-weather electric field at ground. Such relations can be studied in long-term analyses but also in case studies like with the mentioned geomagnetic storm [102]. In order to be able to obtain more conclusive results and to investigate local dependencies (e.g. latitude, longitude), collecting data

from multiple geographically distributed sensors is crucial. The EFM network at the Auger Observatory will contribute to this endeavor.

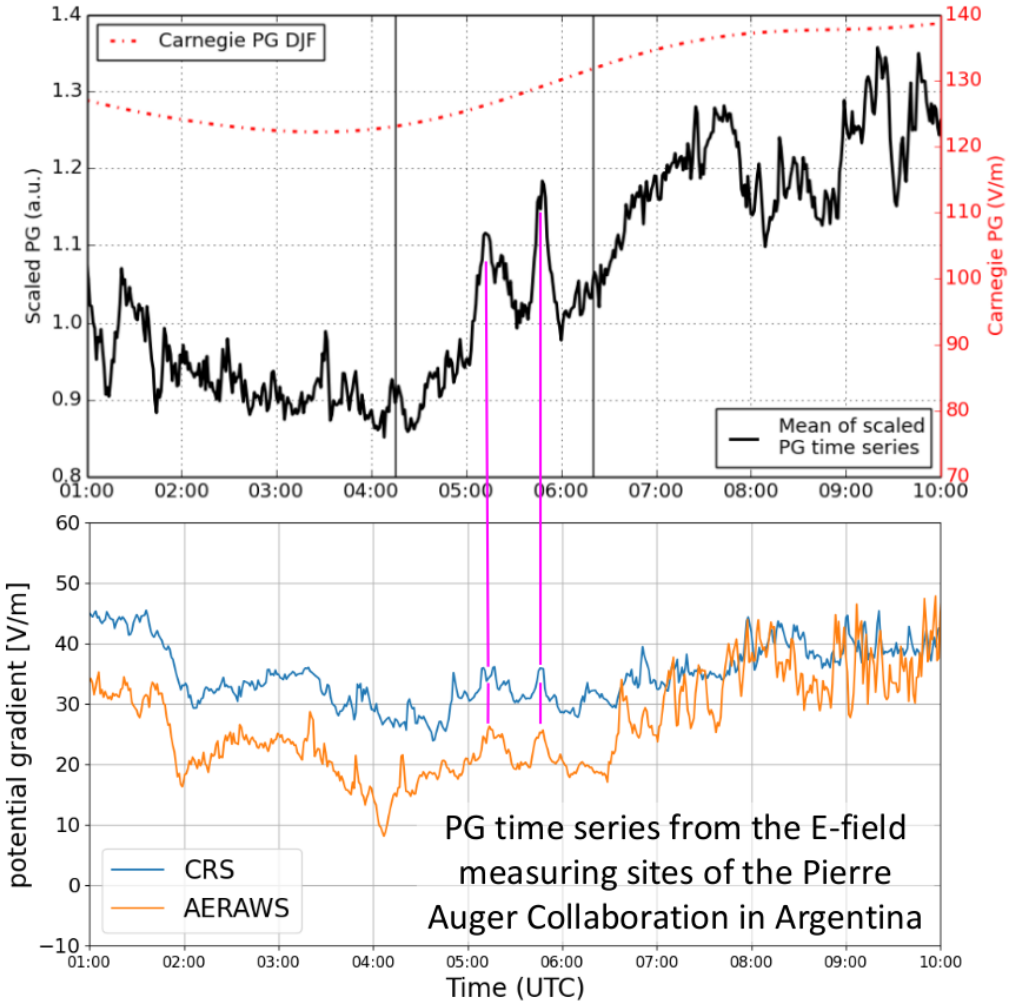

Figure 4.29: Two plots of near-surface electric-field measurements during the Hunga Tonga-Hunga Ha'apai eruption. The top plot shows the averaged time series of the potential gradient from multiple EFM recordings at different positions around the world. For reference, the Carnegie curve is shown. The bottom plot depicts the potential gradient records taken with the CRS and AERAWS EFMs at the Pierre Auger Observatory, aligned in time. At the time stamps of the two peaks, which strongly stand out in the averaged time series, peaks are also visible in the Auger data, as marked by the magenta lines. Figure taken from [103].

As the last example, EFMs may be useful tools in the observation of strong volcanic eruptions. The footprint of the Hunga Tonga-Hunga Ha'apai eruption on 15/01/2022 on the GEC was studied in [104]. As part of the study, the authors investigated responses of the eruption in time series of the electric potential gradient (PG), which is the negative of the electric field, from multiple EFM recordings around the earth. They found two peaks in the PG time series that hint towards an impact from the eruption. The averaged PG time series with the clear two peaks between 5:00 and 6:00 UTC are shown in the top plot of Fig. 4.29. After conclusion of their analysis, the authors learned about the electric-field measurements at the Pierre Auger Observatory and requested a look at

the EFM data from the day of the eruption. The electric-field traces from the CRS and AERAWS stations are shown in the bottom plot of Fig. 4.29 where the time axis is aligned with the top plot. At the time stamps of the two peaks from the averaged PG time series, also enhancements in the electric-field data from the CRS and AERAWS are clearly visible. Although the latter data were not analyzed comprehensively, they support the suggestions made by the authors of [104]. Moreover, the value of the long-term electric-field data taken at the Pierre Auger Observatory for outside research is evident.

The various active research fields and the use-case example of the volcanic eruption make clear how valuable the EFM data are, both from the old stations and from the new calibrated network. Apart from the Auger-internal purpose of thunderstorm flagging for the RD, the data will be of interest to other scientists and research groups. In one case, an individual agreement was already concluded about sharing the EFM data. Still, making these data open and publicly available would be a further step for the purpose of collaborative science. A few years ago, the GloCAEM (Global Coordination of Atmospheric Electricity Measurements) project was initiated with the goal to collect as many electric-field datasets from around the world as possible and provide a uniform database for them [105]. GloCAEM is a sensible place, where the EFM data from Auger could be added and would receive visibility, as long as new contributions are still accepted. From the technical point of view, the data would need to be brought into the unified GloCAEM format. Alternatively, publication of EFM data could happen independently in the context of the Auger Open Data initiative [106].

4.6 Summary

In the context of the installation of the new RD at the Pierre Auger Observatory, the need for large-scale monitoring of the atmospheric electricity with the purpose of thunderstorm flagging at the observatory arose. The typical tool for this task are EFMs and therefore a new network of EFMs was designed, compiled, tested, deployed and commissioned in this work. The task benefited in many aspects from the experience with the already installed EFMs at AERA. In addition to the request for thunderstorm flagging, a target of the network was to provide electric-field measurements with an absolute calibration. This goal put extra requirements on the design of the stations. Ultimately, the decision fell for remote stations that are linked via WiFi to the FD sites of the observatory where they are connected to the Auger network.

The components of the stations were acquired and prepared at KIT, where also a test setup was built in early 2022 that confirmed the basic functionality of the design. In August and November of the same year, the stations were installed in the field at the observatory. Over the course of 2023, technical problems were tackled to establish and improve remote connection to the stations and a stable, automatic readout. The data acquisition of one of the stations was embedded into the routines that already existed for the two former EFMs. For the other four stations, a new virtual machine was created on the servers at the campus of the Pierre Auger Observatory in Malargüe. Subsequently, automatic syncing of the data into the Auger monitoring database was put in place to provide easy access for all collaborators with a time delay of one day. Tools for processing the electric-field data and instructions for troubleshooting technical problems with the stations are provided.

Simple analyses of the first data show that the new EFM stations are in general in a good shape. The BATATA station was dropping out at night during several months as the old battery, that was installed there, was drained. This problem was fixed when all stations received fresh batteries in November 2023. Ongoing connection problems to the station at LL can be attributed to issues in the network infrastructure at the corresponding FD site, which can likely be solved soon. Checks of the supplementary data recorded by the EFMs will allow to keep monitoring the operational status of the stations. The first data also contain several traces from thunderstorms which were qualitatively analyzed and showed potential for tracking thunderstorm movements across the array and for cross-calibrating the old EFMs with the new network. Basic ideas for the development of a thunderstorm-flagging algorithm on a large scale were presented. The accuracy of the new electric-field data is estimated at 6.5%.

Additionally, the new EFM network will be a useful instrument of the Pierre Auger Observatory beyond the application for the RD. Especially cosmo-geophysics related research can benefit from the additional information about atmospheric electricity at the observatory. One example of possible signatures from a volcanic eruption in the electric-field data illustrate how the measurements from the EFMs at Auger could become part of a global network for the monitoring of atmospheric electricity which would benefit associated fields of research and broaden the scientific portfolio of the Pierre Auger Observatory.

In the context of this work, we discussed how thunderstorm flagging of air-shower events from AERA is performed with the two old EFMs at the CRS and AERAWS. This flagging will be an essential step in the preparation of an event dataset for the analysis on the radio energy scale with AERA (see Sec. 8.1.3.1). With the new EFMs, we provide the necessary data to also conduct thunderstorm flagging of RD-measured air-shower events. Thereby, the same step in the event selection for a future energy-scale analysis with the RD is secured. The recipe and the ingredients of the energy-scale analysis, that we present in the coming chapters for the use case of AERA, conceptually apply in the same way to the RD. Following our blueprint in the application for the RD is left to future work. Our direct contribution to that RD analysis is concluded with the provision of the new EFM network.

5

Uncertainty study for the Galactic calibration of radio antenna arrays

Parts of this chapter have been published in:

Study of the uncertainties of the Galactic radio background as a calibration source for radio arrays
M. Büsken, T. Fodran & T. Huege
PoS(ARENA2022)031

Uncertainty study for the Galactic calibration of radio antenna arrays in astroparticle physics
M. Büsken, T. Fodran & T. Huege
PoS(ICRC2023)350

Uncertainties of the 30–408 MHz Galactic emission as a calibration source for radio detectors in astroparticle physics
M. Büsken, T. Fodran & T. Huege
Astronomy & Astrophysics, 679, A50 (2023)

For our envisaged analysis of the radio energy scale with AERA, we rely on an absolute calibration of the measured air-shower signals in a decisive way. An essential ingredient in this aspect is the Galactic calibration that we introduce here and – in more detail – in Sec. 6.1.4. Here, we focus on one part of the Galactic calibration: sky models that provide a prediction of the diffuse Galactic radio emission but which will also pose a significant systematic uncertainty in the energy-scale analysis. In this Chapter, we study the sky models and their uncertainties in great detail. Via a comparison of the models, we determine, to what accuracy the diffuse Galactic emission can be predicted. Work on understanding and describing this emission has a long history in the radio astronomy community.

Already in the 1940s, surveys of the sky at radio frequencies were conducted. Strong emission from the constellation of Sagittarius was found as well as smaller maxima originating in extragalactic sources (e.g., Cygnus A and Cassiopeia A) and at this point also a signal coming from the Sun was seen [107]. In measurement campaigns, the entire sky was mapped at specific frequencies. These maps show strong point-like

sources as well as the diffuse radio emission from the Galaxy. The original motivation for these campaigns was to get a better understanding of the Galaxy and also to use the information from the maps in studies in the fields of astronomy and astrophysics, for example, related to the cosmic microwave background (CMB). To acquire accurate descriptions of the Galactic emission not only from a select number of maps at some specific frequencies but across a broad frequency range for the whole sky, efforts were made to build models of the radio sky based on these reference maps.

These sky models recently became relevant in the field of astroparticle physics for the absolute calibration of radio detection arrays. A number of promising radio detection arrays for the measurement of cosmic particles in the frequency range from a few tens to hundreds of megahertz are in the phase of development or under construction – for example, the Square Kilometer Array low-frequency site (SKA-low) [108] and the Giant Radio Array for Neutrino Detection (GRAND) [109]. Other arrays are already taking data, like AERA, the RD, and the LOw Frequency ARray (LOFAR) [110]. For accurate physics results, like we aim for in the energy-scale analysis with AERA in Chap. 8, an accurate calibration of the radio detectors is required.

Calibrating with a reference antenna emitting a defined signal (e.g., mounted on a drone [111]) has the disadvantage of uncertainties on the emitted signal strength, which are difficult to assess [112]. Also, dedicated calibration campaigns require significant effort and are almost impossible to perform on a regular basis for large arrays. A different calibration approach uses the diffuse Galactic radio emission – which poses a natural background to the detection of radio emission from particle showers – as the reference signal. It typically poses the dominant background from natural sources at these frequencies [113]. Although we often only refer to it as the Galactic emission in this work, we implicitly include subdominant extragalactic components as well. The calibration method based on the Galactic emission is called Galactic calibration and it also offers the opportunity to directly compare the calibrations of different radio arrays as they at least partially see the same sky. Moreover, the method can be applied as regularly as background data are available and it does not require dedicated field campaigns. The Galactic calibration was already applied in a full study to the LOFAR low-band antennas [112] and, as we discuss in Sec. 6.1.4 and what is essential to the energy-scale analysis in Chap. 8, to AERA. First steps towards a full-fledged Galactic calibration of the RD at the Pierre Auger Observatory were also made [114, 115].

In the Galactic calibration, the measured background signal from the Galaxy is compared to predictions made with the aforementioned sky models. Knowing the uncertainty on these predictions is thus crucial for a useful absolute calibration. In this work, we therefore conducted a comparison of seven publicly available radio sky interpolation models for the frequency range from 30 to 408 MHz. We did this by generating outputs with the models, calculating the average sky temperature from the outputs and determining the level of agreement between the models. From this comparison we derived an estimate for the systematic uncertainties of the modeled background predictions for the Galactic calibration.

First we present these models (Sec. 5.1) and summarize the reference maps on which they are based (Sec. 5.2). Afterwards, we explain how we performed a global comparison while also showing other, less detailed descriptions of the radio background (Sec. 5.3). We subsequently adjusted the comparison for the sky seen by an observer at a specific

location on Earth. We further conducted the comparison tailored to a set of selected radio arrays from the present and future, namely the Radio Neutrino Observatory Greenland (RNO-G) [116], LOFAR [110], GRAND [109], Owens Valley Radio Observatory Long Wavelength Array (OVRO-LWA) [117], SKA-low [108], the radio detectors of the Pierre Auger Observatory, and IceCube [118]. Additionally, we studied the influence of other natural sources in the radio sky (Sec. 5.5). Finally, we discuss implications of the results for the application of the Galactic calibration (Sec. 5.6) to radio detectors in astroparticle physics and, in particular, to AERA and the RD.

5.1 Radio sky interpolation models

In the past years, a couple of models for predicting the diffuse foreground emission of the sky in the radio and microwave regimes were developed with the purpose of calibrating radio arrays and to be used in foreground removal for 21-cm cosmology [119, 120]. Motivation for developing these models was also given through efforts to map the CMB with high accuracy [121]. Moreover, radio sky models can be used for better estimating fluxes from pulsars and fast radio bursts [122].

These models interpolate between reference sky surveys at various frequencies conducted with telescopes at different locations. In the surveys, the sky brightness at given coordinates is mapped in terms of the brightness temperature T_B. This is the temperature of a thermal radiator, that is, a black body, that would show the same brightness as the one measured. In the classical limit $h\nu \ll k_B T_B$ of Planck's law for black body radiation, where h is the Planck constant, ν is the considered frequency and k_B is the Boltzmann constant, the Rayleigh-Jeans law is applicable. The brightness temperature is then directly proportional to the observed brightness I_ν [$\mathrm{Wm^{-2}Hz^{-1}sr^{-1}}$]:[123]

$$T_B = \frac{c^2}{2k_B\nu^2} I_\nu, \tag{5.1}$$

where c is the speed of light in vacuum. In the frequency range from a few 10 MHz to a few 100 MHz, most of the electromagnetic background in the sky is presumably synchrotron radiation from electrons gyrating in the magnetic field of the Galaxy [124]. Although this is nonthermal emission, the description of the radio sky by a brightness temperature is still practical because of its proportionality to the brightness I_ν. The frequency dependence of the brightness temperature can be described at lower radio frequencies by a power-law

$$T_B \propto \nu^\beta \tag{5.2}$$

with a spectral index β. Recent studies of the spectral index at frequencies from 50 MHz to 200 MHz lie in the range $-2.62 < \beta < -2.46$, depending on the region in the sky [125, 126, 127]. Around 200 MHz and again above 400 MHz, changes of the spectral index are observed with a steepening towards higher frequencies [128, 129, 130].

This power-law relation can be used to scale a single full-sky reference map from a survey conducted at a low frequency to any other frequency. One model, called Low Frequency map (LFmap), uses this approach of spectral scaling with frequency- and region-specific spectral indices for interpolation. LFmap is included in the model comparison of this work. Other popular interpolation models use the approach of a principal

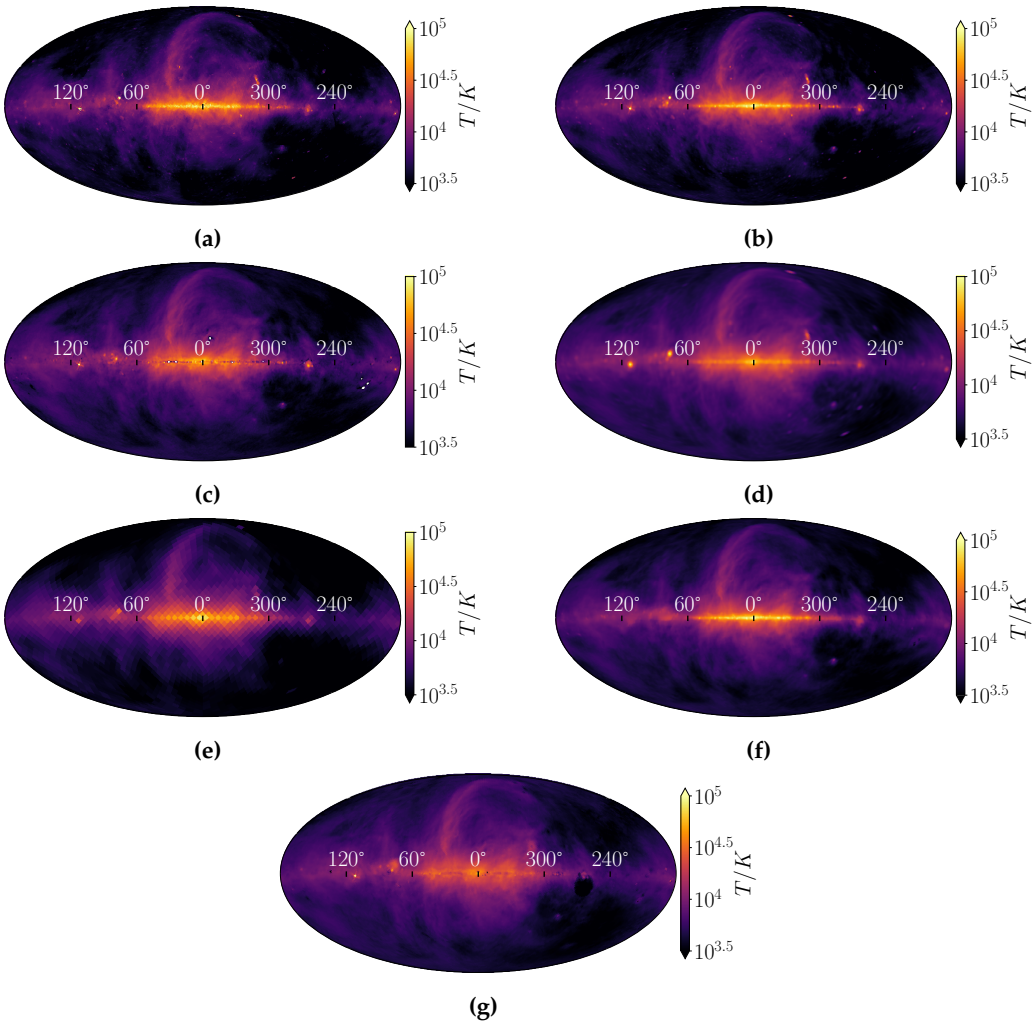

Figure 5.1: Maps of the radio sky at 50 MHz generated by each of the models in Galactic coordinates: (a) LFmap, (b) GSM, (c) GSM16, (d) LFSM, (e) GMOSS, (f) SSM, (g) ULSA.

component analysis (PCA) of multiple reference maps to produce frequency-dependent descriptions of the radio sky. In this inventory, three such models are considered, namely the Global Sky Model (GSM) in its first [131] and improved [132] version, as well as the Low Frequency Sky Model (LFSM) [133]. Lastly, three more models are included in this study which assume a physical model of the diffuse radio emission, that they fit to reference maps. These are the Global MOdel for the radio Sky Spectrum (GMOSS) [134], the high-resolution Self-consistent whole Sky foreground Model (SSM) [135], and the UltraLong-wavelength Sky Model with Absorption (ULSA) [136]. A short summary of all models, their core modeling approach, and whether they include the CMB contribution is given in Tab. 5.1. Example fully-sky maps at 50 MHz generated with each of the seven models are shown in Fig. 5.1. At first sight, the maps look very similar, although some differences – for example in the region of the Galactic center – are recognizable. Hence, we go into quantitative comparisons of the total sky brightness but also touch on sky-regional differences.

Table 5.1: Overview of the compared radio sky models. For the models that do not include the CMB, we added it manually in our comparison. References: (1) [137]; (2) [131]; (3) [132]; (4) [133]; (5) [134]; (6) [135]; (7) [136].

Sky model	Modeling approach	Includes CMB	Refs.
LFmap	Spectral scaling	Yes	1
GSM (2008)	PCA	No	2
GSM (2016)	PCA	Yes	3
LFSM	PCA	Yes	4
GMOSS	Physical emission model	No	5
SSM	Spectral scaling + point sources	Yes	6
ULSA	Physical emission model + spectr. scaling	Yes	7

5.1.1 Low frequency map (LFmap)

The LFmap software ([137]) is a radio sky interpolation software based on the simple power-law model for the sky brightness temperature (Eq. 5.2). The 408 MHz map ([138]) in the revisited version ([139]) is scaled down with spectral indices from a spectral index map from the same reference to frequencies down to a minimum frequency f_{bend}. To take spectral bending into account, new spectral indices are used for frequencies below the bending frequency f_{bend}, which are calculated such that each pixel of the downscaled map at f_{bend} scales onto the same pixel of a 22 MHz map ([140]). Part of the region around the Galactic center is affected by HII absorption, which becomes relevant only below 45 MHz. Therefore, an intermediate step at the absorption frequency $f_{absorption}$ is introduced, where the affected region of the map is replaced by the average of the surrounding area, that is unaffected by HII absorption. Below $f_{absorption}$ the procedure of calculating spectral indices is done with the original 22 MHz map. In a similar manner, regions not covered in the 22 MHz map are replaced with averages from surrounding areas. Most point-like sources are not treated individually, except for the two brightest ones, Cassiopeia A and Cygnus A, for which adapted spectral indices are used to scale their brightness temperatures. In this study, we used the default settings of LFmap, or more specifically, $f_{bend} = 180$ MHz and $f_{absorption} = 45$ MHz.

5.1.2 Global sky model (GSM, 2008)

Three other considered radio sky interpolation models use a principal component analysis (PCA) to generate all-sky maps at any intermediate frequency. Of these models, GSM [131] is the oldest, which uses the fewest reference maps. The advantage of a PCA is that also maps of limited sky coverage can be used rather easily. However, different angular resolutions and levels of quality between the used maps pose challenges for this approach. In GSM, also maps at gigahertz frequencies are used, which can have a significant influence on the low-frequency results in regions where there is otherwise only sparse map coverage. The sky temperature component from the CMB was subtracted from the reference maps before building the model. In our analysis, we added this component again to the generated maps.

The PCA in GSM is used to decompose the spatial structures of the diffuse radio sky from the information of the 11 input maps. The algorithm was performed for the

region of the sky that is covered by all of the reference maps. In a fit, the principal components were modeled to best match in the remaining sky regions. At minimum, there is information from six maps per pixel. However, for a large part of the southern hemisphere, sub-gigahertz information is only available from the all-sky maps at 45 MHz and 408 MHz, possibly reducing the model accuracy in this region at these frequencies, which is relevant for experiments located in the southern hemisphere. The authors used three principle components for the final model, because they are sufficient to explain almost all of the emission seen in the reference maps. These first three principal components were also interpreted as to how they relate to the physical components of the diffuse radio emission. In order to be able to generate full sky maps with these principal components at any frequency between 10 MHz and 100 GHz, the components were fitted as a function of the logarithmic frequency using a cubic spline. This way, frequency spectra for each of the principal components were obtained. No special treatment for point-like sources is mentioned although they were removed in some of the used reference maps.

The accuracy of the model was determined by taking one of the reference maps out of the calculation of the principal components and calculating the difference of this map to the output of the model at that frequency without the information from the map. This was done for all frequencies at which a reference map is available leading to an estimate for the accuracy of around 12% for the sub-gigahertz maps. However, the model does not account for individual uncertainties associated with the reference maps or systematic temperature shifts of a map over the whole sky, that could be introduced by inaccurate calibration.

5.1.3 Global sky model (GSM, 2016)

The original GSM received an update in which further reference maps were included and the model algorithm around the PCA was improved [132]. The frequency range of the model was extended to 5 THz by including recently published surveys in the microwave regime. At lower radio frequencies, maps at 85 MHz and 150 MHz were added. With this enhanced set of surveys, there is no common region covered by all of them, that could be used for conducting the PCA as in the original GSM. Instead, an iterative algorithm was implemented, which fits the principal components to the reference maps to the desired accuracy. For the zeroth iteration, a subset of maps was used that overlap by at least 5% in sky coverage. Then, the remaining maps were fed into the model. Finally, six principal components were used, compared to three components in the original GSM. Within the PCA algorithm, point-like sources are removed.

A level of model accuracy is determined in the same way as for the original GSM and found to be around 8% for the sub-gigahertz frequencies. When compared to the original GSM, the accuracy of the improved model is better for all sub-gigahertz frequencies by a factor of up to 2. However, since the original GSM is still widely used and since most of the newly added reference maps are at higher frequencies than we considered here, we included both versions of the GSM in the comparison of this study.

5.1.4 Low frequency sky model (LFSM)

Based on the sky surveys at the Long Wavelength Array Station 1 (LWA1) [141] in the USA at frequencies from 40 MHz to 80 MHz, a low-frequency sky model was constructed [133]. Additional surveys from the literature were included. The model itself is based on the PCA approach as performed in the original GSM. Similar to the improved GSM, an iterative procedure was used to tackle the problem of not having a sky region that is commonly covered by all maps. The final number of principal components in the model is three and maps can be generated within a total range from 10 to 408 MHz. Same as for GSM, no individual treatment of point-like sources is mentioned.

As a measure of accuracy, the relative difference between the LWA1 survey at 74 MHz and the model prediction at the same frequency was calculated. Deviations are found to be at an overall level of 10%. The LWA1 surveys nicely cover the low-radio regime below 100 MHz. However, the LWA1 is stationed in the northern hemisphere. This could lead to additional uncertainties in the interpolated maps at Galactic latitudes below $-40°$, which would become relevant for experiments in the southern hemisphere. Furthermore, the temperature scale of the LFSM output strongly depends on the calibration of the LWA1 surveys, as these represent a large fraction of the total ensemble of input maps. Potential systematic errors in the calibration would thus directly bias the interpolation model.

5.1.5 Global model for the radio sky spectrum (GMOSS)

GMOSS is based on a physical model of the mechanisms of the diffuse radio emission in the sky, most importantly synchrotron radiation, thermal radiation, and free-free emission. This model is the basis for a parameterization of the sky brightness temperature spectrum. The parameterization was fit to the data from six reference maps for each pixel of a full-sky map at $5°$ resolution. The CMB contribution to the sky temperature was subtracted from the reference maps, which we added again to the generated maps in our comparison. Four of the reference maps are measured ones from 150 MHz to 23 GHz, while the other two were generated with GSM, at 22 MHz and 45 MHz. These generated maps are assumed to be close to the reference maps at the same frequencies, that were used to build GSM but are not full-sky. However, this way a level of correlation between the outputs of GSM and GMOSS is introduced. The fit parameters of the GMOSS model were constrained to stay within physically reasonable limits. The fractional deviation between the fitted model and the reference data is within 17% for most of the pixels.

5.1.6 Self-consistent whole sky foreground Model (SSM)

The SSM is a model of the radio sky that separately estimates the diffuse emission and the emission from point-like source and adds them up. The temperature of the diffuse emission is modeled with the usual spectral power law, while the spectral index is taken as frequency- and direction-dependent. This dependency was accounted for by expanding the spectral index first in the logarithm of the frequency and then setting up the resulting relation to the sky temperature for each pixel in the sky. The parameters of this polynomial were then fitted using data from in total 13 reference maps, where

the 408 MHz map ([142]) acted as the basis map. The 408 MHz map was scaled to any frequency using the power law with the fitted form of the spectral index.

Prior to the fit, point sources were removed from those reference maps which originally included them. In SSM, point sources are separately modeled onto the diffuse emission with two catalogs. The spatial distribution of the point sources, as well as the spectral behavior of their emission were determined from these catalogs, which are at two different frequencies, 843 MHz and 1.4 GHz. Finally the diffuse emission and the emission from the point sources were added up for the final model output.

5.1.7 Ultralong-wavelength sky model with absorption (ULSA)

Special emphasis on ultra-long wavelength radio emission down to frequencies around 1 MHz is given in the work of the ULSA model. In ULSA, free-free absorption in the Galaxy is taken into account that affects the brightness spectrum at frequencies below 10 MHz. Nevertheless, the model can also be used to generate maps up to 408 MHz.

In the model, the sky temperature is assumed as a sum of a Galactic and an isotropic extragalactic component with a reduction of the temperature due to Galactic absorption. The Galactic contribution was estimated from a cylindrically symmetric parameterization of the Galactic emissivity with a frequency dependence. A model for the 3D Galactic electron density was used to estimate the magnitude of the absorption effect.

Different treatments for the frequency dependence of the Galactic emission are included in ULSA, namely a spectral scaling using a single spectral index, a frequency-dependent spectral index, and a direction-dependent spectral index. In this work, we used the latter setting of the model, because we believe this to be more accurate than a single spectral index and we did not observe a significant difference between using a single spectral index or a frequency-dependent index.

The direction-dependent spectral indices were obtained from a fit to the information from nine reference maps between 35 MHz and 80 MHz, where also a model of the contribution from free-free emission was included. The reference maps at low frequencies are numerous, albeit all except for one map are from the LWA1 survey [133], which therefore should have a large influence on the model output. A separate spectral index was used for isotropic extragalactic emission. Galactic free-free absorption is treated with special care in ULSA. However, this effect is only relevant at frequencies lower than those that we considered here.

5.1.8 Other parametrizations of the Galactic background brightness

Besides the interpolation models for generating all-sky maps, there are also some parametrizations of the spectrum of the average brightness of the Galactic background. We did not include them in the comparison of the interpolation models but present and show them here for completeness.

One of these parametrizations was introduced in Ref. [143] and assumes a superposition of Galactic and extragalactic contributions to the brightness including absorption by the Galactic disk and was fitted to a multitude of measurements of the polar regions of the Galaxy. This yields lower brightness temperatures than expected for an average of

the whole sky because the bright Galactic center is not considered here. To accommodate for this, a correction factor of ~1.3 to the Galactic brightness contribution was found in Refs. [144] and [145]. In this work, we show the such-corrected parametrization and refer to it as "Cane."

The parametrization by Cane was revisited again by Tokarsky, Konovalenko, and Yerin [146], where the corrections were summarized and another expression for the average brightness temperature as a function of frequency was given based on results from Ref. [147]. We refer to this parametrization here as "TKY." Both descriptions of the Galactic background brightness are applicable only for the low-frequency radio regime (< 100 MHz), where the Galaxy is the dominant contribution to the background.

Furthermore for comparison purposes, we show the simple approach of scaling a full-sky map with just one single spectral index. As the reference map, we used the 408 MHz map from Ref. [138] as improved in Ref. [142]. Here, we refer to this description as "Haslam," but also did not include it in the comparison of the interpolation models because of its drawbacks. Using a single spectral index does not represent reality, as the spectral index varies for different regions of the sky and different frequency regimes [126, 148]. Although often used in studies of fast radio bursts, the Haslam description should not be seen as equivalent to the more sophisticated interpolation models [122]. We show the Haslam results for a spectral index between -2.62 and -2.46.

5.2 Reference maps

The presented radio sky interpolation models rely on a number of reference maps. Consequently, the accuracy of the models is dependent on the accuracy of these maps and their inherited uncertainties. Therefore, in the following, we give an overview of the reference maps used in the considered interpolation models.

10 MHz:

This map was obtained using the 10-MHz array at the Dominion Radio Astrophysical Radio Observatory (DRAO) in Canada. The observations were done during winter nights to minimize ionospheric influence. Thus, the sky coverage is limited in right ascension from 0^h to 16^h. Relative calibration of the received signal strength to sky brightness temperature was performed by comparing the observations to a published 178 MHz map from Ref. [153], that was scaled using a power-law relation as in Eq. 5.2 and spectral indices of -2.40 and -2.75 for the Galactic and extragalactic isotropic emission, respectively. The sky brightness is mapped in contours indicating specific temperature levels. The contour interval between these levels is 2×10^4 K.[149]

22 MHz:

The sky map at 22 MHz was also produced from measurements done at the DRAO. The applied antenna gain is based on an assumed value for the flux density of Cygnus A [154]. A cross-check of the map with the 408 MHz map from Ref. [138] was performed to compare the temperature scales by producing scatter plots of the brightness temperatures (T-T plots) from both maps for different declinations from the zenith. Then, the temperature scale of the 22 MHz map was tuned to overall match the ratio at the zenith, for which the authors believed their instrument to be understood better. The T-T plot for the zenith direction showed no discrepancy with the zero-level of the temperature scale.

Table 5.2: Summary of all presented reference maps with their sky coverage and quoted uncertainties. The two values for the relative scale uncertainty of map No. 4 refer to the two different estimations for this in the publications of the northern and southern part of the survey, respectively. For scale uncertainties with a (*) no explicit value was given by the authors. Instead, we estimated it by taking half of the smallest contour interval of that map and dividing it by its minimum brightness temperature. In the same way, zero-level errors with a (†) were estimated by taking half of the smallest contour interval. To give the zero-level errors as a fraction of the average sky temperature, we calculated the latter from Eq. 5.4, where we took the average from using all seven considered sky models. For indicating in which models the maps are used, we use the following notation: 1 = GSM, 2 = GSM16, 3 = LFSM, 4 = LFmap, 5 = GMOSS, 6 = SSM, 7 = ULSA. Numbers in parentheses mark that the map is only used indirectly in the respective model. References: (1) [149]; (2) [140]; (3) [133]; (4) [150]; (5) [151]; (6) [152]; (7) [153]; (8) [138]; (9) [139]; (10) [142].

Map no.	Freq. ν (MHz)	Covered declination	σ_k (%)	σ_{T_0} (K)	σ_{T_0} normalized (%)	Used in	Refs.
1	10	$-6° < \delta < 74°$	9*	$2 \cdot 10^4$	6.8	1,2,3,6	1
2	22	$-28° < \delta < 80°$	16	$5 \cdot 10^3$	11.0	1,2,3,4,6	2
3	35	$-40° < \delta < 90°$	20	10	0.1	7	3
4	38	$-40° < \delta < 90°$	20	10	0.1	7	3
5	40	$-40° < \delta < 90°$	20	10	0.1	3,7	3
6	45	$-90° < \delta < 65°$	10/15	125†	1.5	1,2,3,(4),6,7	4, 5
7	50	$-40° < \delta < 90°$	20	10	0.2	3,7	3
8	60	$-40° < \delta < 90°$	20	10	0.2	3,7	3
9	70	$-40° < \delta < 90°$	20	10	0.4	3,7	3
10	74	$-40° < \delta < 90°$	20	10	0.4	7	3
11	80	$-40° < \delta < 90°$	20	10	0.5	3,7	3
12	85	$-25° < \delta < 25°$	7	120	6.8	2,6	6
13	150	$-25° < \delta < 25°$	5	40	9.4	2,5,6	6
14	178	$-5° < \delta < 88°$	10	15	5.4	(1,2,3,6)	7
15.a	408	$-90° < \delta < 90°$	10/5	3	9.0	1,5	8
15.b	408	$-90° < \delta < 90°$	10/5	3	9.0	4	9
15.c	408	$-90° < \delta < 90°$	10/5	3	9.0	2,3,6,7	10

Also, the differential spectral index derived from the T-T plot between the 22 MHz map and the 408 MHz map was in agreement with other measurements.[140]

LFSS 35 MHz, 38 MHz, 40 MHz, 50 MHz, 60 MHz, 70 MHz, 74 MHz, and 80 MHz:
Within the LFSS at the LWA1, sky maps were produced at a variety of frequencies. The gain of the LWA1 antennas was derived from an electromagnetic antenna model in combination with a correction using bright pulsars at different elevations as reference sources. Previous observations of the flux density of Cygnus A from Ref. [155] were used to convert the measurements into sky temperature. A temperature calibration system was used to achieve absolute accuracy of 10 K or better.[133]

45 MHz:
At 45 MHz, there are two separate sky surveys available, one covering the northern hemisphere and one covering the southern hemisphere, conducted at the Middle and

Upper Atmosphere Radar in Japan and the Maipu Radio Astronomy Observatory in Chile, respectively. Calibration of the temperature scale of the latter survey was performed by using a spectral interpolation from data in a well-observed reference region and comparison with the measurements. The map was later used to calibrate the map of the northern hemisphere as both cover the region from 5° to 19° in declination.[150, 151]

85 MHz, 150 MHz :

Surveys at 85 MHz and 150 MHz were made using the Parkes 64 m telescope in Australia. Calibration of the temperature scale was done after every scan with well-matched noise diodes that could be connected to the receivers of the telescope.[152]

408 MHz:

Multiple sites (Jodrell Bank MkI(A) telescope in England, Effelsberg 100 m telescope in Germany, and Parkes 64 m telescope in Australia) were used to observe the sky at 408 MHz. The originally assembled map by Haslam et al. was calibrated with reference to a sky survey at 404 MHz from Ref. [156].[138]

The authors of Ref. [142] believe that the brightness temperature scale is more accurate (~5%) than originally quoted (~10%). Because of its importance in the field of radio astronomy, the map and its raw data were restudied multiple times, including destriping it and removing point-like sources [139, 142].

Summary:

The reference maps are listed in Tab. 5.2 together with their quoted uncertainties on the temperature scale, which are typically described by a linear relation. The true temperature T_{true} is assumed to relate to the observed temperature T_{obs} as

$$T_{true} = kT_{obs} + T_0. \tag{5.3}$$

The scaling factor k ideally has a value of 1, but it inherits the relative scale uncertainty σ_k, which goes up to 20% for the reference maps presented here, while the largest uncertainties are quoted for the results of the Low Frequency Sky Survey (LFSS) (map No. 3 to 5, 7 to 11). The zero-level T_0 represents an absolute offset of the temperature scale and deviations from the ideal case ($T_0 = 0\,K$) are reflected in the zero-level error σ_{T_0}. The zero-level errors of the reference maps are given in Tab. 5.2 as absolute values and also relative to the average brightness temperature of the whole sky at the respective frequency, where the average sky brightness temperature is calculated using Eq. 5.4. The relative zero-level errors amount up to ~11%, while they are negligible for the LFSS results.

Furthermore, Tab. 5.2 gives the information, in which models each reference map is used. This information is also visualized in Fig. 5.2, where for each model the covered sky regions of all used reference maps are superimposed. LFmap relies on only two reference maps with the approach of spectral scaling. ULSA uses the most reference maps with a maximum of ten maps covering the region between −40° and 65° of declination. However, there is a lack of available reference maps for all models around the south celestial pole.

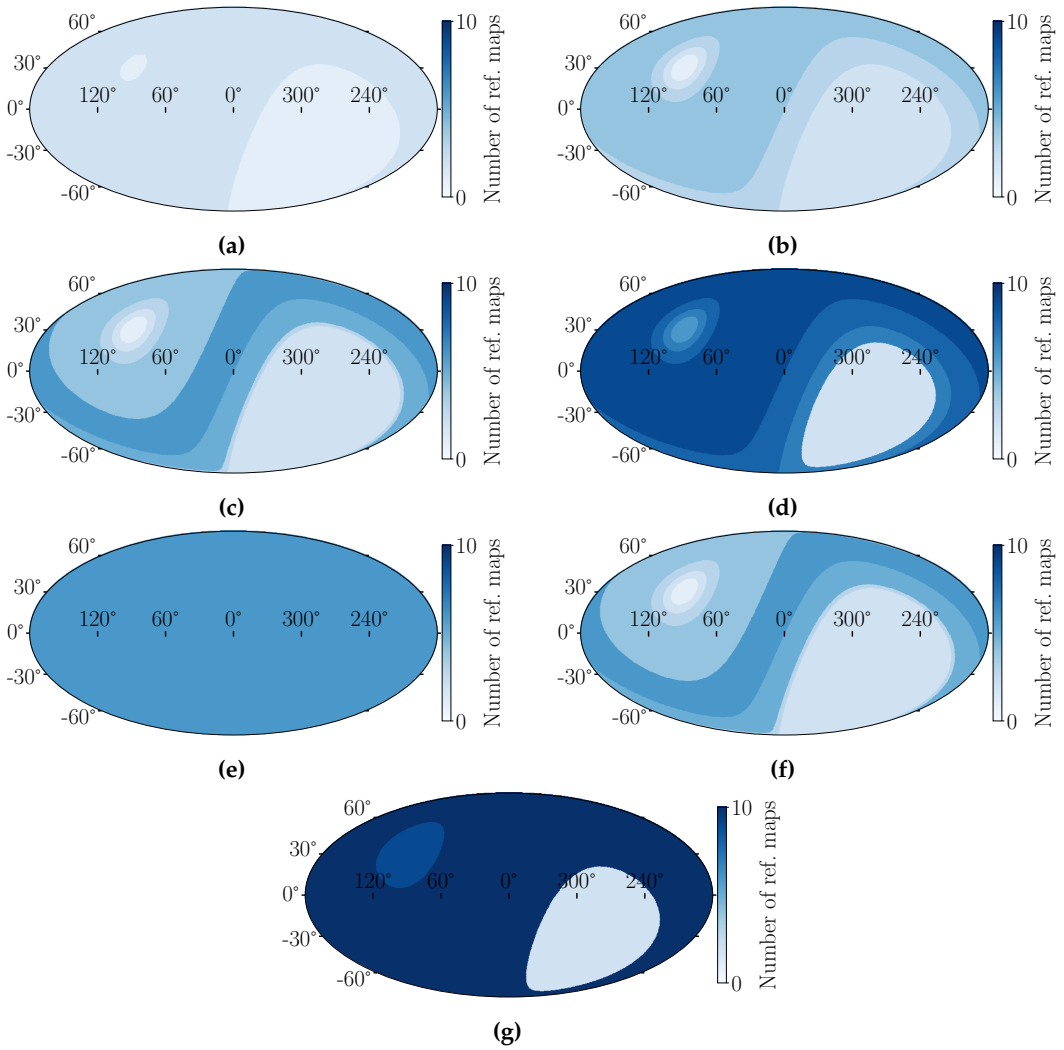

Figure 5.2: Sky coverages of the used reference maps for each sky model laid on top of each other and plotted in Galactic coordinates. The models are numbered (a) LFmap, (b) GSM, (c) GSM16, (d) LFSM, (e) GMOSS, (f) SSM, (g) ULSA. For regions of lighter color fewer measurements from reference maps are available than for regions of darker color.

Corrections to the maps at 45 MHz, 150 MHz, and 408 MHz:

The sky surveys at 45 MHz that are used in the interpolation models considered here were done separately for the southern [150] and northern hemisphere [151]. In a later study, the maps were combined into an all-sky survey with a correction of the zero-level of −544 K [157] to the combined map. This corresponds to ~6.5% of the average sky temperature at that frequency and is more than three times larger than the originally quoted error on the zero-level. In the same study, also a zero-level correction for the original 408 MHz map of −3.46 K was determined, which corresponds to ~10.4% of the average sky temperature.

Another recalibration was performed for the combined 45 MHz map (although without the mentioned zero-level correction) and for the 150 MHz map [158]. There, the maps were corrected for temperature scale and zero-level to best match data taken with

the Experiment to Detect the Global EoR (epoch of reionization) Signature (EDGES) [159]. Scale correction factors are 1.076±0.017 and 1.112±0.012 for the sky temperature of the 45 MHz and 150 MHz maps, respectively. Zero-level corrections for the surveys are −160±78 K and 0.7±6.0 K, which correspond to 1.9±0.9% and 0.2±1.4% of the average sky temperature at the respective frequencies.

Corrections to the temperature scale and zero-level by matching to other, sometimes newer data can be bigger than originally quoted uncertainties. This hints towards an underestimation of the latter and poses a challenge when trying to place trust on individual surveys.

Additional maps at higher frequencies:
Further maps at higher frequencies are used in the interpolation models as well. Many of them were generated from data taken with the space-based instruments Wilkinson Microwave Anisotropy Probe (WMAP) and Planck [160, 161]. These maps are important for modeling sky regions where fewer low-frequency surveys were performed, but they are not discussed in more detail here.

5.3 Comparison of the sky model predictions

Besides the quoted accuracies of the reference maps, which propagate into the interpolation models, we compared the output of the models directly. We studied the deviations between them and determined their level of agreement, which we use as an estimator for the systematic uncertainty in predicting the diffuse Galactic radio emission on an absolute scale.

The `PyGDSM` [162] package was used as an interface to GSM, GSM16, and LFSM. It employs the `healpy` [163] package to provide the temperature map output of the models in the `HEALPix` [164] format. The source codes of LFmap, GMOSS, SSM, and ULSA are all separately available at their authors' respective repositories[1]. After generating the output maps using these four models, we converted them as well into the `HEALPix` format. A software toolkit for the Galactic calibration, which also includes a unified, simpler access to all considered models, is available [165].

As examples, we show sky maps in Fig. 5.3 which display the temperature ratio between the output of each model and the average at 50 MHz. The average is calculated pixelwise from all seven models at the same frequency. At 50 MHz LFmap, GSM, GMOSS, and SSM predict a hotter Galactic center than the other three models, while away from the center their predictions are colder, or close to average in the case of SSM. By this depiction, also spatial structures of the differences between the models are visible, for example, some stripe-like features for GSM. In this work, we considered an application of these models for radio antennas with a rather broad beam width, so that spatial structures are averaged out. Therefore, we did not investigate these structures more deeply.

In this study, the comparison was conducted for the frequency range from 30 to 408 MHz. Typically, radio arrays for the detection of cosmic particles are not operated

[1] LFmap: `https://github.com/epolisensky/LFmap`
GMOSS: `https://github.com/mayurisrao/GMOSS`
SSM: `http://tianlai.bao.ac.cn/~huangqizhi`
ULSA: `https://github.com/Yanping-Cong/ULSA`

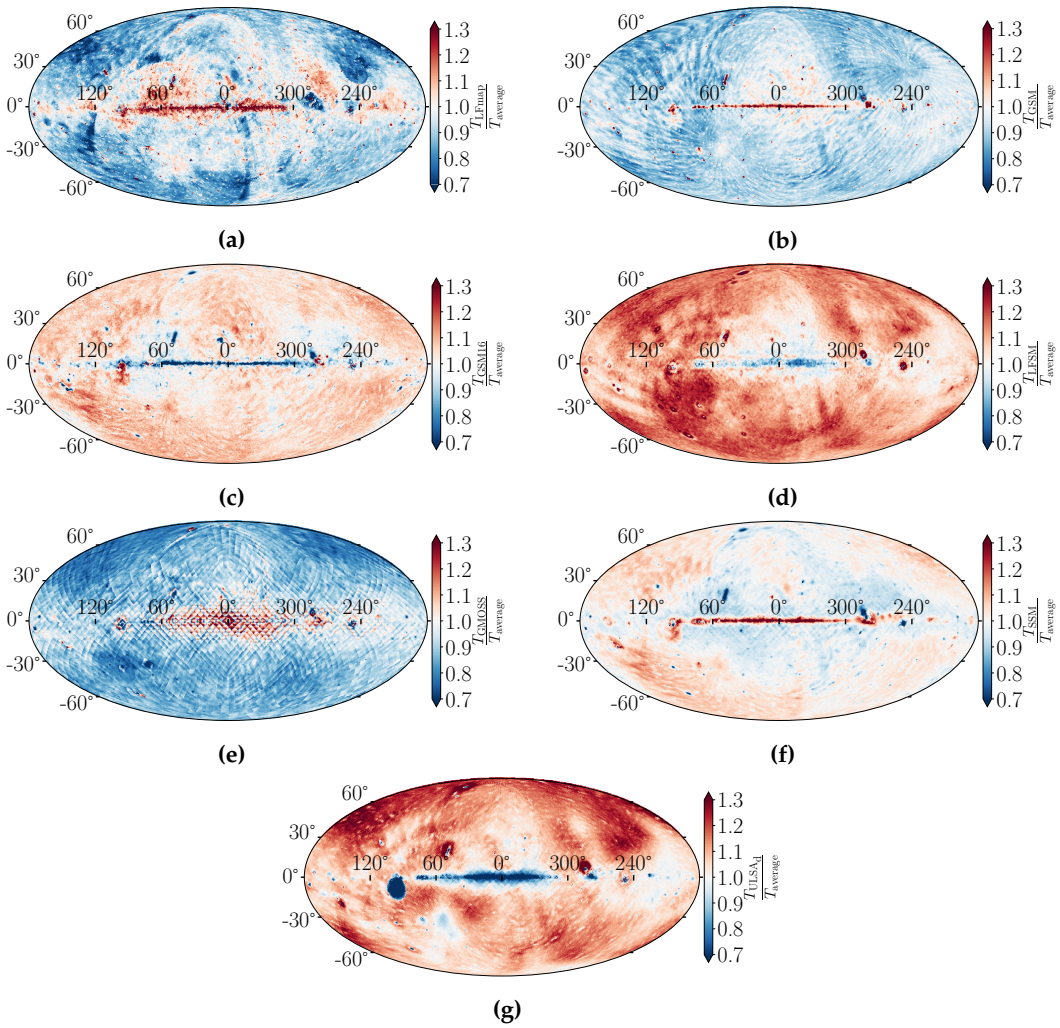

Figure 5.3: Sky maps showing the temperature ratio of each model to the average from all seven models at 50 MHz in Galactic coordinates. The models are denoted as (a) LFmap, (b) GSM, (c) GSM16, (d) LFSM, (e) GMOSS, (f) SSM, (g) ULSA.

below 30 MHz because of the presence of strong atmospheric noise as we discuss in Sec. 5.5.2. The upper bound arises from limitations within the LFmap and LFSM models.

5.3.1 Comparison of the total sky

The average temperature of the sky at a given frequency ν is calculated as

$$\bar{T}(\nu) = \frac{1}{4\pi} \int_{-\pi}^{\pi} d\ell \int_{\frac{-\pi}{2}}^{\frac{\pi}{2}} db \cos(b)\, T(\nu; \ell, b), \tag{5.4}$$

where ℓ is the Galactic longitude and b is the Galactic latitude. The brightness temperature at a specific location in the sky $T(\nu; \ell, b)$ is taken from maps in Galactic coordinates produced with the sky models. The observable $\bar{T}(\nu)$ is used for the first part of the comparison. It gives compressed information of a sky map while ignoring spatial structures. For the Galactic calibration of an antenna without a narrow beam, taking

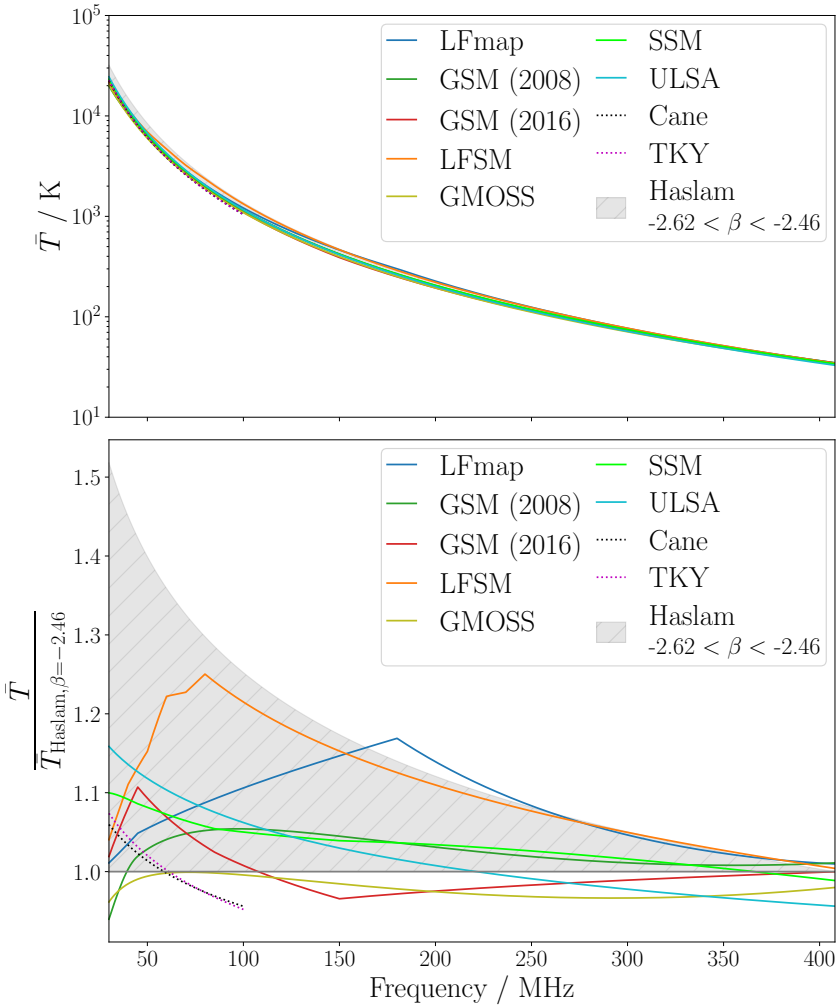

Figure 5.4: Average sky temperature as a function of the frequency is plotted for the interpolation models as solid lines and for the parameterizations Cane and TKY as dashed lines. The gray band shows the results for the 408 MHz Haslam map when scaled down with a spectral index β between −2.62 and −2.46. The upper plot shows the absolute values, while in the lower plot the results are normalized to those for the scaled Haslam map and a spectral index $\beta = -2.46$.

into account fine spatial structures is not as relevant, because the measured quantity of received power is a folding of the whole visible sky through the antenna pattern.

The upper plot in Fig. 5.4 shows the average sky temperature as a function of the frequency for the interpolation models in solid lines from 30 MHz to 408 MHz. The gray band was obtained from the Haslam description of the sky brightness by using a spectral index β between −2.62 and −2.46 and is shown for comparison. The range for the spectral index was deduced from recent measurements [125, 126] around the relevant frequencies. Furthermore, the previously introduced parametrizations of the average sky brightness below 100 MHz, Cane and TKY, are shown for comparison as black and magenta dotted lines, respectively.

The comparison shows that the interpolation models agree well in their shapes over the whole frequency range, while they are systematically shifted relative to each other.

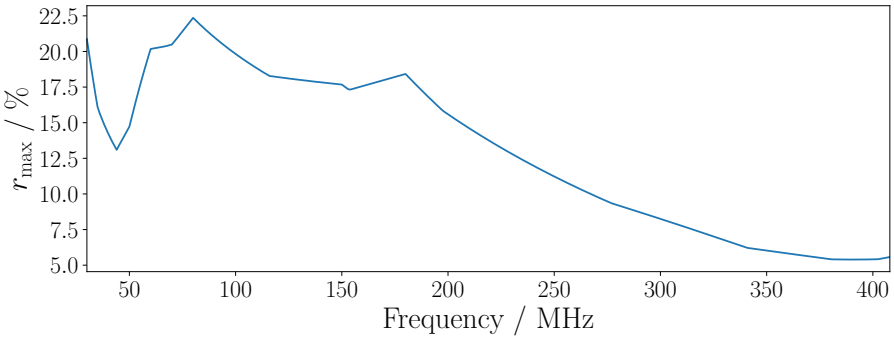

Figure 5.5: Maximum relative difference of the average sky temperature between any two of the considered models as a function of frequency. The maximum relative difference is calculated as in Eq. 5.5.

This can be seen more quantitatively in the lower plot of Fig. 5.4, in which the data are normalized to the Haslam results with a spectral index $\beta = -2.46$, to better show spectral behavior of the models.

We subsequently calculated the relative difference of the average sky temperatures at a given frequency for any combination of models m_1 and m_2. From that, we evaluated the maximum relative difference

$$r_{max}(\nu) = \max \left| 2 \frac{\bar{T}_{m_1}(\nu) - \bar{T}_{m_2}(\nu)}{\bar{T}_{m_1}(\nu) + \bar{T}_{m_2}(\nu)} \right|, \tag{5.5}$$

which we plot as a function of the frequency, shown in Fig. 5.5. The maximum relative difference is around 20% for the lowest frequencies and drops to values around 7% for frequencies larger than ~200 MHz.

To gauge the level of agreement between the models more concisely, for each of them we integrated the average sky temperature over the frequency range from 30 to 408 MHz, and calculated a relative difference r_{m_1,m_2} pairwise as

$$r_{m_1,m_2} = 2 \frac{\int_{30\,\mathrm{MHz}}^{408\,\mathrm{MHz}} \bar{T}_{m_1}(\nu) - \bar{T}_{m_2}(\nu)\, d\nu}{\int_{30\,\mathrm{MHz}}^{408\,\mathrm{MHz}} \bar{T}_{m_1}(\nu) + \bar{T}_{m_2}(\nu)\, d\nu}, \tag{5.6}$$

again with any combination of models m_1 and m_2. The results are listed in Tab. 5.3. By this comparison, all models agree with each other at a level of 14.3% or better. We observe a rather homogeneous distribution of the models in terms of the average sky brightness that they predict. There is no aggregation of models in the results of this comparison and, in particular, there is no correlation of the average brightness of the model's prediction with the modeling approach. For example, when looking at the models that use a PCA, LFSM on average predicts the brightest skies while GSM predicts relatively faint skies. The prediction from GSM16 comes out in between. We conclude that the modeling approach is not the dominant reason for differences between the predictions of the models.

The extremes in the results of the comparison are represented by LFSM and GMOSS, which in general predict the brightest and faintest skies, respectively. In the frequency range from 30 to 80 MHz, ULSA produces the second brightest sky maps. Interestingly, this is the frequency range, in which the set of LWA1 reference maps lie that are used

Table 5.3: Value of r_{m_1,m_2} listed for each combination of the interpolation models. The header row gives the model m_1 and the leftmost column gives the model m_2. Positive values show that the model m_1 produces maps with higher average temperatures than the model m_2.

r_{m_1,m_2} (%)	LFmap	GSM	GSM16	LFSM	GMOSS	SSM	ULSA
LFmap	-	4.3	0.7	−7.3	7.0	−1.8	−4.8
GSM	−4.3	-	−3.6	−11.7	2.7	−6.1	−9.1
GSM16	−0.7	3.6	-	−8.1	6.3	−2.5	−5.5
LFSM	7.3	11.7	8.1	-	14.3	5.5	2.6
GMOSS	−7.0	−2.7	−6.3	−14.3	-	−8.8	−11.8
SSM	1.8	6.1	2.5	−5.5	8.8	-	−2.9
ULSA	4.8	9.1	5.5	−2.6	11.8	2.9	-

in both LFSM and ULSA but no other model. In light of this, it would be interesting to investigate whether the calibration of the LWA1 has a systematic bias towards higher temperatures. In general, however, the complex character of how the models are correlated with each other in multiple ways makes it very hard to determine why predictions deviate and which models may be more trustworthy than others.

5.3.2 Comparison of the local sky

The differences between the models are not just reflected in general deviations of the temperature scales. They also show structural variations on larger scales that become noticeable by comparing specific sky regions, for instance, on/off the Galactic plane. These variations influence the model comparison when confining their output maps to the sky coverage of a specific radio-detection experiment on Earth. The local sky of an observer changes with the local sidereal time (LST) and solely depends on the observer's geographic latitude if the experiment is operated both day and night.

The average temperature of a local sky was obtained by converting a map into the horizontal coordinate system with the two angles azimuth α and altitude a (the elevation angle above horizontal), thus limiting it to the visible half of the sky above the horizon and integrating over this region. The results were then averaged for varying LST from 0 h to 24 h as

$$\bar{T}_{\text{local}}(\nu, \ell) = \frac{1}{2\pi}\frac{1}{24\,\text{h}}\int_{0\,\text{h}}^{24\,\text{h}} dt_{\text{LST}} \int_{0}^{\pi} da \int_{\frac{-\pi}{2}}^{\frac{\pi}{2}} d\alpha \cos(a)\, T(\nu, \ell, t_{\text{LST}}; a, \alpha) \tag{5.7}$$

for a given latitude ℓ of the observer on Earth. We further integrated the average temperature of the local sky over a frequency range $[\nu_{\text{lower}}, \nu_{\text{upper}}]$:

$$\mathcal{T}(\ell) = \int_{\nu_{\text{lower}}}^{\nu_{\text{upper}}} \bar{T}_{\text{local}}(\nu, \ell)\, d\nu. \tag{5.8}$$

The result of this integral is plotted for each interpolation model and for the two frequency ranges [30 MHz, 100 MHz] and [100 MHz, 408 MHz] as a function of the ob-

server's latitude in Fig. 5.6 in the top row. It is clear that $\mathcal{T}$ changes depending on the exposure to the radio-bright center of the Galaxy. At the northern celestial pole (90° latitude) this exposure is the smallest and thus $\mathcal{T}$ is the lowest over all frequencies, while the maximum exposure takes place at around −60° of latitude.

Furthermore, differences between the interpolation models are recognizable. Apart from a general shift in the temperature scale, there are latitude dependent variations, which are probably due to different ratios in the models between the coldest and hottest regions of the sky.

The bottom row of Fig. 5.6 shows the results from the top row normalized to those of GMOSS, which on average gives the coldest sky maps. Here the overall level of agreement is found to be around 20% for latitudes around the north celestial pole and around 13% around the south celestial pole. From the variation of the level of agreement across the geographical latitude, we conclude that the reference maps of the models, which often do not cover the full range in latitude and therefore affect the predictions in only limited parts of the sky, have a major role in the total uncertainty of how well the diffuse Galactic emission can be predicted.

Comparing the results for the two chosen frequency ranges, the models rank differently in the sky brightness they predict. However, the relative spread between faintest and brightest model remains the same, as can be seen from the plots with normalization.

5.4 Comparison for selected radio experiments

The comparison of the sky models based on the local sky was further carried out for selected radio arrays for the detection of cosmic particles, namely RNO-G (surface antennas) [116], LOFAR [110], GRAND [109], OVRO-LWA [117], SKA-low [108], the Pierre Auger Observatory (AERA and the RD), and the radio antennas of the IceCube surface array [118]. The sky models compare differently for each of the experiments. This is due to them being situated at different geographical latitudes and using different frequency bands. For this study, we made the simplifying assumption of a constant antenna sensitivity over the whole frequency band for all arrays. Further, we also restricted the local sky seen by the antennas to altitude angles between 15° and 90° above the horizon to simulate a uniform gain pattern in that range. This gain pattern is a toy model, that attempts to resemble the typically wide beam widths of radio antennas used in astroparticle physics. Using array-specific antenna patterns, obtained either from simulations or data, would be favorable. However, most of this information is not publicly available, if at all (e.g., for arrays under construction or development). At this level of detail, one would need to take into account frequency-dependent responses of the electronic components in the signal chain as well, which is beyond the scope of this work and we leave that to dedicated analyses of the Galactic calibration of the individual arrays. Therefore, we also ignored a potential polarization of the diffuse radio emission and polarization characteristics of the individual antennas.

With the antenna toy model, the average temperature of the local sky integrated over LST is calculated analogous to Eq. 5.7 as

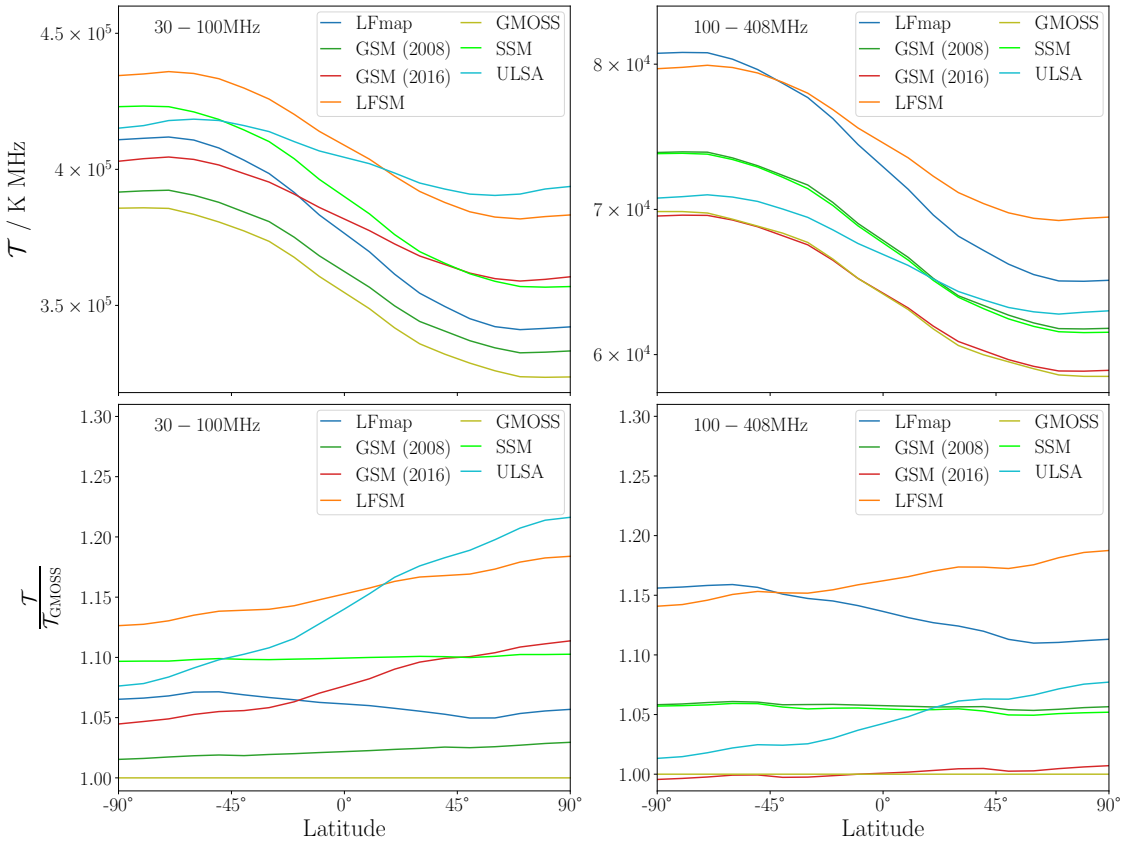

Figure 5.6: Values of $\mathcal{T}(\ell)$ for each sky interpolation models as a function of latitude. The results for the frequency ranges [30 MHz, 100 MHz] and [100 MHz, 408 MHz] are shown on the left and right side, respectively. In the top row, absolute values are shown while in the bottom row, values are normalized to GMOSS.

$$\bar{T}_{\mathrm{exp}}(\nu, \ell_{\mathrm{exp}}) = \frac{1}{2\pi}\frac{1}{24\,\mathrm{h}}\int_{0\,\mathrm{h}}^{24\,\mathrm{h}} dt_{\mathrm{LST}} \int_{15^\circ}^{90^\circ} \cos(a)\,da \int_{\frac{-\pi}{2}}^{\frac{\pi}{2}} T(\nu, \ell_{\mathrm{exp}}, t_{\mathrm{LST}}; a, \alpha)\,d\alpha, \tag{5.9}$$

with the latitude of the respective experiment ℓ_{exp}. We integrated $\bar{T}_{\mathrm{exp}}(\nu, \ell_{\mathrm{exp}})$ over the corresponding frequency band $[\nu_{\mathrm{exp,\,lower}}, \nu_{\mathrm{exp,\,upper}}]$ to obtain

$$\mathcal{T}_{\mathrm{exp}}(\ell_{\mathrm{exp}}) = \int_{\nu_{\mathrm{exp,\,lower}}}^{\nu_{\mathrm{exp,\,upper}}} \bar{T}_{\mathrm{exp}}(\nu, \ell_{\mathrm{exp}})\,d\nu. \tag{5.10}$$

Further, any two sky models m_1 and m_2 were compared by their relative difference

$$r_{\mathrm{exp};\,m_1,\,m_2} = 2\frac{\mathcal{T}_{\mathrm{exp},\,m_1}(\ell_{\mathrm{exp}}) - \mathcal{T}_{\mathrm{exp},\,m_2}(\ell_{\mathrm{exp}})}{\mathcal{T}_{\mathrm{exp},\,m_1}(\ell_{\mathrm{exp}}) + \mathcal{T}_{\mathrm{exp},\,m_2}(\ell_{\mathrm{exp}})}. \tag{5.11}$$

The largest relative differences obtained for each experiment are listed in Tab. 5.4 together with the properties of the experiment and the combination of sky models between which the largest relative difference occurs. These differences range from ~12%

Table 5.4: Largest relative deviation $\max(r_{\mathrm{Exp};\,m_1,\,m_2})$ between any two sky models m_1 and m_2 for each of the selected radio experiments. Site locations and frequency bands of the experiments are quoted from latest design plans. For RNO-G the LPDA surface antennas were considered, which are sensitive up to ~1 GHz, but the comparison was done only up to 408 MHz because of the limitations of the LFmap and LFSM sky models. The complete table can be found in appendix B.1. References: (1) [116]; (2) [110]; (3) [166]; (4) [109]; (5) [117]; (6) [108]; (7) [167]; (8) [118].

Experiment / observatory	ℓ_{exp} (°)	Frequency band (MHz)	$\max(r_{\mathrm{exp};\,m_1,\,m_2})$ (%)	Corresponding sky models
RNO-G (1)	72.58	100 to 408	17.1	LFSM / GSM16
LOFAR low (2)	52.91	30 to 80	19.8	ULSA / GMOSS
LOFAR high (3)	52.91	110 to 190	18.4	LFSM / GSM16
GRAND (4)	42.93	50 to 200	21.5	LFSM / GMOSS
OVRO-LWA (5)	37.23	30 to 80	19.3	ULSA / GMOSS
SKA-low (6)	-26.70	50 to 350	15.1	LFSM / GMOSS
Auger (7)	-35.21	30 to 80	11.7	LFSM / GMOSS
IceCube (8)	-90.0	70 to 350	20.3	LFSM / GMOSS

to ~22%. Again, the brightest and faintest skies are predicted mostly by LFSM and GMOSS, respectively. However, because of the unique locations and frequency bands, the models in the roles of the extrema are different for RNO-G, LOFAR, and OVRO-LWA. In dedicated analyses of the arrays regarding the Galactic calibration, instead of using all models, the effort to predict the Galactic emission can be reduced to just using these border models. An extended overview of the comparison results for each of the experiments including every combination of models is given in appendix B.1.

5.5 Influence of other natural sources of radio emission

The Galaxy is not the only natural source of background radio emission, although it is dominant for remote locations in the considered frequency range. In the following, we discuss contributions to the radio background by the quiet Sun, the ionosphere, and Jupiter and how they may influence the Galactic calibration of radio antenna arrays.

5.5.1 The quiet Sun

Another source of radio emission in the sky is the Sun. Here, we studied the influence of the quiet Sun on the average sky brightness, which describes the continuous thermal emission of solar radiation. There is also a concept of the active Sun, which includes enhanced emission during sunspot activity as well as emission in the context of solar flares. These contributions take place on limited timescales from seconds to hours and may be significantly brighter than the quiet sun. The slowly varying thermal emission from the sun reaches up to two times the maximum brightness temperature of the quiet state, whereas the brightness temperature of the rapidly varying solar emission components may be five or more magnitudes larger than the quiet state, depending on the emission mechanism [168]. However, we did not cover the active sun in this study. At AERA, several types of solar signals have been seen and studies [169]. The maximum

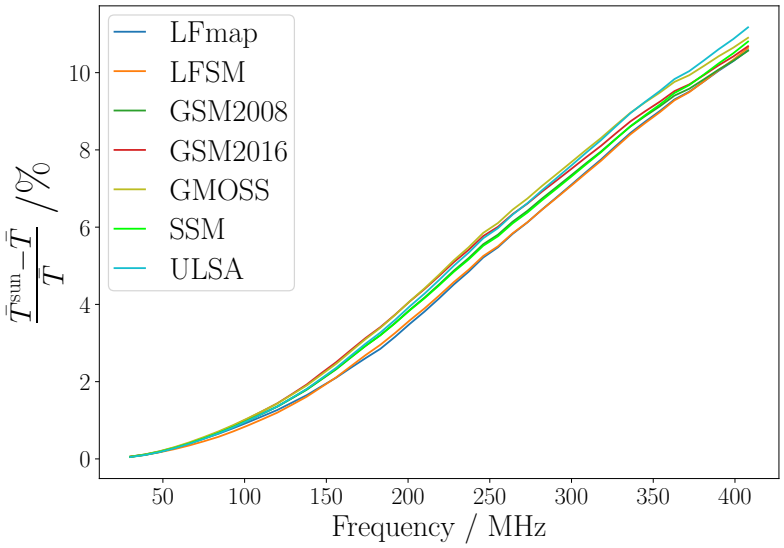

Figure 5.7: Influence of the Sun on the average sky temperature for each of the models. The plot shows the relative difference of the average sky temperature as a function of the frequency for when a Sun sized circle of the corresponding brightness temperature (quiet Sun) is added to the maps. Kinks in the curves are due to quantization effects in the calculations.

usable frequency (MUF) for radio communication affects the operation of radio arrays below 40 MHz and is tied to the solar cycle. Solar Radio Bursts, several of which have been detected and identified with AERA, heavily disturb the signal traces and can cause radio blackouts. Time periods affected by such phenomena can be flagged and taken out from regular analyses of air showers. However, most of the data taking period of AERA by chance happened during a quiet phase of the solar cycle, meaning that air-shower analyses from these data are mostly unaffected by active-sun phenomena.

Radio emission of the quiet Sun at frequencies from tens of megahertz to tens of gigahertz is larger than expected from a 6000 K black body spectrum and reaches brightness temperatures up to 10^6 K around 50 MHz [168]. To investigate how large the influence of the Sun is, we generated sky maps with a disk of constant brightness projected onto it. Data on the brightness temperature of the quiet Sun as well as its effective size as a function of the frequency were taken from a summary of recent measurements given in [170]. In the considered frequency range, the quiet Sun appears in a rather elliptical shape and the data of the measured radius are given in the north-south and east-west direction separately. We determined a conservative estimate for the solar influence on the average sky temperature by modeling the Sun as a circular disk using the larger radius data of the east-west direction.

With the superimposed quiet Sun the average sky temperature of the map was calculated as before and its relative difference to the average sky temperature of the unmodified map was determined. This is shown for each of the sky interpolation models in Fig. 5.7. While the influence is negligible at the lowest frequencies, it grows to a level of ~11% at 400 MHz.

Furthermore, we adapted this procedure to the local skies of the selected radio arrays, again restricting them to elevations from 15° to 90° above the horizon and taking

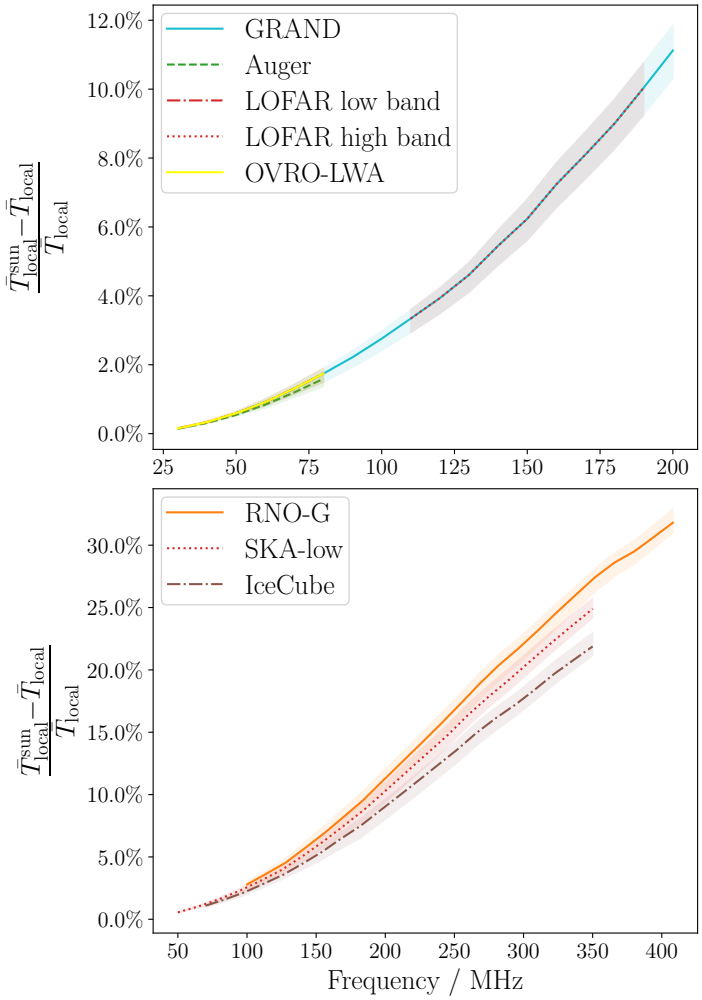

Figure 5.8: Relative difference of the average temperature of the local sky induced by the quiet Sun for the selected radio arrays. The lines represent the average results from using the seven sky models to produce the maps, while the maximum and minimum contribution from any model is shown by the colored bands. Arrays at lower frequencies are shown in the top part, while arrays at higher frequencies are shown in the bottom part. Kinks in the curves are due to quantization effects in the calculations.

the mean of the average sky temperatures over the course of 24 h of LST. The relative difference caused by the Sun is shown for all arrays over their frequency bands in Fig. 5.8. The arrays at the lowest frequencies are shown on the left and the ones reaching to larger frequencies are shown on the right.

Analogous to Fig. 5.7, the relative differences increase with frequency, while they are scaled up here because only a portion of the total sky is considered. The differences are on the level of 1% for Auger, OVRO-LWA, and the low band of LOFAR and go up to 30% for RNO-G at around 400 MHz. However, we note that also for the arrays at lowest frequencies the quiet Sun might become relevant, if the respective antenna's gain pattern is narrower than in our toy model, increasing the relative solar contribution during the time of passage through the main lobe of the beam pattern. Deviations between the

arrays at the same frequencies are attributable to the different exposure to the Galactic center due to their geographical positions.

5.5.2 The ionosphere

The ionosphere is a reflective medium for radio waves below 20 MHz [33]. Therefore, at these frequencies, noise from sources in the atmosphere (for example from thunderstorms) can be picked up from large distances by radio antennas, and would in fact dominate over the Galactic signal. The ionosphere's ion density and consequently the atmospheric noise is expected to be the largest during summer daytime in phases with high sunspot activities [33, 113].

Radio antenna arrays in astroparticle physics are typically operated at frequencies above 30 MHz to avoid the atmospheric noise due to reflections from the ionosphere [35]. However, even at frequencies above 30 MHz, the background signal measured in a radio detector may be affected by refractive and absorptive effects of the ionosphere. It is reported that there are daily variations of the ionosphere's opacity for radio waves [171] but they can also appear on more irregular timescales, such as in the sporadic E-layer [172]. These variations may have an impact on the sky-averaged measurements in the Galactic calibration. While those ionospheric effects are significant for the detection of EoR signals [173], detailed studies are necessary to determine whether they are relevant for the calibration of radio detectors in astroparticle physics. A useful web-tool, called prop, shows real-time maps of the critical frequency up to which radio waves get bounced off of the ionosphere [174]. This tool could help determining whether there is ionospheric influence on the measurements of a radio detector at a given time. Investigations based on a little more than one year of data from the RD show that ionospheric noise is widely present between 30 MHz to 40 MHz with modulations on various timescales: daily, (half-)yearly, and with the solar cycle [169, 115].

5.5.3 Jupiter

Jupiter is a source of radio emission with a unique and dynamic spectrum dominated by several components of nonthermal emission. This spectrum has a hard cutoff at 40 MHz up to which frequency Jupiter emits intense decametric (DAM) radio waves [175]. Jovian DAM emission occurs in irregular intervals with time scales of minutes and hours [176]. The antennas of the radio detectors considered in this work have a rather wide beam and a potential signal from Jupiter would always enter these together with a large-scale contribution from the Galaxy. Because of this and due the cutoff in its emission spectrum, Jupiter can be safely ignored above 40 MHz. Below 40 MHz we cannot give a definitive answer as to how Jovian emission influences the Galactic calibration. We advocate a dedicated analysis that takes into account the antenna gain pattern as well as the temporal features of Jupiter's spectrum. The probability for an observer to see Jovian emission at a specific time can be predicted well, for example using the Jupiter Radio Probability Tool [177]. We leave this to future work.

5.6 Discussion

This study gives estimates for the systematic uncertainty in predicting the diffuse Galactic radio emission in the 30 to 408 MHz range. Moreover, it provides an overview of the available models that are used for making these predictions and their corresponding reference measurements.

5.6.1 General discussions

A considerable realization from this overview is that probably a significant level of correlation exists between the systematic uncertainties of the sky models and the reference maps. Some reference maps served as calibrators for other maps and have thus an increased weight in the sky interpolation models. In general, for the sky models considered here, there was no substantial attention paid to weighting the individual reference maps during the modeling process, which can lead to biases on the absolute temperature scale. These biases are almost impossible to untangle.

The generally small number of reference maps in the studied frequency range further complicates the situation. While many surveys included a careful treatment of their uncertainties, others lack this kind of thoroughness, which in some cases may just be a consequence of the age of these surveys and the unavailability of some tools and techniques at the time of their execution.

In the future, these difficulties can be coped with by including more and newer reference maps into the sky interpolation models and weighting them based on their inherited uncertainties. New sky surveys at megahertz frequencies are on the horizon or have been published in the recent past, including direct comparisons to other maps or sky models [178, 179, 180].

Regarding the application of the Galactic calibration for radio arrays in astroparticle physics, we argue that the viability of this method is given if systematic uncertainties are carefully taken care of, which means that the parameters of the considered radio array are important. From our studies, we see that the Galactic calibration exhibits larger uncertainties at higher frequencies. There, the Galaxy's contribution to the radio background diminishes and sources such as the Sun become stronger. In the case of an array with a large frequency band, it might be a solution to conduct the Galactic calibration only with night-time measurements to minimize systematic uncertainties. Alternatively, the solar emission may be modeled on top of the Galactic calibration similar to how we did in Sec. 5.5.1. Solar emission on short timescales, which is part of the so-called active sun, can be much brighter than the quiet sun. Therefore, time periods with contributions from the active sun may have to be excluded from Galactic calibration campaigns to prevent distortions in the calibration.

Some of the radio arrays mentioned in this study have made significant progress in characterizing and using the Galactic background. While at LOFAR a full Galactic calibration has already been conducted [112], the predicted Galactic signal is being extended from using only LFmap to the palette of sky models discussed in this work [181]. At RNO-G, a comparison of previously collected background data to sky-model predicted Galactic signal shows good agreement, although not yet exploiting the multitude of sky models [182]. The two guest arrays at the Pierre Auger Observatory, IceCube@Auger

and GRAND@Auger, report seeing the Galactic background with potential for future calibration analyses [183, 184]. These developments show that characterization of the Galactic background is becoming a fundamental step in the commissioning of radio arrays with a clear perspective on using the Galaxy as the standard candle for the absolute calibration of those detectors. Still, many of these arrays will face the discussed challenges (lower dominance of the Galactic signal at higher frequencies, impact of solar emission) that are not relevant to those detectors at lower frequencies, for which the Galactic calibration has already been developed to advanced stages – LOFAR and AERA. Moreover, the performance of the Galactic calibration can be limited by thermal effects through temperature dependent system noise [185, 115]. Therefore, having accurate and permanent temperature measurements at the antenna stations is important for refining the accuracy of the Galactic calibration at arrays with strong temperature variations. On the other hand, this issue is likely irrelevant for the future radio detector at IceCube.

5.6.2 Relevant aspects specific to AERA and the RD

The Galactic calibration has been developed quite extensively already for the radio detectors at the Pierre Auger Observatory. This especially holds for AERA, where it has been used to study and show its long-term stability over many years [186], a work that is built upon and being continued with the RD. In our uncertainty study for the Galactic calibration, we find an uncertainty estimate for the location and frequency band used for both AERA and the RD. However, several assumptions are held at a generalized level. For example, we assume a toy antenna model with a uniform directional sensitivity between 15° and 90°. This assumption already breaks in the case of radio detection at the Pierre Auger Observatory, as the antenna types of AERA and the antenna type of the RD exhibit clear differences in their gain patterns.

A weak spot in the Galactic calibration of the radio detectors at the Pierre Auger Observatory is its location in the southern hemisphere. As mentioned already in Secs. 5.1.2 and 5.1.4 and as is evident from Fig. 5.2, most reference maps used in the sky models were taken with a telescope on the northern hemisphere. Therefore, coverage of the Galactic radio sky as seen from the southern hemisphere is comparatively sparser. In turn, the prediction of the part of the Galactic signal most relevant to radio arrays from the southern hemisphere, like AERA and the RD, can be expected to be less accurate from the point of view of reference map coverage. However, it is difficult to quantify this circumstance.

5.7 Conclusion

We compared seven interpolation models that produce full-sky maps of the Galactic radio emission at frequencies between 30 and 408 MHz. The models partially rely on the same reference measurements and differ to a greater or lesser extent by their interpolation approach. A summary of the used reference maps shows relative uncertainties on the temperature scales of up to 20% and zero-level errors that can be as large as up to 11% of the average temperature of the sky at that frequency. In a global comparison, we find that the predictions of the interpolation models all agree within 14.3%, which we suggest as an estimate for the systematic uncertainty of the model predictions. This estimate

incorporates both the individual temperature scale uncertainties of the reference maps and uncertainties because of different modeling methods.

Furthermore, we compared the models based on the local sky at a given experiment's latitude on Earth. This step reveals further differences between the models and in combination with specific frequency bands of selected radio-detection arrays deviations vary considerably. Depending on the experiment, the level of agreement lies between 11.7% and 21.5%.

Additionally, we studied the influence of the quiet Sun on the radio background of the selected arrays and find it to be negligible at lower frequencies. However, the contribution increases to ~30% at around 400 MHz. While the strongest ionospheric contributions happen below 30 MHz, which is the lowest frequency typically used by radio arrays, there are effects that can disturb measurements even above this frequency. Therefore, a dedicated study of those effects is needed. We do not expect emission from Jupiter to play a role in the applicability of the Galactic calibration above 40 MHz. For frequencies below 40 MHz, we suggest the conduction of a quantitative analysis about Jupiter's influence.

The relative uncertainties in sky temperature quoted above determine the signal power measured in radio detection arrays for cosmic particles – whereas the energy scale for the energy of the detected particles scales with the electric field amplitudes, that is, the square root of the signal power. We will give a broader overview of the relevant observables in Sec. 7.1. The relevant systematic uncertainty on the energy scale of particle detection thus corresponds to approximately half of the values quoted here. In particular, the systematic uncertainty for AERA and the RD, which we estimate at 11.7% on the brightness temperature scale, amounts to 5.9% on the cosmic-particle energy scale. These uncertainties are competitive with those achieved with external calibration sources – if not better – and thus confirm the value of the Galactic calibration approach. If models with even higher accuracy for the Galactic emission in the frequency band from 30 to 408 MHz become available in the future, radio detection arrays for cosmic particles will profit from these retroactively.

With regard to the energy-scale analysis with AERA in this work, it is clear that the Galactic calibration is the best method to calibrate the signals in the detector on an absolute scale. Our sky-model comparison gives a systematic uncertainty estimate on the energy scale of 5.9% and we find other permanent natural sources of radio emission to not have a large impact on the Galactic calibration for AERA. The results of this study apply in the same way to the RD, which is convenient for future analyses with RD data – especially on the radio energy scale. As part of the next chapter, we give an overview of the realized calibration efforts for AERA that are relevant for the energy-scale analysis of this thesis. In particular, the implementation of the Galactic calibration of AERA is reviewed, which employs the same sky models as we compared in this chapter.

6

Calibration of AERA and reconstruction of air-shower radio signals

In the last chapter, we studied sky models for the Galactic calibration of radio detection arrays in depth and derived an estimation of the systematic uncertainty that is attached to them for various relevant arrays. With an uncertainty estimate of 5.9% on the cosmic-ray energy scale for the case of AERA, the great value of the Galactic calibration within the important absolute detector calibration for the energy-scale analysis in Chap. 8 is already perceptible. Following on from this study, we explain how the the Galactic calibration is performed in practice for AERA and how we use it for the energy-scale analysis. Furthermore, we discuss the many efforts of calibrating AERA in other aspects.

We also review the processing and reconstruction of air-shower data from AERA. Each of those steps involves sophisticated work and in combination, they constitute a critical foundation for previous analyses of the cosmic-ray energy scale with AERA (see Sec. 7.3) as well as the new approach that we present in Chap. 8. With the ingredients that we discuss here, we will have all the necessary components to conduct calibrated measurements with AERA and reconstruct air-shower events to the required stage for our energy-scale analysis.

None of the studies presented in this chapter were conducted within this thesis but by colleagues from or related to the Pierre Auger collaboration. We review the studies here because of their central importance to the previous energy-scale analyses and to our new approach and we give references to the respective works.

In Sec. 6.1, we present the efforts made to calibrate AERA with unprecedented accuracy. Afterwards, we go through the ingredients of the radio event reconstruction in Sec. 6.2.

6.1 Calibration of AERA

Many efforts are needed to ensure that air-shower detection with AERA can be done in a calibrated way. To this end, a lot of work has been done during the development and before deployment and commissioning of the antenna stations but also during the operation of AERA with some studies still going on. All these efforts are necessary to be able to conduct high-quality physics analyses with AERA. Moreover, many lessons learned from these efforts went into the design and development of the RD.

6.1.1 Calibration of electronics components in the lab

The analog components in the signal chain of each radio station have individual gains and impose group delays on the signal, both of which are in general frequency-dependent. The analog chain consists of the low-noise amplifier (LNA), filter amplifier (FA) and coaxial cables. Moreover, the digitizer that succeeds the analog signal chain might contain a frequency dependence in its gain of the digitization process. All these responses distort the processed signals, which poses a significant challenge when aiming to perform absolute-calibrated radio measurements of air-showers. Also, these responses can vary from unit to unit. Therefore, in the past the responses of all individual units of each of the electronics components were measured in the laboratory [187, 188, 189]. This information is stored in a database and is used to correct for the signal responses of the components during the radio reconstruction (see Sec. 6.2.4). Furthermore, the response measurements are applied in the detector simulation when, for example, simulated signals from air-showers or the Galactic background in AERA are predicted.

Malfunction and failure of individual units require replacement with spare parts from time to time. The information on when these replacements were done, for which detector station, and with what spare unit, were tracked in a database as well. This monitoring effort ensures that the correct signal response is used in the radio reconstruction.

6.1.2 Antenna gain characteristics

The central analog component in the signal chain is the physical antenna that picks up the electric field from the radio emission and converts it into a measurable voltage in each of the two channels that are used in the AERA stations. The parameters of the voltage traces depend on the characteristics of the antenna gain. This gain is a function of frequency, arrival direction and orientation of the incoming electric-field vector. In the reconstruction process, the antenna pattern needs to be unfolded from the measured voltage traces in order to obtain a reconstructed electric-field vector. Therefore, an accurate description of the antenna gain as a function of frequency, azimuth angle and zenith angle is required.

In this regard, several efforts have been made to calibrate the gain characteristics of both the LPDA and Butterfly antennas with. Most of these works have been conducted by the group from RWTH Aachen. The efforts can be separated into simulation studies and measurements using reference emitters, the latter mostly conducted in drone-borne campaigns. Typically, the sequence of work consists of simulations of the vector effective length (VEL) that were conducted with the NEC-2 simulation software [190] preceded by a measurement in the field to cross-check the simulations.

The VEL is a complex quantity that relates the voltage induced by a wave of a certain frequency coming in from a certain direction with a certain orientation to what would be received in equivalence from an electric current flowing through a conductor of a certain length in a reference position [191]. In Offline, a description of the VEL of a given antenna binned in frequency, zenith angle and azimuth angle is stored. For the absolute calibration of AERA that we seek to build on in the energy-scale analysis in Chap. 8, the absolute calibration of the antenna patterns is not critical, as we rely on the Galactic calibration in that regard (see Sec. 6.1.4). On the other hand, a well-calibrated

description of the directional dependency of the antenna gain is important, which is not available from a study with the Galactic signal.

6.1.2.1 Log-periodic dipole antennas (LPDA)

The LPDA antenna was simulated with NEC-2 according to its real specifications and to the environmental conditions at AERA [192, 193]. This simulated model was used as standard in the reconstruction for a long time. Early on, a calibration measurement of a deployed LPDA antenna from AERA Phase I using a reference antenna on a balloon was conducted. A cross-comparison between the measurement and a simulation showed good agreement [192].

At a later stage, the deployed LPDA station setup was calibrated in a more sophisticated campaign using a reference antenna mounted on an octocopter [194]. The calibration setup was also simulated in NEC-2 to be able to perform a valid cross-comparison. Although measured and simulated VEL agreed for most of the phase space, deviations in a few aspects showed up. Therefore, the original simulated antenna pattern was modified with correction factors to match to the results from the real and simulated octocopter measurements [194]. The resulting tuned antenna pattern is what is currently used in the radio reconstruction with AERA.

6.1.2.2 Butterfly antennas

Very similar to the LPDA antenna, the Butterfly was simulated in NEC-2 and in the same drone-borne calibration campaign, the VEL of the Butterfly antenna was measured in the field [195]. In the same way as done for the LPDA antenna, the measured VEL of the Butterfly was compared to a VEL derived from NEC-2 simulations of the calibration setup, obtaining correction factors that were used to modify the original NEC-2 simulated Butterfly pattern to match the drone measurement [195]. However, in the case of the Butterfly antenna, larger discrepancies between measurement and simulation were found – especially at higher frequencies – than in the case of the LPDA.

There are a few considerations as to why adapting the procedure of rescaling the simulated LPDA antenna pattern is unfavorable for the Butterfly antennas. In particular, the octocopter calibration campaign was conducted with flights only along the two polarization directions of the antenna, i.e. North-South and East-West. For rescaling the simulated antenna pattern in between those cardinal directions, the corrections from the comparison of measurements and simulations were linearly interpolated. This procedure is likely inappropriate in case of the Butterfly antenna, since the antenna is comparably low to the ground and its pattern is fairly sensitive to the electronics box mounted below, which is expected to introduce an asymmetry in the gain pattern. In earlier revisions of the Galactic calibration of AERA, it has been seen that the predicted Galactic signal as a function of frequency matches much better to the measured signal when using the simulated Butterfly pattern than the pattern with corrections towards the measured pattern [196, 197]. This observation may be due to the impact of the electronics box not being well represented in the drone measurements if the azimuthal asymmetry introduced by the box is not well sampled.

Instead of interpolating the correction factors for the antenna pattern between the four cardinal directions, a drone-measurement campaign with finer sampling in azimuth

is necessary. In November 2023, a new drone campaign was conducted [198]. Although aimed at calibrating the SALLA antenna pattern of the RD, measurements at two AERA stations were performed as well, one with an LPDA and Butterfly antenna each. This campaign reached a new level of sophistication and measurements were conducted at significantly more directional positions compared to the previous campaign. The evaluation of the AERA measurements – in particular for the Butterfly antenna – of this campaign is yet to be done and quite complex since the used reference emitter on the drone was comparatively strong in order to work best with the SALLA antenna, which is less sensitive than the AERA antennas. In the test flights at the Butterfly station, the drone-borne emitter partially saturated the station. Still, many insights from conducting the new drone campaign revealed that an ambitious level of detail in many aspects of the analysis is necessary to reach a high level of precision. In retrospective, this level of detail – in particular finely covering the directional phase space – may not have been reached in the first drone campaign sufficiently to use the measurements to modify the simulated antenna pattern [199]. Therefore, we only use the original simulated Butterfly antenna pattern in the radio reconstruction for this work.

6.1.3 Temperature correction of amplifier gains

The signal gains of the LNAs and FAs in the AERA stations are temperature dependent. This dependence was measured individually for the two amplifier components and can be described well by a linear relation in the relevant temperature range [188, 189, 193]. From the temperature fluctuations observed at the Pierre Auger Observatory, the variation of the signal gain within an air-shower event data set covering the full seasonal range is estimated at 4% [200]. This variation is expected to increase the scatter of the reconstructed signals of such an event data set and will thus also increase the scatter of reconstructed energies. In addition, it will introduce a bias if the temperature of the LNAs and FAs is on average different from the temperature, at which these components were calibrated in the laboratory.

While there are temperature sensors next to or directly on the board with the FAs providing an accurate temperature measurement for the latter, the LNAs do not contain individual temperature sensors. However, they are mounted outside the electronics boxes of the stations – as opposed to the FAs – directly at the mechanical antennas. Therefore, the air-temperature measurement from the weather station at the CRS is considered a sufficient estimate for the temperatures of the LNAs. A procedure was developed by members of the AERA group to correct measured voltage traces with the known temperature dependencies to a reference temperature of 20 °C and its implementation in Offline, documented in [201], is briefly discussed in Sec. 6.2.4.

In Fig. 6.1, adapted from [201], the RMS of the signal amplitude of the periodically triggered signal traces is plotted between 2015 and 2020 with and without the temperature correction applied. The seasonal modulation is visibly reduced albeit not removed entirely. The remaining fluctuation may be associated with second-order dependencies of the gain of the components on heating of the housing that is not accountable for with the available temperature measurements.

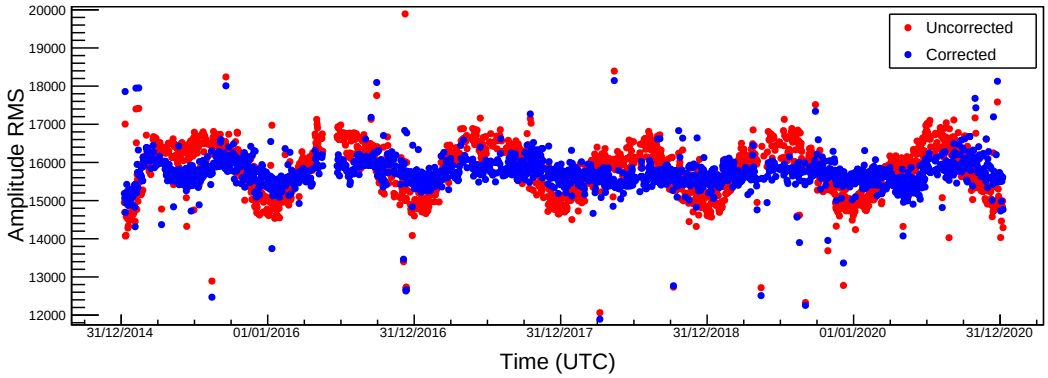

Figure 6.1: Variation of the RMS of the signal amplitude of AERA station 41 (Butterfly) over six years, with and without temperature correction in blue and red, respectively. The data were always taken from 18:00 LST to ensure that the Galactic background signal is the same in all samples. Adapted from [201].

6.1.4 Galactic calibration

At the heart of the absolute calibration of radio arrays in astroparticle physics is the Galactic calibration. In case of AERA, the Galactic calibration has been studied previously [196, 197] and was finally implemented in a standard module in the reconstruction pipeline in Offline in [202], which is used for the studies in this thesis. In Chap. 5, we already introduced the basic idea of the Galactic calibration, we discussed its growing importance but also its current accuracy limitations with regard to the predicted Galactic signal. To this end, we studied the intrinsic differences between available sky models that can serve as estimates for the systematic uncertainty of the Galactic calibration. However, this uncertainty study was decoupled from the actual implementation of the Galactic calibration in the reconstruction of a radio array. The study was conducted on the level of sky temperatures, while implementations act on the level of quantities measured by the detector, typically the voltage induced in the antenna. It is also relevant, how the comparison of measured and predicted Galactic signal is done concretely. Therefore, we briefly discuss the implementation of the Galactic calibration for AERA carried out by the Fluminense Federal University group.

The employed method in [203] is based on work done for LOFAR in [112], in which the received power in the antenna from the Galactic emission was compared to the predicted power. The template method was extended in a few aspects, for example by using the seven sky models presented in Sec. 5.1 instead of just LFmap [204]. The predicted power is simulated by folding the sky brightness temperature from a sky model through the complete analog signal chain of AERA in Offline with the characteristics of the electrical components as discussed in Sec. 6.1.1 and using the antenna gain pattern as described in Sec. 6.1.2. Both, measured and simulated power are calculated for each individual antenna separate for each of the two polarization channels for bins in frequency (1 MHz resolution) and in local sidereal time (LST) (1 h resolution) [203].

An example scatter plot of measured against simulated power from the Galactic signal from the analysis in [186] is shown in Fig. 6.2 for one channel of one Butterfly station from one month of data. The colored points refer to samples at different frequencies. From the variation of the Galactic-signal strength with LST – the Galactic center passing through

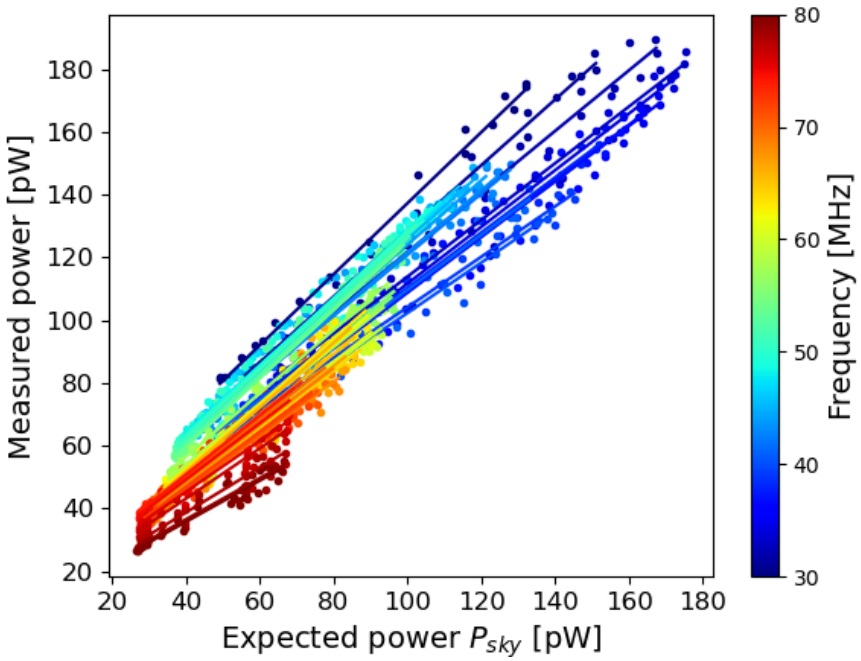

Figure 6.2: Calibration fits for the Galactic calibration of one channel of an example Butterfly station for one example month with power measured in noise traces plotted against the simulated power from a sky model folded through the detector response. Colored points depict data samples at a specific frequency and lines of the same color are the corresponding linear fits. Taken from [186]

the sensitive field of view of the antenna and disappearing periodically – the samples for a given frequency move up and down a correlation line that in good approximation is linear. Therefore, a linear function is fitted to the correlation line for each frequency bin. The linear function allows for an offset that is attributed to a sum of temporally constant noise contributions. The linear scaling is attributed to the squared factor $C_0^2(\nu)$, which is defined such that $C_0(\nu)$ acts as a linear scaling factor on voltage level – and effectively also on cosmic-ray energy level. Details about the procedure and about preceding steps of cleaning of spectrograms can be found in the respective study in [203].

The calibration constants are determined per frequency bin, per channel, per antenna, per month for each of the seven implemented sky models. When averaging the constants over time, frequency and for all stations of either antenna type, the mean calibration constants for LPDA and Butterfly, separate for the two channels, are compatible with unity within uncertainties [186]. This result certifies a remarkable accuracy to the previous efforts made in calibrating AERA with antenna simulations and measurements of individual components of the signal chain in the laboratory. Nevertheless, the small absolute scale offsets from one, probably accumulated from several stages, are corrected for by the Galactic calibration.

Moreover, the long-time operation of AERA allows to study the calibration constants as a function of time, looking for a potential drift in any of the involved components. In [186], no significant or relevant aging is observed over the studied period from 2014 to 2020, which is in line with the expectations. Averaged over all stations, an estimate of the aging of (-0.32±0.51)% per decade is obtained [186]. In conclusion and generalizing from

this result, the radio technique can be used as a stable calibrator in hybrid operation with other detector types. At the Pierre Auger Observatory, AERA – and in the future also the RD – may be used to quantitatively investigate aging of the SD and the FD. However, in the discussed implementation of the Galactic calibration for AERA, a remaining seasonal modulation of the calibration constants of a few percent was found that could not be explained by an unaccounted for dependency, e.g. on solar irradiance [205]. Deeper investigations found a possible cause of the modulation in the implicit assumption of the applied Galactic calibration analysis that the non-Galactic noise is constant in time and suggest moving from a Galactic calibration with data samples only binned in LST to binning in both LST and temperature [115]. Further development of the Galactic calibration of AERA in this regard are out of the time frame for the conclusion of the energy-scale analysis in Chap. 8. However, the current implementation with the remaining seasonal modulation is not adverse to the absolute calibration as is needed in our study. On average, the Galactic calibration is expected to be unbiased from this modulation when applying it in that study.

Since the long-term study of the calibration constants in [186] revealed the effective aging of AERA to be compatible with zero, a binning per month is not necessary. Therefore, in the event reconstruction for the energy-scale analysis, we use calibration constants per station, per channel, per frequency bin that are averaged over the entire used time period. Furthermore, a choice of sky model is required. From a conceptional point of view, the sky models may be discussed on the basis of their level of sophistication in accurately modeling the Galactic emission in order to find a *best model*. However, this discussion requires deep knowledge and expertise from radio astronomers, which is outside of our domain. Ideas have been discussed on how to determine a *best fitting model* in a data-driven way. For example, one could attempt to measure the Galactic modulation, i.e. the temporal shape of the Galactic signal from the rising and setting of the Galactic center. This measured modulation could then be compared to the predicted modulation from the models to find a best match. Such a study is outside of the scope of this work. Instead, we take the average calibration constants from all seven sky models. An advantage of this procedure is that systematic uncertainties can be applied symmetrically to the calibrated signals. In Fig. 6.3, a histogram of all calibration constants is shown. The distribution is centered close to one. The tails to both sides can be attributed to specific frequency ranges, in which the Galactic calibration finds a larger disparity between measured and simulated Galactic signal. Overall, the Galactic calibration attributes great success to previous calibration steps but ultimately sets the absolute scale of measurements with AERA.

6.2 Reconstruction of air-shower radio signals

We use the standard framework for the reconstruction of measured air showers with the detectors of the Pierre Auger Observatory, called $\overline{\text{Off}}\underline{\text{line}}$ [206]. Besides event reconstruction, $\overline{\text{Off}}\underline{\text{line}}$ also contains a description of all detectors. These descriptions are used to propagate simulated physical signals through the detector response in a full detector simulation. This way, simulated air-showers can be used like measured events in the $\overline{\text{Off}}\underline{\text{line}}$ event reconstruction. $\overline{\text{Off}}\underline{\text{line}}$ includes a separate package for storing reconstructed air-shower data and relevant information about the detector and the

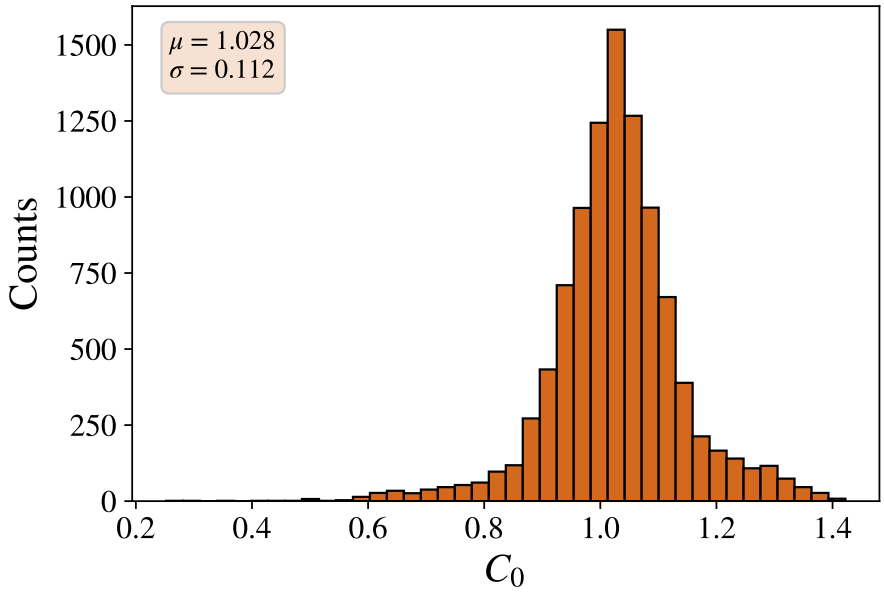

Figure 6.3: Distribution of the Galactic calibration constants of all stations used in the energy-scale analysis. The distribution individually includes both channels of each station and all frequency bins.

reconstruction itself, called *Advanced Data Summary Tree* (ADST). Reconstructed showers can be visualized in the accompanying `EventBrowser`.

Single steps of the reconstruction are developed and provided in a modular way and a full reconstruction pipeline is essentially a compilation of these modules in a particular order. The used modules and in which order they are executed is defined in a file typically called `ModuleSequence.xml`. Default parameters of the individual modules can be modified and overwritten for a reconstruction pipeline by configuring them in a file called `bootstrap.xml`. For the analysis of this work, we use module sequences and bootstraps taken from standard applications called `RdObserverEnergyScale_AERA` and `RdSimulationObserver_AERA` for the reconstruction of measured and simulated events, respectively. These standard applications have been gradually developed by the collaboration over many years. More details about the configurations are discussed in Secs. 8.1.2.1 and 8.1.2.2. Here, we briefly explain the individual steps in which raw measured and simulated data are pre-processed and in which the air-shower candidate events are reconstructed. The radio applications in Offline are generally dependent on the SD related parts, many of which are summarized in [207]. An overview on the radio-related part of Offline can be found in [208] and many details are provided in [209]. However, these references are already partially outdated as Offline is permanently evolving. Collaborative development is organized in a Gitlab repository[1].

An illustrated overview of a selection of the steps in the radio reconstruction is given in Fig. 6.4. The details are explained in the following. Other ingredients were already discussed in the previous sections and chapters.

[1] https://gitlab.iap.kit.edu/auger-observatory/offline

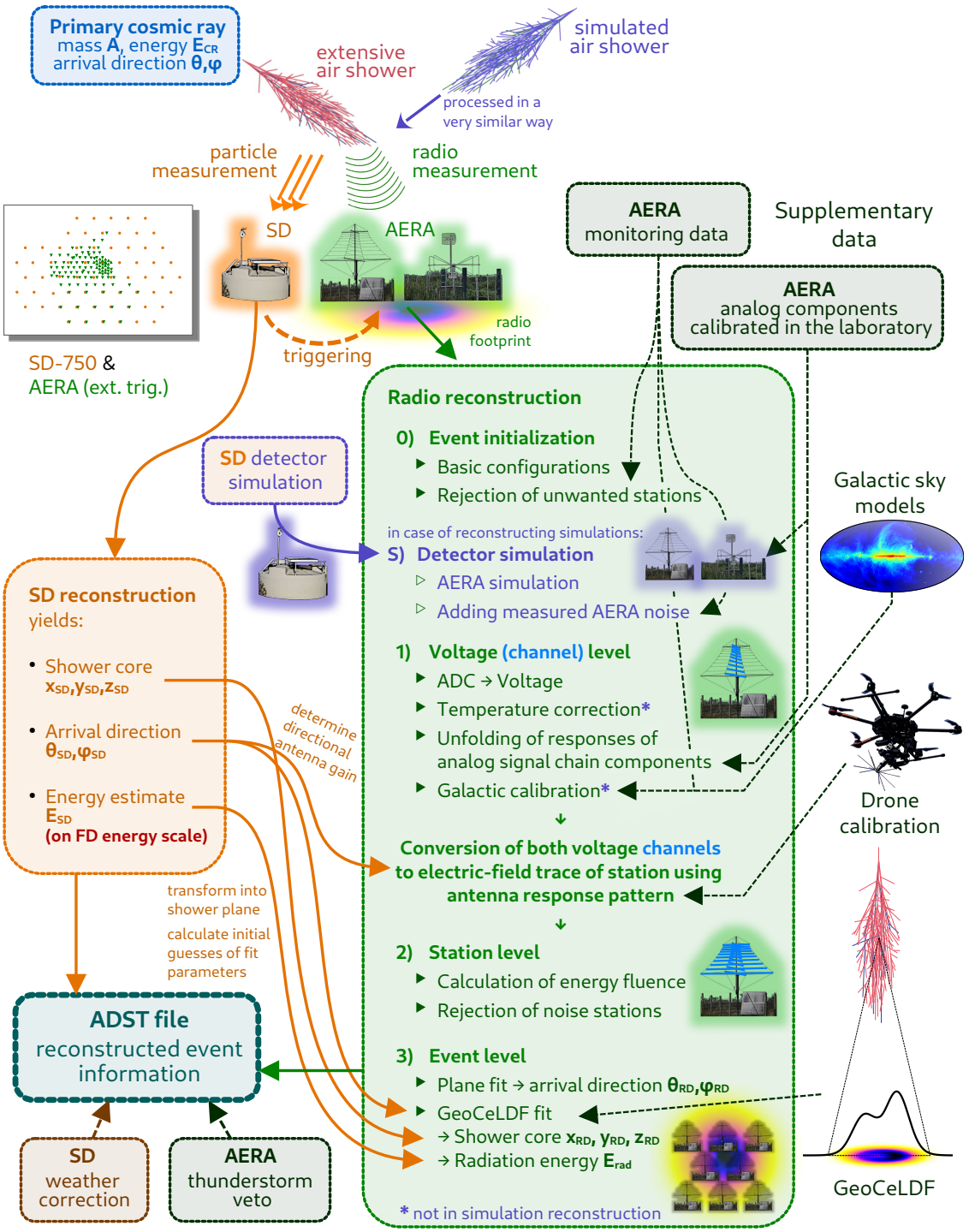

Figure 6.4: General overview of the radio reconstruction of air-shower events with the aid of the reconstruction of particle measurements from the SD-750 in hybrid mode. The most important steps and key ingredients are listed. Details are explained in the text. The reconstruction is done in very similar ways for measured and simulated air showers. The shower and radio-footprint illustrations are adapted from [210].

6.2.1 Data acquisition with external triggers

As explained in Sec. 3.4, AERA was developed and installed in different phases. Of the 100 antenna stations deployed in Phase II, a part of them employed only an internal trigger system as opposed to the majority of the stations that are both internally and externally triggered from the other detectors, especially from the SD. In this work, we only use data from the externally triggered stations. The data are compiled and saved in binary format as run files (a run usually lasts one week) on a local machine at the Coihueco FD site, from where they are copied to the central data storage and computing cluster used by the collaboration at IN2P3 in Lyon. There, the binary data are converted into `ROOT` format in daily files. These `ROOT` files are subsequently merged with the daily files from the other detectors, at which point true hybrid events are obtained. The merged files are used as input in the reconstruction with Offline.

From the binary files, monitoring data are extracted as well, that contain periodically triggered traces taken every 100 s. These data serve multiple purposes. First of all, these traces are used to calculate the Galaxy-dominated background signal in the Galactic calibration. Furthermore, these traces serve as noise measurements that can be added to simulations to create a realistic representation of a real measurement, like we do in the energy-scale analysis (see Sec. 8.1.4). Lastly, the traces allow to monitor the performance of the stations. With the `RdMonitoring` application in Offline, periods of malfunction of a station are detected and converted into `SQL` entries to be fed into the `BadPeriod` database [211, 212]. This database can be queried during the reconstruction to remove AERA stations from participating in an event reconstruction if it was malfunctioning at the time of detection.

In the following sections, the individual steps and modules of the event reconstruction on channel-, station- and event-level are presented, approximately in the order as they should be executed in. We confine our explanations to those steps that concern the reconstruction as is done for the energy-scale analysis in Chap. 8. Several additional modules are available in Offline for different applications.

6.2.2 SD reconstruction & pre-selection of measured events

Measured hybrid events are read in and their SD data is reconstructed, the details of which we skip here. Afterwards, the radio event is initialized.

- **`EventFileReaderOG + EventCheckerOG`**
  The chosen data file, containing either measured events or simulations, is read in. If the file contains multiple events, the first or next file is picked. The current event is checked for any missing critical information.

- **`SdCalibrationSelection` (Sequence)**
  This sequence includes a multitude of steps that check for a good performance of SD components and conduct necessary corrections. Explaining the details of those steps is out of the scope of this thesis. Ultimately, the sequence ensures that all events that pass the reconstruction, have been properly triggered by the SD, which is important for the energy-scale analysis.

- **`SdReconstruction` (Sequence)**
  In this sequence, the actual reconstruction of shower parameters from the SD reconstruction is performed including a geometrical fit of the signal arrival times and fit of the LDF. The reconstruction yields several important parameters of the air shower, like arrival direction and total shower energy, E_{SD}. These parameters act as input parameters for some of the modules of the radio reconstruction.

- **`RdEventPreSelector`**
  This module conducts a basic selection of events, including how the events were triggered (e.g. externally triggered only).

- **`RdEventInitializer`**
  Here, a number of settings are initialized for the event, for example which geometry is taken as reference. In this work, we reconstruct data in two stages. In the first stage, we use event geometries from a preceding SD reconstruction, and in the second stage we use external information (see Sec. 8.1.2.1). In addition, the time windows in the traces, in which the signal is expected to be found and from which the noise should be estimated, is defined in this module.

- **`RdStationRejector`**
  As mentioned in Sec. 6.2.1, malfunctioning radio stations or otherwise unwanted stations (like prototype detector stations) are rejected from the participation in the reconstruction. In this module, a few stations are rejected per default, for example the internally triggered stations as well as stations in experimental status, at which a different antenna is deployed or additional non-standard components are installed. Moreover, the `BadPeriod` database is queried to check if any other station was in a faulty state and rejects affected stations.

6.2.3 Detector simulation, SD reconstruction & pre-selection of simulated events

In order to treat simulated events in the same way as measured events, a few specific steps are taken at the beginning of the reconstruction pipeline, including a simulation of the detector responses.

- **`EventGeneratorOG + SdSimulationTabulated` (Sequence)**
  First, event structures are created that are of the same format as for measured showers. These event structures are prepared to be filled with information from the simulated signals. In many steps, the simulated particle signals are folded through the responses of the individual components of the SD detector stations (e.g. the PMTs and the station-level trigger).

- **`CentralTriggerSimulatorXb + CentralTriggerEventBuilderOG + EventBuilderOG`**
  The central data acquisition is simulated in which event-level triggers are formed to decide whether or not the data from relevant stations are sent. Like in reality, upon triggering an event is formed and stored.

- **`SdSimReconstruction` (Sequence)**
  In this sequence, those modules of the SD calibration and SD reconstruction are executed which also apply to simulated events.

- **`RdStationAssociator + RdStationSimulationRejector`**
  Here, the electric-field traces from the radio simulation of the shower are associated with the stations of the radio detector to be able to simulate the expected signals recorded in each station. Stations which should not participate in the reconstruction (the reasons overlap with those mentioned for the `RdStationRejector`) are removed.

- **`RdEventInitializer + RdSimulation` (Sequence)**
  After initializing the appropriate settings for each event, the radio detector response to the simulated electric fields is simulated. To this end, first the electric fields are folded through the VEL of the antenna type of the corresponding station to calculate the voltage trace that is picked up in each of the two channels. Then, the responses of the analog components of the signal chain are incorporated and their responses as measured in the laboratory are imprinted on the signal. The artificially precise and complete time information on the signal is reduced to the level of what the real detector is capable of recording by resampling the voltage traces to the sampling rate of the detector and by subsequently truncating the trace to the matching signal window length. Afterwards, the task of the digitizer is emulated by converting the voltage signals into ADC traces and a realistic timing accuracy is imitated by adding a time jitter to the traces.

- **`RdChannelNoiseImporter_AERA`**
  To finish matching the simulated traces to the real counterparts, for each channel, measured noise from the same channel of the corresponding station is imported from the periodically triggered data and added. In case of event simulations, noise measurements to be added are required to be from within 10 min of the event time. If no such noise recording is available, the station is rejected.

6.2.4 Signal reconstruction on voltage (channel) level

The reconstruction of radio signals begins on the voltage channel level, where the signal in each channel of each station is reconstructed separately.

- **`RdChannelADCClipper` (simulation only)**
  In case of saturated channels from larger signals, the ADC traces are clipped to the allowed range given by the digitizer.

- **`RdChannelSelector`**
  When a channel is found to be saturated in the high-gain, its low-gain can be selected to be used in the reconstruction if a low-gain channel was active in the measurement.

- **`RdChannelADCToVoltageConverter`**
  In starting to fold the detector out of the recorded ADC traces, the analog-to-digital conversion of the digitizer is taken out of the ADC counts to convert them to voltage traces.

- **`RdChannelAmplitudeTemperatureDependenceCorrector` (data only)**
  The temperature dependencies of the LNAs and FAs as discussed in Sec. 6.1.3 are corrected for by scaling the voltage traces with a factor according to the temperature measurement recorded at the time of the event. Details are explained in [201].

- **`RdChannelPedestalRemover`**
  In case that there is a DC offset in the traces, this offset is subtracted.

- **`RdChannelResponseIncorporator`**
  The responses of the analog signal chain components in form of their gain and group delay impacts on the signal as discussed in Sec. 6.1.1 are corrected for using the calibration measurements of the components from the laboratory.

- **`RdChannelGalacticCalibrator` (data only)**
  In this module, the Galactic calibration constants determined with the method from [203] reviewed in Sec. 6.1.4 are applied to the data. The calibration constants are drawn from a file that was generated in a separate Offline application [213]. If there are no calibration constants available for a specific station, that station is rejected. Such a case may occur when the periodically triggered data of a station contain traces with spectral densities that are either incomplete in LST or of insufficient quality. An analysis and overview of the spectral densities recorded by the AERA stations between 2013 and 2020 is given in [214]. Details on the implementation of how Galactic calibration constants are calculated and applied are provided in [202].

- **`RdStationPositionCorrection + RdChannelBeaconTimingCalibrator` (data only)**
  The positions of the radio stations were originally determined from the internal GPS units. Those GPS measurements can be imprecise, which led to wrong timing in relation to the other stations. This problem was solved in August 2014 by replacing the GPS position data in the AERA detector electronics with reference measurements of the true positions acquired with a differential GPS campaign [215]. For events recorded before the fix, imprecise positions are corrected in this module. Afterwards, the relative timing between the stations is improved to a level of 2 ns or better by checking the phase differences between the stations of the signal from the beacon emitter at the Coihueco FD site.

- **`RdChannelBeaconSuppressor`**
  After the beacon signal has been used in the timing calibation, its "continuous wave" narrow-band contribution in the frequency spectra of the traces is suppressed.

- **`RdStationTimingCalibrator + RdStationTimeWindowConsolidator` (data only)**
  For a few stations, a general station timing offset was found in a dedicated analysis. Here, those offsets are corrected for. Afterwards, the signal search windows are checked to be within the traces. If necessary, the windows are clipped.

- **`RdChannelTimeSeriesTaperer`**
  The time traces are tapered at the beginning and end using a Hann window in order to suppress unphysical features in the frequency spectrum that could cause biases in the subsequent signal reconstruction steps.

- **`RdChannelBandstopFilter`**
  This optional module removes narrowband RFI from the frequency spectra of the channel traces by setting the signal strength in the corresponding frequency bin(s) to zero. Recognition of bins as stemming from narrowband RFI can be defined manually by specifying frequencies or automatically by searching for bins in which the signal exceeds a threshold.

- **`RdChannelUpsampler`**
  The signal is upsampled to a higher sampling rate in the time domain by zero padding in the frequency domain.

- **`RdAntennaChannelToStationConverter`**
  Finally, the corrected and calibrated channel traces are combined with the response pattern of the corresponding antenna type and an arrival direction from the SD reconstruction to reconstruct the electric-field trace at the station.

6.2.5 Signal reconstruction on station level

After combination of the two channels in each station, the signals are reconstructed on station level.

- **`RdStationSignalReconstruction` (Sequence)**
  In this part, several properties of the radio signal on station level are reconstructed including the signal arrival time, the energy fluence and the electric-field vector. The energy fluence is estimated with the noise subtraction method [200]: first, the squared Hilbert envelopes of the electric-field strength traces in the signal window and separately in a noise window are integrated. Then, the two terms are subtracted from each other normalized to the same window length. The noise subtraction method is discussed further in [216] in a comparison to a promising new estimation method for the energy fluence based on the Rice distribution.
  At this step in the reconstruction, also the signal-to-noise ratio (SNR) is calculated, which is defined as the squared ratio of the peak amplitude of the Hilbert envelope of the electric-field trace and the RMS of the trace in the noise window. At a later stage, stations are marked as *signal station* if their SNR exceeds a threshold value. In case of the noise subtraction method for the energy fluence for AERA, this threshold is set to 10.

- **`RdNoiseStationRejector` (Sequence)**
  In several ways, noisy stations are rejected and only stations with good recordings that belong to the air-shower signal are selected to participate in the event-level reconstruction. On the one hand, for each individual station, the signal trace is searched for an exceeding amount of RFI and the estimated charge-excess fraction of the station signal is checked to be within expectations. On the other hand, stations outside of the cluster of signal stations associated with the SD-

reconstructed air shower are rejected. In an iterative procedure, a plane wave of the arriving radio signals is fitted to the station signals and stations that degrade the fit quality by some criterion or completely break the fit are rejected as well. Some aspects of reconstructing signals with AERA in the presence of pulsed RFI are discussed in [217].

6.2.6 Signal reconstruction on event level

Lastly, the radio signals reconstructed for the individual stations are combined to perform calculations on event-level.

- **`RdPlaneFit`**
  Those signal stations that are ensured to be associated with the measured air-shower candidate and whose signal is of good quality are used in a plane wave fit that determines the barycenter of those stations and the arrival direction of the shower.
- **`RdGeoCeLDFFitter`**
  In this module, the GeoCeLDF, a model of the lateral distribution based on the contributions from the two dominating macroscopic emission mechanisms, is fitted to the energy fluence estimates of the signal stations. Details about the LDF model are given in [210]. The radiation energy, E_{rad}, and the geometrical distance to the shower maximum, $d_{X_{max}}$, are determined. If at least five signal stations are available in the fit, also the core position in the horizontal plane is included as a fit parameter. In that case, the LDF can be fit around the radio core, which is assumed to be more accurate than the SD core that acts as an initial guess. The GeoCeLDF was initially developed and validated for zenith angles below 60°.
- **`RdEventPostSelector + RdTraceProcessingForWriteOut` (Sequence)**
  After all reconstruction steps have been completed, the events are prepared for storage in an ADST file. Only those events are selected which meet configurable criteria based on the reconstruction (e.g. number of signal stations, successful geometry reconstruction). In order to reduce the file size, only the part of the electric-field trace of each station from a window around the signal pulse is being stored.
- **`RdREASSimPreparatorNG`**
  From the event reconstruction, input cards for the simulation of the detected shower with CoREAS can be automatically prepared.
- **`EventFileExporterOG + RecDataWriterNG`**
  For those events that passed the complete reconstruction and that were selected to be written out, the raw data from the input file are exported again. This allows to re-reconstruct these events without needing to process again also those events that do not pass the reconstruction. All reconstructed parameters are stored in an ADST file for high-level analyses.

6.2.7 Post-processing of the reconstructed events

There are a few processes associated with the reconstruction and characterization of the events that are executed on the obtained ADST files outside of Offline.

For one, a weather correction is applied to the SD reconstructed energies, since the air density affects the shower development and hence has an impact on the SD shower size estimator [218]. The change in the total shower energy due to the weather correction is within $\pm 5\%$ for the SD events that are used in the analysis in Chap. 8.

On the radio-detection part, events affected by strong atmospheric electric fields from thunderclouds are rejected. A rejection flag is put on the individual events in ADST files, from where it can be read in the standard event selection tool or in independent analyses. Some details on the methodology of the flagging and on the implementation were provided in Sec. 4.4.2.1. For details on how it is used in the energy-scale analysis, refer to Sec. 8.1.3.1.

6.2.8 Summary

In this chapter, we have reviewed efforts made by the Pierre Auger Collaboration and especially its radio detection group to calibrate AERA in many aspects and to reconstruct measured and simulated air-shower events end-to-end with high accuracy. The presented steps are necessary ingredients in the previous energy-scale analyses with AERA, which we discuss in the next chapter, and in our new approach that we present in Chap. 8. In particular, the Galactic calibration and the temperature correction of the AERA amplifier gains are new and essential additions in our analysis. With all of the collected components, we are in a position to perform cosmic-ray air shower measurements with the radio detection technique to an unprecedented level of accuracy and sophistication.

7

Air-shower energy measurements at the Pierre Auger Observatory

The radio detection technique has shown to be competitive in several fundamental studies of cosmic rays and air showers. With a considerable event set collected over the years of operation, AERA has contributed substantially in these aspects (e.g. in studies of the mass composition [219] and the muon content in air showers [220]). Another fundamental study that can be done with measurements from AERA and that is performed in this thesis is the determination of the energy scale of cosmic rays. With the presentations in the previous chapters, we have introduced the necessary ingredients to reconstruct air-shower events from radio signals for such an analysis. The Galactic calibration as the central component for the absolute calibration of measured radio signals was discussed extensively. Our energy-scale analysis is presented in Chap. 8. Before that, we provide a general overview of energy-related observables that are measured by the FD, SD or AERA in this chapter. Further, we review previous studies that were conducted regarding the radio energy scale with AERA and which led up to our analysis.

7.1 Energy related observables of cosmic-ray air showers

The central energy of interest in the observation of cosmic rays via air showers is the energy of the primary particle itself, the *cosmic-ray energy*. However, this energy cannot be probed directly. Instead, certain energies related to parts of the initiated air showers can be measured from which the cosmic-ray energy is reconstructable. The largest fraction of the latter is the *calorimetric energy*, E_{cal}, which encapsulates the total energy deposit by the particles of the shower into the atmosphere. It is the complete energy that is visible to the detectors through the atmospheric calorimeter. In contrast, a comparably small fraction of the total energy is carried away by neutrinos and highly energetic muons that reach the ground before depositing their energy in any way. Since this energy remains hidden to the atmosphere, it is referred to as *invisible energy*. The invisible energy of a shower can be estimated and added to the estimate of the calorimetric energy to obtain the cosmic-ray energy.

The major portion of the calorimetric energy is deposited into the atmosphere by the particles of the electromagnetic part of the shower: electrons, positron and photons. This portion is called *electromagnetic energy*. There is a small fraction of non-electromagnetic but calorimetric energy that is deposited by low-energetic muons and hadrons. A schematic overview of the mentioned energies is given in Fig. 7.1. Only a vanishingly small but defined fraction of the energy deposited by the electromagnetic shower component is release in the form of radio waves. The amount of energy released in this form is called *radiation energy*. In this work, we use this term to specifically refer

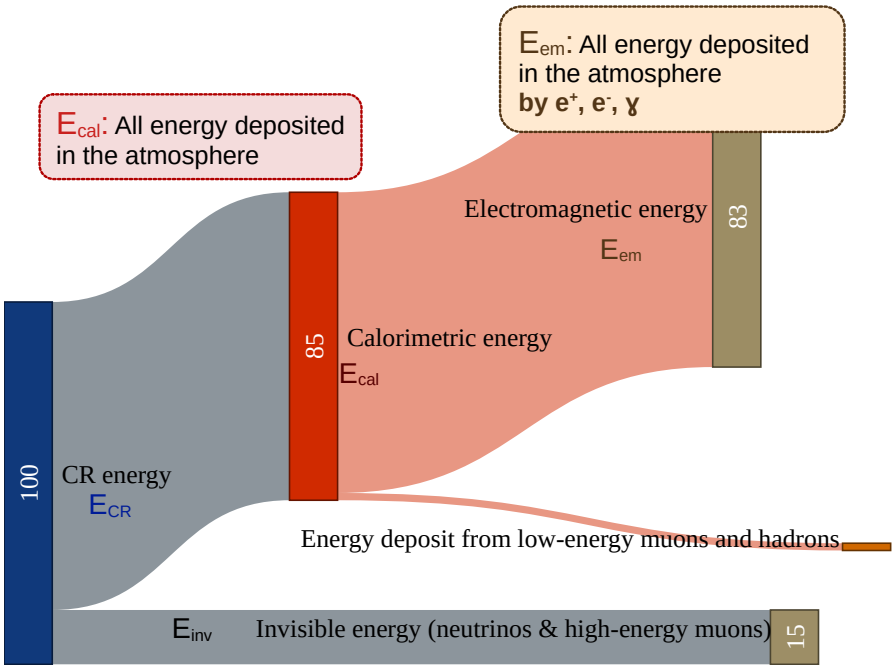

Figure 7.1: Overview of a few fundamental energies of air showers. The fraction numbers are only approximate for the case of a 10^{18} eV air shower and for the estimation of the invisible energy fraction used by the Pierre Auger Collaboration.

to the energy released in the form of radio waves in the frequency band from 30 MHz to 80 MHz. The amount of radiation energy is significantly dependent on a few geometrical and environmental parameters. Therefore, a normalized observable can be defined, called *corrected radiation energy*, the details of which we discuss further in Sec. 7.2.

7.2 Energy measurements at the Pierre Auger Observatory

In Tab. 7.1, energy-related observables are listed that are important for understanding how the cosmic-ray energy scale can be accessed at the Pierre Auger Observatory. In good approximation, the listed observables scale with the cosmic-ray energy either linearly or quadratically which is indicated in the table as well as the information by which detectors the observables can be probed.

The calorimetric energy is directly measured by the FD. From the observation of the fluorescence light, the longitudinal profile of the energy deposit of the shower is recorded. The energy deposit is estimated from the number of fluorescence photons that hit the pixels of the telescopes and induce signals in the PMTs which are recorded as ADC counts. The longitudinal profile of the energy deposit is fitted with a Gaisser-Hillas function, the integral of which yields E_{cal}. Therefore, the FD provides an access to the cosmic-ray energy scale. This energy scale is in fact the designated energy scale of the Pierre Auger Observatory.

There are a few ingredients and steps in the energy estimation with the fluorescence technique that are essential for its energy scale. A central factor is the *fluorescence yield*. This observable denotes the number of fluorescence photons emitted by the air molecules per unit energy deposit from the shower and is taken from a dedicated laboratory

Table 7.1: Overview of a few air-shower energy related observables. The classification into linear and quadratic scaling with cosmic-ray energy only holds in an approximation on intermediary energy scales for some of the observables but it serves to understand how relative uncertainties determined on the level of a specific observable are propagated onto cosmic-ray energy level. Relative uncertainties on observables that scale quadratically with the cosmic-ray energy (e.g. radiation energy in good approximation) need to be divided by two to propagate them onto the cosmic-ray energy scale.

Observable		**Scales with**	**Symbol**	**Measured or**
indirectly: approx. $\sim E_{CR}$	indirectly: approx. $\sim E_{CR}^2$	**(approximately)**		**reconstructed by**
Channel-/Station level				
Voltage		$\sim E_{em}$	V	Radio
Electric field amplitude		$\sim E_{em}$	$\vec{E}$	Radio
	Energy fluence	$\sim E_{em}^2$	f	Radio
Event level				
Shower size		$\sim E_{cal}$	S_{35}	SD
	Radiation energy	$\sim E_{em}^2$	E_{rad}	Radio
	Corrected radiation energy	$\sim E_{em}^2$	S_{rad}	Radio
Electromagnetic energy		$\sim E_{CR}$	E_{em}	Radio
Calorimetric energy		$\sim E_{CR}$	E_{cal}	FD
Invisible energy		$\sim E_{CR}$	E_{inv}	SD + FD
Cosmic-ray energy			E_{CR}	

measurement but it can also be estimated with simulations [55]. Understanding the physics of the fluorescence processes in air is essential for the accuracy of the derived energy estimates from the fluorescence detection technique. We discuss a few more aspects about the determination of the fluorescence yield in Sec. 8.1.8. On the way from the emission by the air molecules to the detection in the FD, the fluorescence light can get attenuated, for example by scattering or absorption of the photons. Dedicated instruments monitor the atmosphere with regard to its molecular and aerosol contents that both contribute differently to the attenuation of fluorescence light [31]. Clouds above the array are being detected to take into account if the view of the FD on parts of a shower was blocked by them. For the absolute calibration of the FD telescopes, various laborious efforts have been made. Currently, the calibration of the FD is set from spectral calibration campaigns with a drum-shaped light source [221]. All of these aspects play a role in setting the FD energy scale and in its systematic uncertainty, which amounts to 14% in total. A concise discussion of the ingredients and critical aspects of the FD energy scale is given in [54].

In order to have measurements from the SD being on the same energy scale as the FD, the former is calibrated with the latter. The SD reconstructs an energy estimator for the detected showers from the measured lateral distribution of the shower particles. This energy estimator is called *shower size* and is specified as S_{450} for the reconstruction with the SD-750 array. The energy estimator S_{450} is the expected signal in the SD at a distance of 450 m from the shower core. This estimator suffers from a zenith dependent bias. At full detection efficiency, the cosmic-ray arrival directions can be expected to be isotropic but at large zenith angles attenuation in the atmosphere reduces the intensity of observed air showers due to the increased amount of traversed air. Therefore, a correction formalism, called *Constant-Intensity-Cut* (CIC) [222], is applied that assigns a corrected

shower size estimator S_{35}, which refers to the lateral signal at 450 m from a shower arriving with an inclination of 35°. In a power-law fit of S_{35} against the cosmic-ray energy reconstructed from the calorimetric measurement of the FD, a clear correlation is found that is close to linearity. The fit is performed with hybrid FD-SD events.

With an estimation of the invisible energy, the cosmic-ray energy can be calculated. At the Pierre Auger Observatory, a data-driven estimation is employed to approximate the invisible energy, for which hybrid showers from the SD-1500 and FD were used [223]. Some details on this estimation are discussed in Sec. 8.1.4.3.

Radio detectors can measure the electromagnetic energy, which in turn scales with the cosmic-ray energy. With an estimate of the difference between the calorimetric and electromagnetic energies and with a model for the invisible energy, the cosmic-ray energy can be reconstructed from radio measurements. In Sec. 6.2, we discussed the various steps in which the radio signals are reconstructed from channel level to event level. The amplitude of the voltage trace measured in an antenna channel is already indirectly dependent on the cosmic-ray energy, approximately in a linear relation. Since the Galactic calibration constants are calculated and applied on voltage level (see Sec. 6.1.4), their relative uncertainties are propagated directly onto the cosmic-ray energy scale. On station-level the *energy fluence* from the radio-emission footprint is reconstructed. This observable stands indirectly in a quadratic relation to the cosmic-ray energy as it is calculated from the squared electric-field trace.

On event-level, the area integral of a fit to the lateral distribution of the reconstructed energy fluences yields the radiation energy. In order to define a universal energy estimator of the cosmic-ray energy based on the radiation energy, a few dependencies need to be corrected for as was derived in [224] and is briefly summarized here. On the one hand, the amount of released radiation energy critically depends on the (usually dominating) geomagnetic emission, specifically on the the incoming direction of the shower with respect to the geomagnetic field, which is given by the geomagnetic angle α between those two directions. To take this dependency out of the energy estimator, one may define a corrected radiation energy as

$$S_{\mathrm{rad}}^{\alpha} = \frac{E_{\mathrm{rad}}}{\sin^2 \alpha}. \tag{7.1}$$

However, there are further relevant dependencies. For one thing, $S_{\mathrm{rad}}^{\alpha}$ scales with the strength of the geomagnetic field, B_{Earth}, at the place of observation. Furthermore, the radiation energy release slightly depends on the air density in the region where the shower develops. Additional second-order dependencies can be neglected in the context of experimental measurements, and so an improved corrected radiation energy as a suitable and universal energy estimator can be defined as

$$S_{\mathrm{rad}} = \frac{E_{\mathrm{rad}}}{a'(\rho_\theta)^2 + (1 - a'(\rho_\theta)^2) \sin^2 \alpha \left(\frac{B_{\mathrm{Earth}}}{0.243\,\mathrm{G}}\right)^{1.8}} \frac{1}{(1 - p_0 + p_0 \exp[p_1(\rho_\theta - \langle\rho\rangle)])^2}. \tag{7.2}$$

Here, a' represents the fractional contribution of the charge-excess emission to the radiation energy of the shower. It has been parameterized as a function of the air density at the location of the shower maximum, ρ_θ. The subscript θ denotes that the air density at X_{max} is determined from a parameterization with the zenith angle, not assuming any

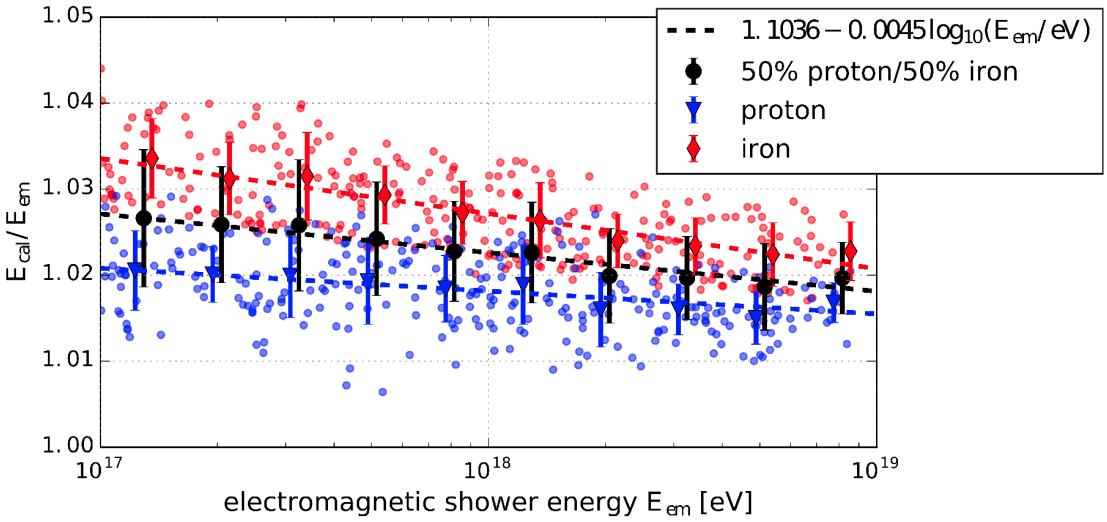

Figure 7.2: Ratio of calorimetric to electromagnetic shower energy as a function of electromagnetic shower energy. The data was obtained from CORSIKA simulations. The small dots in the background show the value of each simulated air showers. The black filled circles denote the mean and spread of the ratio per energy bin. The blue triangles and red diamonds show the same for proton and iron induced air showers respectively. The dashed lines show a fit of a straight line to the full data (black), proton-induced (blue) and iron-induced air showers (red). Figure and caption taken from [200].

knowledge on the depth of shower maximum of the individual shower. The parameter $\langle\rho\rangle$ is an arbitrarily chosen average air density value that the correction is normalized to. The geomagnetic field correction is normalized to a reference field strength of 0.243 G, which was the corresponding value for the location of the Pierre Auger Observatory at the time of the study. For details, refer to [224].

In a power-law fit of the corrected radiation energy to the electromagnetic energy by the function

$$S_{rad} = A \times 10^7 \text{eV} (E_{em}/10^{18}\text{eV})^B, \tag{7.3}$$

the parameters A and B as well as p_0 and p_1 were determined using simulated air showers, resulting in $A = 1.629 \pm 0.003$ and $B = 1.980 \pm 0.001$ [224]. The slight deviation of the B parameter from quadratic scaling is due to the zenith-angle parameterization of the air density at X_{max}. When using the true air densities at shower maximum from the atmospheric profiles of the simulations, the B parameter comes out very close to 2. Eq. 7.3 allows to estimate the electromagnetic shower energy from the radio measurements. The ratio between the calorimetric and electromagnetic energies can be estimated from simulations as is shown in Fig. 7.2. It has a slight decreasing trend towards higher energies and lies between about 2 and 3% depending on the primary particle for the relevant energy range for AERA [200]. If desired, this difference can be added to the electromagnetic energy to obtain the calorimetric energy and subsequently, by adding the invisible energy, to estimate the cosmic-ray energy.

7.3 Previous studies on the energy scale with AERA

The FD energy scale is currently the designated energy scale of the Pierre Auger Observatory. With the alternative access to the cosmic-ray energy scale through the radio detection of air showers, several studies have already been performed using measurements from AERA and simulations aiming at comparing the energy scales from FD and radio. In Chap. 8, we present a new approach in this regard. Before that, we reflect on the previous studies that paved the way in longstanding efforts and we explain how the findings in those studies motivated our new approach.

In an initial study with data from the first two years of AERA operation, $S_{\mathrm{rad}}^{\alpha}$ was presented as a cosmic-ray energy estimator [225, 226]. The study used hybrid events measured by the SD-750 and AERA to investigate the correlation between $S_{\mathrm{rad}}^{\alpha}$ and cosmic-ray energy. With a power-law fit like in Eq. 7.3 but using the cosmic-ray energy instead of electromagnetic energy, an estimate for the absolute radiation energy released in air showers was obtained. At a cosmic-ray energy of 10^{18} eV, if the arrival direction is perpendicular to the geomagnetic field at the site of the Pierre Auger Observatory, the released radiation energy in the frequency band from 30 MHz to 80 MHz amounts to 1.58×10^{7} eV. This estimate was published as a calibrator for other cosmic-ray radio arrays against the FD energy scale from the Pierre Auger Observatory.

In a simulation study, the energy estimator was investigated in greater detail [224] and improved to S_{rad} from Eq. 7.2. The study also yielded a value for the expectation of the radiation energy released in air showers as reviewed in Sec. 7.2 from a fit of Eq. 7.3. This value was derived on the basis of first principles from classical electrodynamics implemented in the radio emission calculation in the simulations, which was done with CoREAS. At LOFAR, the improved corrected radiation energy was used to compare the energy scales of the LOFAR particle detector array, called LORA, and the Pierre Auger Observatory [227].

The improved energy estimator S_{rad} was subsequently also reconstructed from the measured showers detected in hybrid mode by the SD and AERA. This estimator was correlated to the calorimetric energy reconstructed with the SD data and a power-law fit analogous to Eq. 7.3 was performed that allowed to read off the measured corrected radiation energy at a reference calorimetric energy on the FD energy scale. By correcting for the difference between calorimetric energy and electromagnetic energy, the measurement was brought face to face with the expectation obtained in the simulation study. Comparing these two values completed the proposed recipe for comparing the energy scales from FD and radio in [200]. In this recipe, the radio energy scale was compiled to be set by the first principles from classical electrodynamics from which the radio emission of simulated air showers is calculated. The underlying classical electrodynamics are an eminently solid theory of physics. In the implementation for the prediction of air-shower radio emission, the exact formalism and the description of the particle cascade and its interactions are crucial for the accuracy that can be attributed to what can be called the *radio emission yield* – in analogy to the *fluorescence yield*. In our analysis, the prediction of radio emission from simulations keeps the same important role in the radio energy scale. We discuss this aspect in the next chapter in more detail.

Some ingredients of the previously conducted analysis were improved further on. It was found that the uncertainties on energy-fluence estimations were underestimated

which propagates into the calibration fit. Therefore, bootstrapping was used to test the range of best-fit values of the power-law parameters upon shuffling the dataset. The bootstrapping method resulted in asymmetric uncertainty estimates.

The statistics of the measured event set were still comparably low at that time. In a subsequent study, a richer dataset between 2013 and 2018 was used to perform the correlation fit [228]. In addition, the influence of specific steps in the radio reconstruction on the fit result was tested. Choosing a non-standard station-signal reconstruction method or RFI filter for signal cleaning can yield significantly different results.

Another study performed the analysis entirely in simulations but matching the details of the reconstruction to the data analysis from [228] to test the procedure [229]. In using an equivalent reconstruction pipeline, the results turned out in general to be in agreement between the studies on data and simulations.

Further investigations on the impact of the individual steps in the radio reconstruction pipeline found an effective loss of signal [230, 231]. Therefore we continued studying the behavior of the power-law fit under changes to the noise reduction and signal estimation in the radio reconstruction [232] (see Sec. 8.1.7.3), suggesting a relation to the found signal loss. Continuation of the previous analyses based on calibration fits with the goal of comparing the energy scales from the FD and radio data requires a detailed understanding of potential signal losses and reconstruction biases in the individual reconstruction steps. This conclusion motivates a new approach for the energy scale comparison that is presented in Chap. 8. Furthermore, the previous studies on the energy scale with AERA have not used the Galactic calibration. Instead, the absolute scale was set from the drone-calibration campaign (see Sec. 6.1.2), which provided a less accurate reference signal than the Galaxy does. In our analysis, we will improve on the absolute calibration of AERA by relying on the Galactic calibration.

7.4 Summary

We reviewed a selection of observables that are related to energy measurements of air showers. Specifically, we discussed the developments that have been made about defining a cosmic-ray energy estimator from radio measurements and the difficulties that come with it. These developments led to studies of the radio energy scale with AERA in comparison to the FD energy scale provided through hybrid measurements with the SD-750 array. In following up these studies, we have found incentives to take a new approach that we present in the next chapter. The previous studies discussed here paved the way to conduct and conclude our analysis.

8

Determining the cosmic-ray energy scale with AERA

Parts of this chapter have been published in:

Towards a Cosmic-Ray Energy Scale with the Auger Engineering Radio Array
M. Büsken for the Pierre Auger Collaboration
PoS(ARENA2024)035 (2024)

Analyses on the radio energy scale with AERA have been in development for a long time as reviewed in Sec. 7.3. With additional time of continued AERA measurement having passed and with the calibration of the detector and the radio reconstruction now being in a well-advanced state, we have the necessary ingredients to conclude this analysis. In Chap. 4, we presented new electric field mills for the rejection of thunderstorm-affected events. While these instruments were already in-place for AERA, the new devices secure the ability to also perform the corresponding event quality selection for an energy-scale analyses with the RD in the future. In Chap. 5, we estimated the accuracy to be expected from the Galactic calibration in general. We present the state of the detector calibration of AERA and the event reconstruction from its signals in Chap. 6 with an introduction to the necessary ingredients required for the analysis in this chapter. With regard to previous analysis on the energy scale, we discussed the problem of potential signal loss in the reconstruction pipeline in the last chapter. To eliminate this factor from the result, we take a shift in the approach to the analysis that we present and execute in Sec. 8.1. We discuss the results and provide an outlook in Sec. 8.2. In Sec. 8.3, we give a short summary.

8.1 Comparison of the energy scales from FD and AERA

In a new approach, we perform a cross-check between the cosmic-ray energy scales set by the fluorescence and radio techniques. For this, we use measurements from the FD-calibrated SD-750 and from AERA. In the following, we use the acronym SD to refer specifically to the SD-750 array or to overarching SD-related concepts. Where applicable, we explicitly refer to the sparse SD array as the SD-1500

8.1.1 Analysis with measured data and end-to-end event simulations

Our analysis is based on a direct comparison of air showers measured at the Pierre Auger Observatory and matched end-to-end simulations, performed on an event-by-event level. We use data of air showers that were detected in hybrid mode by the SD-750 and AERA and we create individual simulations, which are configured to resemble the recorded events as realistically as possible. The result of the analysis is a metric that states how well the energy scales from the FD and AERA agree with each other. The radio energy scale is thereby fundamentally defined by a requisitely good absolute calibration of AERA and set by the radio emission yield predicted in the simulations resting on first principles of classical electrodynamics. We discuss these aspects in depth qualitatively and quantitatively in Sec. 8.1.8.

The core logic of the analysis approach is illustrated in Fig. 8.1 with measured events on the left and simulated events on the right. Air showers recorded in hybrid mode by the SD and AERA are reconstructed separately using the measured signals from either of the two detectors. The SD reconstruction is performed with the particle traces recorded by the WCD and provides an estimate of the shower size S_{35} that is translated to the total energy of the shower, E_{SD}, via the CIC correction and FD-SD energy calibration. The energy E_{SD} is the cosmic-ray energy E_{CR} as reconstructed from the SD measurement. On the other hand, the radio reconstruction is performed on the radio signals recorded by AERA and yields an estimate for the radiation energy, E_{rad}^{data}, which is bound to the radio energy scale. This radio reconstruction is partially dependent on the SD reconstruction, as explained further in Sec. 8.1.2.

For each measured air-shower event, we create two simulations using the SD-reconstructed shower energy to determine a cosmic-ray energy as input to the simulations. In order to be able to perform a meaningful comparison between the radio signals of the simulations and the measured events, we match the simulations on the level of calorimetric energy instead of cosmic-ray energy. Details about this process are described further in Sec. 8.1.4.

The two simulations per event only differ by the choice of the primary cosmic-ray particle, proton or iron, and by a primary-dependent adjustment of the input cosmic-ray energy. Since we do not have information about the primary particle type of the measured showers on an event-by-event level, by simulating both a proton and an iron shower we cover the expected range of mass composition. Later in the analysis, we can use the separate proton- and iron-simulations to test for a systematic effect stemming from missing knowledge about the exact mass composition.

As is done for the input energy, the other settings of the simulations are also configured to match the simulated showers as closely as possible to the measured showers (for details, see Sec. 8.1.4). The simulated shower signals are processed through the SD and AERA detector simulations. The simulated radio traces are then reconstructed in the same way as done with the measured radio traces. This way, any signal loss or reconstruction bias that may be introduced during one or multiple steps of the radio reconstruction pipeline (see Sec. 6.2), can be expected to cancel out. In Sec. 8.1.7.3, we test whether this premise for the analysis holds.

Like in the reconstruction of measured events, the reconstruction of the simulated radio signals yields an estimate of the radiation energy E_{rad}^{sim}. This estimate is bound to

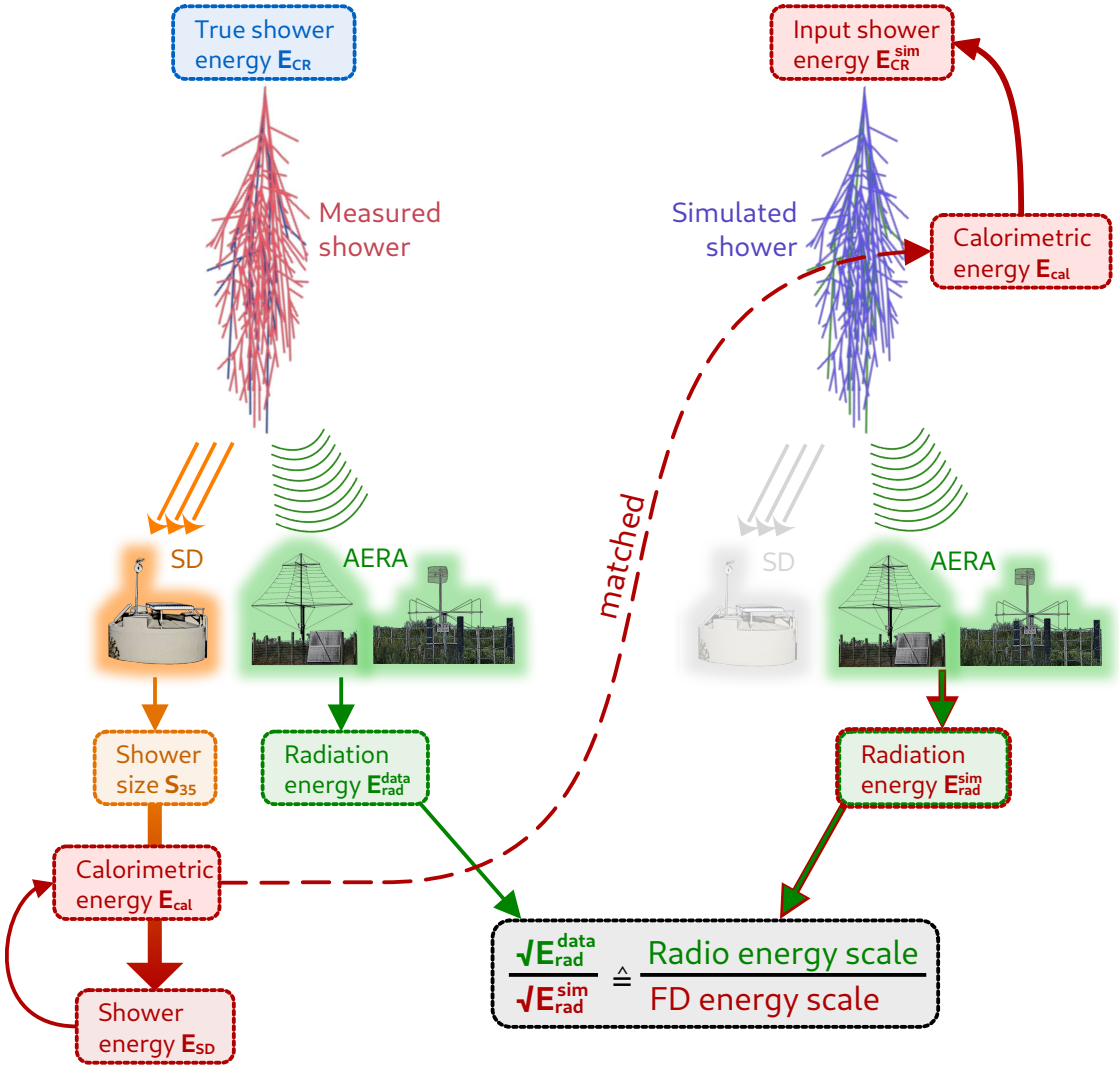

Figure 8.1: Logic for event-by-event comparison of measured and simulated air showers for determining the agreement between the FD and radio energy scales. Observables depicted in red are on the FD energy scale. The orange and green colors represent SD and radio measurements, respectively.

the FD energy scale since the simulation input energy is defined by the SD measurement, onto which the FD energy scale was imposed through the FD-SD energy calibration.

Having reconstructed the two estimates E_{rad}^{data} and E_{rad}^{sim} which are bound to the radio and FD energy scales, respectively, they provide a direct way to compare the two energy scales. As explained in Sec. 7.2, the radiation energy scales to good approximation quadratically with the electromagnetic energy, which in turn scales with the cosmic-ray energy. Therefore, in the comparison of the cosmic-ray energy scales from FD and radio in Sec. 8.1.6 we use metrics that consist of the square roots of radiation energies.

In our analysis, we stay on the level of radiation energies and do not need to correct the radio energy estimator for effects like was done before, as we reviewed in Sec. 7.3. Compared to previous studies, we also do not rely on a power-law fit that brings a few difficulties with it, e.g. defining and well understanding a likelihood for the fit or

systematics related to the "anchor point", by which the normalization parameter of the power law is defined. Therefore, we save ourselves from a few pitfalls by staying on the level of radiation energies.

8.1.2 Reconstruction of measured and simulated events

All modules of the radio reconstruction in Offline were presented in Sec. 6.2 and steps that are particularly important for the reconstruction of calibrated air-shower signals were covered in Sec. 6.1. Here, we discuss the sequence in which we perform the reconstruction to prepare the dataset for the energy scale comparison and we explain the necessary differences between the reconstruction of measured and simulated events for an appropriate matching of the latter two.

8.1.2.1 Reconstruction of measured events

In collecting the air-shower event data set for this analysis, we start from a reference set of SD-reconstructed data. This event data set was produced from SD-only raw data with a full SD reconstruction[1] and the derived shower energies are calibrated with parameters from a specific SD-FD calibration, which defines the FD energy scale that is referenced in this analysis and which the radio energy scale will refer to[2]. In Fig. 8.2, the events of the calibration dataset are shown with the shower size estimator from the SD reconstruction, S_{35}, plotted against the shower energy from the FD reconstruction. The fitted power law and resulting fit parameters are given in the figure.

The raw air-shower data from AERA are already merged with the corresponding raw data from SD since we use the data stream from AERA that relies on external triggers from the SD. We reconstruct these raw data in two stages in Offline. In both stages, the reconstruction chain is compiled from the modules described in Sec. 6.2 and differs only in a few details.

The main idea of the first stage is to perform a pre-selection of the data. In carrying out the analysis, we tested several different changes to the radio reconstruction. However, since the raw data volume for the relevant time period amounts to roughly 36 TB, performing a new complete reconstruction for each of these changes on the entire raw data would be unreasonably time consuming. Therefore, we perform a base reconstruction, the output of which constitutes selected raw data of those events that pass this base reconstruction with a total data volume of only 84 GB. In this first stage, we process the raw data with a precedent standard SD reconstruction and a subsequent radio reconstruction. The precedent SD reconstruction is needed to provide some reference information and initial parameter estimates for the radio reconstruction. The exact configuration of the base reconstruction is given in App. C.1. A substantial difference to the final radio reconstruction for the analysis is the usage of the `RdChannelBandstopFilter` module. It removes RFI lines from the radio signals in the frequency domain. This noise removal approach is known to increase the number of reconstructable events but also cut away significant parts of the air-shower signals. Hence, we do not use it in

[1] Specifically, we use the `SDInfill` production for Auger Phase I reconstructed with the `icrc2025-test2` tag of Offline.

[2] The SD-FD calibration was done using the *ICRC 2023* FD event reconstruction.

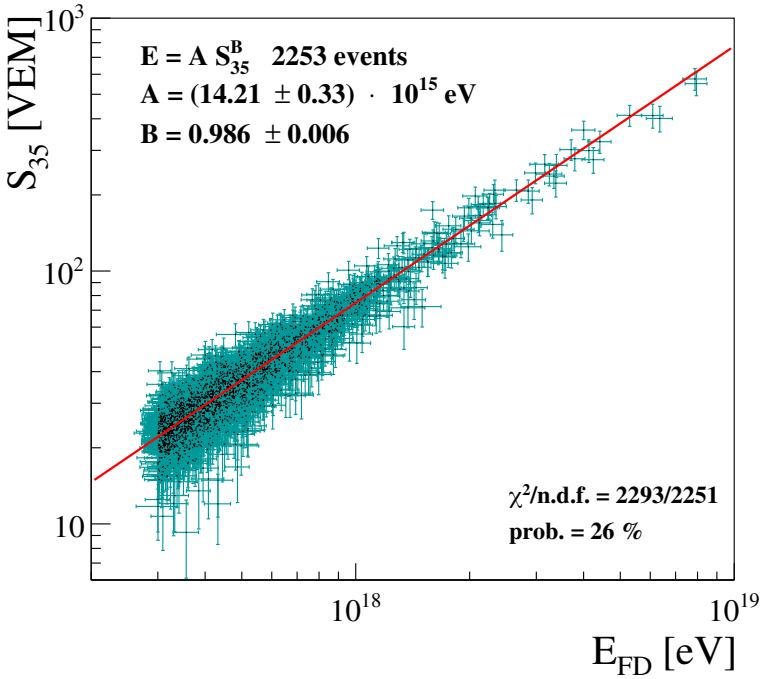

Figure 8.2: Energy calibration of the shower size estimator of the SD-750 S_{35} correlated with the total shower energy from the FD. Figure from [233].

the final reconstruction of the second stage but we use it in this first stage to have a fast and simple module to clean the radio traces from RFI such that more air-shower events are likely to be pre-selected for the second stage reconstruction. In the meantime, there has been development on a comparably fast but cleaner way of removing RFI lines based on discrete-time Fourier transforms, which may become a standard solution in the future [234].

In the second stage, the reference SD-dataset and the pre-selected AERA events are combined. No precedent SD reconstruction is performed in this stage but at the start of the radio reconstruction, the `RdEventInitializer` module is configured to read in external information on the geometry, timing and energy of the official SD reconstruction of the air shower. There, the required information is taken from the reference SD-dataset and passed on to the module. Afterwards, a radio reconstruction is performed, the full configuration of which is given in App. C.2 for the final reconstruction used in the main results of the analysis. In particular, the radiation energy obtained from the GeoCeLDF fit in this reconstruction is the key ingredient in the analysis. As an example, we show a measured air-shower event from the final dataset with the fitted GeoCeLDF in Fig. 8.3. For tests and studies of systematics, the configuration was slightly modified and modules were added or removed. A few radio reconstruction modules require external input, e.g. the `RdAntennaChannelToStationConverter` needs a direction for the incident radio waves to determine the directional gain of the antenna. By using information from the reference SD dataset in these cases, the radio reconstruction is dependent on the SD reconstruction. At the end of the radio reconstruction of each event, input cards for simulations with CORSIKA and CoREAS are automatically generated based on the

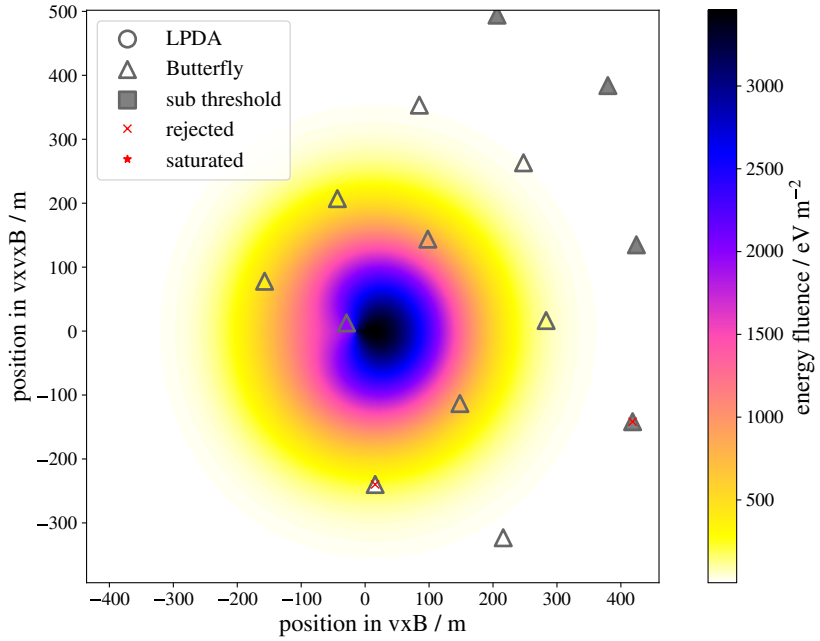

Figure 8.3: AERA measurement of the event with the ID `190884209200`, measured on 2019/03/29. The arrival direction of the air shower was reconstructed with a zenith angle of 45° and with an azimuth angle of 17°. The reconstruction of the air shower from the particle measurements with the SD yielded an estimate of the cosmic-ray energy of 4.7×10^{18} eV. The diagram is arranged in shower coordinates. The colored markers represent the reconstructed energy fluence in each station. The two-dimensional footprint is generated with the `Python` implementation of the GeoCeLDF [235] using the fitted parameters of the LDF obtained from the implementation of the GeoCeLDF in Offline. The colors of the station markers blending in with the fitted footprint implies a good fit of the LDF to the measurements.

reconstructed parameters. These input cards are modified regarding a few settings explained in Sec. 8.1.4 to be used for the production of the event simulation data set in this analysis.

8.1.2.2 Reconstruction of simulated events

The radio reconstruction of simulated air showers is fundamentally the same as for measured showers (the full details are provided in App. C.3). However, at first the full SD detector response is folded into the simulated particle signals, including not only the responses of the detector components but also a full SD trigger simulation. After a subsequent standard SD simulation reconstruction, the radio part is initialized and the responses of the AERA components are folded into the simulated radio signals. The AERA detectors simulation yields ADC traces modeled as if they were recorded by the real detector. Before any treatment of the simulated radio traces is performed, measured noise is added to the signals in order to create a realistic situation for the reconstruction. Thereafter, the radio simulation reconstruction is performed.

8.1.2.3 Differences in the reconstruction of measured and simulated events

Besides technical differences in the reconstruction pipelines for measured and simulated radio signals that were presented in Sec. 6.2, two steps conceptually only apply in the reconstruction of measured events.

- **Temperature correction:** The known and lab-measured temperature dependencies of the different filters employed in AERA are corrected for. In practice, the channel traces are multiplied with a correction factor calculated using the known dependencies and temperature measurements from the time of each event to rescale onto the reference temperature of 20 °C. This correction is only done in the reconstruction of measured events but not in the reconstruction of simulated events since in the AERA detector simulation of the latter, responses of the signal filters are used that were determined in the lab under conditions close to the reference temperature.

- **Galactic calibration:** Like the temperature correction, the Galactic calibration is only applied in the reconstruction of measured events. It absorbs any absolute scale offsets in the measurement that might have been introduced through the environment or by components in the detector and were not taken control of in any of the other calibration and reconstruction steps. The Galactic calibration establishes an equivalence to the controlled conditions in the simulations. The fact that the calibration constants derived in the Galactic calibration for AERA are on average compatible with 1 within uncertainties indicates a collectively good laboratory calibration of the detector components [186].

With these two steps – especially with the Galactic calibration – absolute scale differences between measured and simulated signals are conceptually accounted for. The reconstruction of measured and simulated signals is equalized as far as possible.

8.1.3 Event selection

In this analysis, we use hybrid SD-AERA data from January 1st of 2014 until December 31st of 2020 that we reconstruct with the procedure described in Sec. 8.1.2. The date when the AERA data taking was transferred from a test phase into a central data acquisition that allowed for an automatic merging with the SD data stream was in April 2013. However, the AERA stations and data acquisition were still in an unstable state for some time. Therefore, we decided to only use data starting from 2014. The end of the dataset is the point in time until which we are currently able to make a statement about the long-term stability of AERA, where at the moment we do not observe relevant aging. For the years 2021 onward, the methodology of the Galactic calibration – as it is implemented at the time of this analysis – is not conclusive regarding the long-term stability of AERA. The data of those years exhibit an unsteady behavior over time that is most likely due to incomplete data coverage resulting from degrading battery conditions which are a natural consequence from longstanding operation in combination with reduced maintenance resources during these times because of the labor-intensive deployment of the new RD going on in parallel.

In order to extract a set of high-quality events for the analysis from the given time period, we apply cuts to the outcome of the data reconstruction. The cuts are applied in two stages: First, a selection of base quality cuts are applied to both the SD- and AERA-part of the hybrid events. For all events of this pre-selection, simulations are created as described in Sec. 8.1.4. Afterwards, additional cuts are applied on the measured radio events to fine-tune the quality of the dataset in a trade-off with statistical power. Lastly, all radio-related quality cuts are also applied to the reconstructed data set of the simulated events.

Some of the cuts were introduced only during the development of this work after we had already ran through the complete analysis for the first time. Before making all of these steps, we implemented a blinding procedure that allowed us to develop the analysis without any risk of making biased decision – for example, to obtain a more favorable end result. Therefore, the presented cuts in the event selection were chosen solely based on the objective improvement they bring to the analysis. We explain the blinding procedure in more detail in Sec. 8.1.6.1.

8.1.3.1 Pre-selection for the simulation set

For the preparation of the simulations, we pre-select events which are already of high-quality in order not to waste computing resources in simulating events that will not be used in the analysis anyway. However, we choose to apply only a set of basic (but strict) cuts and skip some more refined cuts. This procedure gives us the option to test, polish and possibly lift those more refined cuts if needed, even after creation of the simulations.

In the following list, the cuts for the pre-selection are explained. A rundown of these cuts and how many events remain after each step is given in Tab. 8.1.

- **SD cuts:** For the compilation of the pre-selected events, the reference SD dataset is filtered with standard SD cuts[1] before merging with the AERA data. These SD cuts consist of:
  - **`!lightning`:** Lightning strikes can induce spurious signals in the PMT cables of the SD that make it into the air-shower data stream. The affected events are vetoed.
  - **`minRecLevel 3`:** There are different levels up to which the SD reconstruction could be successfully performed. By choosing level 3, we require a reconstructed shower axis and a completed LDF fit.
  - **`maxZenithSD 55.`:** With restricting to events arriving from zenith angle directions below 55°, full efficiency of the SD above 3×10^{17} eV is ensured.
  - **`T4Trigger 2`:** Each event needs to have produced a T4 trigger in the SD.
  - **`T5Trigger 2`:** Each event needs to have produced a 6T5 trigger in the SD, meaning that all stations in the hexagon around the hottest SD station – i.e. the station with the strongest signal – were triggered.

[1] Specifically, we use the official SD cuts for the ICRC2023, only except for four events that are manually removed in the official cuts. We do not manually reject those events but we checked that they did not enter our dataset anyway.

  - **`T5TriggerUB 2`:** The 6T5 trigger is extended to only accept SD stations which are still equipped with the Phase I electronics board UB at the time of the event. Thereby, stations with the Phase II electronics board UUB are implicitly rejected. At the time of this analysis, the SD reconstruction with UUB-equipped stations (or a mixture of UB- and UUB-equipped stations) was not yet validated. However, the first UUB in the SD-750 array was deployed in November 2021, which is after the end point of our dataset.
  - **`minLgEnergySD 17.0`:** To save computing time in the subsequent analysis pipeline steps, an intermediate energy cut at 1×10^{17} eV is already used here. Later, a further at 3×10^{17} eV is applied for full detection efficiency of the SD.
  - **`badPeriodsRejectionFromFile`:** Bad periods of the SD were tracked and stored in a file that is queried here to reject events that fall in any of those periods.
  - **`timeInterval {params: 130101 210101}`:** The dataset is limited in time to the period that was explained above.

- **Core confinement:** The SD cores are required to fall inside the sub-array of AERA that is used in this analysis. Specifically, from the shower core as the origin, there must be at least one AERA station in each of the four quadrants North-East, North-West, South-East and South-West. This way, outlying events are filtered, which only induce signals in AERA stations that are on the tail of the radio-emission footprint. Through the confinement cut, events with a better-constrained LDF fit are generally favored. As phase III of AERA was deployed in March 2015, which is within the time interval of the used data period, the confinement cut for events before that deployment is configured to require the shower cores to be within the externally triggered sub-array of AERA phase I+II.

- **$E_{SD} > 3\times10^{17}$ eV:** In the script that runs the energy scale comparison, the final cuts are applied. The first of these cuts is the cut on the SD energy at 3×10^{17} eV ensuring full SD efficiency. At this point, the hybrid dataset contains 3245 events and no cuts on the radio part are made yet.

- **Thunderstorm veto:** Strong atmospheric electric fields in the presence of thunderstorms or electrified clouds can alter the radio emission from air showers. Therefore, we monitor the electric field at AERA with two EFMs and build a thunderstorm veto as explained in Sec. 4.4.2.1. The impact of this veto is shown in the comparison between the left and middle plots of Fig. 8.4, in which all reconstructed radiation energies in the dataset with the previous cuts are plotted against the corresponding SD energies. In the middle plot, the thunderstorm veto is applied, in the left plot it is not. While most points lie on a correlation line, the left plot shows several outlier events with a significantly increased radiation energy by up to multiple orders of magnitude. With the thunderstorm veto applied, most of the outliers are removed. The few remaining outliers in the region of enhanced radiation energy are otherwise of insufficient quality and get removed by the subsequent cuts.

  With respect to the number of events after the SD related cuts, the thunderstorm veto removes 7.1% of events from the dataset. This fraction is slightly larger than the estimated percentage of thunderstorm conditions above AERA. This percentage

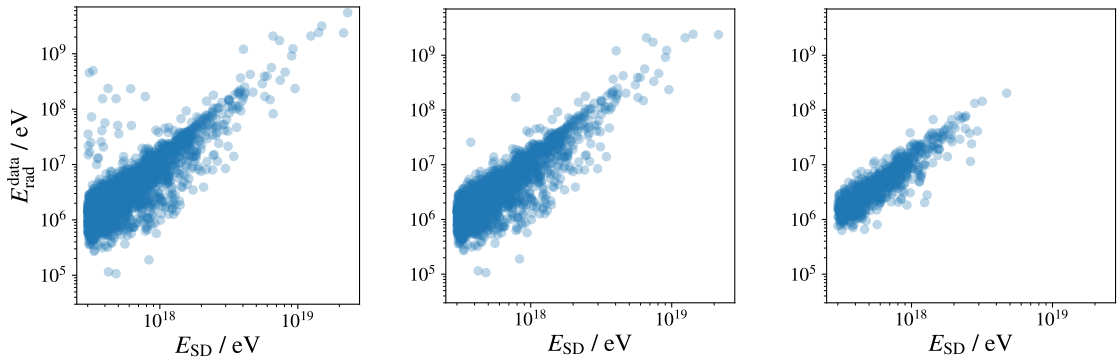

(a) SD cuts (incl. energy) and core confinement

(b) Cuts from (a) and thunderstorm veto

(c) Full quality cuts as described in Tab. 8.2

Figure 8.4: Plots of the reconstructed radiation energy from the measured event data set for different levels of the event selection.

was studied with the same thresholds for the identification of thunderstorms as used in this work and yielded values between 3.3% and 5.9% [85, 80]. However, those values are calculated using data from each of the two EFMs individually. The fraction of removed events being larger than those thunderstorm fraction estimates is likely due to two situations: first, there are periods where only one of the EFMs reported thunderstorm conditions so that the combination of the thunderstorm periods from the two individual EFMs will be larger than either of the periods. Second, there may be periods when neither of the two EFMs were operating. Events taken during these periods are rejected as well, which effectively increases the removal fraction of the thunderstorm veto.

- **Base radio cuts:** The base radio cuts ensure a fundamental level of event quality:
  - $\mathbf{N_{stations,signal} \geqslant 5}$**:** We require for each event that at least five non-rejected AERA stations recorded a signal[1]. This number of signal stations is a prerequisite for a complete GeoCeLDF fit including a fit of the shower core from the radio data. The signal-station cut is the most rigorous one on the radio side. It removes 63.6% of the previous events.
  - $\mathbf{E_{rad}}$ **reconstructed:** The energy scale comparison is done based on radiation energies. Therefore, requiring a successful reconstruction of the radiation energy in the GeoCeLDF fit is a logical requirement.
  - $\boldsymbol{\sigma_{E_{rad}}}$ **reconstructed:** Even if a radiation energy is reconstructed, in some cases no uncertainty can be assigned to it if the covariance matrix of the fit parameters is not fully determined by the likelihood minimizer. We filter those events.
  - **Radio core reconstructed:** Because we require at least five signal stations, the shower core is fit as a free parameter in the GeoCeLDF. In principle, the

[1] A station is considered a signal station if its signal-to-noise ratio $\mathrm{SNR} = (A_{\mathrm{signal}}/\mathrm{RMS}_{\mathrm{noise}})^2$ fulfills $\mathrm{SNR} > 10$, where A_{signal} is the amplitude of the Hilbert envelope of the electric-field time trace and $\mathrm{RMS}_{\mathrm{noise}}$ is the root mean square of the trace in a noise window far away from the signal.

minimization procedure can still fail. However, in our dataset, all events remain after this cut.

After the base radio cuts, 902 events remain that we simulate as described in Sec. 8.1.4.

Table 8.1: Event cuts for the pre-selection of the hybrid dataset in the preparation of matched simulations. The survival fractions always relate to the previous selection step.

Cut or requirement	N_{events}	Survival fraction
SD cuts + cores confined in AERA		
$E_{SD} > 3{\times}10^{17}$ eV	3245	-
Thunderstorm veto	3015	92.9 %
Base radio cuts		
$N_{stations,signal} \geqslant 5$	1096	36.4 %
E_{rad} reconstructed	1062	96.9 %
$\sigma_{E_{rad}}$ reconstructed	902	84.9 %
Radio core reconstructed	902	100.0 %

8.1.3.2 Quality selection for the analysis

With the simulations prepared for the event data set that includes the base radio cuts, we refine the quality level with a few more cuts on the radio reconstruction. These cuts were introduced after we first executed the analysis with the event set after base radio cuts. We found outliers in checks for systematics (see Sec. 8.1.7) that exhibited insufficient quality in the conditions of the measurement or in the reconstruction. With the following cuts, these outliers were removed. However, we note that the fraction of filtered events by these cuts is below 7% and, most important, the cuts only reduce the uncertainty of the final result of the comparison but not its central value in a significant way.

- **No saturated station within** 500 m**:** Radio signals from showers can saturate the antenna channels of a station. In particular, saturation appears more often in the case of small shower inclinations and affects stations close to the shower axis. Saturated stations are identified and taken out of the reconstruction. Therefore, they cannot directly bias any result. However, if one or more of the stations closest to the shower axis are rejected in the reconstruction because of saturation, only stations on the tail of the footprint may remain resulting in a badly constrained GeoCeLDF fit. Thus, we reject all events with one or more saturated stations within 500 m of the shower axis.

- $\boldsymbol{\chi^2/N_{df} < 10}$**:** As a metric for the goodness of the GeoCeLDF fit we use the reduced χ^2, i.e. the χ^2 divided by the number of degrees of freedom in the fit N_{df}, to identify events with a bad quality fit. We only apply a weak cut at a value of 10, just to remove exceptional outliers this way. The distribution of the reduced χ^2 values in the event dataset before the cut is shown in Fig. 8.5.

- $\boldsymbol{\alpha > 20°}$**:** For most air showers, the radio emission is dominated by the geomagnetic mechanism. However, this is not true for small geomagnetic angles α between the shower axis and the geomagnetic field. At this point in the event selection, only a few events with small geomagnetic angles remain. However, these events

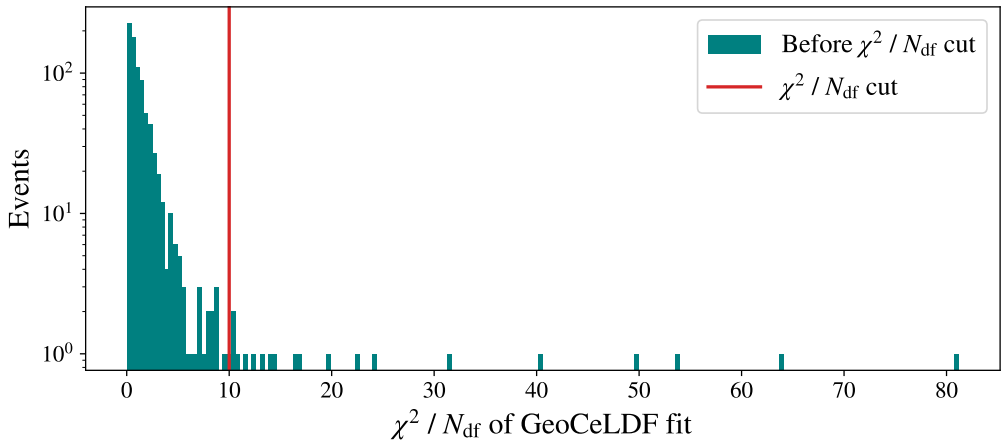

Figure 8.5: Values of the reduced χ^2 of the GeoCeLDF fit for the measured events.

tendentially appear as outliers in the energy scale comparison, likely because the low fraction of the geomagnetic emission tends to result in a lower quality reconstruction. Therefore, we remove them by requiring a geomagnetic angle of at least 20°.

We apply all radio-related cuts as well to the reconstructed event simulations. In Tab. 8.2, the cuts and how each of them act on the event data sets are summarized. For the 844 high-quality data events, the generated corresponding simulation can be reconstructed in around 94% (97%) of the cases with proton (iron) as the primary. The missing 6% (3%) are simulations, for which the number of AERA stations with sufficiently large signal fell below the critical number of three that are necessary for a radio reconstruction – concretely, for a plane wave fit.

When we apply the radio cuts to the reconstructed simulations, the requirement for at least five AERA signal stations is again the most rigorous cut. It removes around 30% (16%) of the proton (iron) simulations. The striking difference between proton and iron as primary is likely a consequence of an assumed but unverified detection efficiency bias of AERA. On average, proton showers will be deeper, i.e. have a larger value of X_{max} than iron showers. Deeper showers have a smaller signal footprint at ground resulting in a smaller number of signal stations on average. Therefore, AERA is expected to have an efficiency bias towards heavier primaries with the cut at five signal stations. In Sec. 8.1.8, we estimate a systematic uncertainty that covers such a potential bias.

All subsequent cuts combined remove not more than 3% of the reconstructed simulations, as expected. These cuts mostly probe the quality of the radio reconstruction, which was already ensured to be high for these events from the same cuts on the data reconstruction.

Ultimately, we obtain a set of 537 (674) high quality hybrid events from SD-AERA with matching proton (iron) simulations that we use for the comparison of the cosmic-ray energy scales from FD and radio in Sec. 8.1.6.

Table 8.2: Quality selection cuts for the event set for the energy scale comparison. The survival fractions always relate to the previous selection step. Simulations were already created for all 902 events after the base cuts had been applied to the measured events. We applied the three additonal radio cuts on data only afterwards. Thus, they also remove some events, for which a simulation had already been created. At the stage, when we list the event numbers with available corresponding simulations, there are a few events for which simulations were created but could not be reconstructed successfully, which affected more proton simulations than iron simulations. We explain this further in the text.

Cut or requirement	N_{events}	Survival fraction
SD cuts & base cuts (see Tab. 8.1)	902	
Additional radio cuts on data		
No saturated stations within 500 m	873	96.8 %
$\chi^2/N_{df} < 10$	854	97.8 %
$\alpha > 20°$	844	98.8 %
Simulation available p / Fe	792 / 817	93.8 % / 96.8 %
Radio cuts on simulations		
$N_{stations,signal} \geqslant 5$	549 / 684	69.3 % / 83.7 %
E_{rad} reconstructed	542 / 678	98.7 % / 99.1 %
$\sigma_{E_{rad}}$ reconstructed	538 / 677	99.3 % / 99.9 %
Radio core reconstructed	538 / 676	100.0 % / 99.9 %
No saturated stations within 500 m	538 / 676	100.0 % / 100.0 %
$\chi^2/N_{df} < 10$	537 / 676	99.8 % / 100.0 %
$\alpha > 20°$	537 / 674	100.0 % / 99.7 %

8.1.4 Event simulations

For each of the events in the selected dataset with the base radio cuts, a matched simulation of each a proton and and an iron nucleus as primary cosmic ray is created. Realistic simulations that are well matched to the measured events are an integral part of this analysis. Therefore, we carefully prepare the simulations in all aspects. By using CORSIKA 7.7550 [26] for the simulation of the air-shower particles with Sibyll 2.3d [236] and UrQMD [237] as the choice of high- and low-energy hadronic interaction model, respectively, together with CoREAS 1.4 [42] for the microscopic simulation of the air-shower radio emission, we build on state-of-the-art simulation frameworks. In the following, the choice of input parameters and settings for the simulations are described in detail.

8.1.4.1 Approximations in the modeling of the particle cascade

In the particle simulation in CORSIKA, two settings are particularly influential on the amount of radio emission that is predicted by the radio simulation in CoREAS: the `STEPFC` parameter and the thinning settings. The `STEPFC` parameter defines the multiple scattering length for electrons and protons. With a value greater or lower than the default 1.0, the tracks of the particles are simulated coarser or finer, respectively, which has a significant impact on the microscopic modeling of the radio emission from the electromagnetic cascade [238]. When reducing the `STEPFC` from the default value to

0.05, the resulting radiation energy of the simulated shower was found to increase by about 11% on average. At this point, a plateau is reached where the yielded radiation energy does not change significantly when further reducing the `STEPFC` parameter. In a technically different but practically similar way, the maximum allowed magnetic deflection angle of particles is a parameter that defines the particle track lengths. A study with CORSIKA 8 showed that the radiation energies predicted by simulations produced with the CoREAS and ZHS formalisms agree much better when using small track lengths [239, 240]. These studies confirm that a fine particle tracking is necessary to obtain accurate radio signals from air-shower simulations on an absolute scale. Therefore, we set the `STEPFC` parameter to 0.05 in all simulations with the drawback that the computing time increases by a factor of 4 compared to the default setting.

Thinning is a procedure in the simulation of particle cascades in which individual particles are represented by one particle with an appropriate weight once the energies of the individual particles fall below a certain threshold. Through this merging of particles, the particle shower is "thinned out" which significantly reduces the computing time. In CORSIKA, the level of thinning can be set through the parameter `EFRCTHN`. This parameter is the fraction of the energy of the primary particle below which a particle is drafted into the thinning procedure. Larger values of `EFRCTHN` reduce computing time but also affect the amount of radiation energy produced in the simulation, while the amount is consistent for values of 10^{-5} or smaller [224]. We set `EFRCTHN` to 10^{-6} to avoid any bias through thinning.

To process these high-precision simulations in a comparably short time, we ran them with *MPI* (Message Passing Interface) parallelization on the *HoreKa* (Hochleistungsrechner Karlsruhe) supercomputer. Each simulation was processed on one of the 602 standard- and high-memory servers of Horeka. Each server contains 76 CPU cores that the tasks of one simulation were divided among.

8.1.4.2 Choice of atmospheric model & station selection

CORSIKA allows to configure the atmospheric model that is used in the air-shower simulation. The choices range from predefined atmospheric models at different levels of complexity to providing a file with a specific atmospheric profile. With the latter option, atmospheric density and refractivity profiles from measurements stored in the Global Data Assimilation System (GDAS) can be used. A program called `gdastool` [241] allows to easily compile such GDAS atmospheres for given coordinates and time. In our simulations, we use GDAS atmospheres generated for the location of AERA and for the event times of the corresponding measured air-showers. The time resolution of the GDAS database is 3 h.

In CoREAS, the radio signals from the air shower are calculated for a given list of observers, whose coordinates need to be provided. The `RdREASSimPreparatorNG` module in Offline automatically produces such a list at the end of an event reconstruction with the coordinates of those AERA stations that are close enough to the shower axis such that one can expect them to perceive a measurable radio signal. More specifically, all stations within a defined distance from the shower axis in units of Cherenkov radii are selected and written to the list. We chose to select all stations within 4 Cherenkov radii, which is a compromise between the exhaustiveness of the simulations with respect to matching the measured events and a reasonable amount of computing resources [70].

If selecting stations only up to a shorter distance, there is the risk of omitting stations with a low but relevant radio signal, which may lead to biases in the reconstruction of the simulated event. If selecting stations within a larger distance, valuable computing time would be wasted on calculating radio signals that are irrelevant to the simulation event reconstruction. The Cherenkov radius is calculated individually in the event reconstruction in the `RdREASSimPreparatorNG` module using the SD-reconstructed shower axis and assuming a depth of shower maximum of $600\,\mathrm{g\,cm^{-2}}$, which is at the lower end of the expected X_{max} range for simulated showers in the relevant energy range and well below measurements. Therefore, the Cherenkov radii are conservatively overestimated and all signal-relevant AERA stations are expected to be included in the simulations.

8.1.4.3 Input geometry & input energy

The input geometry for each simulation, meaning arrival directions and shower cores are taken from the SD-reconstructions of the measured showers. This way, the simulations are prepared practically independent of the radio reconstruction of the measured showers. Modifications to the radio reconstruction can safely be made later without the need to rerun the simulations. The shower core estimate from the SD reconstruction is known to be biased in the direction of the shower axis in the order of a few ten meters. However, we do not expect this to have an effect on the analysis as we use the lateral integral of the fitted GeoCeLDF as the key ingredient, which we expect to be stable against such a core bias.

One input parameter for each event simulation that is of great relevance to the results of the analysis is the cosmic-ray energy. Here, we cannot use the energy estimate derived from the SD reconstruction, E_{SD}. In the calculation of E_{SD}, a data-driven estimate of the invisible energy in the shower [223] is used, which is shown as a function of calorimetric energy in Fig. 8.6. At the same total energy, the invisible energy fraction in a simulation is systematically different from that found in data, a consequence of the "muon puzzle". Therefore, the calorimetric and electromagnetic energies of the simulated shower would not be expected to match those of the measured shower and in turn the radio signals from data and simulation would not be comparable.

We thus create simulations whose radio signals are comparable to the data events by matching the calorimetric energies E_{cal} of the simulations to the calorimetric energies of the measured events. To that end, in a first step, we calculate the calorimetric energy of a measured shower with a given SD-reconstructed total shower energy E_{SD}. As explained earlier, E_{SD} contains an invisible energy correction that was obtained in a data-driven way [223]. The invisible energy is parameterized as a function of E_{cal} as

$$E_{inv}(E_{cal}) = f(\theta)E_{inv}^{l} + f(\theta)\frac{1}{2}\left[1 + \tanh\left(K\log_{10}\frac{E_{cal}}{E_{cal}^{A}}\right)\right](E_{inv}^{h} - E_{inv}^{l}), \tag{8.1}$$

where the zenith angle dependency is covered in the function $f(\theta)$. The spectral behavior of the invisible energy is separately described for lower and higher energies by E_{inv}^{l} and E_{inv}^{h}, respectively:

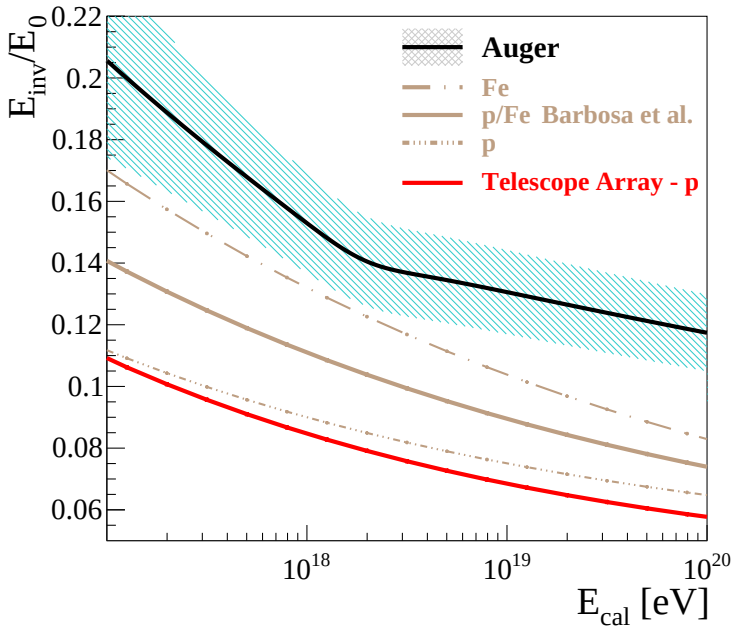

Figure 8.6: Fraction of the invisible energy in the total shower energy as a function of the calorimetric energy. In black, the data-driven estimation from the Pierre Auger Collaboration is shown with a band representing the systematic uncertainty. The fraction used by the Telescope Array collaboration is depicted in red. In brown, results of a simulation study by [242] is shown for pure proton primaries (dotted), iron primaries (loosely dashes) and a 50:50 mix (solid). Taken from [223].

$$E_{inv}^{l} = a \left(\frac{E_{cal}^{A}}{10^{18}\,\mathrm{eV}} \right)^{b} \left(\frac{E_{cal}}{E_{inv}^{A}} \right)^{b_{extr}} \tag{8.2}$$

$$E_{inv}^{h} = a \left(\frac{E_{cal}}{10^{18}\,\mathrm{eV}} \right)^{b} . \tag{8.3}$$

The invisible energy fraction is shown as a function of calorimetric energy in Fig. 8.6 in black. More details and the parameter values can be found in [223]. In order to calculate the calorimetric energy of a measured event as a function of the total shower energy, we finely sample $E_{tot}(E_{cal}) = E_{inv}(E_{cal}) + E_{cal}$ for values of E_{cal} between 10^{17} eV and 10^{20} eV and using E_{inv} from Eq. 8.1. Then, we perform a cubic inverse interpolation of the calorimetric energy as a function of the total shower energy. The interpolation is tuned to give results with an accuracy better than 0.001%. In the calculation of E_{inv}, we chose $\theta = 35°$ as this is the reference angle for the SD-750 shower size S_{35}, which approximates the median of the zenith angle distribution of events measured with the SD-750.

Next, we take the newly calculated calorimetric energy of each measured event and estimate the cosmic-ray energy E_{CR}^{sim} that needs to be put into a simulation such that the calorimetric energy of that simulation will have on average the same value as the calorimetric energy of the measured event. We use samples of the ratio of

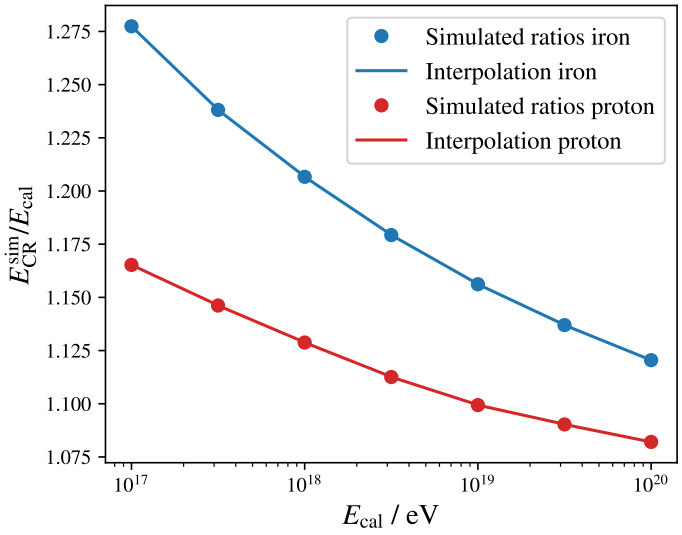

Figure 8.7: Ratio of the cosmic-ray energy to the calorimetric energy in simulations as a function of calorimetric energy, in red and blue for proton and iron primaries, respectively. The dots represent samples created with CONEX and Sibyll 2.3d and the lines are an interpolation of the samples. Figure from [245].

total to calorimetric shower energy $E_{\mathrm{CR}}^{\mathrm{sim}}/E_{\mathrm{cal}}$ for calorimetric energies between 10^{17} eV and 10^{20} eV and perform a linear interpolation in logarithmic space. The samples are calculated from simulations with the same hadronic interaction model as is used for the final simulations, Sibyll 2.3d, and are calculated for both proton and iron as choice of primary cosmic ray. In order to reduce the computing time in the generation of theses samples, the CONEX program [243, 244] was used instead of full Monte-Carlo simulations. CONEX simplifies the modeling of the particle cascade by numerically solving the cascade equations for selected types of particles in the cascade. Such a simplification in the simulation of particle cascades cannot compete in accuracy with a full Monte-Carlo approach as is taken for the event simulations in this analysis. However, there are applications where it proves suitable, which include the estimation of the invisible energy fraction for this work. The sample points and the interpolation of the total-to-calorimetric energy ratio are shown in Fig. 8.7.

Using the obtained interpolations for the invisible energy fractions for both measurements and simulations, we calculate the simulation input energies $E_{\mathrm{CR}}^{\mathrm{sim}}$ such that the calorimetric energies of the measured and simulated showers are expected to match on average. The ratios between the simulation input energies and the SD-reconstructed total shower energies of the corresponding measured events are shown in Fig. 8.8. Compared to the total shower energies of the measured events, the simulation input energies need to be about 1–2% larger – according to our matching of calorimetric energies – when using iron as the primary cosmic ray and about 4–6% smaller when using proton as the primary cosmic-ray with a visible energy dependence for both primaries. The kink around 2×10^{18} eV is an imprint of the similar kink in the data-driven invisible energy estimate which is due to the break in elongation rate observed by Auger [223].

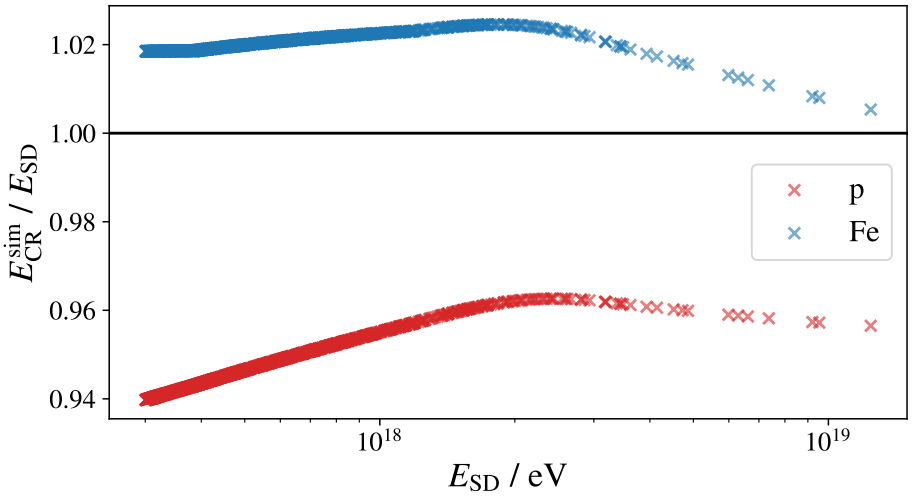

Figure 8.8: Ratio of the cosmic-ray energy that is used as input for the simulation to the total shower energy estimated of the corresponding measured event as a function of the latter.

With the described accommodations in the simulation preparation to have a close matching of the calorimetric energies of measured and simulated events, we created simulations for the event data set presented in Sec. 8.1.5. We observe a small mismatch between the calorimetric energies of the simulated showers, $E_{cal,sim}$ and the intended values, $E_{cal,rec}$, that were the basis on which we calculated the input cosmic-ray energies E_{CR}^{sim}. The ratios between the calorimetric energies of the simulations and the intended values are plotted as a function of the intended values in Fig. 8.9. On average, the calorimetric energies turn out to be 2–3% too large while the scatter is larger for proton simulations compared to iron simulations. The average offset is constant over energy and most likely a consequence of using `CONEX` for the estimation of the invisible energy fraction in simulations rather than the same full CORSIKA Monte-Carlo that is used for the event simulations. We use the ratios shown in Fig. 8.9 later to rescale the results of the simulation such that we achieve the desired matching of calorimetric energies between measured and simulated air showers. Details of that are discussed in Sec. 8.1.6.

In the simulations, only the radio signals from the air-showers are calculated but no noise contribution is added. Having realistic noise in the simulated events is crucial for a meaningful comparison to measured events. At AERA, the noise picked up by the stations is permanently monitored in a separate data stream with periodic triggers. We add measured noise from this data stream to the simulated signals during the processing in Offline directly before the event reconstruction as explained in Sec. 8.1.2. The measured noise is taken from around the time when the measured event was recorded, within at most 10 min. This way, a realistic representation of the noise at AERA in the simulated events is guaranteed.

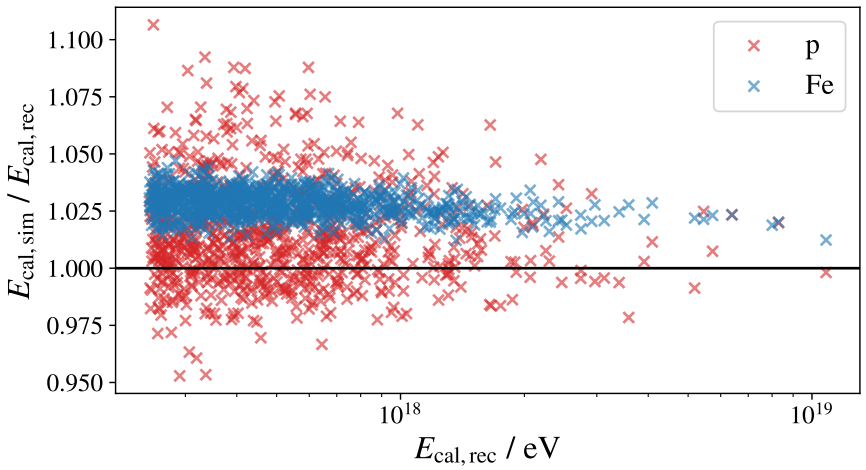

Figure 8.9: Ratio of the calorimetric energy directly calculated from the simulated events to the reconstructed calorimetric energy from the corresponding measured events as a function of the latter.

8.1.5 Event data set

With the hybrid data set collected and simulations for proton and iron primaries generated, we look at the distributions of a few observables of the events. At this stage all quality cuts for the event selection as presented in Sec. 8.1.3 are applied. In Fig. 8.10, the shower cores from the SD reconstruction of the measured events are shown. Because of the confinement cut, they all fall into the sub-array of the externally triggered AERA stations. As expected, there is no core fully contained in the most sparse region of the Phase-III sub-array in the southern part. The stations there are spaced at distances of 750 m, aimed at inclined shower detection.

The core distribution exhibits an inhomogeneous structure that is also not unexpected and mostly because of the irregular spacing of AERA. The densest patch of cores is in the area of the Phase-I sub-array with the smallest AERA station spacing, where air-showers at smaller zenith angles and at lower energies can reach the five signal station requirement the easiest.

In Fig. 8.11 on the left, the event distribution in SD-reconstructed azimuth angle is shown. The distribution of all measured events after quality cuts is depicted by the black line. It exhibits a distinct asymmetry in the North-South direction with most events arriving from the south and few to no events arriving from north. From the full efficiency of the SD, a flat distribution is expected. The observed asymmetry is the result of an azimuthal detection efficiency of AERA due to strength of the important geomagnetic radio emission depending on the geomagnetic angle. For a shower coming from the south, the geomagnetic emission is significantly stronger than for the same shower arriving from the north, making a good event reconstruction far more likely. The geomagnetic cardinal directions roughly align with the geographic counterparts. In addition to this natural disfavor of events from the north, the geomagnetic angle cut in the event selection (see Sec. 8.2) removes any remaining events within 20° of the geomagnetic north.

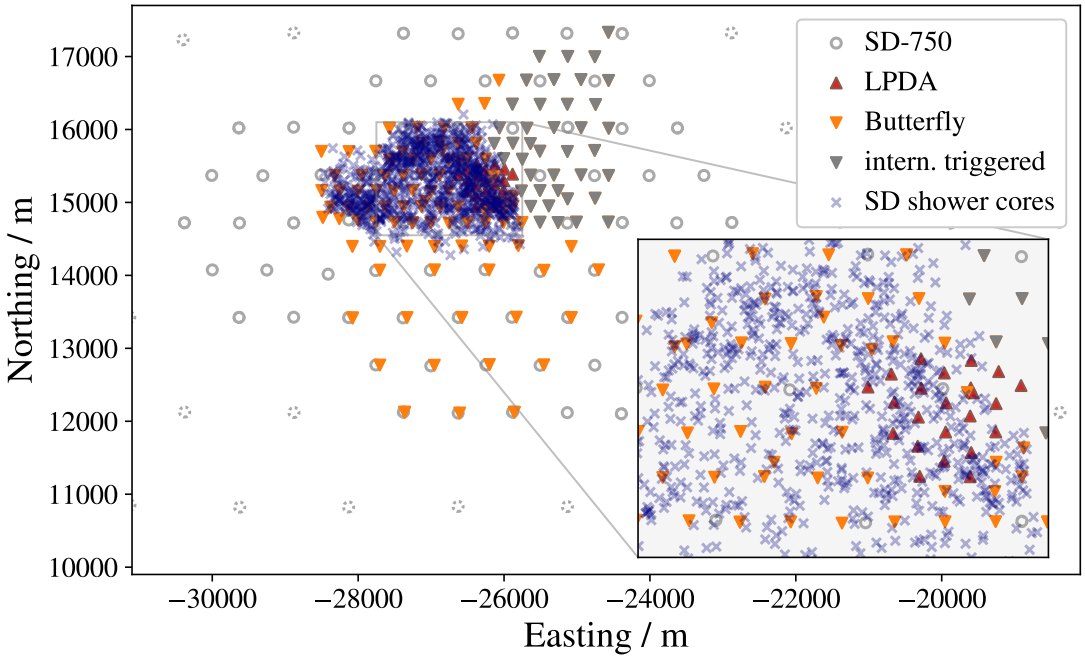

Figure 8.10: Distribution of the SD-reconstructed shower cores of the event set with quality cuts applied. The positions of the SD-1500 stations are shown as dotted circles while the SD-750 stations are shown as full circles. The AERA stations that were used for this analysis with Butterfly and LPDA antennas are depicted as triangles in orange and red, respectively. The unused purely internally triggered stations are depicted in gray. An inset gives a zoomed-in view on the more densely populated shower cores around AERA Phase I.

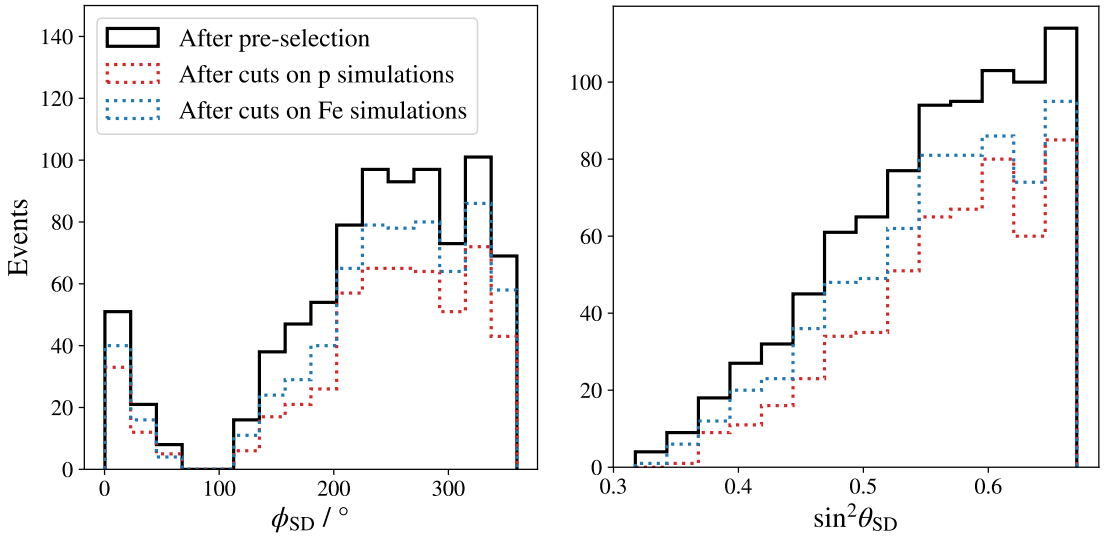

Figure 8.11: Distributions of the SD-reconstructed arrival direction angles of the quality event set. *Left:* azimuth angle, *right:* zenith angle.

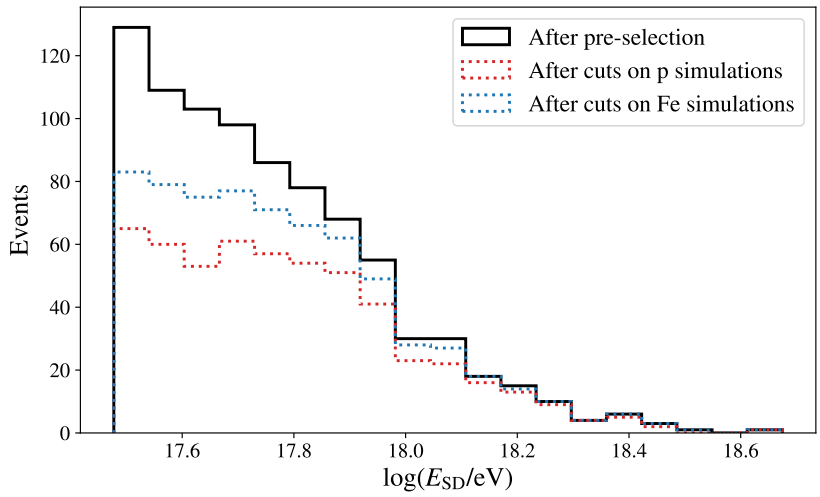

Figure 8.12: Distribution of the logarithmic SD-reconstructed energies of the quality event set.

In red and blue, the distributions are shown for those events that also have a high-quality reconstruction from a matched simulation with a proton or iron primary, respectively. Those distributions are consistent in shape with the black histogram, scaled down by the reduced statistics as reported in Tab. 8.2.

Very similar observations as for the azimuth angle distributions can be made for the zenith angle distributions in Fig. 8.11 on the right. Most events arrive from the highest inclinations within the zenith range until 55°. In $\sin^2 \theta_{SD}$, one would expect a flat distribution from an isotropic flux of cosmic rays and a fully efficient event selection. Towards lower zenith angles, the projected radio-emission footprint of an air-shower on the ground will be smaller on average, therefore being less likely to induce large-enough signals in the required number of five stations [246]. The distributions for events with matched simulations generally follow the same shape as the black distribution.

Further, we show the distribution of SD-reconstructed energies in Fig. 8.12. Starting from the sharp edge at the full-efficiency threshold energy of the SD at $3{\times}10^{17}$ eV, the black distribution of all high-quality measured events falls with energy. The distributions of events with cut surviving proton or iron simulations agrees well with the black distribution beyond roughly 10^{18} eV. At the lower energies, there is a distinct deviation. For either primary, the distribution is much flatter than the black one. From Tab. 8.2, it is clear that most events lost from the cuts on the reconstructed simulations are due to the five signal-station requirement. Since there is some correlation between the shower energy and the number of signal stations, that requirement by tendency removes events at the lower part of the energy range.

Lastly, we inspect the distribution of the depths of shower maximum of the simulations. In Fig. 8.13, the X^{MC}_{max} distributions are shown for all created simulations – including simulations that do are not reconstructable in Offline– and for those simulations that make it into the final event dataset, separate for proton and iron as the primary particle. First, it is clearly visible that almost all proton-induced air showers are deeper than the iron showers. The X^{MC}_{max} distribution of iron showers only gets slightly shifted towards lower depths of shower maximum through the event selection. On the other hand, the

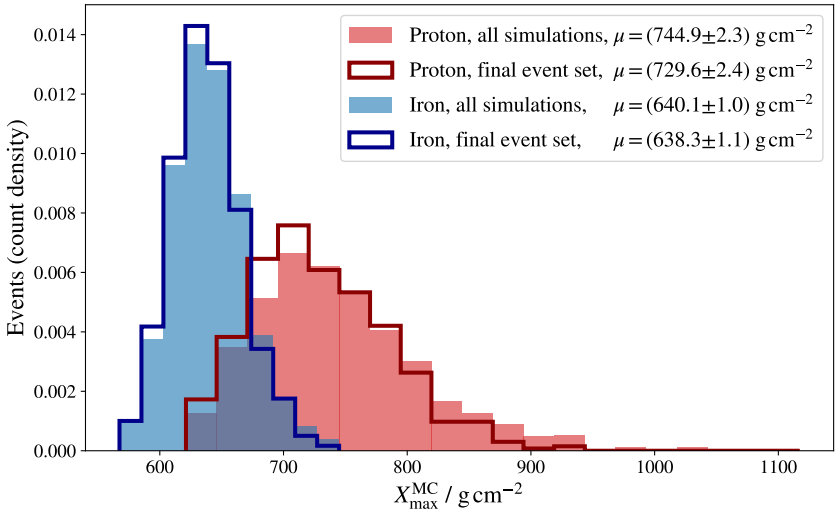

Figure 8.13: Distributions of depth of shower maximum for the created proton and iron simulations (filled histograms) and the final event selection (step histograms). The histogram counts are normalized to better expose the shifts introduced through the event selection.

distribution for proton showers gets signficantly shifted towards lower $X_{\mathrm{max}}^{\mathrm{MC}}$ values with the mean value decreasing by about $15\,\mathrm{g\,cm^{-2}}$. These observations clearly give a hint that AERA – under consideration of the quality event cuts – has an efficiency bias against deeper showers that produce smaller footprints.

In summary, we present a data set of vertical air showers up to 55° inclination between 3×10^{17} eV to 4×10^{18} eV, measured in hybrid by the SD and AERA. With the applied selection cuts, as a particle-radio event set, it is of unprecedented quality and statistical power in the respective energy range.

8.1.6 Energy scale comparison

With the event set presented in Sec. 8.1.5, we perform the energy scale comparison as explained in Sec. 8.1.1. Concretely, we look at the event distributions of relations between the square root of radiation energies from the data reconstruction and from simulation reconstruction, $E_{\mathrm{rad}}^{\mathrm{data}}$ and $E_{\mathrm{rad}}^{\mathrm{sim}}$. A defined parameter of those distributions, the choice of which is discussed in this section, provides the metric that quantifies the agreement between the energy scales from the FD and from radio measurements. Before comparing the radiation energies, we correct for the small mismatch between the actual and the intended calorimetric energies of the simulations plotted in Fig. 8.9. For each simulation, we take the ratio shown in that figure and divide the square root of the radiation energy from the simulation reconstruction by it. We assume that across the size of these factors – mostly within ±5% – the linear rescaling of the simulation energy is valid.

8.1.6.1 Self-blinded development of the method

The result of this analysis is virtually a check of the previously stand-alone FD energy scale. Inevitably, there is a level of expectation within the scientific collaboration as to

how the result of the comparison may turn out. An agreement between the energy scales within uncertainties would support many efforts and previous work on the FD energy scale. Leaning towards decisions in the development of the analysis that would rather confirm than contradict previous results, is a natural human behavior [247]. The original goal of the analysis – discovering truth from the data – could thus get out of focus. At several steps in the energy-scale analysis, decisions about, for example, which event cuts to use and how to quantitatively determine the agreement between the energy scales had to be made. Those situations pose risks to decide in such a way that the final result will be in line with expectations.

In order to obviate any consciously or unconsciously introduced biases through such decisions, from the very beginning of the analysis we had adopted a blinding procedure. There are various options how to employ blinding in the kind of analysis we conduct – for example, as simple as removing labels from plots [247].

We used a blinding factor that was multiplied to E_{rad}^{data}, with the same value for all events. As a result, the studied distributions and any quantity representing the center of a distribution were shifted by the square root of the unknown blinding factor. Therefore, absolute values of any metric were unusable for premature interpretations of the result. Still, the size and direction of relative changes in those metrics could be and were used to test impacts of individual ingredients in the analysis. Also, investigations about the shape of the distributions and checks for systematics were possible without any limitation. The blinding factor was drawn from a uniform distribution in the interval $[0.75, 1.25]$. For the most straight-forward metric in the comparison, the ratio $\sqrt{E_{rad}^{data} \cdot BF}/\sqrt{E_{rad}^{sim}}$, a blinding range of $^{+11.8\%}_{-13.3\%}$ was thereby imposed.

After finalization of the analysis and approval by the Pierre Auger Collaboration, the blinding factor was lifted to unblind the results as are shown in the following. The blinding factor had a value of 0.797, by chance being close to the lower end of the possible range.

8.1.6.2 Results

As mentioned in the previous section, the ratio $\sqrt{E_{rad}^{data}}/\sqrt{E_{rad}^{sim}}$ is the metric that directly provides a quantitative comparison of the energy scales from FD and radio measurements. Therefore, using this metric to give a number to the result of the analysis seems straightforward. However, the distribution of the ratios of two variables will by construction be asymmetric (the range of 0 to 1 on one side corresponding to the range of 1 to infinity on the other side), making the determination of a central value a difficult problem [248]. Therefore, we prefer to calculate the logarithm of the ratios, $\log_{10}\left(\sqrt{E_{rad}^{data}}/\sqrt{E_{rad}^{sim}}\right)$, and take the mean value of the logarithmic ratios as the central value.

In Fig. 8.14, the distribution of the logarithmic ratios is shown for the event set matched with proton simulations on the left, and with iron simulations on the right. The shape of the distributions is rather symmetric. Their mean values with uncertainty and standard deviations of the distributions are given. In order to obtain the quantified agreement between the FD and radio energy scales, we calculate ten to the power of the mean values:

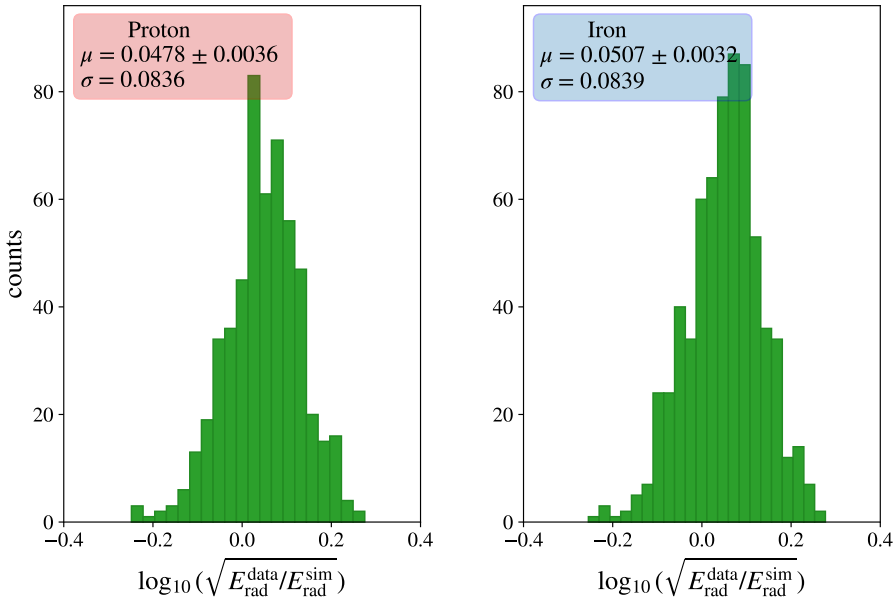

Figure 8.14: Distribution of the logarithmic square root ratios of the reconstructed radiation energies from measured events and the corresponding simulations. *Left:* results for proton simulations, *Right:* results for iron simulations.

$$
\begin{aligned}
&\textbf{Proton:} && 10^{0.0478} = 1.116 \\
&\quad \text{Stat. unc. up :} && 10^{0.0478+0.0036} = 1.126 \\
&\quad \text{Stat. unc. down :} && 10^{0.0478-0.0036} = 1.107 \\
&\textbf{Iron:} && 10^{0.0507} = 1.124 \\
&\quad \text{Stat. unc. up :} && 10^{0.0507+0.0032} = 1.132 \\
&\quad \text{Stat. unc. down :} && 10^{0.0507-0.0032} = 1.116
\end{aligned}
\tag{8.4}
$$

By construction of the analysis, we do not expect to see a difference between the results from proton or iron simulations. In the preparation of the simulations, the input energies were chosen to account for the systematic difference between the invisible energies in showers from either primary. We use simulations that agree in the calorimetric energies of the shower, and which are thus expected to also agree in the radiation energies. In the step of extracting the radiation energy from the station signals, the GeoCeLDF is used that we test for a bias against the shower primary in Sec. 8.1.7.4. The results for both simulation primaries agree within the statistical uncertainties.

We take the mean of the results from using proton and iron simulations with a 50:50 weighting. We also average the statistical uncertainties to each side. We obtain a ratio of the cosmic-ray energy scales from the FD and radio measurement of

$$
\frac{\text{Radio energy scale}}{\text{FD energy scale}} = 1.120^{+0.009}_{-0.008} \tag{8.5}
$$

The result implies that the radio energy scale is 12% higher than the FD energy scale. In other words: A 10^{18} eV air shower measured on the FD energy scale has an energy of 1.12×10^{18} eV on the radio energy scale. The statistical uncertainty of the result is 0.8%.

8.1.7 Studies of systematics

We perform investigations in search for possible systematics or biases in the result of the analysis. All of these checks and any resulting decisions for the analysis, e.g. event selection cuts (see Sec. 8.2), were made before unblinding the result to ensure an unbiased procedure. For the purpose of readability, we do not show the logarithmic ratio of the square root radiation energies but just the square root ratios[1]. Some of the shown results are produced with the proton simulation set. In those cases, the results obtained when using the iron simulation set are moved to App. C.4 as they mostly yield the same conclusions. Differences between the results for proton and iron simulations are pointed out where applicable.

8.1.7.1 Long-term evolution & monthly variation

First, we look at the long-term and monthly behavior of the comparison result to check for systematic effects from environmental measurement circumstances or from instrumental conditions like detector aging. In Fig. 8.15, the square root ratio of radiation energies is shown binned into all years of the dataset from 2014 until 2020. Both the mean and median values per year fluctuate within uncertainties. There is no long-term trend visible. When considering all detector systems that take a role in the analysis and whether they could possibly introduce a long-term drift through aging effects, no such influence is expected from the FD and AERA. While the FD is known to have aging components [249], it enters into the analysis only via a single calibration factor in the FD-SD calibration, so any aging is averaged out by construction.

As discussed in Sec. 6.1.4, it has been shown with the Galactic calibration that AERA operates stably over many years with an estimate of its aging[2] that is compatible with zero [186].

The SD is known to suffer from aging which can be tested by looking at the rate of detected events above a threshold energy [251]. In a study that also covered most of the data period that we use here an increase of the rate of events above 3×10^{18} eV measured with the SD-1500 of 0.58% per year was found [252]. More detailed checks indicate a softening of the event rate increase for the later years, which are overlapping the data period used in this work, possibly even compatible with a constant evolution, i.e. no aging of the SD. To conclude, the energy-scale analysis does not show any long-term trend, which is qualitatively compatible with the non-expectation of any strong aging effects in the involved detectors.

[1] In the following figures, mean and median values of the ratios are drawn. The difference between the mean of ratios and the slightly different metric that we use for the comparison – ten to the power of the mean logarithmic ratio – is small since the ratios are rather close to 1. Therefore, we figure that plotting the mean (or median) ratios is a valid way to perform the checks for systematic effects.

[2] The term *aging* is used here to be in line with the naming of the long-term drifts seen in the FD and SD. However for radio detectors, actual aging of the antenna parts or the electronics components is not expected.

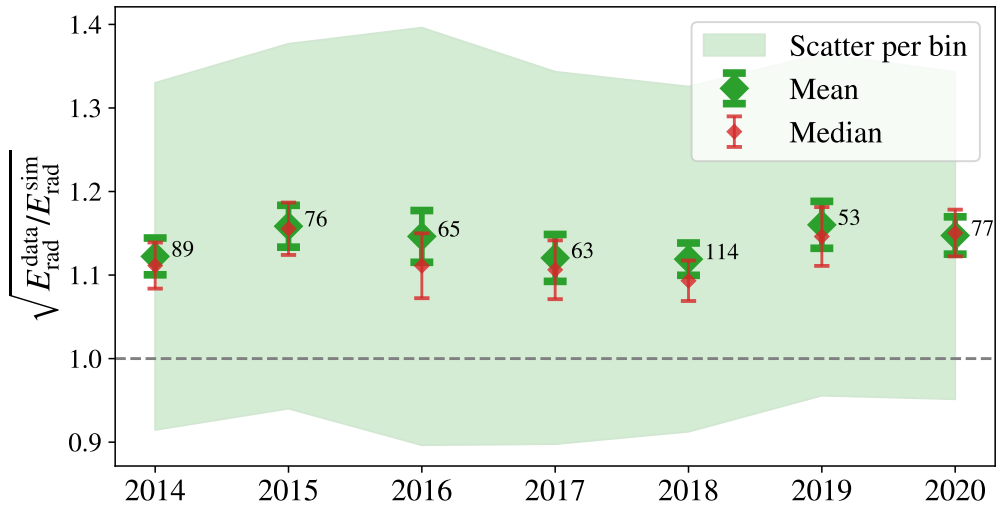

Figure 8.15: Evolution of the mean and median square root ratio of radiation energies across the years covered by the event set. The uncertainty on the median is calculated as the uncertainty on the mean multiplied by 1.253 [250]. The shown diagram is the result for proton simulations.

In a similar way, we look at the evolution of the energy scale comparison over the months. Fig. 8.16 shows the square root ratio of radiation energies binned per month. No year-round modulation is visible, indicating that the most probable cause for any such effect – a temperature dependency – is taken out by the temperature correction in the radio reconstruction (Sec. 6.1.3). Compared to the other months, the mean value of the July bin may be perceived as an outlier albeit being compatible with statistical fluctuations. When focusing on the median values per bin, the perception of the bin as an outlier is weaker.

8.1.7.2 Study of systematic dependencies

The distributions in Fig. 8.14 look reasonably symmetric giving an indication that the comparison does not inherit any major systematic dependency that would skew the distributions in one direction. Nevertheless, the scatter of the distributions is quite sizeable. Varying the result (Sec. 8.1.6) by one σ of the distribution in either direction yields ratios of the FD and radio energy scales between 1.363 and 0.920. Most of the scatter is probably due to a combination of the energy resolutions of the SD and AERA and shower-to-shower fluctuations. Nevertheless, we perform checks for systematic dependencies of the energy scale comparison that might contribute to the scatter.

In the multiple plots of Fig. 8.17, the square root ratios of radiation energies are shown as a function of several observables. We start from the top left and go through the plots row by row to discuss them. The green dots are a scatter plot of all events while in red, they are grouped in bins of the same statistical size. In the figure legends, the standard deviation of the mean values of all bins is given.

SD energy:

We first look at the energy scale comparison as a function of the SD-reconstructed shower energy. There is no significant systematic trend and the scatter of the bin mean values is

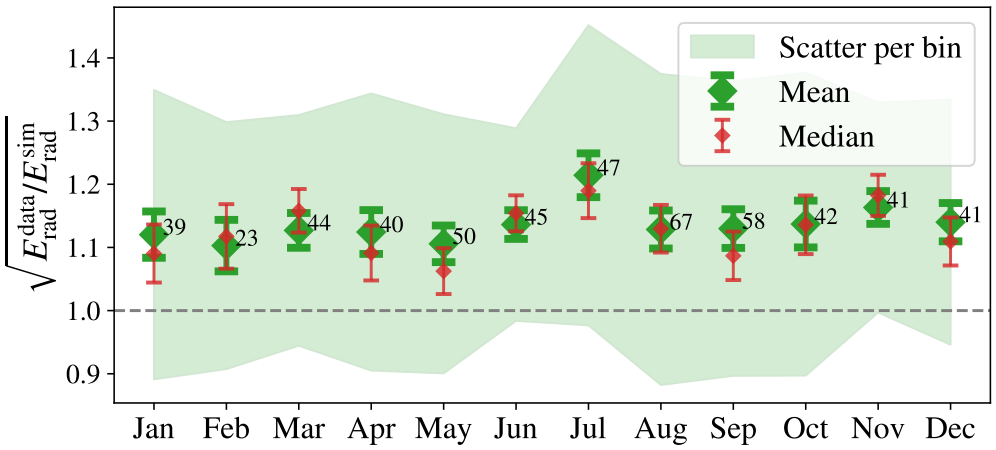

Figure 8.16: Variation of the mean and median of the square root ratio of radiation energies throughout the year. The uncertainty on the median is calculated as the uncertainty on the mean multiplied by 1.253 [250]. The shown diagram is the result for proton simulations.

small. We also tested slightly larger values for the lower energy threshold (3.3×10^{17} eV, 3.5×10^{17} eV, 4×10^{17} eV) and the changes in the comparison result stayed well within the statistical uncertainties. This is an important result as it means that the result on the energy scale is valid and constant across the full covered energy range from 3×10^{17} eV to 4×10^{18} eV. The radio measurement of the highest-energy event of the dataset is shown in Fig. 8.3.

Depth of shower maximum:

There is a slight tendency of an increasing energy scale ratio towards deeper simulated showers. Since we do not select a specific value for X_{max} in the simulations but effectively leave the choice of this parameter to the randomness of shower-to-shower fluctuations, there is also a randomness as to how well that value and in turn the simulated shower in general matches to the measured shower. In this context, we also note that some detection inefficiency of AERA towards deeper showers, which generally have smaller radio-emission footprints than showers with a lower value of X_{max} and which therefore have a higher chance not to pass the five signal station criterion, is expected. In combination, these considerations depict a rather complex picture and explaining the observation of the X_{max} dependency in the energy scale comparison is non-trivial. However since the dependency is small, investigating it in detail is not critical to the validity of the result of this work.

Azimuth angle:

The scatter plot of the square root radiation energy against azimuth angle does not exhibit any systematic behavior as expected.

Zenith angle:

There is a dependency on the zenith angle as the energy scale ratio decreases towards larger shower inclinations. The size of the dependency is not large but it might be an imprint of a possible zenith-angle-dependent bias in the descriptions of the antenna

response patterns that are used in the radio reconstruction. We use the standard deviation of the mean values of 2.6% in the estimation of the systematic uncertainty introduced by said descriptions of the antenna patterns in Sec. 8.1.8.

Number of radio signal stations:

In the plot of the ratio against the number of AERA signal stations, there is some noticeable dependency as well. The ratio is on average slightly lower for events with five or six signal stations. The dependency appears weaker in the case of the comparison with iron simulations in Fig. C.3.

Reduced χ^2 of the GeoCeLDF fit:

There is no critical dependency on the reduced χ^2 of the GeoCeLDF fit in the data reconstruction. Since the station signal reconstruction that we use to calculate the energy fluences for the GeoCeLDF fit is known to underestimate the signal uncertainties [216], the absolute χ^2 values may be biased. We used the plot as a way to define the cut value on the reduced χ^2 such that outlier events due to poor fits are removed (see Sec. 8.2).

Geomagnetic angle:

Similar to the reduced χ^2, we used the plot of the comparison as a function of the geomagnetic angle to define a cut that removes badly reconstructed events due to a very small geomagnetic component in the radio signal. The plot does not exhibit a systematic behavior, which is expected as the geomagnetic angle is closely related to the azimuth angle.

Temperature:

Lastly, we look at the scatter plot of the energy scale ratio against the ambient temperature at the time of the event. The temperature information is taken from the weather sensor at the CRS. There is a small but uncritical systematic trend perceptible, which is most likely due to the fact that the temperature at the CRS does not exactly match the temperature inside the housings of the AERA amplifiers. The latter temperature is probably prone to heating from solar irradiance while the temperature from the CRS weather sensor is not. Thus, there is no indication that the temperature correction in the radio reconstruction is not working as intended.

8.1.7.3 Impact of signal biases in the radio reconstruction

In the analysis logic for the energy scale comparison, one important premise is that a potential loss of signal introduced in one or multiple steps of the radio reconstruction cancel out by treating measured and simulated events in the same way. In past work, such signal loss was observed directly in checks of the signal at several test points in the reconstruction [231] but also indirectly through the impact of various noise reduction methods on previous studies on the energy scale with AERA [232].

For the validity of the result of this work, it is imperative to test the premise of immunity against such reconstruction biases. Therefore, we perform a test in which we add a noise reduction method, the `RdChannelBandstopFilter`, to the radio reconstruction – for both data and simulations. A brief description of the module is provided in Sec. 6.2.4.

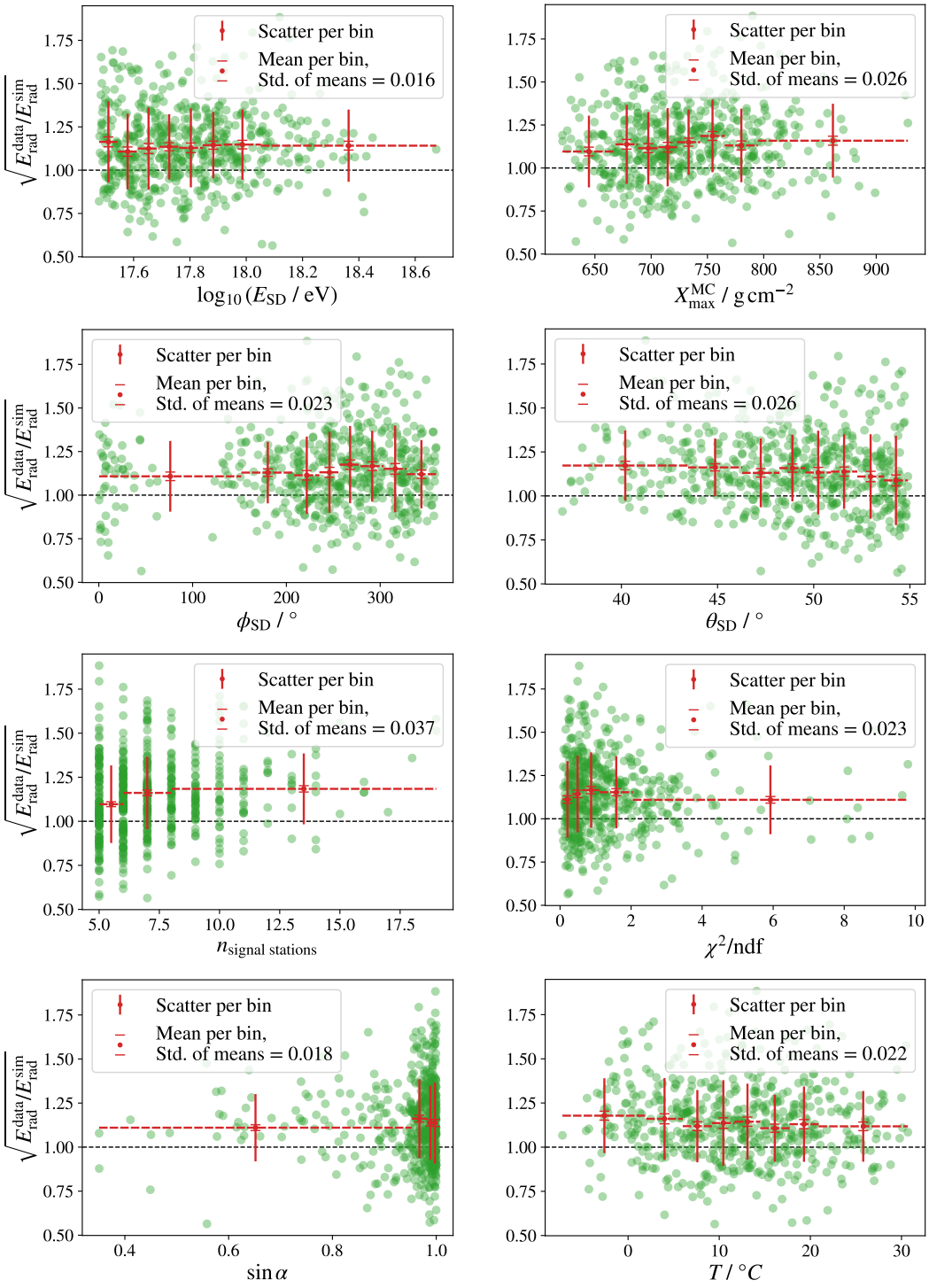

Figure 8.17: Plots of the square root ratio of radiation energies against several observables. In green dots, scatter distributions of the individual events are shown. The bin sizes for the red markers are chosen such that each bin contains the same amount of events. The horizontal dashed bars indicate those bin widths. From left to right and from top to bottom: total shower energy, depth of shower maximum of the simulated event, reconstructed azimuth and zenith angle, number of AERA signal stations, reduced χ^2 of the GeoCeLDF fit, geomagnetic angle, air temperature from the weather station at the CRS at the time of the measured event. If not otherwise specified, the observables are taken from the reconstruction of the measured event. The shown diagrams are the results for proton simulations.

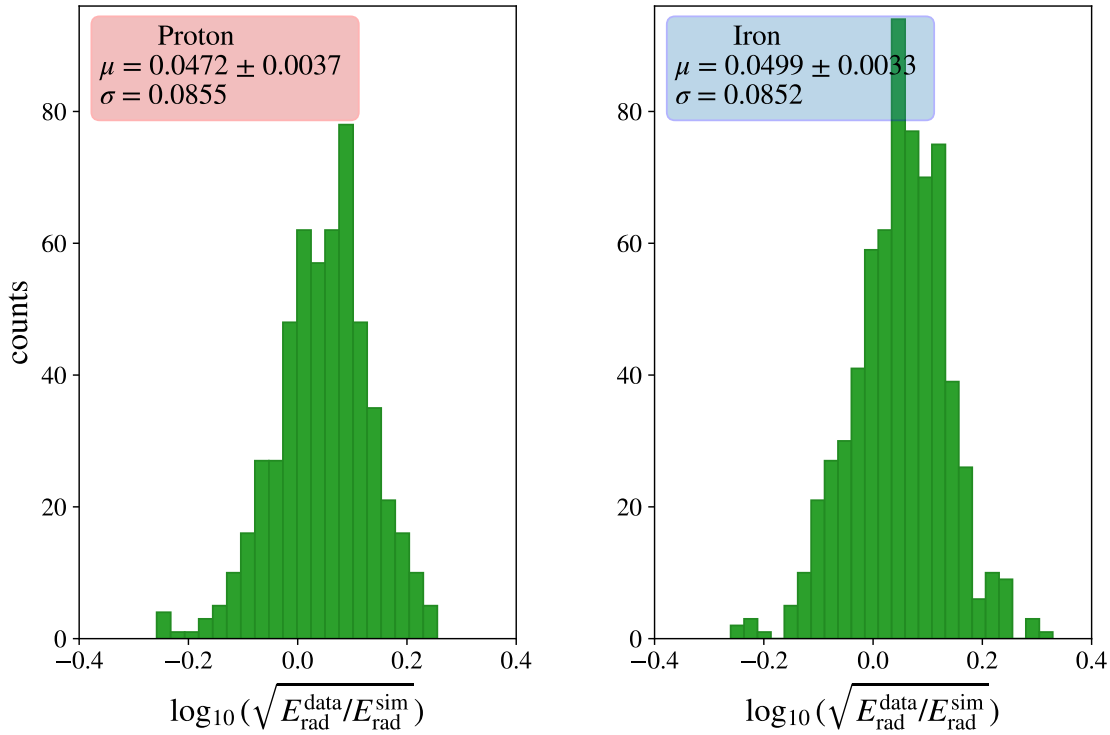

Figure 8.18: Distribution of the logarithmic square root ratios of radiation energies from the reconstruction including the `RdChannelBandstopFilter`. *Left:* proton simulations, *Right:* iron simulations.

In the test on the reconstruction with the `RdChannelBandstopFilter`, the module was inserted into the `ModuleSeuquence.xml` from Apps. C.2 and C.3 in between the `RdChannelTimeSeriesTaperer` and `RdChannelUpsampler`.

In comparison to the default reconstruction, using the `RdChannelBandstopFilter` yields radiation energies that are on average 10.4% smaller. Albeit this large difference, the impact on the energy scale comparison is small. In Fig. 8.18, the same histograms of the logarithmic square root ratio of radiation energies are shown as in Fig. 8.14, on the left for proton simulations and on the right for iron simulations. The results yield the following comparison of the FD and radio energy scales:

$$\begin{aligned} &\textbf{Proton:} && 10^{0.0472} = 1.115 \\ &\textbf{Iron:} && 10^{0.0499} = 1.122 \end{aligned} \tag{8.6}$$

The averaged value is 1.1185, which differs from the main result (Eq. 8.5) by less than 0.2σ of the statistical uncertainty of the latter. This test shows that the premise for the logic of the analysis – systematic loss of signal in the reconstruction cancels out – is valid.

8.1.7.4 Study of biases in the GeoCeLDF fit

Primary particle

The GeoCeLDF fit that yields the radiation energy from the integral of the fitted LDF is a crucial part of the analysis. We check the performance of the LDF model and fit for two possible sources of biases: primary cosmic ray type and a core offset.

In Fig. 8.19, a scatter plot of all simulations is shown. On the horizontal axis is the true calorimetric energy E_{cal} of the simulation. On the vertical axis is the corrected radiation energy S_{rad}^{sim} (see Sec. 7.2) divided by the true calorimetric energy to the power of 1.98 and multiplied by a factor of 10^{29} to normalize the scale[1]. The corrected radiation energy is calculated from the radiation energy yielded in the radio reconstruction of the simulation. By dividing S_{rad}^{sim} by $E_{cal}^{1.98}$, the energy dependence is removed accurately enough to compare the mean values of the populations of each primary. The exponent 1.98 is chosen in accordance with the expectations for how we calculate the corrected radiation energy (Eqs. 7.2 and 7.3 together with the results from [224]).

We obtain mean values of the metric on the y-axis of $(3.302 \pm 0.022)\ \mathrm{eV}^{-0.98}$ for proton simulations and $(3.367 \pm 0.018)\ \mathrm{eV}^{-0.98}$ for iron simulations. The mean values for proton and iron simulations differ by 1.9%, which is small. However, the statistical uncertainties on the means values are small as well and they only agree within 2.3σ of combined uncertainties. Therefore, there could be a significant albeit small bias of the estimated radiation energy with respect to the primary particle.

Core offset

We also check for a bias in the GeoCeLDF fit through a systematic shift of the reference shower core. There is an alternative framework for the SD reconstruction of measured air showers (CDAS Herald). The shower cores reconstructed with this framework and with the reconstruction in Offline differ in the down-stream direction by about 15 m on average [253]. With the quality event selection for this analysis, the reconstruction of all events includes a shower core that is fitted from radio data as part of the GeoCeLDF fit. We test how stable the GeoCeLDF fit is against variations of the reference shower core – which is used as a start parameter in the fit – of the size of the difference between the two alternative SD reconstructions. In the radio reconstruction (Sec. 8.1.2), we artificially shift the external shower cores by 20 m to the north. The resulting radiation energies of the modified radio reconstruction are compared event-by-event to the default reconstruction, which is shown in Fig. 8.20. Only a handful of events exhibit a significant difference. On average, the radiation energies change by 0.07% clearly indicating that the GeoCeLDF is stable against relevant shifts of the external shower core estimates.

8.1.7.5 Conclusions

The studies of systematic dependencies or behavior in summary do not show any problems of the analysis. Light systematics that are found, e.g. a trend of the result with the zenith angle, will be used in the quantification of some of the systematic uncertainties, which are discussed in the next section. Of great importance is the finding that there is

[1] This factor accounts for the 29 orders of magnitude difference between the squared calorimetric energies that are on the EeV / 10^{18} eV scale and the corrected radiation energies that are on the ten MeV / 10^{7} eV scale.

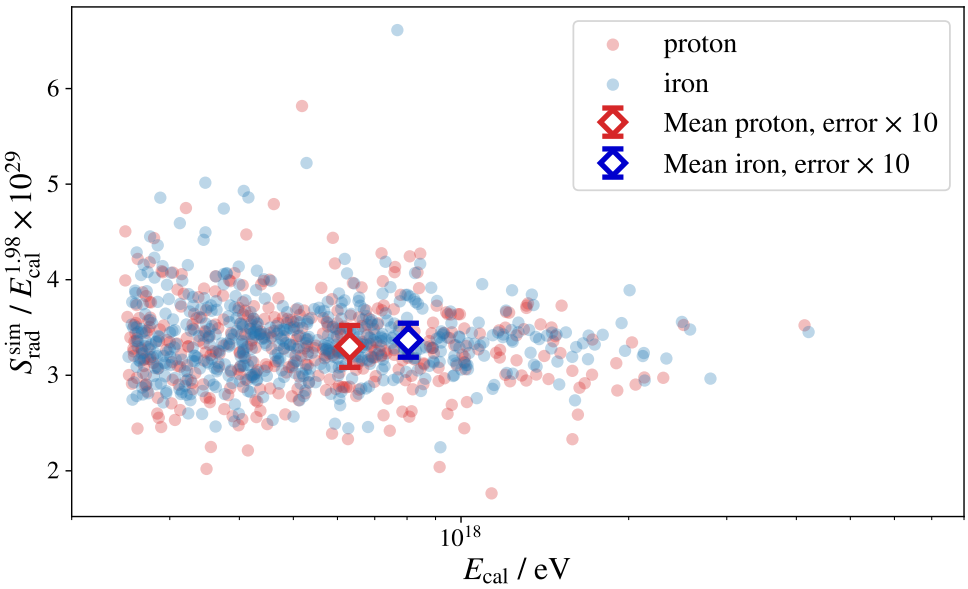

Figure 8.19: Corrected radiation energies from the reconstruction of the simulated showers with the GeoCeLDF normalized to the Monte Carlo calorimetric energy to the power of 1.98 plotted against calorimetric energy. The markers for the mean values are placed in arbitrary positions. The small uncertainties on the mean values are displayed with a multiplication by 10 to make them visible.

no energy dependency of the result meaning that the radio energy scale as probed in this analysis is valid and constant between 3×10^{17} eV and 4×10^{18} eV.

8.1.8 Uncertainties in the energy scale comparison

In the following, sources of systematic uncertainties in the determination of the radio energy scale are collected and discussed. The sources and their uncertainty contributions are listed in Tab. 8.3, divided in experimental uncertainties related to the detector calibration and the event reconstruction and theoretical uncertainties related to the simulations. All uncertainties are quantified on the cosmic-ray energy level if not mentioned otherwise.

8.1.8.1 Experimental uncertainties

Galactic calibration

The absolute calibration of the radio signals measured with AERA, which is essential for the validity of the energy-scale analysis, relies on the accuracy of the Galactic calibration. However, determining this accuracy is a complex task. In Chap. 5, we conducted an in-depth study of the foundations of the Galactic calibration – the sky models that are used to predict the diffuse Galactic emission. Through comparisons of the available sky models, the intrinsic systematic uncertainty of the predicted Galactic signal is estimated to be 11.7% for the radio detectors at the Pierre Auger Observatory (Sec. 5.4). This uncertainty refers to the predicted signal on the level of sky brightness temperature

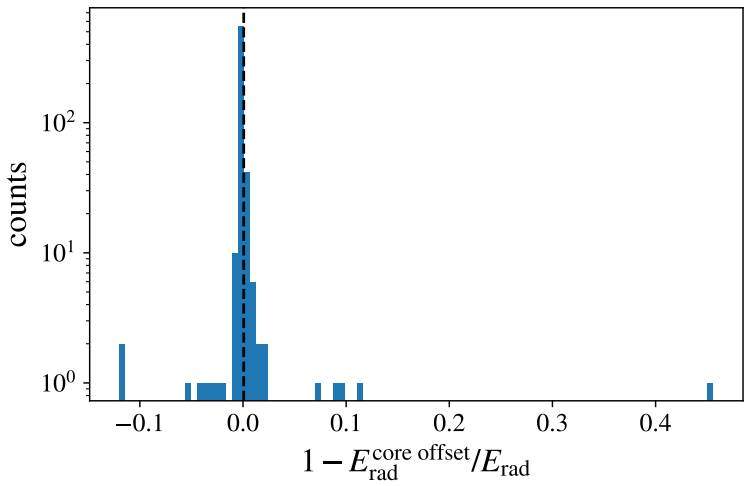

Figure 8.20: Relative difference in the reconstructed radiation energy for the measured event if shifting the reference core systematically by 20 m, which is used as an initial guess in the GeoCeLDF fit.

and is deduced from the difference between the two models that predict the upper and lower extreme, respectively. As explained in Sec. 5.7, uncertainties in the sky brightness temperature propagate into the cosmic-ray energy scale approximately by half. Therefore, we deduce a systematic uncertainty estimate of about 6% from the direct comparison of the sky models.

However, probing just the prediction of the Galactic emission is strongly related but not equivalent to probing the accuracy of the full Galactic calibration method. The latter depends on the specific implementation of the method as well. In our sky model study, we determined the accuracy based on the averaged absolute sky temperature. In the Galactic calibration, the measured signals are scaled with a gain factor essentially derived from the slope between the largest and lowest received signal. In other words, the implemented Galactic calibration is primarily sensitive to how accurate the Galactic modulation is predicted, i.e. the difference between the Galactic center being maximum and minimum present in the antenna gain pattern. In [186], the systematic uncertainty on this prediction of the Galactic modulation was directly probed by comparing the averaged calibration constants obtained with the various sky models. The difference between the two models that yield the smallest and largest calibration constants was taken as the systematic uncertainty estimate and results in 6% on the cosmic-ray energy scale as well.

There is a strong correlation between the two derived uncertainty estimates. Since both come out to be 6%, we use this number as the systematic uncertainty in the accuracy of the Galactic calibration. The decision to use this estimation of the systematic uncertainty is arguable and to some extent boils down to a philosophical discussion. While the variety of available sky models is quite comfortable – and will improve further in the future – it cannot be excluded that all models might be wrong by some offset on the absolute scale. There are a few reference maps that are used in the majority of the models and thus possess a large weight in the absolute temperature scales of the model comparison. In particular, the full-sky map at 408 MHz is used in all seven

models – although in three different versions that include independent corrections and improvements to the map.

On the other hand, the prominent status of the 408 MHz map is likely most relevant for the prediction of the sky models at hundreds of MHz but not so much for the frequency range of AERA. Furthermore, the majority of the individual maps is only used in a few models. Some of these maps were generated from measurements with the same instrument and would share any inherent systematic biases. Still, the maps represent a large variety of different astronomical telescopes and instruments that were independently calibrated. This variety with independent absolute calibrations is propagated to some degree into the sky models. Therefore, we consider the likeliness of a significant global scale offset of all models to be small.

Estimating the accuracy of the sky models with regard to the absolute scale is in general the duty of the respective authors. Most of them performed checks to quantify the accuracy and the results were at the same level or lower than our systematic uncertainty estimate (see Sec. 5.1).

With the intent to get a very conservative estimate of the systematic uncertainty, one could add the quoted uncertainties in the temperature scales of the individual reference maps to the number that results from the model comparison. The authors of the reference maps estimate uncertainties of their temperature scales ranging between 5% and 20%[1]. However, while trying to untangle how those uncertainties exactly propagate into the comparison of the sky models seems virtually impossible, we believe that those uncertainties are already reflected in our systematic uncertainty estimate and adding them in some form would be double counting [2].

We add a contribution of 1% to the systematic uncertainty from the model comparison. That contribution comes from the choice in the analysis of using time averaged calibration constants instead of monthly constants as they were originally calculated. When running the analysis with time averaged constants, we observe a difference to using monthly constants that is of the order of 1%. The conclusion that performing the Galactic calibration constants in monthly periods is not beneficial in the application in physics analyses led to a proposal for improving the method, which is work in progress. We add this contribution in quadrature to the systematic uncertainty in order to stay consistent with the current implementation of the Galactic calibration. In summary, the systematic uncertainty from the Galactic calibration amounts to 6.1%.

Antenna response pattern

Calibrating the response patterns of the antennas is a challenging task. The absolute scale calibration is uncritical – at least in this analysis – as any offsets are absorbed by the Galactic calibration. Achieving a high accuracy in the gain pattern description in the

[1] We note that there are substantial differences with regard to how much effort the authors of the individual publications put into estimating the accuracy of their maps.

[2] In a simplified picture, the sky models can be conceived as fits to sample points, representing the reference maps. Each sample point in this picture has an individual uncertainty assigned to it – representing the temperature scale uncertainties of the reference maps – that can be assumed uncorrelated. The different models bring a variability of which sample points is fitted against, since each model is built with a different set of reference maps. Having seven models that bring this variability means that the uncertainties of the individual reference maps propagate into the output of the models, which come out as part of the result of the model comparison (similar to a bootstrapping method for estimating the uncertainties of parameters in the fit of a function).

directional phase space, on the other hand, is all the more relevant and cannot be done with the Galactic calibration as it is implemented[1]. Directionally dependent offsets would cause biases in several aspects of the reconstruction chain. This complexity and the efforts made to provide an accurate description of the antenna patterns were discussed in Sec. 6.1.2. Here, we are mostly concerned with the case of the Butterfly antenna which is the dominant antenna type in the dataset of the analysis. Also, we consider the LPDA antenna pattern to be understood better. Unfortunately, there is no fit estimate for the systematic uncertainty of just the directionally dependent component of the accuracy of either antenna pattern. Indirectly, a directionally dependent bias in the antenna pattern would show up in higher-level analyses. We observe a zenith-angle dependent bias in the energy scale comparison (Sec. 8.1.7.2) that we attribute to zenith-angle dependent systematic effects in the antenna pattern. We use the observed variation of the analysis result with the zenith angle of approximately 2.6% to assess the size of the systematic uncertainty of the antenna pattern. This contribution would account for wrong antenna gains in the direction of the incoming shower. In addition, a systematic offset could be introduced by a wrong antenna pattern in the Galactic calibration. In that case, not just a gain offset in a specific direction would matter but rather a misdescription of the pattern on large scales that would lead to a wrong integrated folding of the full-sky Galactic signal through the antenna pattern. Therefore, we conservatively estimate the systematic uncertainty due to the antenna response pattern at 5%. A dedicated study will presumably be able to lower this uncertainty considerably. In particular, within the recently performed drone calibration campaign for the AugerPrime RD, also calibration flights at AERA stations. These measurements will be used to validate the simulated antenna patterns.

LDF model

The performance of the GeoCeLDF model in reconstructing the radiation energy of a shower was tested on simulations across an energy range well exceeding the one covered in this work [210]. The relative differences between the reconstructed and true radiation energies are distributed with a mean value around 1% and a scatter of 4%. The bias of 1% on radiation energy scales to 0.5% on cosmic-ray energy.

Atmosphere

Although the radio detection technique is far less dependent on the atmospheric conditions than, for example, the fluorescence technique, the refractive index of the air does impact the amount of radiation energy that is produced. A 10% change in $n - 1$, where n is the refractive index at sea level, corresponds to to a 3% variation in the radiation energy [224]. Throughout the seasons, the refractive index at the Pierre Auger Observatory scatters by about 7% as determined from GDAS data. In a simulation study for the yearly scatter of the radiation energy due to the atmosphere, also taking into account the variation of the air-density profile, the cumulated systematic uncertainty on cosmic-ray energy was estimated to be 1.25% [200].

In this work, the actual impact because of the atmosphere is likely significantly smaller since we use GDAS atmospheric profiles from the time of the measured events.

[1] Unfolding the directional antenna pattern from the observation of the Galactic background is thinkable with more sophisticated mathematical frameworks like information field theory [254].

This way, most of the seasonal variations should be corrected for. However, it is difficult to quantify the accuracy of the GDAS profiles. Therefore, we use the estimate of 1.25% as an upper limit to the systematic uncertainty contribution from the atmosphere.

Ground conditions

The soil beneath the antennas can reflect the incoming radio emission adding a signal contribution from below, if the antenna is sensitive in that direction. This issue is expected to be more relevant for vertical showers than for inclined showers and is also expected to be stronger for the Butterfly antennas compared to the LPDA antennas [255]. In the NEC-2 simulations of the antenna gain patterns, the effect is taken into account by placing the detector model on a varying ground with defined values for the conductivity and permittivity of the soil. Default values are taken from soil measurements at AERA. The conductivity and permittivity vary for different locations in the array and as a function of the wetness of the soil. In a NEC-2 simulation study for the RD, the impact of ground conductivity and permittivity on the reconstruction of the electromagnetic energy was studied [256]. The soil parameters were varied well beyond the range found in a measurement campaign at AERA [193]. The study found a bias on the level of cosmic-ray energy of 1.8% with a scatter of 4.4%. This result was specifically derived for the RD but with assumptions on the ground conditions covering well beyond the real situation at AERA. Therefore, we assume that the found bias of 1.8% also holds – at least as an upper limit – as a systematic uncertainty from varying ground conditions for measurements with AERA.

Quiet sun

The sun is a natural emitter of radio waves. Fortunately, the data period used in this work falls into a quiet phase of the solar cycle. Also, high-amplitude emission from the active sun can be detected by AERA [169] and affected periods could therefore, in principle, be flagged as bad periods in air-shower reconstruction. On the other hand, the quiet sun permanently adds to the background signal detected by the AERA stations while it is present in the sky and can therefore influence the Galactic calibration. In Sec. 5.5.1, this impact on the Galactic calibration was estimated with a toy model to be at the level of 0.5% on cosmic-ray energy.

Primary type bias

The GeoCeLDF was tested for a bias in the estimated radiation energy against the primary particle of the shower (Sec. 8.1.7.4.) We adopt the found bias of 1.9% as a systematic uncertainty from the unknown shower primaries.

Mass composition bias with respect to Auger mix

In the process of matching the simulated showers to the measured counterparts by calorimetric energy, we subtract the invisible energy (Eq. 8.1) from the total shower energy estimate E_{SD}. By that, we implicitly assume that our dataset has the same mass composition as the *Auger mix*, which is the mass composition that is measured by the fully efficient SD and that is inherently contained in the invisible energy estimate through the data-driven method it was estimated by. However, AERA – and in particular the dataset for this analysis – is not fully efficient and likely has a composition bias against lighter primaries (deep showers). In turn, the SD energies of the measured showers

in our event dataset would be biased on average. From those energies, we calculate the input energies for the creation of our simulations, at which point the bias would propagate into our analysis.

For an upper limit estimate on the size of this mass composition bias, we consider a maximum thinkable – even if highly unrealistic – difference between the mass compositions that are detected by the SD and by AERA. This maximum difference appears in the scenario that the SD only observes proton showers while AERA only sees iron showers, or vice versa. In Fig. 8.6, estimates of the invisible energy fraction as a function of calorimetric energy by Barbosa et al. [242] are shown for a 50:50 mixed composition and for pure proton and iron showers. The difference between the invisible energy estimates of proton and iron showers propagates to a 5% difference on cosmic-ray energy, which we use as a current estimate on the systematic uncertainty through a mass composition bias.

However, we note that this uncertainty can likely be reduced significantly with a more sophisticated estimation. From the radio reconstruction of the simulation set for this work and from the event selection, it is already clear that the assumed scenario is too strict. About 36% of the proton simulations and 20% of the iron simulations are either not reconstructed or do not pass the quality cuts (see Tab. 8.2), which gives an estimate on the size of the mass bias of AERA and the radio reconstruction and that is significantly smaller than the considered 100:0 scenario.

One idea to estimate the mass composition bias is to use an SD-simulation dataset with full efficiency and reweight its $X_{\mathrm{max}}^{\mathrm{MC}}$ distribution to match the distribution in our event dataset from Fig. 8.13 through an appropriate event selection. The change in the mean energy of the simulation dataset before and after reweighting would give a handle on the systematic bias introduced by a mass composition bias from AERA.

Signal loss during reconstruction

The premise for the logic of the analysis that potential signal loss and biases introduced in the radio-event reconstruction are canceled out by treating measured and simulated events in the same way was tested and validated (Sec. 8.1.7.3). The found bias is of the order of 0.2σ and thus much smaller than the statistical accuracy of the method. Therefore, we skip this contribution.

8.1.8.2 Theoretical uncertainties

Radio emission yield

What the Galactic calibration delivers on the side of the measurements, is provided on the simulation side by the microscopic description of the air-shower radio emission through CoREAS. The radio energy scale is grounded on the absolute scale of the predicted *radio emission yield* in simulations, i.e. the amount of radio emission released in a shower with a given electromagnetic energy. The physical description of the emission of electromagnetic radiation at radio wavelengths due to the electromagnetic shower component from first-principles classical electrodynamics is arguably rock-solid and does not contribute to the systematic uncertainties. However, the implementation of this physical description into Monte-Carlo software can introduce uncertainties. As discussed in Sec. 2.2.5.2, there are mainly two popular frameworks that calculate the radio emission

from air-showers, CoREAS and ZHS, and they do it with different implementations, the *endpoints* and *ZHS* formalisms.

In trying to assess a systematic uncertainty of the radio emission yield, a similar problem occurs as for the estimation of the systematic uncertainty of the Galactic calibration. The only proper and currently available handle for this assessment is the comparison of available implementations. However, regardless of how well the frameworks agree, conceptually they may all be off from the truth. We decided to give two estimates for the systematic uncertainty of the radio emission yield that each reflect a certain point of view on what level of profundity is necessary to adequately probe this uncertainty. It is also a matter of how much trust is given to the Monte-Carlo implementations of the air-shower radio emission without an external validation from an experimental measurement.

First, we estimate the systematic uncertainty under the assumption that the implementations in CoREAS and ZHAireS exhibit a sufficient level of sophistication and a cross-comparison between them alone is an appropriate way to approximate the uncertainty. Fortunately, comparison studies for the frequency band from 30 MHz to 80 MHz have already been conducted. In [238], the radio emission yield from showers generated with CORSIKA and ZHAires was compared finding 5.2% more radiation energy predicted by CoREAS. This result suggests an agreement between the two codes and with that a systematic uncertainty on cosmic-ray energy level of 2.6%. Contained in that value is also a contribution from the different employed electromagnetic interaction models in CORSIKA and ZHAireS.

Extended comparisons were also performed in [240] with the aid of the new CORSIKA 8 framework. Both radio-emission formalisms are implemented in CORSIKA 8 allowing for an even more direct comparison of them independent of the Monte-Carlo implementation of the air-shower development and independent of the electromagnetic interaction model[1] performed with the exact same showers. When simulating the tracks of the particles in very fine steps – enhancing the accuracy of the simulations but also heavily increasing the necessary computing time – the difference between the endpoint formalism as originally implemented in CoREAS and the ZHS formalism levels out at about 1% on cosmic-ray energy showing tremendous agreement[2]. In a comparison of showers from CORSIKA 8 and from CORSIKA 7 with CoREAS, the latter predicts 8.3% more radiation energy translating to an agreement on cosmic-ray energy at 4.2%.

Therefore, a systematic uncertainty derived from comparing the available code implementations for the prediction of the radio emission yield from air showers is made based on these two studies. Conservatively the estimate is rounded up to 5%.

Experimental validation of the simulation codes is a challenging task. The UHECR-induced extensive air-showers, whose radio emission they calculate, cannot be replicated in a laboratory. Nevertheless, modified experimental setups can be constructed in an attempt to represent a real shower. In a setup at SLAC, the SLAC T-510 experiment measured the radio emission from the particle shower created in the collision of an electron bunch with a High-Density Polyethylene target [257]. The electron beam had a fixed energy that resulted in a particle shower equivalent to an air shower from a 4×10^{18} eV cosmic ray, which is within the energy range of the analysis in this work. The

[1] CORSIKA 8 uses yet another electromagnetic interaction model than CORSIKA 7 and ZHAireS

[2] The configuration of the simulations for our analysis are equivalent to those settings.

analysis of the SLAC T-510 measurement was later improved for previously unaccounted systematics [258]. The experimental setup and the particle shower was simulated in GEANT4 [259] with a subsequent calculation of the radio emission using the endpoints and ZHS formalisms. In comparison of the peak voltage from the recorded signals between the experimental data and the predictions from simulations, good agreement was found, at the level of 5%. The systematic uncertainties of the measurement were estimated at approximately 10%. However, the used antennas in the measurement were sensitive in the frequency band from 200 MHz to 1200 MHz and for the analysis, the band from 300 MHz to 900 MHz was used. This aspect is inevitable to be able to probe the measured cascade that was much smaller than an extensive air shower. In this context, the good description of the measurement through the simulations is especially notable. However, it poses a difficulty in the concrete interpretation of the result for our application that is based in the 30 MHz to 80 MHz band.

The SLAC T-510 measurement can be interpreted as a first experimental validation of the radio-emission calculation in air-shower simulations. In that case, a systematic uncertainty on the radio emission yield of ~10% may be assigned for the energy-scale analysis of this work, which is taken from the systematic uncertainties on the measurement.

The question remains, if either value – 5% from the prediction comparison or ~10% from the systematic uncertainties of the SLAC T-510 experiment – can serve as an appropriate and well-motivated estimate for the systematic uncertainty. A similar situation evolved around the determination of the absolute scale of the fluorescence yield, which is fundamental for the energy scale with the fluorescence technique (see Sec. 7.2). This topic has been discussed extensively, particularly in a series of dedicated workshops [55, 260, 261]. Contributing investigations concern both simulation studies and meta analyses of experimental measurements of the fluorescence yield. These efforts were necessary to provide a confident understanding of the associated molecular physics leading to accurate air fluorescence models used in the reconstruction of cosmic-ray induced air showers. For the FD energy scale of the Pierre Auger Observatory, the systematic uncertainty contribution from the fluorescence yield is estimated at 3.6% [54]. It was attempted to agree on a unitary fluorescence model to be used among the various experimental collaborations [29, 262], but still different models are used which have to be taken into consideration in cross-comparisons of energy-involved results.

This analogy should be an impulse to understand the radio emission yield from showers of charged particles on a comparable level of accuracy. However, this impulse does not imply the necessity to conduct the same amount of experimental measurements of the radio emission yield as was done for the absolute scale determination of the fluorescence yield. Fundamentally, the situation is different in the sense that the physics foundations enter into the question of accuracy with different levels of complexity. Fore example, the molecular physics relevant to the fluorescence yield concern several quenching processes that depend on atmospheric conditions, like pressure and temperature, in various ways. The classical electrodynamics that establishes the description of the release of radio signals from moving charges is a precisely understood theory. It would not be the aim of experiments like the SLAC T-510 to probe this theory. Instead, what defines the uncertainty on the radio emission yield in simulations is the concrete implementation of classical electrodynamics as well as the accuracy of the simulation of the electromagnetic cascade. We discussed already that the two principal formalisms,

endpoints and ZHS, show agreement at the level of 1% if the shower particles are tracked very finely. Therefore, a major contribution to the uncertainty would need to come from the code implementation of the electromagnetic interactions. The latter was tested in the mentioned comparison studies between CORSIKA 7, CORSIKA 8 and ZHAireS that conclude in an agreement within 5%.

Choice of hadronic interaction model

We use Sibyll 2.3d and UrQMD for the hadronic-interaction modeling in the simulations. There are several other models available that can be used instead and that cover the phase space of the most popular theories about air-shower physics. The differences in the hadronic shower component, which are important in many aspects of UHECR research, play a minor role for the total amount of simulated radio emission. A test switching between QGSJetII-04 and EPOS-LHC for the high-energy part of the hadronic-interaction modeling and FLUKA and UrQMD for the low-energy part in simulations of showers of 10^{18} eV energy results in a variation of the predicted radiation energy that corresponds to a systematic uncertainty on the cosmic-ray energy of 0.13% [224]. Due to this small number, we refrained from cross-checking our analysis with other hadronic interaction models.

Thinning

In this work, we use a thinning level of 10^{-6}. Using an even finer thinning level does not result in higher accuracy but only in an increased simulation runtime for the prediction of radiation energies from simulated air showers. In this regard, our setting is expected not to introduce any bias [224].

Energy thresholds of shower particles

The particles in the simulation are only tracked until they fall below a certain threshold energy. This threshold is set differently for different particle types. We use standard values (300 MeV for hadrons, 10 MeV for muons and 250 keV for electrons, positrons and photons) that ensure an accurate result. A study showed a bias on the level of 0.5% on cosmic-ray energy when varying those values within a reasonable range [224].

8.1.8.3 Summary of uncertainties

The statistical uncertainty in the result of the energy scale comparison is remarkably small at 0.8%. This high accuracy is due to the large statistics of the hybrid SD-AERA dataset at a high level of event quality.

In stating a systematic uncertainty, we draw a distinction between two points of view on the contribution from the absolute scale of the radio emission yield in simulations: There is the profound question – that we discussed in the previous section – whether a cross-comparison between code implementations for the radio emission of charged shower particles is sufficient to gauge this systematic uncertainty, or whether an experimental validation is indispensably needed. In the first case, we conclude from previously conducted studies that the systematic uncertainty can be estimated at 5% and we obtain a total systematic uncertainty on the radio energy scale of 11.2%. In the second case, we can currently only refer to the SLAC T-510 measurement that agrees with simulations at

Table 8.3: Summary of uncertainties on the radio energy scale.

Source of uncertainty	Size
Experimental uncertainties	**9.9 %**
Galactic calibration	6.1 %
Antenna response pattern	5 %
LDF model	0.5 %
Atmosphere	<1.25 %
Ground conditions	<1.8 %
Quiet sun	0.5 %
Simulation primary bias	1.9 %
Mass composition bias wrt. Auger mix	5 %
Theoretical uncertainties	**5.1 % / ~10.1 %**
Radio emission yield	5.0 % / ~10 %
Choice of hadronic interaction model	0.13 %
Thinning	<0.15 %
Energy thresholds of shower particles	<0.5 %
Stat. unc. of energy scale comparison	**0.8 %**
Total absolute scale uncertainty	**Stat.: 0.8 % ‖ Syst.: 11.2 % / ~14.2 %**

the level of 5% and we can adopt its systematic uncertainty of ~10% resulting in a total systematic uncertainty of ~14.2%.

Of course, the contribution from the radio emission yield to the total systematic uncertainty has a significant impact. An uncertainty contribution of ~10% dominates the total uncertainty as can be seen in Tab. 8.3. With a contribution of 5%, the radio emission yield is currently on a par with the Galactic calibration, the antenna response pattern and a possible mass composition bias from AERA. The latter two contributions are conservatively estimated at the moment and can likely be reduced significantly in the near future. The Galactic calibration was already studied quite extensively but probing its accuracy is difficult. Therefore, its systematic uncertainty contribution will likely stay in the (co-)dominant position.

The other sources of systematic uncertainties that we tested turn out to be of minor size. Some of these are probably still estimated conservatively and could be reduced in dedicated studies.

8.2 Discussion of the results & Outlook

Currently, the cosmic-ray energy scale of the Pierre Auger Observatory is defined by the scale provided by the FD. Most of the scientific results obtained with the Pierre Auger Observatory depend to a greater or smaller extent on the cosmic-ray energy. Thus, the interpretation of and the implications drawn from these results rely on the absolute energy scale. The FD energy scale has an estimated systematic uncertainty of 14% [54]. This uncertainty is dominated by the contribution from the calibration of the telescopes at about 10%.

In this work, we find a ratio of the radio energy scale to the FD energy scale of 1.12±0.8%. The statistical uncertainty is close to being negligibly small. The systematic uncertainty is estimated at 11.2% / ~14.2% for a contribution from the radio emission yield based solely on simulation comparisons (case $\mathcal{A}$) or building on the results from the SLAC T-510 experiment (case $\mathcal{B}$), respectively. While the analysis finds a 12% difference between the energy scales, the result is compatible with unity within the uncertainties from the FD side and from the radio side in case $\mathcal{B}$. In case $\mathcal{A}$ for the systematic uncertainty of the radio energy scale, the result translates to a 1.1σ difference of the FD energy scale from the radio energy scale when only taking into account the systematic uncertainty of the radio energy scale.

However, the systematic uncertainties in both energy scales can be assumed to be uncorrelated. Combining them yields an overall systematic uncertainty of 18% / ~20% for cases $\mathcal{A}$ and $\mathcal{B}$, respectively. The combined uncertainties leave enough room for a number of systematic effects that could – in summary – explain the found difference between the energy scales.

In the recent past, a new method for the absolute calibration of the FD has been put in place and calibration measurements for several of the telescopes have been conducted [249]. This method employs the so-called *XY-Scanner* to perform a pixelwise calibration. The systematic uncertainty of the method has been estimated to be notably smaller than the uncertainty of the previous method that is currently in use for the absolute calibration and energy scale determination of the FD. Once calibration measurements with the XY-Scanner are completed for all telescopes and the analysis is concluded, a comparing study of a potentially updated FD energy scale to the result of the this work will be of interest.

As discussed in Chap. 2, measuring the energy spectrum is a cardinal science objective in the study of UHECRs. In the results on the energy spectrum from the Pierre Auger Observatory and the Telescope Array, a significant disagreement is found [263]. While the energy spectra might naturally differ due to covering mostly separate declination bands, the discrepancy can partially be resolved by shifting the energy scales of the two observatories [264]. The spectrum from Telescope Array in general shows a larger particle flux compared to the spectrum from the Pierre Auger Observatory. Our analysis with the radio energy scale would find very good agreement between the energy scales if the FD energy scale were to be increased. As the joint studies on the energy spectra from the Pierre Auger Observatory and Telescope array show, such an increase would to some extent also mitigate the tension between the spectra.

The result obtained in this work applies to the energy range between 3×10^{17} eV and 4×10^{18} eV and to vertical showers up to 55°. For the highest energies and for inclined air showers, the result needs to be validated. However, the RD will be covering this exact phase space and it is just beginning operation at full scale. The presented method can thus act as a blueprint for an analogous study with the RD and the SD-1500 array.

8.3 Summary

This study concludes the work done by many collaborators over a time period of more than a decade to understand and be able to evaluate the cosmic-ray energy scale with the radio detection in measurements. In this time, the numerous ingredients that

go into the analysis have been collected and brought to accuracies on the percent level. In a revised approach, we compare the energy scales from the FD and from radio for energies between 3×10^{17} eV and 4×10^{18} eV and zenith angles below 55°. We find that with the radio energy scale shower energies are obtained that are 12% larger than with the FD energy scale. Within the current estimation of the systematic uncertainties, the energy scale difference is compatible with unity. However, a reduction of those uncertainties in the near future is possible. Therefore, a dedicated study to understand the systematic difference between the energy scales is advised. The presented analysis and its result certainly serve as an important cross-check of the established energy scale of the Pierre Auger Observatory. Once systematic effects and uncertainties are discussed and unanimously appraised – on the radio side this specially concerns the discussion on the radio emission yield – the FD and radio energy scales may be combined to define the energy scale of the Pierre Auger Observatory from both detection techniques.

9

Summary

The field of astroparticle physics is advancing with great steps in the research of ultra-high energy cosmic rays. Observations of cosmic-ray induced extensive air showers are understood to a comprehensive level of detail. The UHECR energy spectrum, for instance, is measured with great precision. Such scientific successes rest on great quality statistics collected with current observatories, in particular with the Pierre Auger Observatory. However, interpretations of the precise measurements lack a complete understanding of underlying physics and processes. Important open questions remain on the sources of UHECRs, the acceleration mechanisms that can achieve particle energies beyond EeV, the particle composition of the cosmic-ray flux and on the several aspects of air-shower physics. Observatories are upgrading their instruments and are adding new systems aimed at tackling these challenges. At the Pierre Auger Observatory, the recent AugerPrime detector upgrade on the full array-scale initiated Phase II of the project, with new electronics, scintillator surface detectors and the radio detector.

While the more traditional detection techniques for air showers with particle detectors and fluorescence techniques have shaped the current knowledge of UHECRs, the subfield of radio detection has matured to becoming a key player. With the help of digital signal processing, several projects have engineered arrays of radio antennas. These developments are culminating in large-scale radio detector systems around the world that are committed to measuring extensive air showers from cosmic rays. In particular, the Auger Engineering Radio Array (AERA) has paved the way for the design of the Auger Radio Detector (RD). In its recently finished installation, the RD has superseded AERA as the worldwide largest radio detector in this field.

From simulation studies, a rich scientific yield from the RD is expected, especially in the multi-hybrid environment of the Pierre Auger Observatory. Fortunately, the necessary reconstruction tools are already put in place to a large part, as many ingredients can be reused from work in the context of AERA. Another fundamental prerequisite for extraction of physics results is data quality control. One aspect of this part is the identification and removal of bad periods in the data stream. In-air radio emission from particle showers is well understood under fair weather conditions but gets heavily altered in the presence of strong atmospheric electric fields. Such conditions, typically connected to thunderstorms, pose significant problems in the reconstruction of affected air-shower events and potentially introduce biases in high-level results. It has become an established solution to monitor the atmospheric electric field at the site of the radio array with electric field mills (EFMs), for instance with two such devices at AERA. In the offline processing of air-shower data, flags for thunderstorm conditions are created based on the EFM recordings.

In preparation for the arrival of the RD, we designed, tested, constructed and commissioned a new network of EFMs across the entire array of the Pierre Auger Observatory. The network consists of five remote and autarkic stations equipped with an EFM in addition to the existing devices at AERA. We devised a station design that not only is able to withstand the harsh conditions of the Argentinian pampa for an operational time of at least ten years but that also meets the requirements for the electric field data to be recorded with an absolute calibration without the need for dedicated calibration campaigns. After successful tests of the components at Karlsruhe Institute of Technology, the parts were shipped to Malargüe and we deployed all stations in August and November of 2022. They have been taking data for about two years by now that are already used for thunderstorm flagging with the first air showers recorded by the growing RD array. We estimate the absolute calibration of the electric field recordings to have a systematic uncertainty of 6.5%. While this level of accuracy is not needed for thunderstorm identification, it may become beneficial in other use cases of the EFM data. The electric field measured at ground connects to global geophysical systems, like the global electric circuit, that in turn can be influenced by solar and geological phenomena, for example geomagnetic storms and volcanic eruptions. EFMs can serve as an important instrument in understanding these connections. The data from the new EFM stations are already being used in externally conducted geophysical studies from a recently formed research agreement. Besides the main task as part of the data quality control for the RD, the EFM network will expand the scientific impact of the Pierre Auger Observatory in the field of cosmo-geophysics.

Apart from being an engineering project that facilitated the arrival of the RD, AERA detected a sizeable high-quality set of air-shower events in hybrid mode with the SD-750. In this work, the fundamental quality of the radio detection technique to access the absolute cosmic-ray energy scale was exploited in application to those data. Such an analysis requires an absolute calibration of the detector to the highest possible accuracy. In the recent years, the calibration of radio antenna arrays for astroparticle physics via the diffuse Galactic emission has emerged as the prospective standard. Observing and characterizing the Galactic signal in the background has become a standard checkpoint for new arrays. When calibrating a radio detector by the Galaxy, a crucial ingredient is the expected signal that relies on predictions by sky models. We conducted a comprehensive comparison study of seven available sky models in the frequency range relevant to current and upcoming radio detectors. We find that the models agree at a level that corresponds to 7.2% on the cosmic-ray energy scale. In toy models for selected radio arrays – RNO-G, LOFAR, GRAND, OVRO-LWA, SKA, AERA, the RD and the IceCube surface array – using their location and designated frequency bands, we find a variation of the agreement between 10.8% and 5.9% – the latter for the radio arrays at the Auger Observatory – on the level of cosmic-ray energy. We also studied the influence of the quiet sun on the Galactic calibrator, which turns out to be almost negligible for the low frequency band of AERA and the RD but will become relevant for detectors like GRAND and SKA. Furthermore, we touched on the influences of the ionosphere and radio emission from Jupiter. We suggest that the worked out agreement levels between the sky models can be used as estimates of the systematic uncertainty from the predicted signal in the Galactic calibration of a radio detector. Still, the actual calibration has to be implemented with proper consideration of the detector system, like the components

of the signal chain and the response pattern of the antenna. In the case of AERA, the Galactic calibration has recently been implemented with the same set of sky models that we studied here. The implementation also estimated a systematic uncertainty due to the different sky models of 6% giving a consistent picture.

With a comprehensively studied Galactic calibration of AERA as the backbone of its absolute calibration, we performed an analysis to compare the established cosmic-ray energy scale of the Pierre Auger Observatory to the radio energy scale through measurements with AERA. The established energy scale is provided by the fluorescence detector (FD). It is of fundamental importance to the scientific results of the Pierre Auger Observatory, since the reconstructed cosmic-ray energy enters into most studies as a central observable. Our analysis gives the opportunity to provide an independent cross-check of the energy scale and to potentially improve its accuracy. The study is built on over a decade of efforts by several colleagues working directly on developing and advancing the analysis or providing the necessary ingredients. At the foundations of it, the radiation energy that is measured by AERA has been established as a universal energy estimator for accessing the electromagnetic shower energy and in turn the cosmic-ray energy. The previously worked out analysis approach showed a weakness regarding potential loss of signal in the reconstruction pipeline of the radio measurements.

Here, we compiled an updated approach to cross-check the energy scales in a direct data-to-simulation comparison on event-by-event basis. In the beginning, we blinded the analysis result to be able to develop the analysis and define event selection cuts without the risk of introducing a bias towards a favorable result. The analysis is based on hybrid air-shower data from the SD-750 array – that was calibrated with the FD energy scale – and AERA, collected between 2014 and 2020. Following a pre-selection of events to an already substantial level of quality, we simulate each of the 902 showers in CORSIKA with CoREAS in a realistic setting. We perform each simulation twice, for proton and iron as primary particles, respectively. The input parameters of the simulations are chosen such that the radiation energies are defined by the FD energy scale and are meaningfully comparable to those of the corresponding measured showers. After applying final selection cuts to both measured and simulated events we obtain a set of 537 (674) high-quality events with proton (iron) simulations. The ratios of radiation energies from measured and simulated showers explicitly contains the information on the agreement between the two energy scales.

With approval by the Pierre Auger Collaboration, we lifted the installed blinding of the results. From the high-quality event set and averaging the results for proton and iron simulations, we find that the radio energy scale gives larger energies than the FD energy scale by 12%. No major systematic effect is found in detailed stratification checks of the data. In particular, the result is constant across the studied energy range from 3×10^{17} eV to 4×10^{18} eV. We estimate the systematic uncertainty of the result at 11.2% if the accuracy of the radio emission yield in CoREAS simulations is considered to be appraisable solely from the comparison between the implementations of microscopic radio emission in Monte-Carlo codes. The only related experimental measurement, SLAC T-510, may be considered in this evaluation which instead yields an uncertainty of 14.2%. The found energy scale difference is within the systematic uncertainties. However, the uncertainties on the energy scales can likely be reduced in the future. Therefore, dedicated studies are suggested to further investigate the found difference. The conducted analysis and its

result conclude a long way of efforts to cross-calibrate the established FD energy scale of the Pierre Auger Observatory with the independent energy scale of the radio detection technique.

With AERA, we evaluated the radio energy scale for the energy range from 3×10^{17} eV to 4×10^{18} eV for vertical showers up to 55°. The result needs to be validated at higher energies and for inclined events. With the onset of RD operation, hybrid showers at the highest energies and with large inclinations will be collected at pace. The presented analysis can be used as a blueprint of a follow-up study with a high-quality RD/SD-1500 event set. Ingredients on the RD side – from signal reconstruction through detector calibration up to quality data selection – are already far advanced.

A

Appendix to Chap. 4

A.1 Cron jobs on efm-pc

```
## Los Leones
59 * * * * python3 /home/max/efm_readout/readout_station.py LL >> /home/max/efm_readout/output_LL/log.txt 2>&1
55 */4 * * * python3 /home/max/efm_readout/settime_station.py LL >> /home/max/efm_readout/output_LL/log.txt 2>&1
53 4 * * * /home/max/efm_readout/renamefile_station.sh LL >> /home/max/efm_readout/output_LL/log.txt 2>&1
04 */6 * * * python3 /home/max/efm_readout/recover_station.py LL >> /home/max/efm_readout/output_LL/log.txt 2>&1

## Los Morados
14 * * * * python3 /home/max/efm_readout/readout_station.py LM >> /home/max/efm_readout/output_LM/log.txt 2>&1
10 */4 * * * python3 /home/max/efm_readout/settime_station.py LM >> /home/max/efm_readout/output_LM/log.txt 2>&1
08 5 * * * /home/max/efm_readout/renamefile_station.sh LM >> /home/max/efm_readout/output_LM/log.txt 2>&1
19 */6 * * * python3 /home/max/efm_readout/recover_station.py LM >> /home/max/efm_readout/output_LM/log.txt 2>&1

## Loma Amarilla
29 * * * * python3 /home/max/efm_readout/readout_station.py LA >> /home/max/efm_readout/output_LA/log.txt 2>&1
25 */4 * * * python3 /home/max/efm_readout/settime_station.py LA >> /home/max/efm_readout/output_LA/log.txt 2>&1
23 5 * * * /home/max/efm_readout/renamefile_station.sh LA >> /home/max/efm_readout/output_LA/log.txt 2>&1
34 */6 * * * python3 /home/max/efm_readout/recover_station.py LA >> /home/max/efm_readout/output_LA/log.txt 2>&1

## CLF
44 * * * * python3 /home/max/efm_readout/readout_station.py CLF >> /home/max/efm_readout/output_CLF/log.txt 2>&1
40 */4 * * * python3 /home/max/efm_readout/settime_station.py CLF >> /home/max/efm_readout/output_CLF/log.txt 2>&1
38 4 * * * /home/max/efm_readout/renamefile_station.sh CLF >> /home/max/efm_readout/output_CLF/log.txt 2>&1
49 */6 * * * python3 /home/max/efm_readout/recover_station.py CLF >> /home/max/efm_readout/output_CLF/log.txt 2>&1
```

A.2 Troubleshooting

In this section, some typical problems are listed with solutions or instructions on how to find one. If there is a problem with an EFM, check whether the status code that is recorded with the data and look up the status message in the CS110 manual [78] for

possible explanations and tips for a solution. In the case of problems with the readout on the DAQ machines or with the monitoring database, refer to Julian Rautenberg[1].

- **There is no connection to a station from the efm-pc / DAQ13 machine.**
  First, try to find out where exactly the connection is interrupted, i.e. whether only the Moxa of the EFM is unreachable or also the Bullet or Rocket of the link. Try pinging the different components using the IP addresses listed in Table A.1.

  If a Rocket is not reachable, there may be a bigger problem with the corresponding FD site, e.g. a power cut. If the problem persists, contact the IT team of the local staff[2].

  In the case that the Rocket is reachable but the Bullet is not, there may either be a physical interruption of the WiFi link (e.g. the sector antenna of the Rocket or the grid dish antenna of the Bullet is misaligned. Have there been strong winds recently?) or there is a problem with the Bullet itself (e.g. no power).

  Lastly, if the Bullet is reachable but the Moxa is not, there may be a loose cable in the electronics box or the Moxa or PoE adapter is broken. Inspect the electronics box and bring spare components and a key for the electronics box.

- **The stations from the efm-pc are reachable, but the `PyCampbellCR1000` commands throw errors.**
  Probably, the npreal2 driver crashed that establishes the serial port connections to the Moxas. This problem should be fetched automatically by the script `recover_station.py`. However, you can also try to manually run the script `reinstall_driver.sh` on the efm-pc. A reboot of the efm-pc has sometimes been seen to prevent further crashes for a longer time.

- **The stations from the efm-pc are reachable and the npreal2 driver is functional but the readout command still throws errors.**
  There are several possible sources of problems in the readout for which `PyCampbellCR1000` will throw different error messages. In many cases, rerunning the command multiple times will eventually work.

  Sometimes, an error occurs in the midst of downloading data from the EFM buffer. Then, the last line written to the table may be truncated preventing further attempts to download the data. This case should be fetched automatically by the script `readout_station.py` but the line can also be removed manually from the file and it will be downloaded again with the next automatic call of the script.

- **The stations were read out on the DAQ machine but the data synchronization to the monitoring database failed. How to upload the data later?**
  If the connection to the monitoring database is working again, you can run the WeatherReader manually. On the efm-pc, navigate to the unsynchronized tables and unzip them using `bunzip2 <table_name>.dat.bz2`. Then, run

  ```
  /home/max/WeatherReader/Weather_<station> dd mm yyyy
  ```

[1] julian.rautenberg@uni-wuppertal.de
[2] sistemas@auger.org.ar

Table A.1: IP addresses of the DAQ13 and efm-pc and of the Rockets, Bullets and Moxas of the EFMs.

Station	Component	IP address
DAQ13		172.16.1.13
efm-pc		192.168.218.8
CRS	Moxa	172.18.1.192
AERAWS	Bullet	172.17.1.191
	Moxa	172.18.1.191
BATATA	Bullet	172.17.1.194
	Moxa	172.18.1.194
LL	Rocket	192.168.218.122
	Bullet	192.168.218.125
	Moxa	192.168.218.128
LM	Rocket	192.168.218.123
	Bullet	192.168.218.126
	Moxa	192.168.218.129
LA	Rocket	192.168.218.124
	Bullet	192.168.218.127
	Moxa	192.168.218.130
CLF	Moxa	192.168.218.165

with the correct station name `<station>` and date information (day `dd`, month `mm`, year `yyyy`; respect the number of digits, i.e. January is `01`).

On the DAQ13 machine, the WeatherReader scripts are located at the path `/home/monitor/WeatherReader_AERA`. After synchronization, zip the table again using `bzip2 <table_name>.dat`.

A.3 Photos of the EFM stations

Some additional photos of the new EFM stations are provided.

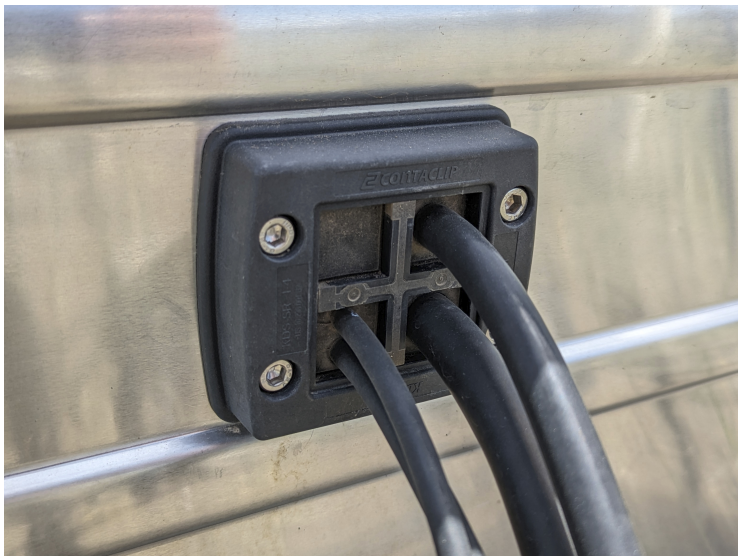

Figure A.1: Picture of the outside of an electronics box showing the cable glands.

Figure A.2: Picture from inside the electronics box at the CLF showing the Moxa TCF-90-M-ST converter and the fiber cable leaving the box.

Figure A.3: Picture of the container at the CLF with the cable tube for the fiber cable to enter into the container.

Figure A.4: Picture of the ground rod at LA with the clamp connecting the rod to the ground cable of the station.

B

Appendix to Chap. 5

B.1 Model comparison for selected radio experiments

Table B.1: Values of $r_{exp;\,m_1,\,m_2}$ for each combination of the interpolation models and for all selected radio arrays.

RNO-G							
$r_{exp;\,m_1,\,m_2}$ (%)	LFmap	GSM	GSM16	LFSM	GMOSS	SSM	ULSA
LFmap	-	5.1	9.6	−7.6	9.2	5.8	2.2
GSM	−5.1	-	4.5	−12.7	4.1	0.7	−2.9
GSM16	−9.6	−4.5	-	−17.1	−0.4	−3.7	−7.4
LFSM	7.6	12.7	17.1	-	16.8	13.4	9.8
GMOSS	−9.2	−4.1	0.4	−16.8	-	−3.4	−7.0
SSM	−5.8	−0.7	3.7	−13.4	3.4	-	−3.6
ULSA	−2.2	2.9	7.4	−9.8	7.0	3.6	-
LOFAR low							
$r_{exp;\,m_1,\,m_2}$ (%)	LFmap	GSM	GSM16	LFSM	GMOSS	SSM	ULSA
LFmap	-	3.4	−5.5	−9.8	6.1	−3.7	−13.8
GSM	−3.4	-	−8.9	−13.2	2.6	−7.1	−17.2
GSM16	5.5	8.9	-	−4.3	11.5	1.8	−8.3
LFSM	9.8	13.2	4.3	-	15.8	6.1	−4.0
GMOSS	−6.1	−2.6	−11.5	−15.8	-	−9.7	−19.8
SSM	3.7	7.1	−1.8	−6.1	9.7	-	−10.1
ULSA	13.8	17.2	8.3	4.0	19.8	10.1	-
LOFAR high							
$r_{exp;\,m_1,\,m_2}$ (%)	LFmap	GSM	GSM16	LFSM	GMOSS	SSM	ULSA
LFmap	-	7.0	12.8	−5.6	12.5	8.1	4.9
GSM	−7.0	-	5.9	−12.6	5.6	1.1	−2.1
GSM16	−12.8	−5.9	-	−18.4	−0.3	−4.8	−8.0
LFSM	5.6	12.6	18.4	-	18.1	13.7	10.5
GMOSS	−12.5	−5.6	0.3	−18.1	-	−4.5	−7.7
SSM	−8.1	−1.1	4.8	−13.7	4.5	-	−3.2
ULSA	−4.9	2.1	8.0	−10.5	7.7	3.2	-
GRAND							
$r_{exp;\,m_1,\,m_2}$ (%)	LFmap	GSM	GSM16	LFSM	GMOSS	SSM	ULSA
LFmap	-	1.8	1.5	−14.3	7.3	1.4	−5.2
GSM	−1.8	-	−0.2	−16.0	5.5	−0.4	−6.9
GSM16	−1.5	0.2	-	−15.8	5.7	−0.1	−6.7
LFSM	14.3	16.0	15.8	-	21.5	15.7	9.1
GMOSS	−7.3	−5.5	−5.7	−21.5	-	−5.9	−12.4
SSM	−1.4	0.4	0.1	−15.7	5.9	-	−6.6
ULSA	5.2	6.9	6.7	−9.1	12.4	6.6	-

Table B.1: continued.

OVRO-LWA							
$r_{exp;\,m_1,\,m_2}$ (%)	LFmap	GSM	GSM16	LFSM	GMOSS	SSM	ULSA
LFmap	-	2.2	−5.8	−11.4	4.6	−5.2	−14.8
GSM	−2.2	-	−8.0	−13.6	2.4	−7.4	−17.0
GSM16	5.8	8.0	-	−5.6	10.4	0.6	−9.0
LFSM	11.4	13.6	5.6	-	16.0	6.2	−3.4
GMOSS	−4.6	−2.4	−10.4	−16.0	-	−9.8	−19.3
SSM	5.2	7.4	−0.6	−6.2	9.8	-	−9.6
ULSA	14.8	17.0	9.0	3.4	19.3	9.6	-
SKA-low							
$r_{exp;\,m_1,\,m_2}$ (%)	LFmap	GSM	GSM16	LFSM	GMOSS	SSM	ULSA
LFmap	-	4.8	7.5	−6.1	9.1	3.4	6.1
GSM	−4.8	-	2.7	−10.9	4.2	−1.5	1.2
GSM16	−7.5	−2.7	-	−13.6	1.6	−4.1	−1.5
LFSM	6.1	10.9	13.6	-	15.1	9.5	12.2
GMOSS	−9.1	−4.2	−1.6	−15.1	-	−5.7	−3.0
SSM	−3.4	1.5	4.1	−9.5	5.7	-	2.7
ULSA	−6.1	−1.2	1.5	−12.2	3.0	−2.7	-
Auger							
$r_{exp;\,m_1,\,m_2}$ (%)	LFmap	GSM	GSM16	LFSM	GMOSS	SSM	ULSA
LFmap	-	4.8	0.7	−5.6	6.0	−3.1	−2.1
GSM	−4.8	-	−4.1	−10.4	1.3	−7.9	−6.9
GSM16	−0.7	4.1	-	−6.3	5.4	−3.8	−2.8
LFSM	5.6	10.4	6.3	-	11.7	2.5	3.5
GMOSS	−6.0	−1.3	−5.4	−11.7	-	−9.2	−8.1
SSM	3.1	7.9	3.8	−2.5	9.2	-	1.0
ULSA	2.1	6.9	2.8	−3.5	8.1	−1.0	-
IceCube							
$r_{exp;\,m_1,\,m_2}$ (%)	LFmap	GSM	GSM16	LFSM	GMOSS	SSM	ULSA
LFmap	-	9.0	13.6	−5.0	15.3	8.6	11.0
GSM	−9.0	-	4.7	−13.9	6.4	−0.4	2.0
GSM16	−13.6	−4.7	-	−18.6	1.7	−5.0	−2.7
LFSM	5.0	13.9	18.6	-	20.3	13.5	15.9
GMOSS	−15.3	−6.4	−1.7	−20.3	-	−6.8	−4.4
SSM	−8.6	0.4	5.0	−13.5	6.8	-	2.4
ULSA	−11.0	−2.0	2.7	−15.9	4.4	−2.4	-

C

Appendix to Chap. 8

C.1 Reconstruction configuration for raw AERA data

ModuleSequence.xml

```
<!DOCTYPE sequenceFile [
  ...
  ]>

<sequenceFile
    ...
  <moduleControl>

    <loop numTimes="unbounded">

      <module> EventFileReaderOG                                  </module>

      <module> EventCheckerOG                                     </module>

      <!-- SD selection and reconstruction -->
      &SdCalibrationSelection;
      &SdReconstruction;

      <module> RdEventPreSelector                                 </module>

      &RdEventInitializationAndStationSelection;

      <module> RdChannelSelector                                  </module>
      <module> RdChannelADCToVoltageConverter                     </module>
      <module> RdChannelAmplitudeTemperatureDependenceCorrector   </module>
      <module> RdChannelPedestalRemover                           </module>
      <module> RdChannelResponseIncorporator                      </module>
      <module> RdChannelGalacticCalibrator                        </module>
      <module> RdStationPositionCorrection                        </module>
      <module> RdChannelBeaconTimingCalibrator                    </module>
      <module> RdChannelBeaconSuppressor                          </module>
      <module> RdStationTimingCalibrator                          </module>
      <module> RdStationTimeWindowConsolidator                    </module>
      <module> RdChannelTimeSeriesTaperer                         </module>
      <module> RdChannelBandstopFilter                            </module>
      <module> RdChannelUpsampler                                 </module>

      <module> RdAntennaChannelToStationConverter                 </module>

      &RdStationSignalReconstruction;

      &RdNoiseStationRejector;

      <module> RdPlaneFit                                         </module>

      <module> RdGeoCeLDFFitter                                   </module>

      <module> RdEventPostSelector                                </module>

      &RdTraceProcessingForWriteOut;

      <module> EventFileExporterOG                                </module>
      <module> RecDataWriterNG                                    </module>

    </loop>

  </moduleControl>

</sequenceFile>
```

bootstrap.xml

```
  <?xml version="1.0" encoding="iso-8859-1"?>

  <!DOCTYPE bootstrap [
    ...
  ]>

<bootstrap
    ...
<centralConfig>
    ...
  </centralConfig>

    <parameterOverrides>

      <configLink id="RdEventPreSelector">
        <RdEventPreSelector>
          <MinNumberOfStations> 3 </MinNumberOfStations>
          <UseExternallyTriggeredEvent> 0 </UseExternallyTriggeredEvent>
          <UseSDTriggeredEvent> 1 </UseSDTriggeredEvent>
          <UseGUITriggeredEvent> 1 </UseGUITriggeredEvent>
          <UseFDTriggeredEvent> 1 </UseFDTriggeredEvent>
          <UseHEATTriggeredEvent> 1 </UseHEATTriggeredEvent>
          <UseAERAletTriggeredEvent> 1 </UseAERAletTriggeredEvent>
          <FirstAllowedEventDateTime> 2010-01-01T12:00:00.0 </FirstAllowedEventDateTime>
          <LastAllowedEventDateTime>  2030-12-31T12:00:00.0 </LastAllowedEventDateTime>
        </RdEventPreSelector>
      </configLink>

    <configLink id="RdEventInitializer">
      <RdEventInitializer>
        <SetCoordinateOriginTo> SDCore </SetCoordinateOriginTo>
        <NoiseWindowStart unit="ns"> 2000.0 </NoiseWindowStart>
        <NoiseWindowStop unit="ns"> 5000.0</NoiseWindowStop>
        <ConsiderSdUncertainity> yes </ConsiderSdUncertainity>
        <SignalSearchWindowOffset unit="ns"> -610.0 </SignalSearchWindowOffset>
        </RdEventInitializer>
    </configLink>

    <configLink id="RdStationRejector">
      <RdStationRejector>
      <stationList> 257 253 252 246 245 185 187 191 198 207 </stationList>
      </RdStationRejector>
    </configLink>

    <configLink id="RdChannelGalacticCalibrator">
      <RdChannelGalacticCalibrator>
        <NameConstantsFile> /path/to/CalibrationConstants.dat </NameConstantsFile>
      </RdChannelGalacticCalibrator>
    </configLink>

    <configLink id="RdChannelBeaconTimingCalibrator">
      <RdChannelBeaconTimingCalibrator>
        <RejectIfNoRefPhaseAvailable> 0 </RejectIfNoRefPhaseAvailable>
        <RejectIfCorrectionFailed> 0 </RejectIfCorrectionFailed>
        <UseCrossCorrelationMethod> 1 </UseCrossCorrelationMethod>
      </RdChannelBeaconTimingCalibrator>
    </configLink>

    <configLink id="RdAntennaChannelToStationConverter">
      <RdAntennaChannelToStationConverter>
        <UsedDirection> SdReconstruction </UsedDirection>
      </RdAntennaChannelToStationConverter>
    </configLink>

    <configLink id="RdTopDownStationSelector">
      <RdTopDownStationSelector>
        <minNumberOfStations> 4 </minNumberOfStations>
        <stopAtFirstStation> 0 </stopAtFirstStation>
        <additionalSystematicError unit="ns"> 7 </additionalSystematicError>
      </RdTopDownStationSelector>
    </configLink>

    <configLink id="RdEventPostSelector">
      <RdEventPostSelector>
        <MinNumberOfStationsWithPulseFound> 3 </MinNumberOfStationsWithPulseFound>
      </RdEventPostSelector>
```

```
    </configLink>

    <configLink id="RdStationTimeSeriesWindowCutter">
      <RdStationTimeSeriesWindowCutter>
        <WindowSize unit="ns"> 2000 </WindowSize>
      </RdStationTimeSeriesWindowCutter>
    </configLink>

    <configLink id="RdPlaneFit">
      <RdPlaneFit>
        <!-- Allow multiple runs of the module (do not lock parameters in ParameterStorage) -->
        <allowMultipleCalls> yes </allowMultipleCalls>
      </RdPlaneFit>
    </configLink>

    <configLink id="RdGeoCeLDFFitter">
      <RdGeoCeLDFFitter>
        <InfoLevel> 3 </InfoLevel>
      </RdGeoCeLDFFitter>
    </configLink>

    <configLink id="SdEventSelector">
      <SdEventSelector>
        <EnableBottomUpSelection> 0 </EnableBottomUpSelection>
      </SdEventSelector>
    </configLink>

  </parameterOverrides>

</bootstrap>
```

C.2 Reconstruction configuration for pre-selected AERA data

ModuleSequence.xml

```
<!DOCTYPE sequenceFile [
    ...
  ]>

<sequenceFile
  ...
  <moduleControl>

    <loop numTimes="unbounded">

      <module> EventFileReaderOG                                  </module>

      <module> EventCheckerOG                                     </module>

      <!-- SD selection and reconstruction -->
      <!-- &SdCalibrationSelection; -->
      <!-- &SdReconstruction; -->

      <module> RdEventPreSelector                                 </module>

      &RdEventInitializationAndStationSelection;

      <module> RdChannelSelector                                  </module>
      <module> RdChannelADCToVoltageConverter                     </module>
      <module> RdChannelAmplitudeTemperatureDependenceCorrector   </module>
      <module> RdChannelPedestalRemover                           </module>
      <module> RdChannelResponseIncorporator                      </module>
      <module> RdChannelGalacticCalibrator                        </module>
      <module> RdStationPositionCorrection                        </module>
      <module> RdChannelBeaconTimingCalibrator                    </module>
      <module> RdChannelBeaconSuppressor                          </module>
      <module> RdStationTimingCalibrator                          </module>
      <module> RdStationTimeWindowConsolidator                    </module>
      <module> RdChannelTimeSeriesTaperer                         </module>
      <module> RdChannelUpsampler                                 </module>

      <module> RdAntennaChannelToStationConverter                 </module>

      &RdStationSignalReconstruction;
```

```
      &RdNoiseStationRejector;

      <module> RdPlaneFit                                    </module>

      <module> RdGeoCeLDFFitter                              </module>

      <module> RdEventPostSelector                           </module>

      &RdTraceProcessingForWriteOut;

      <module> RdREASSimPreparatorNG                         </module>
      <module> EventFileExporterOG                           </module>
      <module> RecDataWriterNG                               </module>

    </loop>

  </moduleControl>

</sequenceFile>
```

bootstrap.xml

In the default implementation, Offline allows to pass external shower geometries (arrival direction, shower core, core time) that can be used in subsequent reconstruction steps but no other shower parameter. We modified the module `RdEventInitializer` to also specify an external shower energy that is written as the SD reconstructed energy and can be used by the radio reconstruction. Hence, in the `bootstrap.xml`, a new configuration for the `RdEventInitializer` is set, which expects external shower geometries that also contain a shower energy estimate with uncertainty.

```
<?xml version="1.0" encoding="iso-8859-1"?>

<!DOCTYPE bootstrap [
  ...
]>

<bootstrap
  ...
  <centralConfig>

    ...

    <configLink
      id         = "RdEventInitializer"
      type       = "XML"
      xlink:href = "/path/to/custom/RdEventInitializer.xml"/>

  </centralConfig>

  <parameterOverrides>

    <configLink id="RdEventPreSelector">
      <RdEventPreSelector>
        <MinNumberOfStations> 3 </MinNumberOfStations>
        <UseExternallyTriggeredEvent> 0 </UseExternallyTriggeredEvent>
        <UseSDTriggeredEvent> 1 </UseSDTriggeredEvent>
        <UseGUITriggeredEvent> 1 </UseGUITriggeredEvent>
        <UseFDTriggeredEvent> 1 </UseFDTriggeredEvent>
        <UseHEATTriggeredEvent> 1 </UseHEATTriggeredEvent>
        <UseAERAletTriggeredEvent> 1 </UseAERAletTriggeredEvent>
        <FirstAllowedEventDateTime> 2010-01-01T12:00:00.0 </FirstAllowedEventDateTime>
        <LastAllowedEventDateTime>  2030-12-31T12:00:00.0 </LastAllowedEventDateTime>
      </RdEventPreSelector>
    </configLink>

    <configLink id="RdEventInitializer">
      <RdEventInitializer>
        <SetCoordinateOriginTo> External </SetCoordinateOriginTo>
        <ReferenceCorePosition> External </ReferenceCorePosition>
        <ReferenceAxis> External </ReferenceAxis>
        <SetSignalSearchWindowRelativeTo> External </SetSignalSearchWindowRelativeTo>
```

```
    <NoiseWindowStart unit="ns"> 2000.0 </NoiseWindowStart>
    <NoiseWindowStop unit="ns"> 5000.0</NoiseWindowStop>
    <!-- <ConsiderSdUncertainity> yes </ConsiderSdUncertainity> -->
    <SignalSearchWindowOffset unit="ns"> -610.0 </SignalSearchWindowOffset>

    <!-- <SignalSearchWindowStart unit="ns"> -1000.0 </SignalSearchWindowStart> -->
    <!-- <SignalSearchWindowStop unit="ns"> 1500.0 </SignalSearchWindowStop> -->

    &ExternalShowerGeometry_user;
  </RdEventInitializer>
</configLink>

<configLink id="RdStationRejector">
  <RdStationRejector>
    <stationList> 257 253 252 246 245 185 187 191 198 207 </stationList>
    <LastAllowedEventDateTime_AERA> 2024-04-30T23:59:59.0 </LastAllowedEventDateTime_AERA>
  </RdStationRejector>
</configLink>

<configLink id="RdChannelGalacticCalibrator">
  <RdChannelGalacticCalibrator>
    <NameConstantsFile> /path/to/CalibrationConstants.dat </NameConstantsFile>
  </RdChannelGalacticCalibrator>
</configLink>

<configLink id="RdChannelBeaconTimingCalibrator">
  <RdChannelBeaconTimingCalibrator>
    <RejectIfNoRefPhaseAvailable> 0 </RejectIfNoRefPhaseAvailable>
    <RejectIfCorrectionFailed> 0 </RejectIfCorrectionFailed>
    <UseCrossCorrelationMethod> 1 </UseCrossCorrelationMethod>
  </RdChannelBeaconTimingCalibrator>
</configLink>

<configLink id="RdAntennaChannelToStationConverter">
  <RdAntennaChannelToStationConverter>
    <UsedDirection> Reference </UsedDirection>
  </RdAntennaChannelToStationConverter>
</configLink>

<configLink id="RdTopDownStationSelector">
  <RdTopDownStationSelector>
    <minNumberOfStations> 4 </minNumberOfStations>
    <stopAtFirstStation> 0 </stopAtFirstStation>
    <additionalSystematicError unit="ns"> 7 </additionalSystematicError>
  </RdTopDownStationSelector>
</configLink>

<configLink id="RdEventPostSelector">
  <RdEventPostSelector>
    <MinNumberOfStationsWithPulseFound> 3 </MinNumberOfStationsWithPulseFound>
  </RdEventPostSelector>
</configLink>

<configLink id="RdStationTimeSeriesWindowCutter">
  <RdStationTimeSeriesWindowCutter>
    <WindowSize unit="ns"> 2000 </WindowSize>
  </RdStationTimeSeriesWindowCutter>
</configLink>

<configLink id="RdREASSimPreparatorNG">
  <RdREASSimPreparatorNG>

    <GenerateEventCards>
      <UseGeometry> SD </UseGeometry>
      <UseEnergy>   SD </UseEnergy>
    </GenerateEventCards>

    <SlantDepthForCherenkovRadius unit="g/cm2"> 600 </SlantDepthForCherenkovRadius>
    <DistInUnitsOfCherenkovRadii> 1 </DistInUnitsOfCherenkovRadii>
    <CherenkovRadii> 4 </CherenkovRadii>
    <MinMaxAntDist unit="meter"> 0 </MinMaxAntDist>

    <WriteAllAERAStations> 0 </WriteAllAERAStations>

  </RdREASSimPreparatorNG>
</configLink>

<configLink id="RdPlaneFit">
  <RdPlaneFit>
    <!-- Allow multiple runs of the module (do not lock parameters in ParameterStorage) -->
    <allowMultipleCalls> yes </allowMultipleCalls>
  </RdPlaneFit>
</configLink>

<configLink id="RdGeoCeLDFFitter">
  <RdGeoCeLDFFitter>
    <InfoLevel> 3 </InfoLevel>
```

```
      </RdGeoCeLDFFitter>
    </configLink>

    <configLink id="SdEventSelector">
      <SdEventSelector>
        <EnableBottomUpSelection> 0 </EnableBottomUpSelection>
      </SdEventSelector>
    </configLink>

  </parameterOverrides>

</bootstrap>
```

C.3 Reconstruction configuration for simulated AERA data

ModuleSequence.xml

```
<!DOCTYPE sequenceFile [
    ...
  ]>

<sequenceFile
  ...
  <moduleControl>

    <loop numTimes="unbounded" pushEventToStack="yes">

      <module> EventFileReaderOG                    </module>

      <!-- change numTimes if you want a simulated event to be processed multiple times -->
      <loop numTimes="1" pushEventToStack="yes">
        <module> EventGeneratorOG                   </module>

        &SdSimulationTabulated;

        <module> CentralTriggerSimulatorXb          </module>
        <module> CentralTriggerEventBuilderOG       </module>
        <module> EventBuilderOG                     </module>

        &SdSimReconstruction;

        <module> RdStationAssociator                </module>
        <module> RdStationSimulationRejector        </module>
        <module> RdEventInitializer                 </module>

        &RdSimulation;
        <module> RdChannelNoiseImporter_AERA        </module>
        <module> RdChannelADCClipper                </module>

        <module> RdStationRejector                  </module>
        <module> RdChannelADCToVoltageConverter     </module>
        <module> RdChannelSelector                  </module>
        <module> RdChannelPedestalRemover           </module>
        <module> RdChannelResponseIncorporator      </module>
        <module> RdChannelBeaconSuppressor          </module>
        <module> RdChannelTimeSeriesTaperer         </module>
        <module> RdChannelUpsampler                 </module>

        <module> RdAntennaChannelToStationConverter </module>
        <module> RdStationSignalReconstructor       </module>
        <module> RdStationEFieldVectorCalculator    </module>

        &RdNoiseStationRejector;

        <module> RdPlaneFit                         </module>
        <module> RdGeoCeLDFFitter                   </module>
        <module> RdEventPostSelector                </module>

        <module> RdStationTimeSeriesWindowCutter    </module>
        <module> RdStationTimeSeriesTaperer         </module>
        <module> RecDataWriterNG                    </module>
      </loop>

    </loop>
```

```
  </moduleControl>

</sequenceFile>
```

bootstrap.xml

```
<?xml version="1.0" encoding="iso-8859-1"?>

<!DOCTYPE bootstrap [
    ...
  ]>

<bootstrap
  ...
  <parameterOverrides>

    <configLink id="Atmosphere">
      <AtmosphereInterfaceConfig>
        <ProfileModel> GDAS </ProfileModel>
      </AtmosphereInterfaceConfig>
    </configLink>

    <configLink id="RandomEngineRegistry">
      <RandomEngineRegistry>
        <DetectorSeed> 100 </DetectorSeed>
        <PhysicsSeed> 200 </PhysicsSeed>
      </RandomEngineRegistry>
    </configLink>

    <configLink id="RdStationAssociator">
      <RdStationAssociator>
        <!-- non standard antennas, should not be used in normal reconstruction
        187, 191, 198, 253: SALLA
        207: tripol antenna
        185, 245, 246, 252, 257: wifi vert
        -->
        <ExcludedStationIds> 187 191 198 253 207 185 245 246 252 257 134
        135 136 143 144 149 158 159 160 169 170 183 184 188 192 193 194 200
        201 202 203 210 211 212 213 222 223 224 225 226 235 236 237 244 251 </ExcludedStationIds>
      </RdStationAssociator>
    </configLink>

    <configLink id="RecDataWriter">
      <RecDataWriter>
        <rootOutput>
          <outputFileName> ADST.root </outputFileName>
        </rootOutput>
      </RecDataWriter>
    </configLink>

    <configLink id="RdChannelResponseIncorporator">
      <RdChannelResponseIncorporator>
        <ForwardResponseOnFirstCall> 1 </ForwardResponseOnFirstCall>
      </RdChannelResponseIncorporator>
    </configLink>

    <configLink id="RdEventInitializer">
      <RdEventInitializer>
        <SetCoordinateOriginTo> SDCore </SetCoordinateOriginTo>
        <SignalSearchWindowOffset unit="ns"> 0 </SignalSearchWindowOffset>
      </RdEventInitializer>
    </configLink>

    <configLink id="RdChannelTimeSeriesTaperer">
      <RdChannelTimeSeriesTaperer>
        <RelativeWindowWidthOnEachSide> 0.03 </RelativeWindowWidthOnEachSide>
      </RdChannelTimeSeriesTaperer>
    </configLink>

    <configLink id="RdAntennaStationToChannelConverter">
      <RdAntennaStationToChannelConverter>
        <CalculateDistanceToXmaxOnTheFly> 0 </CalculateDistanceToXmaxOnTheFly>
      </RdAntennaStationToChannelConverter>
    </configLink>

    <configLink id="RdAntennaChannelToStationConverter">
      <RdAntennaChannelToStationConverter>
        <UsedDirection> LineOfSightStationShowerMaximum </UsedDirection>
```

```
        <DirectionOfXmax> MC </DirectionOfXmax>
        <XmaxEstimator> MC </XmaxEstimator>
      </RdAntennaChannelToStationConverter>
    </configLink>

    <configLink id="RdTopDownStationSelector">
      <RdTopDownStationSelector>
        <minNumberOfStations> 4 </minNumberOfStations>
        <stopAtFirstStation> 0 </stopAtFirstStation>
        <additionalSystematicError unit="ns"> 7 </additionalSystematicError>
      </RdTopDownStationSelector>
    </configLink>

    <configLink id="RdPlaneFit">
      <RdPlaneFit>
        <!-- Allow multiple runs of the module (do not lock parameters in ParameterStorage) -->
        <allowMultipleCalls> yes </allowMultipleCalls>
      </RdPlaneFit>
    </configLink>

    <configLink id="RdStationTimeSeriesWindowCutter">
      <RdStationTimeSeriesWindowCutter>
        <WindowSize unit="ns"> 2000 </WindowSize>
      </RdStationTimeSeriesWindowCutter>
    </configLink>

    <configLink id="RdChannelNoiseImporter_AERA">
      <RdChannelNoiseImporter_AERA>
        <NoiseFileSelection> Automatically </NoiseFileSelection>
        <ExpectSubDirectories> 1 </ExpectSubDirectories>
        <EvtSelInNoiseFile> ByTimestamp </EvtSelInNoiseFile>
        <NoiseFilePath> /path/to/noise/files </NoiseFilePath>
      </RdChannelNoiseImporter_AERA>
    </configLink>

    <configLink id="SdEventSelector">
      <SdEventSelector>
        <EnableBottomUpSelection> 0 </EnableBottomUpSelection>
      </SdEventSelector>
    </configLink>

  </parameterOverrides>

</bootstrap>
```

C.4 Studies of systematics – iron simulations

C.4.1 Long-term evolution & monthly variation

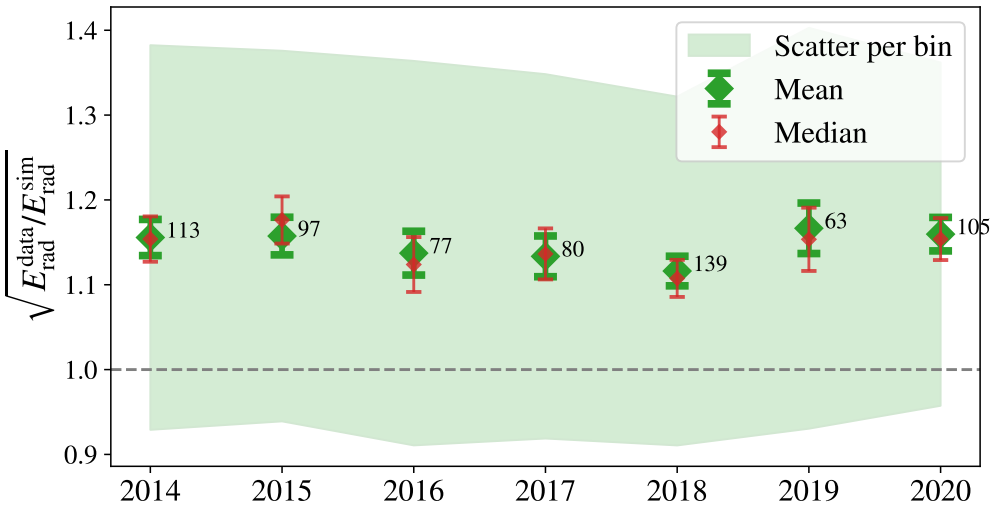

Figure C.1: Same plot as in Fig. 8.15 but for iron simulations.

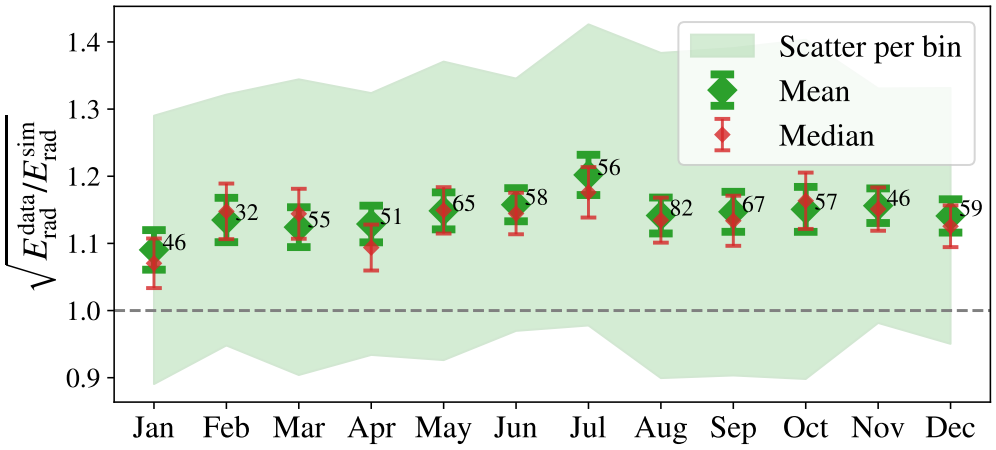

Figure C.2: Same plot as in Fig. 8.16 but for iron simulations.

C.4.2 Study of systematic dependencies

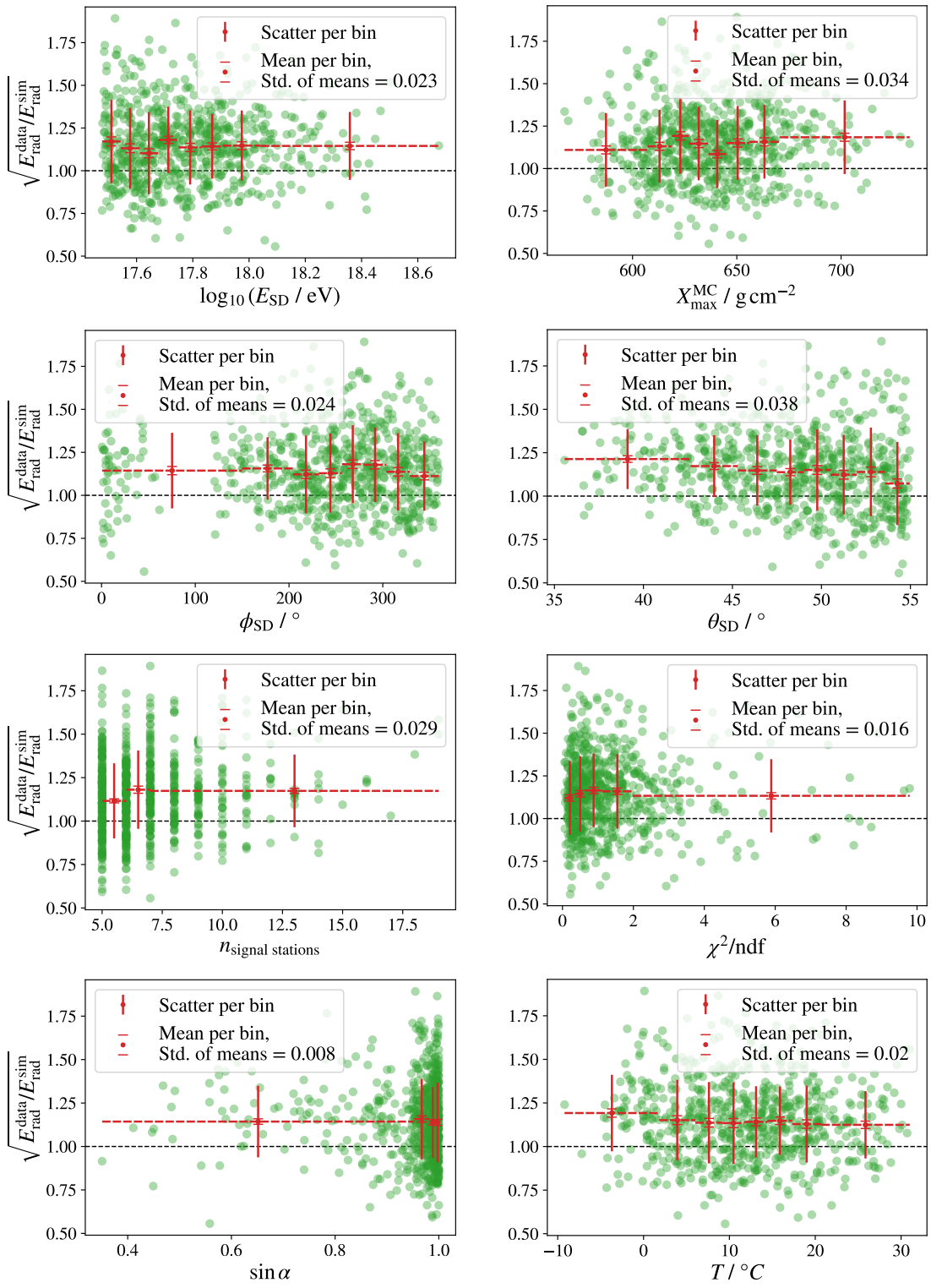

Figure C.3: Same plots as in Fig. 8.17 but for iron simulations.

Acknowledgements

Working on this thesis has been a truly adventurous journey. In the past few years, I was allowed to work with and get to know many great and fascinating people that I am happy to have shared with many experiences. Doing research in a large collaboration brings a few obstacles here and there, but fortunately it gives way more good and fulfilling moments. The many encounters with colleagues have shaped my research and brought it to the state that it finally is in and that I am very proud of. Studying cosmic rays within the Pierre Auger Collaboration is a unique and fascinating experience. I consider myself very privileged for the chance to work in this environment (I love the pampa and its inhabitants 🐄) and for all the places in the world I was allowed to visit. Going on this journey has really been lots of fun.

There are many people, to which I want to express my gratitude as I would not have been able to complete this chapter of my life without them.

First of all, I want to thank Prof. Dr. Ralph Engel for giving me the great opportunity to take on this doctoral research position and being my referee. With a fine eye for the 'bigger picture', you have always given me valuable advice on what it takes to do good research.

To Prof. Dr. Brian Wundheiler I am thankful for taking the role of being my co-referee.

I would like to express my deep gratitude to Prof. Dr. Tim Huege. You have supported me along the entire way and have given me so much valuable feedback. I could not have wished for a better supervisor, for one thing in terms of the research (there is almost nothing to ask you about that you do not have a fast and good answer to) but much more importantly on a personal level. Working with you has always been fun and enjoyable and your advice never lacked thoughtfulness. Thank you for taking me under your wing.

Many thanks and appreciation go out to my fellow colleagues. The group at IAP has always been welcoming and it was a pleasure to do my research within it. A special shout-out goes to Sara for sharing and mastering together many difficulties at the start of our projects, when trying to understand how to get to and survive in Argentina and for sharing many laughs. At ITeDA, my part-time office mates have made the stays in Buenos Aires so much better. Special thanks go to Gaby for helping me in many occasions and for being such a great human being. The colleagues from all the other places in the world also have my thanks. In particular, the Auger radio group has helped me a lot in improving my research and I have enjoyed working with you a lot. The collaboration can only be topped by the fun we had on joint travels, during football matches in Malargüe and through our mutual passion for cows.

My path towards this project was started in Aachen with my good friends Achim, Niklas and Yannic. Thank you for still sharing the fun about those and future times. Special thanks to Niklas and Achim for proofreading my thesis.

I would like to thank my family and friends for always supporting me on this journey and for staying interested in what on Earth I was doing all the time.

My last and most important bit of gratitude goes to Judith for being by my side all the time (even when I was on the other side of the Earth). Your love and support have truly carried me to the finish line. Thank you – and Butz – for constantly reminding me that there are more important things to life.

Bibliography

[1] S. Mollerach and E. Roulet. Progress in high-energy cosmic ray physics. *Progress in Particle and Nuclear Physics*, 98:85–118, 2018.

[2] V. F. Hess. Über Beobachtungen der durchdringenden Strahlung bei sieben Freiballonfahrten. *Physikalische Zeitschrift*, 13:1084–1091, 1912.

[3] M. Spurio. *Particles and Astrophysics*. Springer International Publishing, 2015.

[4] R. L. Workman et al. Review of Particle Physics. *Progress of Theoretical and Experimental Physics*, 2022:083C01, 2022.

[5] G. Di Sciascio. Measurement of Energy Spectrum and Elemental Composition of PeV Cosmic Rays: Open Problems and Prospects. *Applied Sciences*, 12(2):705, 2022.

[6] A. Aab et al. Features of the Energy Spectrum of Cosmic Rays above 2.5×10^{18} eV Using the Pierre Auger Observatory. *Physical Review Letters*, 125:121106, 2020.

[7] P. Abreu et al. The energy spectrum of cosmic rays beyond the turn-down around 10^{17} eV as measured with the surface detector of the Pierre Auger Observatory. *European Physical Journal C*, 81(11):966, 2021.

[8] A. Coleman et al. Ultra high energy cosmic rays The intersection of the Cosmic and Energy Frontiers. *Astroparticle Physics*, 149:102819, 2023.

[9] K. Greisen. End to the cosmic-ray spectrum? *Physical Review Letters*, 16:748–750, 1966.

[10] G. T. Zatsepin and V. A. Kuzmin. Upper limit of the spectrum of cosmic rays. *Journal of Experimental and Theoretical Physics Letters*, 4:78–80, 1966.

[11] T. Stanev. *High Energy Cosmic Rays*, volume 462 of *Astrophysics and Space Science Library*. Springer International Publishing, Cham, 3. edition, 2021.

[12] A. Abdul Halim et al. Large-scale Cosmic-ray Anisotropies with 19 yr of Data from the Pierre Auger Observatory. *Astrophysical Journal*, 976(1):48, 2024.

[13] R. U. Abbasi et al. Search for Large-scale Anisotropy on Arrival Directions of Ultra-high-energy Cosmic Rays Observed with the Telescope Array Experiment. *Astrophysical Journal Letters*, 898(2):L28, 2020.

[14] R. U. Abbasi et al. Indications of Intermediate-Scale Anisotropy of Cosmic Rays with Energy Greater Than 57 EeV in the Northern Sky Measured with the Surface Detector of the Telescope Array Experiment. *Astrophysical Journal Letters*, 790(2):L21, 2014.

[15] A. V. Olinto. UHECR theory and phenomenology: Summary and outlook. *EPJ Web of Conferences*, 53:02001, 2013.

[16] L. A. Anchordoqui. Ultra-high-energy cosmic rays. *Physics Reports*, 801:1–93, 2019.

[17] K. Ferrière. Magnetic fields and UHECR propagation. *EPJ Web of Conferences*, 283:03001, 2023.

[18] A. M. Hillas. The Origin of Ultra-High-Energy Cosmic Rays. *Annual Review of Astronomy and Astrophysics*, 22:425–444, 1984.

[19] P. Auger et al. Extensive Cosmic-Ray Showers. *Reviews of Modern Physics*, 11:288–291, 1939.

[20] R. Engel and D. Schmidt. *Handbook of Particle Detection and Imaging*, pp. 801–849. Springer International Publishing, Cham, 2021.

[21] T. K. Gaisser et al. *Cosmic Rays and Particle Physics*. Cambridge University Press (CUP), Cambridge, 2. edition, 2016. 51.03.03; LK 01.

[22] M. Lapka. CMS Knowledge Transfer: Cosmic rays. CMS Collection., 2017.

[23] J. Matthews. A Heitler model of extensive air showers. *Astroparticle Physics*, 22(5):387–397, 2005.

[24] J. Albrecht et al. The Muon Puzzle in cosmic-ray induced air showers and its connection to the Large Hadron Collider. *Astrophysics and Space Science*, 367(3):27, 2022.

[25] W. Heitler. *The quantum theory of radiation*, volume 5 of *International Series of Monographs on Physics*. Oxford University Press, Oxford, 1936.

[26] D. Heck et al. CORSIKA: A Monte Carlo code to simulate extensive air showers. *FZKA report 6019*, 1998.

[27] S. J. Sciutto. AIRES: A system for air shower simulations. arXiv:astro-ph/9911331, 1999.

[28] R. Engel et al. Towards A Next Generation of CORSIKA: A Framework for the Simulation of Particle Cascades in Astroparticle Physics. *Computing and Software for Big Science*, 3(1):2, 2018.

[29] B. Keilhauer et al. Nitrogen fluorescence in air for observing extensive air showers. *EPJ Web of Conferences*, 53:01010, 2013.

[30] P. Sokolsky. The History of Air Fluorescence. *EPJ Web Conf.*, 283:01003, 2023.

[31] B. Keilhauer. Atmospheric Monitoring for Astroparticle Physics Observatories. In *Proceedings of 38th International Cosmic Ray Conference — PoS(ICRC2023)*, volume 444, pp. 021, 2023.

[32] J. V. Jelley et al. Radio Pulses from Extensive Cosmic-Ray Air Showers. *Nature*, 205(4969):327–328, 1965.

[33] H. Allan. *Progress in Elementary Particles and Cosmic Ray Physics*, pp. 171–302. North-Holland Publishing Company, Amsterdam and London, 1971.

[34] T. Huege. The Renaissance of Radio Detection of Cosmic Rays. *Brazilian Journal of Physics*, 44(5):520–529, 2014.

[35] T. Huege. Radio detection of cosmic ray air showers in the digital era. *Physics Reports*, 620:1–52, 2016.

[36] F. G. Schröder. Radio detection of cosmic-ray air showers and high-energy neutrinos. *Progress in Particle and Nuclear Physics*, 93:1–68, 2017.

[37] C. W. James. Nature of radio-wave radiation from particle cascades. *Physical Review D*, 105:023014, 2022.

[38] S. Chiche et al. Loss of Coherence and Change in Emission Physics for Radio Emission from Very Inclined Cosmic-Ray Air Showers. *Physical Review Letters*, 132:231001, 2024.

[39] O. Scholten et al. A macroscopic description of coherent geo-magnetic radiation from cosmic-ray air showers. *Astroparticle Physics*, 29(2):94–103, 2008.

[40] H. Schoorlemmer. *Tuning in on cosmic rays: polarization of radio signals from air showers as a probe of emission mechanisms*. PhD thesis, Radboud University Nijmegen, 2012.

[41] G. A. Askar'yan. Excess negative charge of an electron-photon shower and its coherent radio emission. *Journal of Experimental and Theoretical Physics*, 41:616–618, 1961.

[42] T. Huege et al. Simulating radio emission from air showers with CoREAS. *AIP Conference Proceedings*, 1535:128–132, 2013.

[43] J. Alvarez-Muñiz et al. Coherent Cherenkov radio pulses from hadronic showers up to EeV energies. *Astroparticle Physics*, 35(6):287–299, 2012.

[44] C. W. James et al. General description of electromagnetic radiation processes based on instantaneous charge acceleration in "endpoints". *Physical Review E*, 84:056602, 2011.

[45] F. Halzen et al. Radiodetection of cosmic neutrinos. A numerical, real time analysis. *Physics Letters B*, 257(3):432–436, 1991.

[46] E. Zas et al. Electromagnetic pulses from high-energy showers: Implications for neutrino detection. *Physical Review D*, 45:362–376, 1992.

[47] M. Desmet et al. Proof of principle for template synthesis approach for the radio emission from vertical extensive air showers. *Astroparticle Physics*, 157:102923, 2024.

[48] O. Scholten et al. Analytic calculation of radio emission from parametrized extensive air showers: A tool to extract shower parameters. *Physical Review D*, 97:023005, 2018.

[49] The Pierre Auger Collaboration. The Pierre Auger Cosmic Ray Observatory. *Nuclear Instruments and Methods in Physics Research Section A: Accelerators, Spectrometers, Detectors and Associated Equipment*, 798:172 – 213, 2015.

[50] The Pierre Auger Collaboration. The Pierre Auger Observatory Upgrade - Preliminary Design Report. arXiv:1604.03637, 2016.

[51] R. Baltrusaitis et al. The Utah Fly's Eye detector. *Nuclear Instruments and Methods in Physics Research Section A: Accelerators, Spectrometers, Detectors and Associated Equipment*, 240(2):410–428, 1985.

[52] T. Abu-Zayyad et al. The prototype high-resolution Fly's Eye cosmic ray detector. *Nuclear Instruments and Methods in Physics Research Section A: Accelerators, Spectrometers, Detectors and Associated Equipment*, 450(2):253–269, 2000.

[53] J. Abraham et al. The fluorescence detector of the Pierre Auger Observatory. *Nuclear Instruments and Methods in Physics Research A*, 620(2-3):227–251, 2010.

[54] B. Dawson for the Pierre Auger Collaboration. The Energy Scale of the Pierre Auger Observatory. In *Proceedings of 36th International Cosmic Ray Conference — PoS(ICRC2019)*, volume 358, pp. 231, 2019.

[55] J. Rosado et al. On the absolute value of the air-fluorescence yield. *Astroparticle Physics*, 55:51–62, 2014.

[56] I. Allekotte et al. The surface detector system of the Pierre Auger Observatory. *Nuclear Instruments and Methods in Physics Research A*, 586(3):409–420, 2008.

[57] G. Cataldi. The upgrade of the Pierre Auger Observatory with the Scintillator Surface Detector. *PoS*, ICRC2021:251, 2021.

[58] J. Pawlowsky for the Pierre Auger Collaboration. Status and expected performance of the AugerPrime Radio Detector. In *Proceedings of 38th International Cosmic Ray Conference — PoS(ICRC2023)*, volume 444, pp. 344, 2023.

[59] A. Abdul Halim et al. AugerPrime surface detector electronics. *Journal of Instrumentation*, 18(10):P10016, 2023.

[60] J. de Jesús for the Pierre Auger Collaboration. Status and Performance of the Underground Muon Detector of the Pierre Auger Observatory. In *Proceedings of 38th International Cosmic Ray Conference — PoS(ICRC2023)*, volume 444, pp. 267, 2023.

[61] P. Abreu et al. Antennas for the detection of radio emission pulses from cosmic-ray induced air showers at the Pierre Auger Observatory. *Journal of Instrumentation*, 7(10):P10011, 2012.

[62] A. M. van den Berg et al. Fiber Communication System for the Auger Engineering Radio Array at the Southern Auger Observatory. Internal Auger note, 2011. GAP 2011-035.

[63] A. Aab et al. Nanosecond-level time synchronization of autonomous radio detector stations for extensive air showers. *Journal of Instrumentation*, 11(01):P01018, 2016.

[64] P. Correa et al. Development of an Autonomous Detection-Unit Self-Trigger for GRAND. In *Proceedings of 10th International Workshop on Acoustic and Radio EeV Neutrino Detection Activities — PoS(ARENA2024)*, volume 470, pp. 060, 2024.

[65] J. Köhler et al. Next-Generation Triggering: A Novel Event-Level Approach. In *Proceedings of 10th International Workshop on Acoustic and Radio EeV Neutrino Detection Activities — PoS(ARENA2024)*, volume 470, pp. 061, 2024.

[66] K. Kotera et al. GRAND: status and perspectives. In *Proceedings of 10th International Workshop on Acoustic and Radio EeV Neutrino Detection Activities — PoS(ARENA2024)*, volume 470, pp. 057, 2024.

[67] O. Krömer et al. New Antenna for Radio Detection of UHECR. In *Proceedings of 31st International Cosmic Ray Conference, Lodz, Poland*, 2009.

[68] J. Pawlowsky for the Pierre Auger Collaboration. Improving the photon sensitivity of the Pierre Auger Observatory with the AugerPrime Radio Detector. In *Proceedings of 10th International Workshop on Acoustic and Radio EeV Neutrino Detection Activities — PoS(ARENA2024)*, volume 470, pp. 028, 2024.

[69] J. Pawlowsky. *Search for inclined photon air showers with the AugerPrime Radio Detector*. PhD thesis, Wuppertal University, Wuppertal, 2024.

[70] F. A. Schlüter. *Expected sensitivity of the AugerPrime Radio Detector to the masses of ultra-high-energy cosmic rays using inclined air showers*. PhD thesis, Karlsruhe Institute of Technology (KIT), 2022.

[71] S. Buitink et al. Amplified radio emission from cosmic ray air showers in thunderstorms. *Astronomy & Astrophysics*, 467(2):385–394, 2007.

[72] M. Ender et al. Radio emission of extensive air showers during thunderstorms. *Proc. 31st ICRC, Lodz, Poland*, 1:219, 2009.

[73] P. Schellart et al. Probing Atmospheric Electric Fields in Thunderstorms through Radio Emission from Cosmic-Ray-Induced Air Showers. *Physical Review Letters*, 114:165001, 2015.

[74] T. N. G. Trinh et al. Determining atmospheric electric fields using MGMR3D. *Physical Review D*, 105(6):063027, 2022.

[75] M. Melissas et al. Weather monitoring at the central radio station. Internal Auger note, 2011. GAP 2011-066.

[76] Q. D. Hasankiadeh and T. Huege. The weather stations at the Auger Engineering Radio Array. Internal Auger note, 2016. GAP 2016-030.

[77] A. Hinckley (Campbell Scientific), private communication.

[78] Campbell Scientific, Inc. CS110 Electric Field Meter Product Manual. https://s.campbellsci.com/documents/us/manuals/cs110.pdf.

[79] A. Hinckley and Campbell Scientific, Inc. CS110 Electric Field Meter Overview. https://s.campbellsci.com/documents/us/technical-papers/cs110_overview.pdf. accessed 9-August-2023.

[80] A. Meidow. Analysis of the Atmospheric Electric Field at the Pierre Auger Observatory. Bachelor's thesis, Karlsruhe Institute of Technology (KIT), 2022.

[81] G. Wörner and K. Daumiller, private communication.

[82] J. L. Kelley et al. Design and Testing of a 5 GHz Commercial Wireless Network for AERA. Internal Auger note, 2012. GAP2012-054.

[83] S. Harrache and L. Darras. PyCampbellCR1000. Communication tools for Campbell CR1000-type Dataloggers, 2012. Available at https://pypi.python.org/pypi/PyCampbellCR1000.

[84] L. Niemietz. *Lightning Detection at the Pierre-Auger-Observatory*. PhD thesis, Wuppertal University, 2017.

[85] J. Neuser. *Cosmic Rays and the Atmospheric Electric Field - Reconstruction and Data Analysis of Radio Emission from Air Showers at the Auger Engineering Radio Array*. PhD thesis, Wuppertal University, 2015.

[86] E. Kessler, editor. *Instruments and techniques for thunderstorm observation and analysis*. University of Oklahoma Press, Norman and London, 1988.

[87] R. G. Harrison. The Carnegie Curve. *Surveys in Geophysics*, 34(2):209–232, 2013.

[88] R. G. Harrison and K. A. Nicoll. Fair weather criteria for atmospheric electricity measurements. *Journal of Atmospheric and Solar-Terrestrial Physics*, 179:239–250, 2018.

[89] M. Gottowik. Thunderstorms, saturation. https://indico.nucleares.unam.mx/event/1608/contribution/3, 2020.

[90] M. Gottowik. *Radio Hybrid Reconstruction and Analysis of Inclined Air Showers with AERA of the Pierre Auger Observatory - Measuring the Hadronic Shower Development and Cosmic Ray Mass Composition*. PhD thesis, Wuppertal University, 2021.

[91] G. Voronoi. Nouvelles applications des paramètres continus à la théorie des formes quadratiques. premier mémoire. sur quelques propriétés des formes quadratiques positives parfaites. *Journal für die reine und angewandte Mathematik*, 133:97–178, 1908.

[92] B. Pont. Building a weather-based thunderstorm flag for RD. https://indico.nucleares.unam.mx/event/2289/session/3/contribution/10, 2024.

[93] F. Aharonian et al. Flux variations of cosmic ray air showers detected by LHAASO-KM2A during a thunderstorm on June 10, 2021. *Chinese Physics C*, 47(1):015001, 2023.

[94] M. Schimassek. *Extending the Physics Reach of the Pierre Auger Observatory using Low-Level Trigger Data*. PhD thesis, Karlsruhe Institute of Technology (KIT), 2022.

[95] J. Dwyer et al. Study of downward Terrestrial Gamma-ray Flashes with the surface detector of the Pierre Auger Observatory. *PoS*, ICRC2023:439, 2023.

[96] M. Schimassek et al. Terrestrial Gamma-Ray Flashes at the Pierre Auger Observatory. *Journal of Physics: Conference Series*, 2398(1):012003, 2022.

[97] M. G. Nicora et al. Atmospheric Electrical Activity in central Argentina and its relationship with phenomena observed at the Auger Observatory. *Journal of Physics: Conference Series*, 2398(1):012005, 2022.

[98] E. R. Williams. The Schumann Resonance: A Global Tropical Thermometer. *Science*, 256(5060):1184–1187, 1992.

[99] J. Tacza et al. Analysis of long-term potential gradient variations measured in the Argentinian Andes. *Atmospheric Research*, 248:105200, 2021.

[100] D. Siingh et al. The DC and AC global electric circuits and climate. *Earth-Science Reviews*, 244:104542, 2023.

[101] Y. R. Velazquez et al. Exploring the global thunderstorm influence on the fair weather electric field in Buenos Aires. *Atmospheric Research*, 299:107182, 2024.

[102] J. Tacza. Effects of high-energetic charged particles on the atmospheric electric field on the ground. https://indico.nucleares.unam.mx/event/2234/session/6/contribution/40, 2024.

[103] J. Bór et al. Immediate effects of the Hunga Tonga - Hunga Ha'apai volcanic eruption on the AC and DC Global Electric Circuits. EGU General Assembly 2023, Vienna, Austria, 24–28 Apr 2023, EGU23-6148, 2023.

[104] J. Bór et al. Responses of the AC/DC Global Electric Circuit to Volcanic Electrical Activity in the Hunga Tonga-Hunga Ha'apai Eruption on 15 January 2022. *Journal of Geophysical Research (Atmospheres)*, 128(8):e2022JD038238, 2023.

[105] K. Nicoll et al. A global atmospheric electricity monitoring network for climate and geophysical research. *Journal of Atmospheric and Solar-Terrestrial Physics*, 184:18–29, 2019.

[106] The Pierre Auger Collaboration. The Pierre Auger Observatory Open Data. arXiv:2309.16294, 2023.

[107] G. Reber. Cosmic Static. *Astrophysical Journal*, 100:279, 1944.

[108] S. Buitink et al. Performance of SKA as an air shower observatory. In *Proceedings of 37th International Cosmic Ray Conference — PoS(ICRC2021)*, volume 395, pp. 415, 2021.

[109] J. Álvarez-Muñiz et al. The Giant Radio Array for Neutrino Detection (GRAND): Science and design. *Science China Physics, Mechanics & Astronomy*, 63(1):219501, 2020.

[110] P. Schellart et al. Detecting cosmic rays with the LOFAR radio telescope. *Astronomy & Astrophysics*, 560:A98, 2013.

[111] A. Aab et al. Calibration of the logarithmic-periodic dipole antenna (LPDA) radio stations at the Pierre Auger Observatory using an octocopter. *Journal of Instrumentation*, 12(10):T10005, 2017.

[112] K. Mulrey et al. Calibration of the LOFAR low-band antennas using the Galaxy and a model of the signal chain. *Astroparticle Physics*, 111, 2019.

[113] International Telecommunication Union. Recommendation ITU-R P.372-14, Radio Noise, 2019.

[114] T. Fodran for the Pierre Auger Collaboration. First results from the Auger-Prime Radio Detector. In *Proceedings of 37th International Cosmic Ray Conference — PoS(ICRC2021)*, volume 395, pp. 270, 2021.

[115] B. Pont. Galactic Calibration for RD: Insights into Ionospheric and Temperature Effects. https://indico.nucleares.unam.mx/event/2289/session/3/contribution/9, 2024.

[116] J. Aguilar et al. Design and sensitivity of the Radio Neutrino Observatory in Greenland (RNO-G). *Journal of Instrumentation*, 16(03):P03025, 2021.

[117] R. Monroe et al. Self-triggered radio detection and identification of cosmic air showers with the OVRO-LWA. *Nuclear Instruments and Methods in Physics Research Section A: Accelerators, Spectrometers, Detectors and Associated Equipment*, 953:163086, 2020.

[118] R. Abbasi et al. Development of a scintillation and radio hybrid detector array at the South Pole. In *Proceedings of 37th International Cosmic Ray Conference — PoS(ICRC2021)*, volume 395, pp. 225, 2021.

[119] J. J. Hibbard et al. Modeling the Galactic Foreground and Beam Chromaticity for Global 21 cm Cosmology. *Astrophysical Journal*, 905(2):113, 2020.

[120] D. Anstey et al. A general Bayesian framework for foreground modelling and chromaticity correction for global 21 cm experiments. *Monthly Notices of the Royal Astronomical Society*, 506(2):2041–2058, 2021.

[121] M. Tegmark et al. Foregrounds and Forecasts for the Cosmic Microwave Background. *Astrophysical Journal*, 530(1):133, 2000.

[122] D. C. Price. Global Sky Models can Improve Flux Estimates in Pulsar and FRB Studies. *Research Notes of the AAS*, 5(10):246, 2021.

[123] T. L. Wilson et al. *Tools of Radio Astronomy*. Springer, Berlin, 2009.

[124] G. B. Rybicki and A. P. Lightman. *Radiative Processes in Astrophysics*. John Wiley & Sons, Ltd, Weinheim, 1985.

[125] T. J. Mozdzen et al. Improved measurement of the spectral index of the diffuse radio background between 90 and 190 MHz. *Monthly Notices of the Royal Astronomical Society*, 464(4):4995–5002, 2016.

[126] T. J. Mozdzen et al. Spectral index of the diffuse radio background between 50 and 100 MHz. *Monthly Notices of the Royal Astronomical Society*, 483(4):4411–4423, 2018.

[127] A. E. E. Rogers and J. D. Bowman. Spectral Index of the Diffuse Radio Background Measured from 100 to 200 MHz. *Astronomical Journal*, 136:641–648, 2008.

[128] C. R. Purton. The Spectrum of the Galactic Radio Emission. *Monthly Notices of the Royal Astronomical Society*, 133(4):463–474, 1966.

[129] A. H. Bridle and J. E. Baldwin. The Spectrum of the Radio Background Between 13 and 404 MHz. *Monthly Notices of the Royal Astronomical Society*, 136(2):219–240, 1967.

[130] A. S. Webster. The Spectrum of the Galactic Non-thermal Background Radiation—II: Observations at 408, 610 and 1407 MHz. *Monthly Notices of the Royal Astronomical Society*, 166(2):355–371, 1974.

[131] A. de Oliveira-Costa et al. A Model of Diffuse Galactic Radio Emission from 10 MHz to 100 GHz. *Monthly Notices of the Royal Astronomical Society*, 388(1):247–260, 2008.

[132] H. Zheng et al. An Improved Model of Diffuse Galactic Radio Emission from 10 MHz to 5 THz. *Monthly Notices of the Royal Astronomical Society*, 464(3):3486–3497, 2016.

[133] J. Dowell et al. The LWA1 Low Frequency Sky Survey. *Monthly Notices of the Royal Astronomical Society*, 469(4):4537–4550, 2017.

[134] M. Sathyanarayana Rao et al. GMOSS: All-sky Model of Spectral Radio Brightness Based on Physical Components and Associated Radiative Processes. *Astronomical Journal*, 153(1):26, 2017.

[135] Q. Huang et al. A high-resolution self-consistent whole sky foreground model. *Science China Physics, Mechanics & Astronomy*, 62(8):989511, 2019.

[136] Y. Cong et al. An Ultralong-wavelength Sky Model with Absorption Effect. *Astrophysical Journal*, 914(2):128, 2021.

[137] E. Polisensky. LFmap: A Low Frequency Sky Map Generating Program. Technical report, Naval Research Laboratory, 2007.

[138] C. G. T. Haslam et al. A 408 MHz all-sky continuum survey. II. The atlas of contour maps. *Astronomy and Astrophysics Supplement Series*, 47:1–143, 1982.

[139] P. Platania et al. Full Sky Study of Diffuse Galactic Emission at Decimeter Wavelengths. *Astronomy & Astrophysics*, 410(3):847–863, 2003.

[140] R. S. Roger et al. The radio emission from the Galaxy at 22 MHz. *Astronomy and Astrophysics Supplement Series*, 137(1):7–19, 1999.

[141] S. W. Ellingson et al. The LWA1 Radio Telescope. *IEEE Transactions on Antennas and Propagation*, 61(5):2540–2549, 2013.

[142] M. Remazeilles et al. An improved source-subtracted and destriped 408-MHz all-sky map. *Monthly Notices of the Royal Astronomical Society*, 451(4):4311–4327, 2015.

[143] H. V. Cane. Spectra of the non-thermal radio radiation from the galactic polar regions. *Monthly Notices of the Royal Astronomical Society*, 189:465–478, 1979.

[144] G. A. Dulk et al. Calibration of low-frequency radio telescopes using the galactic background radiation. *Astronomy & Astrophysics*, 365:294–300, 2001.

[145] N. Durc et al. RFI Report for the US South-West. `ftp://gemini.haystack.edu/pub/lofar/siting_docs/SWUS_RFI.doc`, 2003.

[146] P. L. Tokarsky et al. Sensitivity of an Active Antenna Array Element for the Low-Frequency Radio Telescope GURT. *IEEE Transactions on Antennas and Propagation*, 65(9):4636–4644, 2017.

[147] V. V. Krymkin. The spectrum of background low-frequency radio emission. *Radiophysics & Quantum Electronics*, 14:161–164, 1971.

[148] C. Dickinson et al. The C-Band All-Sky Survey (C-BASS): constraining diffuse Galactic radio emission in the North Celestial Pole region. *Monthly Notices of the Royal Astronomical Society*, 485(2):2844–2860, 2019.

[149] J. L. Caswell. A Map of the Northern Sky at 10 MHz. *Monthly Notices of the Royal Astronomical Society*, 177(3):601–616, 1976.

[150] H. Alvarez et al. A 45-MHz continuum survey of the southern hemisphere. *Astronomy and Astrophysics Supplement Series*, 124(2):315–328, 1997.

[151] K. Maeda et al. A 45-MHz continuum survey of the northern hemisphere. *Astronomy and Astrophysics Supplement Series*, 140(2):145–154, 1999.

[152] T. L. Landecker and R. Wielebinski. The Galactic Metre Wave Radiation: A two-frequency survey between declinations +25° and -25° and the preparation of a map of the whole sky. *Australian Journal of Physics Astrophysical Supplements*, 16:1, 1970.

[153] A. J. Turtle and J. E. Baldwin. A survey of galactic radiation at 178 Mc/s. *Monthly Notices of the Royal Astronomical Society*, 124:459, 1962.

[154] R. S. Roger et al. Spectral flux densities of radio sources at 22.25 MHz. I. *Astronomical Journal*, 74:366–372, 1969.

[155] J. W. M. Baars et al. Reprint of 1977A&A....61...99B. The absolute spectrum of Cas A; an accurate flux density scale and a set of secondary calibrators. *Astronomy & Astrophysics*, 500:135–142, 1977.

[156] I. K. Pauliny-Toth and J. R. Shakeshaft. A survey of the background radiation at a frequency of 404 Mc/s, I. *Monthly Notices of the Royal Astronomical Society*, 124:61, 1962.

[157] A. E. Guzmán et al. All-sky Galactic radiation at 45 MHz and spectral index between 45 and 408 MHz. *Astronomy & Astrophysics*, 525:A138, 2011.

[158] R. A. Monsalve et al. Absolute Calibration of Diffuse Radio Surveys at 45 and 150 MHz. *Astrophysical Journal*, 908(2):145, 2021.

[159] J. D. Bowman et al. An absorption profile centred at 78 megahertz in the sky-averaged spectrum. *Nature*, 555(7694):67–70, 2018.

[160] G. Hinshaw et al. Five-Year Wilkinson Microwave Anisotropy Probe Observations: Data Processing, Sky Maps, and Basic Results. *Astrophysical Journal Supplement Series*, 180(2):225–245, 2009.

[161] Planck Collaboration. Planck 2015 results. I. Overview of products and scientific results. *Astronomy & Astrophysics*, 594:A1, 2016.

[162] D. C. Price. PyGSM: Python interface to the Global Sky Model. Astrophysics Source Code Library, record ascl:1603.013, 2016.

[163] A. Zonca et al. healpy: equal area pixelization and spherical harmonics transforms for data on the sphere in python. *Journal of Open Source Software*, 4(35):1298, 2019.

[164] K. M. Górski et al. HEALPix: A Framework for High-Resolution Discretization and Fast Analysis of Data Distributed on the Sphere. *Astrophysical Journal*, 622:759–771, 2005.

[165] T. Fodran. Radio calibration toolkit. https://github.com/F-Tomas/radiocalibrationtoolkit.

[166] A. Nelles et al. Measuring a Cherenkov ring in the radio emission from air showers at 110–190 MHz with LOFAR. *Astroparticle Physics*, 65:11–21, 2015.

[167] S. De Jong. The Radio detection of inclined showers at the Pierre Auger Observatory. *PoS*, ICHEP2020:829, 2021.

[168] J. D. Kraus. *Radio Astronomy*. Cygnus-Quasar Books, 2nd edition, 1986.

[169] D. Correia dos Santos for the Pierre Auger Collaboration. Study of solar activity with AERA data. In *Proceedings of 10th International Workshop on Acoustic and Radio EeV Neutrino Detection Activities — PoS(ARENA2024)*, volume 470, pp. 032, 2024.

[170] P. Zhang et al. Imaging of the Quiet Sun in the Frequency Range of 20-80 MHz. *Astrophysical Journal*, 932(1):17, 2022.

[171] A. E. E. Rogers et al. Radiometric measurements of electron temperature and opacity of ionospheric perturbations. *Radio Science*, 50(2):130–137, 2015.

[172] K. Davies. *Ionospheric Radio Propagation*. U.S. Dept. of Commerce, National Bureau of Standards, 1965.

[173] A. Datta et al. The Effects of the Ionosphere on Ground-based Detection of the Global 21 cm Signal from the Cosmic Dawn and the Dark Ages. *Astrophysical Journal*, 831(1):6, 2016.

[174] A. Rodland. Development of an Open-Source IRI-based Nowcasting Tool for Ionospheric Electron Density and HF Propagation. In *44th COSPAR Scientific Assembly. Held 16-24 July*, volume 44, pp. 981, 2022.

[175] P. Zarka and W. S. Kurth. Radio Wave Emission from the Outer Planets Before Cassini. *Space Science Reviews*, 116(1-2):371–397, 2005.

[176] B. Cecconi et al. Natural radio emission of Jupiter as interferences for radar investigations of the icy satellites of Jupiter. *Planetary and Space Science*, 61(1):32–45, 2012.

[177] B. Cecconi et al. Jupiter Radio Emission Probability Tool. *Frontiers in Astronomy and Space Sciences*, 10:10, 2023.

[178] J. Singal et al. The Second Radio Synchrotron Background Workshop: Conference Summary and Report. *Publications of the Astronomical Society of the Pacific*, 135(1045):036001, 2023.

[179] M. W. Eastwood et al. The Radio Sky at Meter Wavelengths: m-mode Analysis Imaging with the OVRO-LWA. *Astronomical Journal*, 156(1):32, 2018.

[180] M. A. Kriele et al. Imaging the southern sky at 159 MHz using spherical harmonics with the engineering development array 2. *Publications of the Astronomical Society of Australia*, 39:e017, 2022.

[181] K. Terveer et al. Cosmic ray detection with the LOFAR radio telescope. In *Proceedings of 10th International Workshop on Acoustic and Radio EeV Neutrino Detection Activities — PoS(ARENA2024)*, volume 470, pp. 023, 2024.

[182] J. Stoffels. Observation of Galactic noise and identification of background sources in RNO-G. In *Proceedings of 10th International Workshop on Acoustic and Radio EeV Neutrino Detection Activities — PoS(ARENA2024)*, volume 470, pp. 005, 2024.

[183] S. Verpoest for the IceCube-Gen2 and Pierre Auger Collaborations. Observation of air showers with an IceCube-Gen2 prototype station at the Pierre Auger Observatory. In *Proceedings of 10th International Workshop on Acoustic and Radio EeV Neutrino Detection Activities — PoS(ARENA2024)*, volume 470, pp. 037, 2024.

[184] B. de Errico. GRAND@Auger: status and first results. Poster contribution at the UHECR 2024, Malargüe, Argentina, 2024.

[185] D. Correia dos Santos. Galactic calibration and its long-term stability for the AERA. https://indico.nucleares.unam.mx/event/2289/session/1/contribution/16, 2024.

[186] D. Correia dos Santos for the Pierre Auger Collaboration. Galactic calibration and its long-term stability for the Auger Engineering Radio Array. In *Proceedings of 10th International Workshop on Acoustic and Radio EeV Neutrino Detection Activities — PoS(ARENA2024)*, volume 470, pp. 030, 2024.

[187] J. L. Kelley and C. Timmermans. Calibration of the AERA Phase 1 Digitizer. Internal Auger note, 2011. GAP 2011-028.

[188] D. Charrier. Antenna development for astroparticle and radioastronomy experiments. *Nuclear Instruments and Methods in Physics Research Section A: Accelerators, Spectrometers, Detectors and Associated Equipment*, 662:S142–S145, 2012. 4th International workshop on Acoustic and Radio EeV Neutrino detection Activities.

[189] C. Rühle. *Entwicklung eines schnellen eingebetteten Systems zur Radiodetektion kosmischer Strahlung*. PhD thesis, Karlsruhe Institute of Technology (KIT), 2013.

[190] G. Burke and A. Pogio. Numerical Electromagnetics Code (NEC)-Method of Moments. A User-Oriented Computer Code for Analysis of the Electromagnetic Response of Antennas and Other Metal Structures. Part 1: Program Description-Theory. Part 2: Program Description-Code. Volume 1. Revised. pp. 719, 1981.

[191] C. A. Balanis. *Antenna theory*. Wiley-Blackwell, Chichester, England, 3 edition, 2005.

[192] S. Fliescher. *Antenna devices and measurement of radio emission from cosmic ray induced air showers at the Pierre Auger Observatory*. PhD thesis, Aachen, 2012.

[193] R. Krause. *Antenna development and calibration for measurements of radio emission from extensive air showers at the Pierre Auger Observatory*. PhD thesis, RWTH Aachen University, 2018.

[194] A. Aab et al. Calibration of the logarithmic-periodic dipole antenna (LPDA) radio stations at the Pierre Auger Observatory using an octocopter. *Journal of Instrumentation*, 12(10):T10005, 2017.

[195] F. Schlüter. Unfolding the Electric Field of Radio Emission in Extensive Air Showers by Calibration of the Butterfly Antenna and Deep Learning based Noise Suppression at the Pierre Auger Observatory. Master's thesis, RWTH Aachen University, 2018.

[196] S. Jansen. *Radio for the Masses*. PhD thesis, Radboud University Nijmegen, 2016.

[197] F. Canfora. *Cosmic-Ray Composition Measurements Using Radio Signals*. PhD thesis, Radboud University Nijmegen, 2021.

[198] A. Reuzki for the Pierre Auger Collaboration. Drone-based calibration of AugerPrime radio antennas at the Pierre Auger Observatory. In *Proceedings of 10th International Workshop on Acoustic and Radio EeV Neutrino Detection Activities — PoS(ARENA2024)*, volume 470, pp. 029, 2024.

[199] B. Pont, private communication.

[200] J. C. Glaser. *Absolute energy calibration of the Pierre Auger observatory using radio emission of extensive air showers*. PhD thesis, RWTH Aachen University, Aachen, 2017.

[201] R. Smau et al. The $\overline{\text{Off}}\underline{\text{line}}$ Temperature Dependence Correction Module for AERA data. Internal Auger note, 2023. GAP2023-043.

[202] D. C. dos Santos and R. M. de Almeida. AERA Galactic Calibration implementation within Offline. Internal Auger note, 2023. GAP 2023-036.

[203] D. Correia dos Santos. *Multipolar anisotropy studies of cosmic rays detected with the Pierre Auger Observatory and long-term calibration of the Auger Engineering Radio Array using the diffuse Galactic radio emission*. PhD thesis, Universidade Federal Fluminense, 2024.

[204] D. Correia dos Santos and R. Menezes de Almeida. Galactic calibration using different sky temperature models. https://www.auger.unam.mx/AugerWiki/Calibration_analysis/Radio, minutes from 2023-09-14.

[205] D. Correia dos Santos and R. Menezes de Almeida. Study of hourly modulation and effects of temperature and solar irradiance on galactic calibration. https://www.auger.unam.mx/AugerWiki/Calibration_analysis/Radio, minutes from 2023-03-30.

[206] S. Argirò et al. The Offline software framework of the Pierre Auger Observatory. *Nuclear Instruments and Methods in Physics Research Section A: Accelerators, Spectrometers, Detectors and Associated Equipment*, 580(3):1485–1496, 2007.

[207] D. Veberič et al. Offline Reference Manual SD Reconstruction. Internal Auger note, 2005. GAP 2005-035.

[208] P. Abreu et al. Advanced functionality for radio analysis in the Offline software framework of the Pierre Auger Observatory. *Nuclear Instruments and Methods in Physics Research Section A: Accelerators, Spectrometers, Detectors and Associated Equipment*, 635(1):92–102, 2011.

[209] S. Fliescher et al. The radio extension of Auger Offline. Internal Auger note, 2010. GAP 2010-056.

[210] C. Glaser et al. An analytic description of the radio emission of air showers based on its emission mechanisms. *Astroparticle Physics*, 104:64–77, 2019.

[211] S. Grebe et al. RdMonitoring – An Offline Module to monitor the raw data from AERA. Internal Auger note, 2011. GAP2011-122.

[212] B. Pont. AERA Data Quality Monitoring with RdMonitoring. Internal Auger note, 2019. GAP2019-006.

[213] D. Correia dos Santos, private communication.

[214] D. C. dos Santos and R. M. de Almeida. Analysis and classification of average spectral densities measured by AERA antennas from 2013 up to 2020. Internal Auger note, 2023. GAP 2023-044.

[215] A. Lang and T. Huege. Time Calibration of the Auger Engineering Radio Array (AERA) Using Airplanes. Internal Auger note, 2015. GAP 2015-013.

[216] S. Martinelli et al. Quantifying energy fluence and its uncertainty for radio emission from particle cascades in the presence of noise. arXiv:2407.18654.

[217] T. Huege and C. B. Welling. Reconstruction of air-shower measurements with AERA in the presence of pulsed radio-frequency interference. *EPJ Web of Conferences*, 216:03007, 2019.

[218] J. Abraham et al. Atmospheric effects on extensive air showers observed with the surface detector of the Pierre Auger observatory. *Astroparticle Physics*, 32(2):89–99, 2009.

[219] A. Abdul Halim et al. Demonstrating Agreement between Radio and Fluorescence Measurements of the Depth of Maximum of Extensive Air Showers at the Pierre Auger Observatory. *Physical Review Letters*, 132:021001, 2024.

[220] M. Gottowik for the Pierre Auger Collaboration. Measuring the muon content of inclined air showers using AERA and the water-Cherenkov detector of the Pierre Auger Observatory. In *Proceedings of 10th International Workshop on Acoustic and Radio EeV Neutrino Detection Activities — PoS(ARENA2024)*, volume 470, pp. 033, 2024.

[221] A. Aab et al. Spectral calibration of the fluorescence telescopes of the Pierre Auger Observatory. *Astroparticle Physics*, 95:44–56, 2017.

[222] D. Veberič et al. Constant Intensity Cut: Unbinned Estimation of the Signal Attenuation Function. Internal Auger note, 2015. GAP2015-065.

[223] A. Aab et al. Data-driven estimation of the invisible energy of cosmic ray showers with the Pierre Auger Observatory. *Physical Review D*, 100:082003, 2019.

[224] C. Glaser et al. Simulation of radiation energy release in air showers. *Journal of Cosmology and Astroparticle Physics*, 2016(09):024, 2016.

[225] A. Aab et al. Energy estimation of cosmic rays with the Engineering Radio Array of the Pierre Auger Observatory. *Physical Review D*, 93:122005, 2016.

[226] A. Aab et al. Measurement of the Radiation Energy in the Radio Signal of Extensive Air Showers as a Universal Estimator of Cosmic-Ray Energy. *Physical Review Letters*, 116:241101, 2016.

[227] K. Mulrey et al. On the cosmic-ray energy scale of the LOFAR radio telescope. *Journal of Cosmology and Astroparticle Physics*, 2020(11):017, 2020.

[228] F. L. Briechle. *Measurement of the radiation energy release using radio emission from extensive air showers at the Pierre Auger Observatory*. PhD thesis, RWTH Aachen University, Aachen, 2021.

[229] V. Lenok. *Measurement of the Cosmic-Ray Energy Spectrum Using a Novel Approach to Model the Aperture of Radio Arrays*. PhD thesis, Karlsruhe Institute of Technology (KIT), 2022.

[230] E. M. Holt et al. Influence of the Reconstruction Method on the Scale of the Radiation Energy at the Auger Engineering Radio Array (AERA). Internal Auger note, 2019. GAP 2019-040.

[231] V. Lenok. Evolution of the energy fluence in the signal processing pipeline. https://www.auger.unam.mx/AugerWiki/RadioReconstructionAndEventSelectionMinutes, minutes from 2020-09-16.

[232] M. Büsken. Update on the AERA energy scale analysis. https://indico.nucleares.unam.mx/event/2111/contribution/3, 2023.

[233] V. Verzi, private communication.

[234] H. Schoorlemmer. The Discrete Time Fourier Transform and its application to radio data. Internal Auger note, 2022. GAP 2022-056.

[235] C. Glaser. GeoCeLDF Python implementation. https://github.com/cg-laser/geoceLDF.

[236] F. Riehn et al. Hadronic interaction model sibyll 2.3d and extensive air showers. *Physical Review D*, 102:063002, 2020.

[237] M. Bleicher et al. Relativistic hadron-hadron collisions in the ultra-relativistic quantum molecular dynamics model. *Journal of Physics G: Nuclear and Particle Physics*, 25(9):1859, 1999.

[238] M. Gottowik et al. Determination of the absolute energy scale of extensive air showers via radio emission: Systematic uncertainty of underlying first-principle calculations. *Astroparticle Physics*, 103:87–93, 2018.

[239] N. Karastathis. *Simulating radio emission from air showers with CORSIKA 8 - Relevance for energy and mass reconstruction*. PhD thesis, Karlsruhe Institute of Technology (KIT), 2024.

[240] J. Alameddine et al. Simulating radio emission from particle cascades with CORSIKA 8. *Astroparticle Physics*, 166:103072, 2025.

[241] P. Mitra et al. Reconstructing air shower parameters with LOFAR using event specific GDAS atmosphere. *Astroparticle Physics*, 123:102470, 2020.

[242] H. Barbosa et al. Determination of the calorimetric energy in extensive air showers. *Astroparticle Physics*, 22(2):159–166, 2004.

[243] T. Pierog et al. First results of fast one-dimensional hybrid simulation of EAS using CONEX. *Nuclear Physics B - Proceedings Supplements*, 151(1):159–162, 2006.

[244] T. Bergmann et al. One-dimensional hybrid approach to extensive air shower simulation. *Astroparticle Physics*, 26(6):420–432, 2007.

[245] T. Pierog, private communication.

[246] T. Huege and A. Haungs. Radio Detection of Cosmic Rays: Present and Future. In *Proceedings of International Symposium for Ultra-High Energy Cosmic Rays (UHECR2014)*, pp. 010018, 2016.

[247] R. Maccoun and S. Perlmutter. Blind analysis: Hide results to seek the truth. *Nature*, 526(7572):187–189, 2015.

[248] J. P. Brody et al. Significance and statistical errors in the analysis of DNA microarray data. *Proceedings of the National Academy of Sciences*, 99(20):12975–12978, 2002.

[249] C. M. Schäfer. *The XY-Scanner - A Versatile Method for the Absolute End-to-End Calibration of Fluorescence Detectors*. PhD thesis, Karlsruhe Institute of Technology (KIT), 2023.

[250] J. Maindonald and W. Braun. *Data Analysis and Graphics Using R: An Example-Based Approach*. Cambridge Series in Statistical and Probabilistic Mathematics. Cambridge University Press, 2010.

[251] J. Roberts and G. R. Farrar. SD rate as a diagnostic of energy reconstruction drift. Internal Auger note, 2013. GAP 2013-043.

[252] A. Abdul Halim. Quality and Stability of Cosmic Ray Energy Assignments at the Pierre Auger Observatory. Master's thesis, University of Adelaide, 2021.

[253] M. Büsken. https://www.auger.unam.mx/AugerWiki/MeetingMinutes, minutes from 2024-08-12.

[254] M. Straub. Unfolding Antenna Directivity with the Galactic Background. https://indico.nucleares.unam.mx/event/2020/session/4/contribution/30, 2023.

[255] K. F. Weidenhaupt. *Antenna calibration and energy measurement of ultra high energy cosmic rays with the Auger Engineering Radio Array*. PhD thesis, RWTH Aachen University, 2014.

[256] T. Fodran for the Pierre Auger Collaboration. On systematic uncertainties of the AugerPrime Radio Detector. In *Proceedings of 9th International Workshop on Acoustic and Radio EeV Neutrino Detection Activities — PoS(ARENA2022)*, volume 424, pp. 043, 2023.

[257] K. Belov et al. Accelerator Measurements of Magnetically Induced Radio Emission from Particle Cascades with Applications to Cosmic-Ray Air Showers. *Physical Review Letters*, 116:141103, 2016.

[258] K. Bechtol et al. SLAC T-510 experiment for radio emission from particle showers: Detailed simulation study and interpretation. *Physical Review D*, 105(6), 2022.

[259] S. Agostinelli et al. GEANT4: A simulation toolkit. *Nuclear Instruments and Methods in Physics Research*, A506:250–303, 2003.

[260] F. Arqueros et al. Air fluorescence relevant for cosmic-ray detection—Summary of the 5th fluorescence workshop, El Escorial 2007. *Nuclear Instruments and Methods in Physics Research Section A: Accelerators, Spectrometers, Detectors and Associated Equipment*, 597(1):1–22, 2008. Proceedings of the 5th Fluorescence Workshop.

[261] F. Arqueros et al. Air Fluorescence Relevant for Cosmic-Ray Detection - Review of Pioneering Measurements. *Nucl. Instrum. Meth. A*, 597:23–31, 2008.

[262] Y. Tsunesada et al. A description of the air fluorescence emission for reconstructing extensive air showers. In *33rd International Cosmic Ray Conference*, pp. 1014, 2013.

[263] Y. Tsunesada et al. Measurement of UHECR energy spectrum with the Pierre Auger Observatory and the Telescope Array. In *Proceedings of 38th International Cosmic Ray Conference — PoS(ICRC2023)*, volume 444, pp. 406, 2023.

[264] P. Plotko et al. Differences between PAO and TA spectra: Systematics or indication of a local astrophysical source? In *Proceedings of 38th International Cosmic Ray Conference — PoS(ICRC2023)*, volume 444, pp. 229, 2023.